

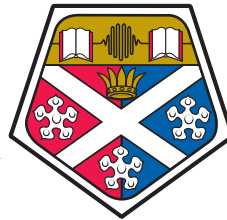
UNIVERSITY OF STRATHCLYDE

Department of Physics

# Hybrid micro-LED devices enabled by elastomeric micro-transfer printing

by

José Filipe Correia Carreira



University of  
**Strathclyde**  
Glasgow

A thesis presented in fulfilment of the  
requirements for the degree of  
Doctor of Philosophy

November 2020

# Declaration of Authorship

This thesis is the result of the author's original research. It has been composed by the author and has not been previously submitted for examination which has led to the award of a degree.

The copyright of this thesis belongs to the author under the terms of the United Kingdom Copyright Acts as qualified by University of Strathclyde Regulation 3.50. Due acknowledgement must always be made of the use of any material contained in, or derived from, this thesis.

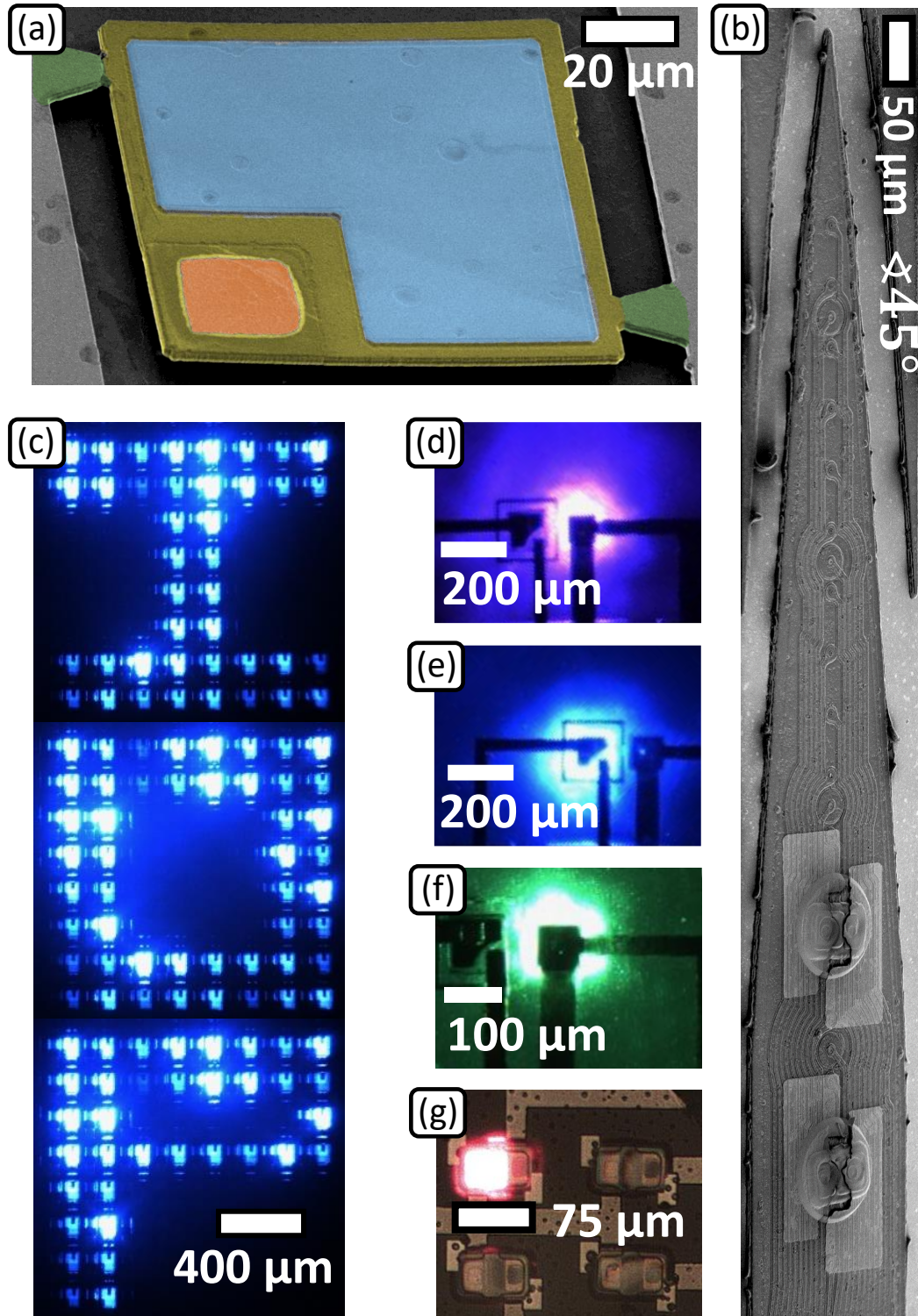
Signed:

---

Date:

---





(a) Colourised scanning electron microscopy (SEM) micrograph of a GaN-based micro-LED platelet; (b) SEM micrograph of a dual-colour micro-LED optrode; (c) CMOS-driven micro-LED array displaying the Institute of Photonics (IoP) logo; (d)-(g) plan-view photographs of violet, blue, green, and red micro-LEDs, respectively.

# *Abstract*

The work presented in this thesis focuses on the development of hybrid micron-sized light emitting diode (micro-LED) devices by elastomeric micro-transfer printing. The main body of this work is divided into the development of dual-colour micro-LED devices and the integration of micro-LEDs with control electronics, mainly for optical communication and optogenetics applications.

Individually addressable III-nitride based blue-green and blue-violet micro-LED arrays and in-series connected blue-green micro-LED arrays were fabricated by micro-transfer printing a blue micro-LED platelet onto to the substrate a pre-fabricated green (or violet) micro-LED. Gigabit per second (Gbps) error-free data rates in free-space visible light communication (VLC) and up to 200 Mbps in highly turbid underwater media have been demonstrated using these dual-colour arrays. Gbps VLC based on III-phosphide red micro-LEDs micro-transfer printed onto diamond and glass substrates is also presented. Furthermore, the integration of III-phosphide red micro-LEDs onto a III-nitride based optrode for dual-colour excitation of different neural populations is also demonstrated. III-nitride based singulated micro-LEDs were directly integrated onto a silicon complementary metal oxide semiconductor (CMOS) drive chip containing a monolithic single photon avalanche diode detector, by elastomeric micro-transfer printing. An 8x8 array was realised with excellent uniformity both in brightness and modulation performance across the full array, which has led to a 128 kbps optical camera communication link, and to a time-of-flight ranging demonstration with cm-scale resolution.

# *Acknowledgements*

This thesis would have not been possible without the help of several people throughout my PhD. First, I would like to thank Prof. Martin Dawson for giving me the opportunity to pursue a PhD at the Institute of Photonics, by believing in me more than I believed in myself. I would like to thank Dr. Michael Strain for his guidance and advice towards the end of my PhD, it was a pleasure to work together. The help of Dr. Johannes Herrnsdorf, Dr. Jonathan McKendry, and Dr. Benoit Guilhabert was life-saving at several moments of my PhD and for that thank you very much! I could not forget to thank Dr. Luis Rino and Dr. Teresa Monteiro for their recommendation.

A huge thank you goes to Dr. Enyuan Xie, who, not only taught me everything I know about microfabrication and micro-LEDs, but also, was a great friend disguised as a mentor (xièxie sh...). I would like to thank Mr. Jim Sweeney for all his hard work in keeping the cleanroom working and also for his help and advice in some processes. Following on that, I would like to thank Dr. Yunzhou Cheng, who also gave me great advice in the cleanroom and from whom I have learnt a lot.

I would like to thank all the colleagues with whom I have collaborated on the application of the devices developed in this thesis. The colleagues at Prof. Harald Haas group from the University of Edinburgh were crucial for this work, in particular Dr. Rui Bian who was always very patient in explaining me OFDM over and over - thank you very much! I would like to thank Dr. Alex Griffiths for all his help with the underwater and CMOS work. I would like to thank Mr. Georgios Arvanitakis for all the work we did together in the underwater measurements and for doing a fantastic job in presenting those results at IPC. Furthermore, during my last months at the IoP I had the pleasure of collaborating with Mr. Ruaridh Winstanley and Prof. Keith Mathieson in the development of novel optrode devices, which was truly exciting!

I would like to thank a few friends who have helped me not only at work but also outside work, and have made the PhD far more enjoyable. I would like to thank Arvan for his friendship and positive thinking throughout these years. I would like to thank Jack for being a great friend and train buddy, I hope he gets to work all right from now on. Jorge and Leire were also such a strong positive influence outside work, and I cannot thank them enough for their company and friendship. Miguel and Ricardo made me feel really welcome when I first arrived, and for that I am very thankful. I would also like to thank Paulo (irmão do outro lado do Atlântico) for his friendship and companionship. Ruaridh was always a cheerful presence in and out of work, always willing to put his work aside to help me or to quote LOTR, thank you Ru! I would like to thank Xiangyu for his friendship and help throughout these years.

I would like to thank the friends I left in Portugal, who were always supportive and made me feel like I had never left, anytime I was back. I would like to thank Ana for all the love, support, and for understanding what it meant to me. In the end, I would like to thank my family, who against their own nature supported my intention of pursuing a PhD abroad and did everything they could to help me.

# Contents

<b>Declaration of Authorship</b>	<b>i</b>
<b>Frontispiece</b>	<b>ii</b>
<b>Abstract</b>	<b>iii</b>
<b>Acknowledgements</b>	<b>iv</b>
<b>List of Figures</b>	<b>ix</b>
<b>List of Tables</b>	<b>xix</b>
<b>Abbreviations</b>	<b>xx</b>
<b>1 Introduction</b>	<b>1</b>
1.1 Brief history of light-emitting diodes . . . . .	2
1.2 Theoretical background . . . . .	6
1.2.1 Introduction to semiconductors . . . . .	6
1.2.1.1 Recombination processes in semiconductors . . . . .	8
1.2.1.2 Intrinsic and extrinsic semiconductors . . . . .	9
1.2.2 Physics of the <i>pn</i> junction . . . . .	11
1.2.3 Double heterostructures and quantum wells . . . . .	13
1.2.4 III-nitride LEDs . . . . .	14
1.2.4.1 Growth on sapphire . . . . .	18
1.2.4.2 Growth on silicon . . . . .	20
1.2.4.3 Dislocations in III-nitrides . . . . .	22
1.2.4.4 Doping . . . . .	23
1.2.4.5 Polarisation effects . . . . .	24
1.2.5 AlGaInP-based LEDs . . . . .	26
1.2.5.1 Growth on GaAs . . . . .	27
1.2.5.2 Doping . . . . .	28
1.2.6 LED efficiency droop . . . . .	28
1.3 Micro-LEDs . . . . .	30
1.4 Micro-transfer printing . . . . .	33
1.5 Summary . . . . .	34
<b>2 Experimental techniques for fabrication of micro light emitting diodes for transfer printing applications</b>	<b>44</b>
2.1 Fabrication of micro-LEDs for transfer printing applications . . . . .	44

2.1.1	Pattern definition . . . . .	45
2.1.1.1	Photolithography . . . . .	45
2.1.2	Pattern transfer . . . . .	47
2.1.2.1	Hard masks by plasma-enhanced chemical vapour deposition . . . . .	47
2.1.2.2	Dry etching . . . . .	48
2.1.2.3	Wet etching . . . . .	50
2.1.3	Metal contacts . . . . .	53
2.1.3.1	Metal deposition by electron beam evaporation . . . . .	53
2.1.3.2	Metal deposition by sputtering . . . . .	54
2.1.3.3	Thermal annealing . . . . .	55
2.2	Mechanics of elastomeric transfer printing . . . . .	56
2.2.1	Physical concepts . . . . .	57
2.2.2	Stamp fabrication process . . . . .	60
2.2.3	Adapted NanoInk NLP 2000 system for micro-transfer printing . . . . .	61
2.2.4	Pixel encapsulation after micro-TP . . . . .	63
2.2.4.1	SU-8 <i>vs</i> Parylene-C . . . . .	66
2.3	Summary . . . . .	68
<b>3</b>	<b>On-chip dual-colour micro-LED arrays and their application in visible light communication and underwater wireless optical communication</b>	<b>72</b>
3.1	Introduction . . . . .	73
3.2	Individually-addressable dual-colour micro-LED arrays . . . . .	76
3.2.1	Device overview . . . . .	76
3.2.1.1	Violet and green micro-LEDs grown on sapphire . . . . .	76
3.2.1.2	Suspended blue micro-LED platelets grown on silicon . . . . .	77
3.2.1.3	Heterogeneous integration by micro-transfer printing . . . . .	77
3.2.2	Electrical, optical and bandwidth performance of single-colour micro-LEDs . . . . .	79
3.2.3	Colour properties of dual-colour micro-LED arrays . . . . .	82
3.2.4	VLC application . . . . .	83
3.2.4.1	VLC modulation schemes . . . . .	83
3.2.4.2	VLC experimental details . . . . .	85
3.2.4.3	Communication performance of the blue-green micro-LED array . . . . .	87
3.2.4.4	Communication performance of the blue-violet micro-LED array . . . . .	89
3.2.5	Underwater Wireless Optical Communication . . . . .	90
3.3	In-series connected blue-green micro-LED array . . . . .	93
3.3.1	Device overview . . . . .	93
3.3.2	Electrical, optical and bandwidth performance of the in-series connected blue-green micro-LED array . . . . .	95
3.3.3	Colour properties of the in-series connected blue-green micro-LED array . . . . .	98
3.3.4	VLC and UWOC application . . . . .	99
3.4	Summary . . . . .	101

<b>4</b>	<b>Integration of AlGaInP red micro-LEDs by micro-TP onto unusual substrates for VLC and optogenetics applications</b>	<b>106</b>
4.1	AlGaInP micro-LED platelets . . . . .	106
4.2	Gbps VLC based on AlGaInP red micro-LEDs micro-transfer printed onto diamond and glass . . . . .	108
4.2.1	Introduction . . . . .	108
4.2.2	Device overview . . . . .	109
4.2.3	Device performance and application . . . . .	110
4.2.3.1	Micro-LED electrical, optical, and bandwidth characteristics . . . . .	110
4.2.3.2	VLC application . . . . .	112
4.3	Dual-colour optrodes for optogenetics application . . . . .	115
4.3.1	Introduction . . . . .	115
4.3.2	Device overview . . . . .	117
4.3.3	Electrical and optical characterisation . . . . .	119
4.4	Summary . . . . .	121
<b>5</b>	<b>Direct integration of micro-LEDs onto CMOS circuitry by micro-transfer printing</b>	<b>125</b>
5.1	Introduction . . . . .	125
5.1.1	Complementary metal-oxide-semiconductor background . . . . .	125
5.1.2	CMOS logic-gate circuits . . . . .	128
5.2	Device overview . . . . .	130
5.2.1	Blue micro-LEDs fabrication . . . . .	130
5.2.2	CMOS chip . . . . .	130
5.2.2.1	Heterogeneous integration by flip-chip bonding . . . . .	131
5.2.3	Heterogeneous integration by micro-transfer printing . . . . .	132
5.2.3.1	Pre-processing of the CMOS chip . . . . .	132
5.2.3.2	Micro-TP of an 8x8 micro-LED array onto a pre-processed CMOS chip . . . . .	135
5.3	Single micro-LED and full array performance . . . . .	137
5.3.1	Single micro-LED electrical, optical, and bandwidth performance . . . . .	137
5.3.2	Micro-LED array performance . . . . .	139
5.4	OCC application . . . . .	140
5.5	On-chip single micro-LED/SPAD operation . . . . .	142
5.5.1	SPAD working principles . . . . .	143
5.5.2	VLC transceiver . . . . .	144
5.5.3	Time-of-flight ranging . . . . .	145
5.6	Summary . . . . .	148
<b>6</b>	<b>Outlook and future work</b>	<b>152</b>
6.1	Future work . . . . .	154
	<b>List of publications</b>	<b>160</b>

# List of Figures

Frontispiece . . . . .	iii
1.1 Photograph of (a) the first red-spectrum GaAsP alloy diode laser and (b) the first GaN <i>pn</i> junction blue LED grown on sapphire (retrieved from [11, 12]). . . . .	3
1.2 (a) Time evolution of the external quantum efficiency (EQE) of visible and ultraviolet LEDs (retrieved from [16]); (b) EQE <i>vs</i> wavelength of high-performance III-nitride and phosphide LEDs and CIE1978 $V(\lambda)$ photopic eye sensitivity function (EQE values and $V(\lambda)$ curve retrieved from [3, 17]).	4
1.3 Everyday applications of LEDs: (a) LED lamp for indoor illumination [18], (b) traffic lights [19], (c) car headlights [20], and (d) heart rate monitoring in wearable fitness trackers [21]. . . . .	5
1.4 Comparison of luminous efficacy of conventional lighting technologies to LED technology (adapted from [22]). . . . .	5
1.5 Cross-section schematic drawing of a packaged high-power LED (adapted from [26]). . . . .	6
1.6 Schematic energy band structures of (a) a direct (e.g. GaAs) and (b) an indirect (e.g. silicon) bandgap semiconductor (adapted from [27]). . . . .	7
1.7 Schematic band diagram illustrating different recombination mechanisms in bulk semiconductors: (a) radiative, (b) Shockley-Read-Hall non-radiative at deep centres, and (c) intraband non-radiative Auger. CB and VB represent the conduction and valence band, respectively (adapted from [16]).	8
1.8 Schematic bond pictures for (a) <i>n</i> -type Si with donor (arsenic) and (b) <i>p</i> -type Si with acceptor (boron); schematic energy band representation of extrinsic semiconductors with (c) donor ions and (d) acceptor ions (adapted from [27]). . . . .	10
1.9 (a) <i>pn</i> junction scheme showing the space charge region, the electric field and the forces acting on the charge carriers; (b) <i>pn</i> junction band diagram under zero bias; (c) <i>pn</i> junction band diagram under forward voltage bias. Adapted from [27, 29]. . . . .	11
1.10 Schematic drawing of (a) homojunction and (b) a double heterostructure both under forward bias (adapted from [3]). The horizontal axis is distance through the structure. . . . .	13
1.11 Schematic band diagram of a quantum well (QW) structure showing the energy difference between the QW ground states ( $E_{e0}$ and $E_{h0}$ ). The $E$ and $z$ axes represent energy and growth direction, respectively (adapted from [30]). . . . .	14



1.12	Bandgap energy <i>vs</i> lattice constant of the AlGaInN material system in wurtzite crystal structure ( $E_g$ and $a_0$ values retrieved from [3]); inset shows a representation of the wurtzite crystal structure (retrieved from [33]).	16
1.13	Epitaxy relationship between <i>c</i> -plane GaN and (a) <i>c</i> -plane sapphire, (b) Si(111) and (c) 6H-SiC (adapted from [36]).	16
1.14	Schematics of (a) polar ( <i>c</i> -plane), (b) semipolar ( $11\bar{2}2$ ), and (c) nonpolar plane ( <i>m</i> -plane) of III-nitride wurtzite crystal structure; (d)-(f) simulated band diagram for $\text{In}_{0.2}\text{Ga}_{0.8}\text{N}(3\text{ nm})/\text{GaN}(15\text{ nm})$ QW grown on <i>c</i> -plane, semipolar ( $11\bar{2}2$ ) and nonpolar ( <i>m</i> )-plane, respectively (adapted from [39]). The vertical axis in (d)-(f) is energy and the horizontal axis is distance through the heterostructure.	17
1.15	(a) Scanning electron microscopy micrograph of patterned sapphire substrate (PSS) [48]; (b) cross-sectional transmission electron microscopy of GaN grown on random-cone PSS (dislocations identified in yellow) [49]; (c) and (d) schematic cross-sectional LED structure and photon trajectories of an LED fabricated in flat substrate sapphire and in PSS, respectively (adapted from [46]).	19
1.16	(a) Atomic force microscopy micrograph of a typical surface of a GaN epilayer grown on a Si substrate, in which each dark spot corresponds to a threading dislocation [36]; (b) GaN on Si after melt-back etching [51]; (c) and (d) examples of cracked GaN LEDs on Si under EL test, showing a non-uniform illumination pattern [36].	21
1.17	(a) <i>In-situ</i> wafer curvature measured during growth of complete $2.8\ \mu\text{m}$ (LED1) and $1.8\ \mu\text{m}$ (LED2) thick LED structures on 6-inch Si substrates (adapted from [55]); (b) and (c) optical images of a badly cracked and a crack free GaN layer on 6 inch Si, respectively [36].	22
1.18	Band diagram of dislocation (a) donor states in conduction band and (b) acceptor states in the valence band; (c) band diagram of GaInN with In rich regions (adapted from [3]).	23
1.19	Schematic cross-section views of surface charges and direction of electric field and polarisation field for spontaneous (sp) and piezoelectric (pz) polarisation in III-nitrides for Ga and N face orientation (adapted from [3]).	25
1.20	Electronic band structure of a quantum well structure showing (left) no QCSE and exhibiting (right) QCSE, resulting in effective bandgap narrowing and spatial separation of electron and hole wavefunctions (adapted from [64]).	25
1.21	Bandgap energy and corresponding wavelength <i>vs</i> lattice constant of $(\text{Al}_x\text{Ga}_{1-x})_y\text{In}_{1-y}\text{P}$ at 300 K. The dashed vertical line shows $(\text{Al}_x\text{Ga}_{1-x})_{0.5}\text{In}_{0.5}\text{P}$ lattice matched to GaAs (retrieved from [3]).	27
1.22	(a) EQE <i>vs</i> current of a AlGaInP-based LED at different temperatures (open black circles indicate the peak position of each curve); (b) efficiency <i>vs</i> current curves of GaN-based UV, blue, and green LEDs at 293 K; - retrieved from [32].	29
1.23	(a) Schematic drawing and (b) scanning electron microscopy micrograph of InGaN/GaN QW micro-LEDs [82]; (c) first III-nitride blue microdisplay [83].	31

1.24	Monolithic (a) green [92] and (b) blue [91] micro-LED microdisplays; illustration of the LiFi concept [95]; micro-LED array integrated with a micro-needle array for neural interfacing [94]. . . . .	31
1.25	(a) Optical image of a flexible GaN-based micro-LED array [117]; (b) optical image of an array of AlGaInP-based micro-LEDs (6x6) tightly stretched on the sharp tip of a pencil [118]; (c) optofluidic neural probe during simultaneous drug delivery and photostimulation [119]; (d) photograph of a 127 ppi full-colour active matrix display on glass in operation [120]; (e) passive-matrix micro-LED display on a flexible substrate [121]; (f) scanning electron microscopy (SEM) micrograph of silicon platelets assembled by micro-transfer printing [122]; SEM micrograph of a polarisation-sensitive cross-nanowire THz detector [123]. . . . .	34
2.1	Schematic process flow for the fabrication of suspended GaN-based micro-LEDs. . . . .	45
2.2	Schematic photolithography process for positive and negative photoresists, respectively. . . . .	46
2.3	(a) Photograph of the mask aligner system used in this work with main features identified; (b) high-pressure mercury lamp typical emission spectrum (from [2]). . . . .	46
2.4	(a) Photograph of an Oxford Plasma 80 Plus plasma-enhanced chemical vapour deposition (PE-CVD) system; (b) schematic drawing of the PE-CVD chamber (adapted from [1]). . . . .	48
2.5	(a) Photograph of an Oxford Plasma 80 Plus reactive ion etching (RIE) system; (b) schematic drawing of an RIE chamber (adapted from [1]). . . . .	48
2.6	(a) Photograph of the inductively coupled plasma (ICP) deep reactive ion etching system used in this work; (b) schematic drawing of an ICP chamber (adapted from [1]). . . . .	49
2.7	Silicon crystal planes and crystallographic directions for (a) (100), (b) (110), and (c) (111) Miller indices (adapted from [1]). . . . .	51
2.8	Schematic of (a) and (b) Si(100) wafer with a SiO <sub>2</sub> square mask opening before and after KOH etching (which exposes the Si(111) planes (identified in red)), respectively; (c) and (d) Si(111) wafer with Si(110) planes exposed (identified in green) before and after KOH etching (which etches the Si(110) plane), respectively (adapted from [1]). . . . .	52
2.9	Plan-view optical microscope images of the KOH etch front progression over time of the planes underneath a GaN platelet. The platelet is 100x100 $\mu\text{m}^2$ . . . . .	53
2.10	(a) Photograph of the e-beam metal deposition system used in this work; (b) schematic drawing of an e-beam deposition chamber (adapted from [1]). . . . .	54
2.11	(a) Photograph of the sputter metal deposition system used in this work; (b) schematic drawing of a sputter deposition chamber (adapted from [1]). . . . .	55
2.12	(a) Photograph of the rapid thermal annealing (RTA) system used in this work; (b) schematic drawing of a RTA chamber (adapted from [1]). . . . .	56
2.13	(a) Scanning electron microscopy (SEM) micrograph of an array of suspended micro-LED platelets; (b) colourised SEM of a single micro-LED platelet. . . . .	56

2.14	Side-view schematic drawing of the generic process flow for kinetically-controlled transfer printing during (a) retrieval and (b) releasing (adapted from [14]). . . . .	57
2.15	Schematic diagram of critical energy release rates for the stamp/film and film/substrate interfaces. The intersection of the horizontal line with the monotonically increasing curve represents the critical peel velocity ( $v_c$ ) for kinetically controlled transfer printing. The horizontal lines at the bottom and top represent very weak and very strong film/substrate interfaces, respectively, corresponding to conditions for which only retrieval and printing can be realised (adapted from [14]). . . . .	58
2.16	(a) Schematic drawing of the four corner pyramidal protrusions (micro-tips) stamp; scanning electron microscopy (SEM) micrographs of the stamp during (b) no contact, (c) roof collapse, and (d) roof de-collapse; (e) adhesion strength as a function of delamination velocity during retrieval (blue curve, stamp in full contact under 1.5 mN preload) and release (green curve, only microtips in contact under 0.2 mN preload) - adapted from [18, 19]. . . . .	60
2.17	Schematic drawing of the elastomer stamp fabrication process flow: (a) SiO <sub>2</sub> deposition on a Si(100) wafer and definition of square openings; (b) definition of pyramidal protrusions by anisotropic wet etching; (c) SiO <sub>2</sub> deposition; (d) definition of the body of the stamp using thick SU-8; (e) pouring of PDMS; (f) PDMS stamp after being peeled-away from the Si(100) mould. . . . .	61
2.18	(a) Photograph of the adapted NanoInk NLP 2000 system for micro-transfer printing; (b) and (c) software interface for the stage motion control and imaging options, respectively; (d)-(i) plan-view (through stamp) optical images acquired with the NLP 2000 system integrated microscope of a micro-LED platelet being transfer printed from its silicon growth substrate onto a rigid substrate without any adhesion enhancement layer. . . . .	62
2.19	(a) Scanning electron microscopy micrograph of a micro-LED transfer printed onto the edge of a rigid substrate (the inset shows in further detail the micro-LED curved edges); (b) atomic force microscopy line scan over the central area of a unbonded micro-LED die and full-length parabolic fit (reproduced from [22]). . . . .	64
2.20	(a) Photograph of the Parylene-C deposition system used in this work; (b) schematic drawing of the Parylene-C deposition system chamber (adapted from [30]). . . . .	65
2.21	Chemical structures of (a) Pa-C and (b) Pa-N [1]. . . . .	66
2.22	Plan-view photographs of a transfer printed micro-LED insulated with (a) SU-8 and (d) Pa-C; (b) and (e) SEM micrographs of a transfer printed micro-LED insulated SU-8 and Pa-C, respectively; (c) and (f) 45°tilted SEM micrographs of a transfer printed micro-LED insulated with SU-8 and Pa-C, respectively. . . . .	66
2.23	(a) Voltage <i>vs</i> current density (JV) curve and (b) optical power density <i>vs</i> current density (LJ) curve of the best performing transfer printed micro-LED insulated with SU-8 (blue squares) and with Pa-C (grey triangles). . . . .	67
2.24	Distribution of voltage at 1 mA and power density at 50 A/cm <sup>2</sup> of a 2x4 array of transfer printed micro-LEDs insulated with (a) SU-8 and (b) Pa-C. . . . .	68

3.1	(a) Full-colour micro-LED display [7]; (b) close-up view of a 48x48 pixelated full-colour LED array, each chip is $100 \times 250 \mu\text{m}^2$ in size [8]; (c) schematic drawing of a full-colour microdisplay with clusters of micro-LEDs acting as VLC transmitters. . . . .	73
3.2	(a) Example of underwater wireless communication applications [11]; (b) schematic of (1) acoustic wave-, (2) microwave-, and (3) optical-based underwater communications [12]. . . . .	74
3.3	Water absorption spectrum (adapted from [19]). . . . .	75
3.4	Schematic drawings of the sapphire substrate micro-LEDs' (violet and green) fabrication process (not to scale, see text for further details). . . . .	76
3.5	(a) and (b) 45 degrees tilted scanning electron microscope (SEM) and atomic force microscope (AFM) micrographs of the PSS, respectively; (c) and (d) 45 degrees tilted SEM and AFM micrographs of the PSS substrate after SU-8 planarisation, respectively. . . . .	78
3.6	Plan-view optical micrographs of the blue-green micro-LED array (a) before and (b) after micro-TP of the blue micro-LED (A and K are the respective anode and common cathode contact pads); plan-view topside optical photograph of the (c) violet, (d) blue and (e) green micro-LEDs individually driven at the current density of $318 \text{ A/cm}^2$ , $15 \text{ A/cm}^2$ and $318 \text{ A/cm}^2$ , respectively; plan-view backside optical photographs of the (f) blue-violet and (g) blue-green micro-LED arrays simultaneously driven at $318 \text{ A/cm}^2$ (green and violet) and $15 \text{ A/cm}^2$ (blue). . . . .	79
3.7	(a)-(c) Voltage <i>vs</i> current density (JV) and optical power <i>vs</i> current density (LJ) curves of the violet, green and blue micro-LEDs, respectively; (d)-(f) electroluminescence (EL) spectra of the violet, green, and blue micro-LEDs, respectively. . . . .	80
3.8	(a) Schematic drawing of the bandwidth measurement experimental setup; (b) photodiode response <i>vs</i> frequency curve (adapted from [25]); (c) E-O bandwidth <i>vs</i> current density curves of the violet, green, and blue micro-LEDs. . . . .	81
3.9	(a) Blue-green micro-LED array CIE1931 coordinates on the CIE1931 colour space chromaticity diagram and photographs of the device at different biases; (b) blue-violet micro-LED array CIE1931 colour coordinates at different biases; (c) electroluminescence spectra from the blue-green and blue-violet array at different integrated area ratios of blue-green and blue-violet, respectively (reproduced from [28]). . . . .	83
3.10	Time waveforms of a on-off keying signal; (b) orthogonal frequency division multiplexing (OFDM) subcarriers in the frequency domain [32]; (c) schematic block diagram of a DC-biased optical OFDM signal generation and demodulation (adapted from [2]). . . . .	85
3.11	Schematic drawing of the experimental setups in wavelength division multiplexing data transmission experiments: (a) setup 1 (WDM1); (b) setup 2 (WDM2). The photograph inset in the schematics is the actual blue-green micro-LED array (wire bonded to a printed circuit board - PCB) being operated in WDM mode. . . . .	86

3.12	Signal-to-noise ratio and allocated bits (at maximum data rate below forward error correction threshold) in both WDM setups achieved by (a) the blue micro-LED and (b) the green micro-LED; (c) blue and green micro-LEDs EL spectra overlaid with the dichroic mirror and bandpass filters optical responses; (d) bit-error-ratio <i>vs</i> data rate for the blue and green micro-LEDs in both WDM setups. . . . .	88
3.13	Signal-to-noise ratio and allocated bits (at maximum data rate below forward error correction) in both WDM setups achieved by (a) the blue micro-LED and (b) the violet micro-LED; (c) blue and violet micro-LEDs EL spectra overlaid with the dichroic mirror and bandpass filters optical responses; (d) bit-error-ratio <i>vs</i> data rate for blue and violet micro-LEDs in both WDM setups. . . . .	89
3.14	(a) Schematic drawing of the experimental setup used in the UWOC demonstration using either FPGA or AWG; (b) photograph of the 1.5 m water tank; (c) plan-view photograph of the 64x64 SPAD array used as detector; (d) schematic drawings of a conventional photodetector, a single SPAD, the SPAD array, and their respective electrical outputs. . . . .	91
3.15	Bit-error-ratio <i>vs</i> Maalox concentration curves of the UWOC WDM demonstration using (a) a FPGA and (b) an AWG to generate the data signal. . . . .	92
3.16	Plan-view optical photographs of (a) the green micro-LED device before micro-TP of a blue micro-LED platelet; (b) the blue-green micro-LED device after micro-TP after electrical vias definition; (c) the blue-green micro-LED device connected in series; (d) the in-series connected blue-green micro-LED array driven at 2 mA. . . . .	94
3.17	(a) Voltage <i>vs</i> current (IV) and optical power <i>vs</i> current (LI) curves of the in-series connected blue-green micro-LED array; (b) IV curve of a comparable single blue micro-LED printed onto glass - inset shows a plan-view photograph of the device; (c) E-O modulation bandwidth of the in-series connected micro-LED array <i>vs</i> current in aggregate, blue component, and green component; (d) E-O modulation bandwidth of a comparable single blue micro-LED printed onto glass. . . . .	95
3.18	(a) Electrical to optical modulation bandwidth <i>vs</i> current density of the L-shaped and the 60x60 $\mu\text{m}^2$ blue micro-LEDs; (b) schematic drawings of the L-shaped and the 60x60 $\mu\text{m}^2$ micro-LEDs (not to scale). . . . .	97
3.19	In-series connected blue-green micro-LED array (a) electroluminescence (EL) spectra and (b) CIE1931 colour coordinates at different driving currents; (c) angular distribution of the integrated area of the blue and green components of the EL spectrum at 9 mA; (d) and (e) EL spectra superimposed with gaussian fits at +45° and -45°, respectively. . . . .	98
3.20	Schematic drawings of the experimental setups employed in the (a) VLC and (b) UWOC data transmission demonstrations. . . . .	100
3.21	(a) Signal to noise ratio and number of allocated bits (at maximum data rate below forward error correction) at 9 and 23 mA of DC bias; (b) bit-error-ratio <i>vs</i> data rate curves for the different DC biases. . . . .	101
3.22	Bit-error-ratio <i>vs</i> Maalox concentration curve of the in-series connected blue-green micro-LED array in an UWOC demonstration. . . . .	101

4.1	(a)-(e) Schematic drawings of the red micro-LED fabrication process (not to scale, see text for further details); (f) plan-view photograph of a 2x2 array of micro-LED platelets on the temporary sapphire carrier; (g) scanning electron microscopy micrograph of a micro-LED platelet backside; (h) representative 5x5 $\mu\text{m}^2$ atomic force microscopy micrograph of a micro-LED platelet backside. . . . .	107
4.2	(a) Illustration of a conceptual micro-LED display [4]; (b) SEM micrograph of an RGB micro-LED IC-controlled pixel [5]; (c) AlGaInP-based micro-LED display [6]. . . . .	108
4.3	(a) Plan-view photograph of the red micro-LED platelets (with the electrical contacts facing up) on the stamp array; (b) plan-view photograph of a 2x2 micro-LED array micro-TP onto glass; (c) schematic drawing of a micro-TP red micro-LED after Pa-C encapsulation and metallisation; (d) plan-view photograph of a finalised 2x2 micro-LED array micro-TP onto glass with a single pixel (S1) driven at 4.3 A/cm <sup>2</sup> . . . . .	109
4.4	(a) Voltage <i>vs</i> current density (JV) and optical power density <i>vs</i> current density (LJ) curves of the micro-LED S1 on-diamond and on-glass; (b) electrical to optical modulation bandwidth <i>vs</i> current density of the single S1 micro-LED on both substrates. . . . .	111
4.5	(a) Electroluminescence (EL) spectra and (b) CIE1931 colour coordinates of the single micro-LED S1 (at 359 A/cm <sup>2</sup> ) on both substrates; (c) EL spectra peak position <i>vs</i> current density of the micro-LED S1 on both substrates. . . . .	111
4.6	Schematic diagram of the visible light communication experimental setup. The photograph inset is the micro-LED on-diamond device (edge of the device is 1 cm). . . . .	112
4.7	(a) Signal-to-noise ratio and number of allocated bits (at maximum data rate below forward error correction of the single micro-LED S1 on both substrates (glass and diamond); (b) bit-error-ratio <i>vs</i> data rate of the single micro-LED S1 and in-parallel micro-LED array P on both substrates. . . . .	113
4.8	(a) Illustration of the optogenetic technique using blue light, which activates Chr2-expressing neuron cells by opening light sensitive channels [20]; (b) electrical stimulation <i>vs</i> optogenetics (excitation/inhibition) (adapted from [26]); (c) schematic of probe insertion and high-pass filtered signals from two separate recording channels showing the depth-dependent activation of neurons <i>in vivo</i> [27]. . . . .	116
4.9	Schematic drawing of the (a) full optrode and (b) the tip of the shank with the micro-LEDs active area highlighted in green; (c) plan-view photograph of the shank tip with micro-LED ( $\mu\text{LED}$ ) and $\mu$ -electrodes identified in blue and green, respectively. . . . .	118
4.10	(a) Schematic process flow of the micro-transfer printing of a red micro-LED platelet onto an optrode (courtesy of Mr. Ruaridh Winstanley); (b) plan-view photograph of an optrode after micro-TP of the red micro-LED platelets. . . . .	118

4.11	45° tilted scanning electron microscopy (SEM) micrograph, after Pa-C encapsulation and metallisation, of (a) the shank tip and of (b) a red and a blue micro-LED ; (c) colourised SEM micrograph (the colours green, blue, purple and red correspond to the micro-electrode, the blue micro-LED, the metal tracks and the red micro-LED, respectively) - courtesy of Mr. Ruairidh Winstanley; (d) plan-view photograph of the red micro-LED after Pa-C encapsulation and metallisation. . . . .	119
4.12	Voltage <i>vs</i> current density and irradiance <i>vs</i> current density curves of (a) the monolithic blue micro-LED and of (b) the transfer printed red micro-LED, respectively, alongside with a plan-view photograph of the shank tip with both micro-LEDs being driven simultaneously at 100 $\mu$ A. . . . .	120
4.13	Monolithic blue and micro-TP red micro-LEDs individual EL spectra superimposed with ChR-2, Chrimson and Jaws opsins absorption spectra (adapted from [29, 30]). . . . .	121
5.1	CMOS-driven micro-LED arrays in several applications: (a) microdisplays [1]; (b) visible light communication [2]; (c) spatial navigation [3]; (d) maskless photolithography [4]; and (e) optoelectronic tweezing [5]. . . . .	126
5.2	Schematic cross-section drawing of (a) NMOS and (b) PMOS (adapted from [6]). . . . .	126
5.3	(a)-(c) Schematic cross-section drawing of an NMOS during cutoff, triode, and saturation regions, respectively; (d) characteristic curves for an NMOS (adapted from [8]). . . . .	127
5.4	(a)-(d) NOT gate block representation, circuit diagram, and operation when the logic input is a logic 1 and a 0, respectively; (e)-(g) NAND gate block representation, circuit diagram, and truth table, respectively; (h)-(j) NOR gate block representation, circuit diagram, and truth table, respectively (adapted from [8]). . . . .	129
5.5	CMOS backplane driver circuit (reproduced from [9]). . . . .	131
5.6	(a)-(c) Schematic drawing of the flip-chip bonding process; (d) micro-LED array flip-chip bump-bonded to a CMOS showing a few defects (reproduced from [10]); (e) blue and (f) green micro-LED arrays flip-chip bump-bonded to a CMOS showing light waveguiding in the sapphire substrate. . . . .	132
5.7	(a)-(c) Optical photographs of the CMOS bare chip and drivers, before any processing, at different magnifications; (d) voltage <i>vs</i> current curves of the <i>LED_VDD</i> to <i>LED_VDD</i> (green curve) and <i>BU_MOD_CONT</i> to <i>BU_COL_SEL</i> (red curve) bonding pads before any process. . . . .	133
5.8	(a) and (b) optical images of the CMOS chip bonding pads after oxygen etching of the Pa-C layer; (c) optical image of a transfer printed micro-LED, after Pa-C etching, being electrical driven by external probes - scale bar corresponds to 100 $\mu$ m; (d) current <i>vs</i> voltage curves of the <i>LED_VDD</i> to <i>LED_VDD</i> (green curve) and <i>BU_MOD_CONT</i> to <i>BU_COL_SEL</i> (red curve) bonding pads after Pa-C etching; (e) scanning electron microscopy micrograph of a CMOS driver and (f) correspondent energy-dispersive X-ray spectroscopy spectrum. . . . .	134
5.9	(a) Plan-view photograph of the CMOS bonding pads and drivers after the Ti/Au patterning step and before the Pa-C etching; (b) plan-view photograph of the CMOS driver after Pa-C etching; (c) <i>LED_VDD</i> and <i>BU_MOD_CONT</i> IV curves of the bare chip (in solid) and after Pa-C etching the CMOS chip with protected drivers (in dash). . . . .	135

5.10	Schematic drawing of the micro-transfer printing process during (a) pick-up and (b) printing of the micro-LED platelet; (c) schematic cross-section drawing of the finalised device; (d) optical image of the CMOS chip with the CMOS drivers array and SPAD identified in red and yellow, respectively; (e) magnification showing in further detail the SPAD active area; (f) magnification of the CMOS chip showing the 8x8 array of transfer printed micro-LEDs; (g) shows, in further detail, the micro-LED <i>p</i> -GaN electrical connection through the adjacent p-MOS driver; (h) plan-view photograph of the motherboard used to interface with the CMOS chip; (i) plan-view photograph of the CMOS driven micro-LED array displaying the Institute of Photonics (IOP) logo. . . . .	136
5.11	CMOS-driven micro-LED voltage <i>vs</i> current density (JV) curve, optical power density <i>vs</i> current density (LJ) curve, and electroluminescence spectrum (EL). . . . .	137
5.12	Schematic drawing of the experimental setup of electrical-to-optical modulation bandwidth measurement. . . . .	138
5.13	CMOS-driven micro-LED electrical-to-optical (E-O) modulation bandwidth <i>vs</i> current density. . . . .	138
5.14	“Heat map” distribution of (a) forward voltage and (b) optical power density at 60 A/cm <sup>2</sup> across the full array. . . . .	139
5.15	Multiple-input-multiple-output (MIMO) optical camera communication link (adapted from [19]). . . . .	140
5.16	The block of frames transmitted for synchronisation, threshold, alignment, and data transmission. . . . .	141
5.17	(a) Bit-error-ratio (BER) measured as a function of received power by the ultrafast camera; (b)-(e) show the captured frames from the 8000 fps video for all active micro-LEDs, alignment conditions, and two different pseudo-random patterns, respectively. . . . .	142
5.18	(a) Schematic drawing of the experimental setup used in VLC ( $\Delta x \sim 2$ cm) and ToF ranging ( $\Delta x = 0:0.2:1.2$ m) demonstrations; (b) schematic drawing of the input electrical signal for the VLC and ToF experiments. . . . .	142
5.19	(a) Illustration of avalanche breakdown and (b) schematic cross-section of a single-photon avalanche diode (adapted from [14, 25]). . . . .	143
5.20	Bit-error-ratio (BER) measured as a function of the incident power on the SPAD. . . . .	144
5.21	Pulsed optical time-of-flight working principle (adapted from [27]). The target is a photograph of the Technology and Innovation Centre building in Glasgow, UK (retrieved from [29]). . . . .	145
5.22	(a) Forward and (b) reverse time-correlated single-photon counting operation modes. . . . .	146
5.23	Photons arrival time histogram acquired at (a) 0 m and at (b) 1.2 m. . . . .	147
5.24	Measured distance plotted as a function of the actual distance in a ranging setup. . . . .	148
6.1	(a) Plan-view photograph of the 2x4 array of dual-colour micro-LEDs (either blue-violet or blue-green); (b)-(d) voltage and optical power density distribution of blue, green, and violet micro-LED arrays, respectively. . . . .	155
6.2	Block diagram of wavelength division multiplexing multiple-input-multiple-output modulation scheme. . . . .	156



---

6.3	Schematic drawing of a red-green-blue (RGB) micro-LED array enabled by micro-transfer printing. . . . .	156
6.4	(a) Schematic of a top-emitting VCSEL (inset shows a cross-sectional electron microscopy micrograph) [7]; (b) scanning electron microscopy micrograph of a single micro-VCSEL printed on glass [8]; (c) schematic cross-section of a micro-VCSEL printed on a CMOS. . . . .	157

# List of Tables

1.1	Important properties of the AlGaInN binary alloys (in wurtzite phase) at room temperature (retrieved from [3]). . . . .	15
1.2	Comparison of <i>c</i> -plane sapphire, Si(111), and 6H-SiC as growth substrates for <i>c</i> -plane GaN (retrieved from [37, 38]). . . . .	17
1.3	Important properties of III-V phosphides and GaAs at room temperature (retrieved from [3]). . . . .	26
2.1	Orientation dependent etch rate ( $\mu\text{m}/\text{min}$ ) for a 30% concentration KOH solution at 70 °C [5]. . . . .	51
3.1	Comparison between OWC and RF, where $P_{opt}$ and $A_{RF}$ correspond to the optical power and amplitude of the RF carrier, respectively [2]. . . . .	84
3.2	Error-free data rates for each channel and aggregated in WDM1 and WDM2 setups achieved by the blue-green micro-LED array. . . . .	88
3.3	Error-free data rates for each channel and aggregated in WDM1 and WDM2 setups achieved by the blue-violet micro-LED array. . . . .	90
3.4	Data rates for the blue-green and blue-violet micro-LED arrays using a FPGA or an AWG. . . . .	93
4.1	State-of-the-art of red LED-based VLC. . . . .	114
5.1	CMOS chip specifications. . . . .	130
5.2	Single photon avalanche diode specifications. . . . .	144

# Abbreviations

<b>3D</b>	3-dimensional
<b>ADC</b>	Analogue-to-digital-converter
<b>AFM</b>	Atomic Force Microscopy
<b>Al</b>	Aluminium
<b>AlGaInP</b>	Aluminium Gallium Indium Phosphide
<b>AlGaN</b>	Aluminium Gallium Nitride
<b>AlN</b>	Aluminium Nitride
<b>Ar</b>	Argon
<b>Au</b>	Gold
<b>AUV</b>	Automated Unmanned Vehicle
<b>AWG</b>	Arbitrary Waveform Generator
<b>BCB</b>	Benzocyclobutene
<b>BER</b>	Bit-Error-Ratio
<b>CB</b>	Conduction Band
<b>ChR-2</b>	Channelrhodopsin-2
<b>CIE</b>	Commission Internationale de l'Eclairage
<b>CMOS</b>	Complementary Metal-Oxide-Semiconductor
<b>CP</b>	Cyclic Prefix
<b>CVD</b>	Chemical Vapour Deposition
<b>DAC</b>	Digital-to-Analogue Converter
<b>DBR</b>	Distributed Bragg Reflector
<b>DC</b>	Direct Current
<b>DCO-OFDM</b>	DC-biased Optical Orthogonal Frequency Division Multiplexing
<b>DD</b>	Direct Detection
<b>EDS/EDXS</b>	Energy-Dispersive X-ray Spectroscopy

---

<b>E-E</b>	Electrical-to-Electrical
<b>EL</b>	Electroluminescence
<b>E-O</b>	Electrical-to-Optical
<b>EQE</b>	External Quantum Efficiency
<b>ESL</b>	Etching Stop Layer
<b>FEC</b>	Forward Error Correction
<b>FFT</b>	Fast Fourier Transform
<b>FPGA</b>	Field Programmable Gate Array
<b>FWHM</b>	Full Width at Half Maximum
<b>GaAs</b>	Gallium Arsenide
<b>GaAsP</b>	Gallium Arsenide Phosphide
<b>GaInP</b>	Gallium Indium Phosphide
<b>Ge</b>	Germanium
<b>HF</b>	Hydrogen Fluoride
<b>ICP</b>	Inductively Coupled Plasma
<b>IFFT</b>	Inverse Fast Fourier Transform
<b>IM</b>	Intensity Modulation
<b>InGaN</b>	Indium Gallium Nitride
<b>InN</b>	Indium Nitride
<b>IOP</b>	Institute of Photonics
<b>IQE</b>	Internal Quantum Efficiency
<b>IR</b>	Infrared
<b>IV</b>	Current <i>vs</i> Voltage
<b>JV</b>	Voltage <i>vs</i> Current Density
<b>KOH</b>	Potassium Hydroxide
<b>LED</b>	Light Emitting Diode
<b>LI</b>	Optical Power <i>vs</i> Current
<b>LiFi</b>	Light Fidelity
<b>LJ</b>	Optical power density <i>vs</i> Current Density
<b>MIMO</b>	Multiple-Input-Multiple-Output
<b>MOCVD</b>	Metal Organic Chemical Vapour Deposition
<b>MOSFET</b>	Metal Oxide Semiconductor Field-Effect Transistor
<b>M-QAM</b>	M-ary Quadrature Amplitude Modulation

---

<b>MQW</b>	Multiple Quantum Well
<b>N<sub>2</sub></b>	Nitrogen
<b>Ni</b>	Nickel
<b>NIR</b>	Near-infrared
<b>NMOS</b>	<i>n</i> -type Metal Oxide Semiconductor
<b>OCC</b>	Optical Camera Communication
<b>OFDM</b>	Orthogonal Frequency Division Multiplexing
<b>OOK-NRZ</b>	On-Off Keying Non-Return-to-Zero
<b>OWC</b>	Optical Wireless Communication
<b>P/S</b>	Parallel-to-serial
<b>Pa-C</b>	Parylene-C
<b>PAC</b>	Photo Active Compound
<b>Pa-N</b>	Parylene-N
<b>PCB</b>	Printed Circuit Board
<b>Pd</b>	Palladium
<b>PDMS</b>	Polydimethylsiloxane
<b>PECVD</b>	Plasma-Enhanced Chemical Vapour Deposition
<b>PGMEA</b>	Propylene Glycol Methyl Ether Acetate
<b>PMOS</b>	<i>p</i> -type Metal Oxide Semiconductor
<b>ppi</b>	pixel per inch
<b>PR</b>	Photoresist
<b>PSS</b>	Patterned Sapphire Substrate
<b>PVD</b>	Physical Vapour Deposition
<b>QAM</b>	Quadrature Amplitude Modulation
<b>QCSE</b>	Quantum Confined Stark Effect
<b>QW</b>	Quantum Well
<b>RF</b>	Radio Frequency
<b>RGB</b>	Red-Green-Blue
<b>RIE</b>	Reactive Ion Etching
<b>RMS</b>	Root-Mean-Square
<b>RT</b>	Room Temperature
<b>RTA</b>	Rapid Thermal Annealing
<b>S/P</b>	Serial-to-parallel

---

<b>SEM</b>	Scanning Electron Microscopy
<b>Si</b>	Silicon
<b>SiC</b>	Silicon Carbide
<b>SiN<sub>x</sub></b>	Silicon Nitride
<b>SiO<sub>2</sub></b>	Silicon Dioxide
<b>SNR</b>	Signal-to-Noise Ratio
<b>SPAD</b>	Single Photon Avalanche Diode
<b>SRH</b>	Shockley-Read-Hall
<b>SU-8</b>	Negative tone photoresist
<b>TCSPC</b>	Time Correlated Single Photon Counting
<b>Ti</b>	Titanium
<b>ToF</b>	Time-of-Flight
<b>TP</b>	Transfer Printing
<b>UV</b>	Ultraviolet
<b>UWOC</b>	Underwater Wireless Optical Communication
<b>VB</b>	Valence Band
<b>VCSEL</b>	Vertical Cavity Surface Laser Emission
<b>VLC</b>	Visible Light Communication
<b>WDM</b>	Wavelength Division Multiplexing

*À minha família*

# Chapter 1

## Introduction

This thesis focuses on the development of hybrid micron-sized light-emitting diode (micro-LED) devices enabled by elastomeric micro-transfer printing (micro-TP). In particular, this work is divided into two main research topics: (1) integration of different colour micro-LEDs onto the same substrate for communications and optogenetics applications; and (2) direct integration of micro-LEDs onto complementary metal oxide semiconductor (CMOS) circuitry for active control over individual pixels. As such, Chapter 1 gives a general introduction to the basic properties and characteristics of LEDs, with a strong emphasis on gallium nitride (GaN) and aluminium gallium indium phosphide (AlGaInP)-based LEDs. This chapter starts with a brief historical perspective on the development of LEDs from early days to today's high performance solid-state light emitters. The physics and operating principles of LEDs are described, and III-nitride and AlGaInP based LEDs discussed in further detail.

Chapter 2 describes the experimental techniques and systems required for the fabrication of micro-LEDs and the mechanics of elastomeric transfer printing. In this chapter, the techniques (lithography, etching, metallisation) and associated tools required for the fabrication of the hybrid micro-LED devices are presented. The technique of elastomeric micro-transfer printing is discussed in further detail, from the basic physical concepts to stamp fabrication. This chapter is concluded by demonstrating the advantages of using Parylene-C as an insulation/encapsulation layer over conventional SU-8 epoxy.

Chapter 3 shows the fabrication, characterisation and application of on-chip dual-colour micro-LED array in visible light communication (VLC) and underwater wireless optical communication. This chapter is divided into two sections: (1) individually-addressable blue-violet and blue-green micro-LED arrays; and (2) in-series connected blue-green micro-LED arrays. Such micro-LED arrays, developed in collaboration with



Dr. Enyuan Xie, achieve free-space gigabit per second (Gbps) VLC data rates and up to 200 megabit per second (Mbps) in highly turbid water environments.

Chapter 4 focuses on the integration of AlGaInP red micro-LEDs by micro-TP onto unusual substrates for VLC and optogenetics applications. First, the AlGaInP structure and fabrication workflow are briefly described. Next, the integration of these micro-LEDs onto glass and diamond substrates and their application in VLC are demonstrated. Thanks to diamond's exceptional thermal properties, VLC data rates up to 6.6 Gbps are achieved by the AlGaInP micro-LEDs, which is currently the record for AlGaInP structures of these dimensions. This chapter is concluded by demonstrating a dual-colour optrode based on monolithic GaN-based LEDs and transfer printed AlGaInP micro-LEDs, and its potential for distinct neural population optogenetic studies.

Chapter 5 presents the direct integration micro-LEDs onto CMOS circuitry by elastomeric micro-TP. This chapter describes the workflow and process optimisation stages that led to the development of a 8x8 array of micro-LEDs with high brightness and modulation uniformity. The potential of the full 8x8 array as an optical camera communication transmitter is demonstrated. This chapter is concluded by showing the operation of the CMOS micro-LED hybrid device as a VLC transceiver and as a time-of-flight ranging device. This thesis closes with conclusions and future work perspectives.

## 1.1 Brief history of light-emitting diodes

Electroluminescence was first reported by Henry J. Round in 1907 [1], when he observed, at room temperature, a yellowish light being emitted by a silicon carbide (SiC) crystal. However, it was not until the 1950s, with the advent of both the theoretical understanding and the development of tools for semiconductors, that researchers shifted their attention towards, what are the basis of modern LEDs, the III-V alloys. This was a key step, and in 1962, infrared (870-980 nm) LEDs and lasers based on gallium arsenide (GaAs) were demonstrated. In the same year, Holonyak and Bevacqua [2] demonstrated the first direct bandgap, visible (red 650 nm) gallium arsenide phosphide (GaAsP) LEDs and lasers (Fig. 1.1(a)). This, not only showed the viability of III-V alloys for LEDs and laser diodes but also contributed towards the commercialization and mass production of such devices [3]. Green emission based on nitrogen doped gallium phosphide (GaP:N) was introduced shortly after by AT&T Bell Labs [4]. These low-brightness early LEDs were mainly used as indicator lights and as displays for calculators and watches [3]. Based on the work developed for visible-spectrum lasers, high-efficiency red LEDs from the aluminium gallium indium phosphide (AlGaInP) material system were reported in the early 1990s [5]. These LED structures are suitable for high-brightness emission in the

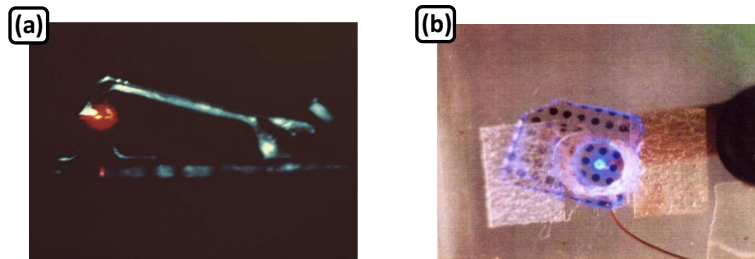


FIGURE 1.1: Photograph of (a) the first red-spectrum GaAsP alloy diode laser and (b) the first GaN  $pn$  junction blue LED grown on sapphire (retrieved from [11, 12]).

red, orange and yellow spectral range and are currently the dominant high-brightness emitters in that wavelength range [3].

The search for shorter wavelength LEDs started in the late 1960s with SiC and gallium nitride (GaN) being considered. The first current injected GaN blue light emitter was announced by Pankove *et al.* in 1972 [6]. However, at the time the growth of high quality GaN was quite challenging and  $p$ -type conductivity continued to elude researchers, which led to the withdrawal of many research groups from the nitride field [3, 7]. In fact, the highly inefficient indirect bandgap SiC blue LED was the commercially available option up until the 1990s. There were two crucial technological processes that enabled the development of  $pn$  junction GaN blue LEDs: (1) growth of high quality GaN films on sapphire substrates by metalorganic vapour phase epitaxy using a low-temperature aluminium nitride (AlN) buffer (in 1986), thus improving the crystal quality and GaN electrical and luminescent properties [8]; (2) the development, in 1989, of  $p$ -type conductivity in magnesium doped GaN by using postgrowth low-energy electron beam irradiation treatment (LEEBI) [9], leading to the first  $pn$  junction GaN blue LED (Fig. 1.1(b)). In the following years, Nakamura *et al.* [10] demonstrated high-brightness InGaN blue, green and yellow LEDs with quantum well structures, laying the foundation for high-performance III-nitride LEDs.

In the development of high-efficiency LEDs two metrics are used to quantitatively evaluate device performance: the internal and external quantum efficiency (IQE and EQE). The IQE ( $\eta_{int}$ ) is defined as the number of photons emitted from the active region per second divided by the number of electrons injected into the LED per second, which can be written as [3]:

$$\eta_{int} = \frac{P_{int}/(h\nu)}{I/e} \quad (1.1)$$

where  $P_{int}$  is the optical power emitted from the active region,  $h$  is Planck's constant,  $\nu$  is the emitted light frequency,  $I$  the injection current, and  $e$  the elementary charge.

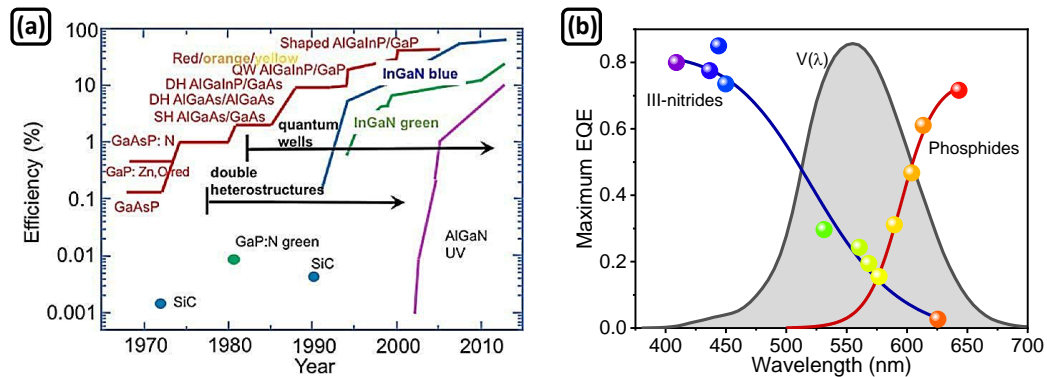


FIGURE 1.2: (a) Time evolution of the external quantum efficiency (EQE) of visible and ultraviolet LEDs (retrieved from [16]); (b) EQE *vs* wavelength of high-performance III-nitride and phosphide LEDs and CIE1978  $V(\lambda)$  photopic eye sensitivity function (EQE values and  $V(\lambda)$  curve retrieved from [3, 17]).

In an ideal LED the active region would emit one photon per electron injected. However, the IQE strongly depends on the active layer crystalline quality and defect density, which depend on growth conditions (temperature, pressure, amongst others), the growth technique and the choice of substrate [13]. Nevertheless, at the present time, IQEs approaching 100% and 90% have been reported for III-phosphide and III-nitride materials, respectively [14, 15].

In an ideal LED, all the photons emitted by the active area are also emitted into free space. However, in a real LED, not all the power emitted by the active area escapes the LED die. Light might be absorbed by the substrate (e.g. GaAs is not transparent in the visible spectral region) and/or undergo total internal reflection being trapped inside the LED die. The ratio between the number of photons emitted into free space per second and the number of electrons injected into LED per second is defined as the EQE, and can be expressed as [3]:

$$\eta_{ext} = \frac{P/(h\nu)}{I/e} = \eta_{int} \cdot \eta_{extraction} \quad (1.2)$$

where  $P$  is the optical power emitted into free space and  $\eta_{extraction}$  is the light extraction efficiency (LEE)\*. Figure 1.2(a) shows the time of evolution of the EQE of visible and ultraviolet LEDs from the initial GaAsP, GaP:N, and SiC to present day AlGaInP phosphide and III-nitrides. Figure 1.2(b) shows the maximum EQE *vs* wavelength of high-performance commercially available III-nitride and phosphide LEDs, from which the decrease of EQE in the green spectral range is obvious. This phenomenon, known as the *green gap*, is almost compensated by the human eye's stronger response in the

\*Different strategies have been employed to increase the LEDs' light extraction efficiency, such as the use of patterned growth substrates (patterned sapphire substrate), post-growth substrate removal or the integration of photonic crystals [3].



FIGURE 1.3: Everyday applications of LEDs: (a) LED lamp for indoor illumination [18], (b) traffic lights [19], (c) car headlights [20], and (d) heart rate monitoring in wearable fitness trackers [21].

green spectral region, as shown by the CIE1978  $V(\lambda)$  photopic eye sensitivity function (grey curve - Fig. 1.2(b)).

High-efficiency LEDs can be found in everyday applications, such as indoor illumination (Fig. 1.3(a)), traffic lights (Fig. 1.3(b)), car headlights (Fig. 1.3(c)), and heart rate monitoring in wearable fitness trackers (Fig. 1.3(d)). The importance of LEDs, especially their application in long-lasting and more efficient white light lamps, was acknowledged in 2014 by the Nobel Prize Committee, who awarded the Nobel Prize in Physics to I. Asaki, H. Amamo, and S. Nakamura “for having invented a new energy-efficient and environment-friendly light source – the blue light-emitting diode” [22].

Figure 1.4 compares different light sources used throughout time, from the oil lamp to the 21<sup>st</sup> century LED lamp<sup>†</sup>. The efficacy of the conversion of electrical power to luminous flux of white light is measured in terms of lumens per watt (lm/W). The lumen is the unit of luminous flux, which represents the light power of a source as perceived by the human eye [3]. In terms of energy saving, white LEDs are theorised to save 95% and

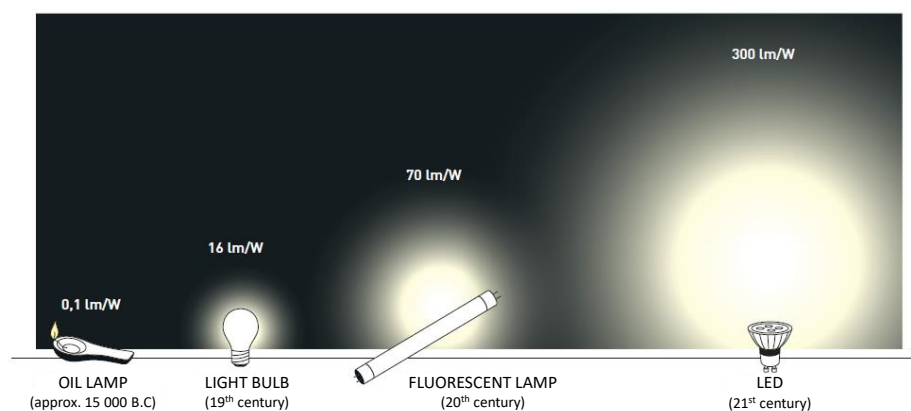


FIGURE 1.4: Comparison of luminous efficacy of conventional lighting technologies to LED technology (adapted from [22]).

<sup>†</sup>An excellent historical perspective on the physics of artificial lighting can be found in reference [23].

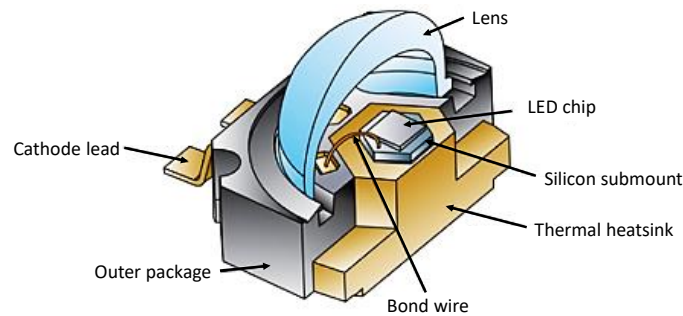


FIGURE 1.5: Cross-section schematic drawing of a packaged high-power LED (adapted from [26]).

80% more energy than incandescent and fluorescent lamps, respectively [24]. In fact, the mechanical robustness, low power consumption, long lifespan and high efficiency of LEDs have been the foundation of the solid state lighting revolution, in which conventional incandescent and fluorescent light lamps have been progressively replaced by greener and lower-cost LED lighting systems.

Figure 1.5 shows the cross-section schematic drawing of a packaged high-power LED ( $> 100 \text{ lm/W}$ ). The LED die, with an active area size between  $300 \times 300 \mu\text{m}^2$  to a few  $\text{mm}^2$ , is mounted on a silicon submount, which sits on top of a thermal heatsink. The die is wire bonded to metal frame and easily electrically addressed by the outer cathode and anode leads (anode not shown in Fig. 1.5). The die is encapsulated with silicone and then covered with a plastic lens, maximising the light output. In low power LEDs, no heatsink is employed and the die is only encapsulated with silicone [3, 25].

## 1.2 Theoretical background

### 1.2.1 Introduction to semiconductors

Solid-state materials can be grouped into insulators, semiconductors, and conductors. A semiconductor is classified as having a conductivity between  $10^{-8}$  to  $10^3 \text{ S/cm}$  [27] and an electronic energy gap between zero and  $\sim 4 \text{ eV}^\ddagger$  [28]. The conductivity of a semiconductor is generally sensitive to temperature, illumination, magnetic field, and minimal amounts of impurity atoms. This possibility of fine tuning a semiconductor's conductivity is what makes the semiconductor one of the most important materials for electronic and photonic applications [27].

---

<sup>‡</sup>It must be noted that there are exceptions to this definition, with terms such as semiconducting diamond and semi-insulating GaAs, with electronic energy gaps of 6 eV and 1.5 eV, respectively, being frequently used [28].

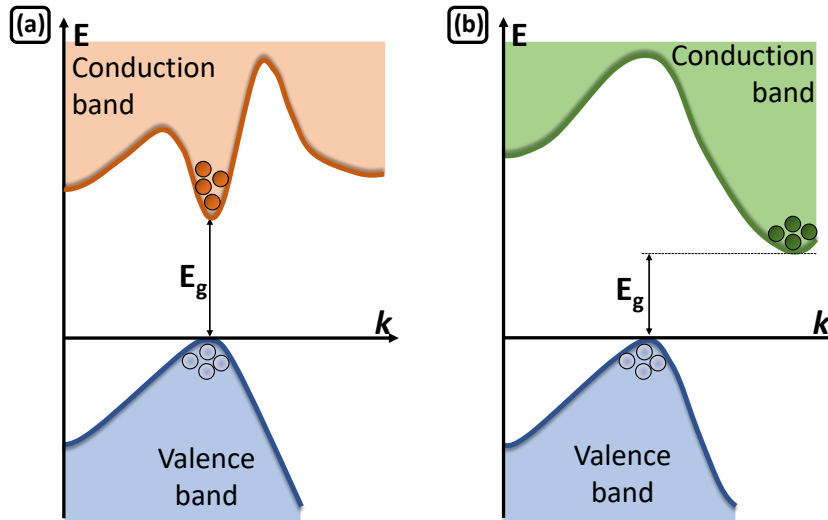


FIGURE 1.6: Schematic energy band structures of (a) a direct (e.g. GaAs) and (b) an indirect (e.g. silicon) bandgap semiconductor (adapted from [27]).

For an isolated atom, the electrons can have discrete energy levels, for example the energy levels of Bohr's hydrogen atom. In the case of bulk materials, such as semiconductor crystals, as the  $N$  isolated atoms that form the crystal are brought together, the orbits of the outer electrons of different atoms overlap and interact with each other. This interaction causes a shift in the energy levels and  $N$  separate but closely spaced levels arise, which for large  $N$  results in an essentially continuous band of energy. At absolute zero ( $T=0$  K), electrons occupy the lowest energy states, so that all the states in the lower band (valence band) are full and all the states in the upper band (conduction band) are empty. The bottom of the conduction band is called  $E_c$  and the top of the valence band is called  $E_v$ . The bandgap energy ( $E_g$ ) between the bottom of the conduction band and the top of the valence band ( $E_c - E_v$ ) is the width of the forbidden energy gap. Physically,  $E_g$  can be regarded as the energy required to break a bond in the semiconductor to free an electron to the conduction band and leave a hole<sup>§</sup> in the valence band [27].

Figure 1.6 shows the energy band structures of 1.6(a) GaAs (electrons orange circles, holes blue circles) and 1.6(b) Si (electrons green circles, holes blue circles). For GaAs the maximum in the valence band and the minimum in the conduction band occur at the same momentum ( $k$ ). GaAs is an example of direct bandgap semiconductor as it does not require a change in momentum for an electron transition from the valence band to the conduction band. On the other hand, for Si the maximum in the valence band and the maximum in the conduction band occur at different momentum  $k$ . Silicon is an indirect bandgap semiconductor because a change in momentum is required in

<sup>§</sup>A hole is the absence of an electron. A hole behaves as a quasi-particle with opposite charge of the electron (positive) and an effective mass [28].

an electronic transition between the valence and the conduction band. This change in momentum is achieved by emission of a phonon, which is defined as a collective vibration of the crystal lattice, resulting in heat [27]. As direct bandgap semiconductors do not require phonons for electronic transitions between the conduction and valence band, they are very efficient at generating photons, and are thus the material of choice for light emitting applications (LEDs and laser diodes).

### 1.2.1.1 Recombination processes in semiconductors

In semiconductors electrons and holes recombine either radiatively (with photon emission) or non-radiatively. The former process is highly preferable in light-emitting devices, while the latter is unwanted in most optoelectronic devices since it often results in detrimental heat generation.

Figure 1.7 illustrates several recombination processes that occur in bulk semiconductors. Radiative recombination occurs when an electron in the conduction band recombines with a hole in the valence band, emitting a photon (Fig. 1.7(a)). The relation between the bandgap energy and emitted photon wavelength ( $\lambda$ ) is given by Eq. 1.3:

$$E_{\text{photon}} = E_g = \frac{hc}{\lambda} \quad (1.3)$$

where  $c$  is the speed of light. On the other hand, non-radiative recombination (without photon emission) can also happen in the semiconductor bulk. Defects in the crystal structure such as: unwanted foreign atoms, native defects (interstitials, vacancies, and

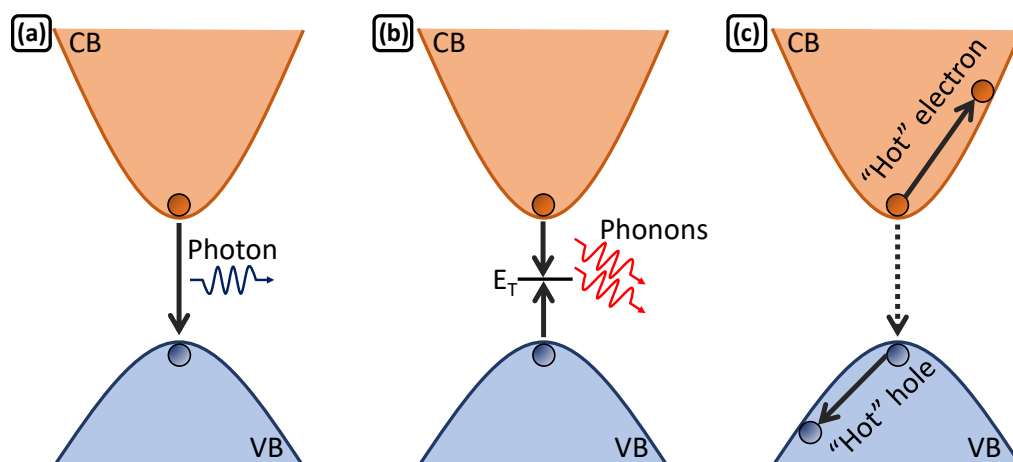


FIGURE 1.7: Schematic band diagram illustrating different recombination mechanisms in bulk semiconductors: (a) radiative, (b) Shockley-Read-Hall non-radiative at deep centres, and (c) intraband non-radiative Auger. CB and VB represent the conduction and valence band, respectively (adapted from [16]).

antisite), and dislocations have different energy level structures that are different from substitutional semiconductor atoms. Thus, they result in energy levels ( $E_T$ ) within the forbidden gap (also known as traps – depicted in Fig. 1.7(b)). The additional energy levels allow relaxation of the charge carriers (electron/hole) by phonon emission resulting in the heat generation previously mentioned. This non-radiative recombination mechanism is known as the Shockley-Read-Hall (SRH) process. Another important non-radiative recombination mechanism is Auger recombination. The energy available from the electron hole recombination is dissipated by exciting a hole deep into the valence band or a free electron high into the conduction band (Fig. 1.7(c)). These highly excited carriers (sometimes referred to as “hot” electrons/holes) relax by multiphonon emission until they are close to the band edge.

Although not shown, non-radiative recombination via surface states is also an important recombination mechanism in semiconductors. These surface states arise from perturbation of the periodicity of the crystal lattice, which creates electronic levels within the forbidden gap of the semiconductor. This allows non-radiative recombination of carriers via phonon emission in a similar process to the one shown in Fig. 1.7(b).

### 1.2.1.2 Intrinsic and extrinsic semiconductors

A semiconductor that contains relatively small amounts of impurities compared with the thermally generated electrons and holes is said to be an intrinsic semiconductor. The distribution of electrons (holes) in the conduction (valence) band is given by the density of allowed quantum states times the probability that a state is occupied by an electron (hole); this is the Fermi-Dirac distribution function. When a semiconductor is doped with impurities, new energy levels are introduced and the semiconductor is said to be extrinsic. Figure 1.8(a) shows the effect of substituting a silicon atom by an arsenic atom with five valence electrons. The arsenic atoms forms covalent bonds with four neighbouring silicon atoms. The fifth valence electron has a relatively small binding energy to the arsenic atoms and this can be ionized becoming a conduction electron at a moderate temperature. The arsenic atom is called a donor, since it donates an electron to the conduction band, and the silicon becomes  $n$ -type because of the addition of this negative charge carrier. Figure 1.8(b) shows the effect of now substituting a silicon atom by a boron atom with three valence electrons. In order to create four covalent bonding around the boron atom an additional silicon valence electron is accepted, creating a positively charged hole in the valence band. Silicon becomes a  $p$ -type semiconductor and boron is referred to as being an acceptor.



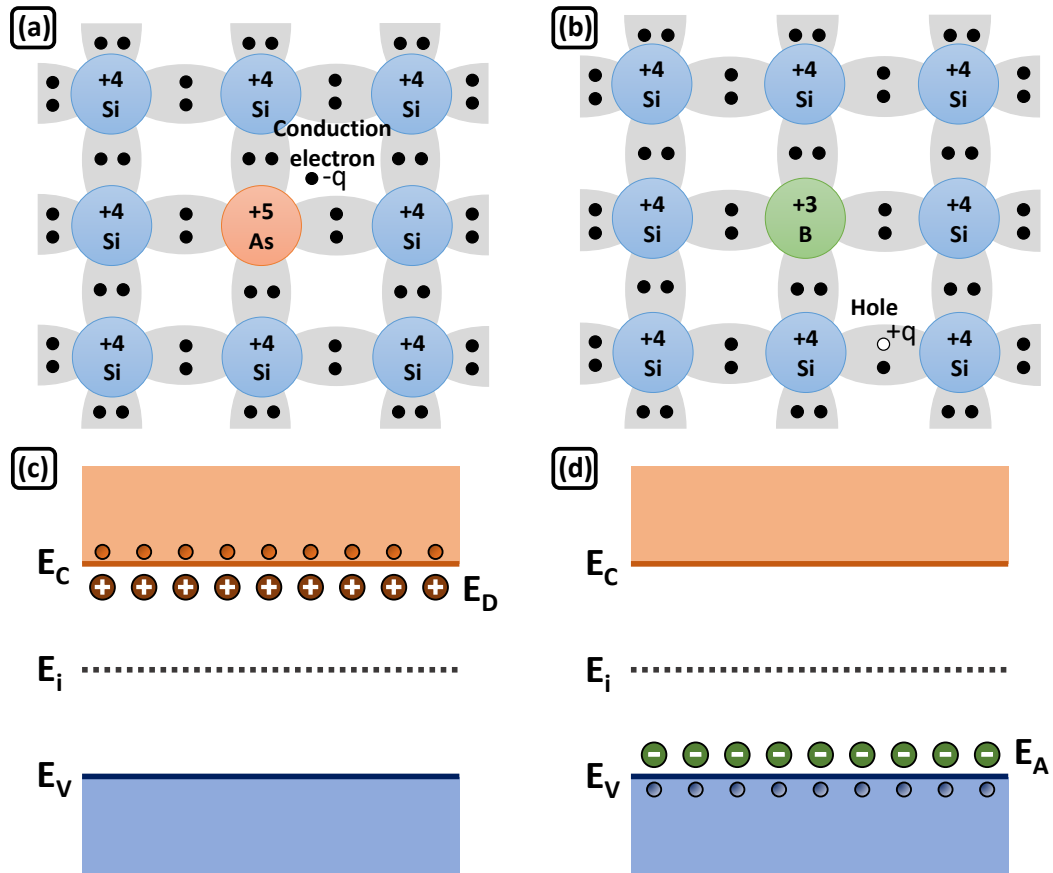


FIGURE 1.8: Schematic bond pictures for (a)  $n$ -type Si with donor (arsenic) and (b)  $p$ -type Si with acceptor (boron); schematic energy band representation of extrinsic semiconductors with (c) donor ions and (d) acceptor ions (adapted from [27]).

Since these impurity atoms are different from the host semiconductor they are regarded as imperfections that affect the periodicity of the lattice, thus creating energy levels within the forbidden gap of the host material. Figure 1.8(c) shows a schematic drawing of a semiconductor energy band after being doped with donor ions. A donor energy level ( $E_D$ ) is created inside the forbidden gap below the conduction band. In the case of shallow donors the thermal energy at room temperature ( $kT \sim 26$  meV) is enough to ionize all the donor impurities and thus provide the same number of electrons in the conduction band. Figure 1.8(d) shows the energy band structure of a semiconductor doped with acceptor impurities. In this case, an acceptor energy level ( $E_A$ ) is created inside the bandgap just above the valence band. In the case of shallow acceptors the thermal energy at room temperature is enough to promote electrons from the valence band to ionize the acceptor impurities and thus leaving the same number of holes in the valence band [27].

### 1.2.2 Physics of the $pn$ junction

Figure 1.9(a) schematically shows a  $pn$  homojunction. It consists of an entire semiconductor in which one of the regions is doped with acceptors ( $N_A$ ) to form the  $p$ -side, whilst the adjacent region is doped with donors ( $N_D$ ) to form the  $n$ -region. The interface separating the  $n$  and  $p$  region is referred to as a metallurgical junction. All dopants are assumed to be fully ionized, such that the free electron concentration is given by  $n = N_D$  and the free hole concentration is given by  $p = N_A$ . At the vicinity of the metallurgical junction there is a very large density gradient in both electron and hole concentrations. Electrons originating from donors on the  $n$ -type side diffuse over to the  $p$ -type side where they recombine. A corresponding process occurs with holes from  $p$ -region diffusing into the  $n$ -region. As a result, a region near the metallurgical junction is depleted of free charge carriers. This region is known as space charge region or depletion region. As electrons from the  $n$ -region diffuse to the  $p$ -side, positively charged donor atoms are left behind. Similarly, as holes diffuse from the  $p$ -region, negatively charged acceptor atoms are uncovered. The net positive and negative charges in the space charge region induce an electric field in the direction from the positive to the negative charge. Assuming that no voltage is applied across the  $pn$  junction, then the junction is said to be in thermal equilibrium – the Fermi energy level is constant throughout the entire system [29].

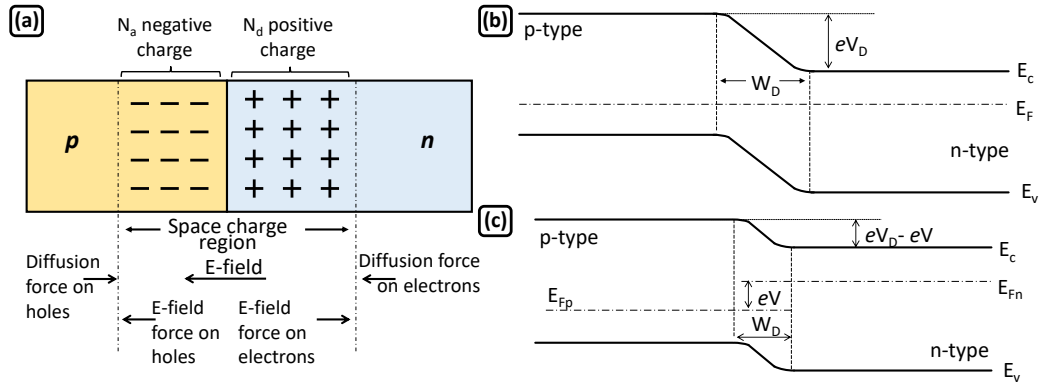


FIGURE 1.9: (a)  $pn$  junction scheme showing the space charge region, the electric field and the forces acting on the charge carriers; (b)  $pn$  junction band diagram under zero bias; (c)  $pn$  junction band diagram under forward voltage bias. Adapted from [27, 29].

Figure 1.9(b) shows the energy band diagram for a  $pn$  junction under zero bias. The conduction and valence band energies must bend as we go through the depletion region, since the relative position of the conduction and valence bands with respect to the Fermi energy changes between  $p$  and  $n$  regions. The space charge region produces a potential called the diffusion voltage ( $V_D$ ) or built-in potential ( $V_{bi}$ ) given by [3]:

$$V_D = \frac{kT}{e} \ln \frac{N_A N_D}{n_i^2} \quad (1.4)$$

where  $k$  is the Boltzmann constant,  $T$  the temperature in Kelvin,  $e$  the electron elementary charge, and  $n_i$  is the intrinsic carrier concentration. The diffusion voltage represents the barrier that free carriers must overcome in order to reach the neutral region of opposite conductivity type. This potential also maintains equilibrium, so no current is produced by this voltage. The width of the depletion region ( $W_D$ ) depends on the diffusion voltage and dielectric permittivity of the semiconductor ( $\epsilon = \epsilon_r \epsilon_0$ ) as follows:

$$W_D = \sqrt{\frac{2\epsilon}{e}(V_D - V) \left( \frac{1}{N_A} + \frac{1}{N_D} \right)} \quad (1.5)$$

where  $V$  is the  $pn$  junction bias voltage [3].

Applying a positive voltage ( $V$ ) to the  $p$ -side with respect to the  $n$ -side, the  $pn$  junction becomes forward biased (Fig. 1.9(c)). Under forward bias, the total electrostatic potential across the junction decreases by  $V$ , thus reducing the depletion region width. In an LED, the charge carriers diffuse into the regions of opposite conductivity type where they will eventually recombine, resulting in the emission of a photon.

The current-voltage (IV) characteristic of a  $pn$  junction diode with a cross-sectional area  $A$  is given by Shockley equation:

$$I = eA \left( \sqrt{\frac{D_p}{\tau_p} \frac{n_i^2}{N_D}} + \sqrt{\frac{D_n}{\tau_n} \frac{n_i^2}{N_A}} \right) \left( e^{\frac{eV}{kT}} - 1 \right) \quad (1.6)$$

where  $D_{n,p}$  and  $\tau_{n,p}$  are the electron and hole diffusion constants and the electron and hole minority carrier lifetimes, respectively. Under forward bias conditions (Fig. 1.9(c)) the diode voltage is much larger than the thermal voltage ( $kT/e$ ) and Eq. 1.6 can be rewritten as:

$$I = eA \left( \sqrt{\frac{D_p}{\tau_p} N_A} + \sqrt{\frac{D_n}{\tau_n} N_D} \right) \left( e^{\frac{e(V-V_D)}{kT}} \right) \quad (1.7)$$

Equation 1.7 shows that the current strongly increases as the applied voltage approaches the diffusion voltage. This turn-around point in the diode behaviour is called the threshold voltage ( $V_{th}$ ) and can be approximated by the semiconductor bandgap energy divided by elementary charge - Eq. 1.8.

$$V_{th} = V_D = E_g/e \quad (1.8)$$

### 1.2.3 Double heterostructures and quantum wells

In a simple  $pn$  junction the minority carriers (electron and holes) diffuse into the opposite conductivity type region by a distance known as diffusion length ( $L_p$  and  $L_n$  for holes and electrons, respectively), as shown in Fig. 1.10(a). In III-V semiconductors, carriers can diffuse  $10 \mu\text{m}$  or even longer before recombination, resulting in a low concentration of minority carriers. The radiative recombination rate is given by the bimolecular rate equation [3]:

$$R = Bnp \quad (1.9)$$

where  $B$  is the bimolecular recombination coefficient and  $n$  and  $p$  are electron and hole concentrations, respectively. From Eq. 1.9 it is clear that low carrier concentration results in a low recombination rate and thus low efficiency of simple  $pn$  junction LEDs. While  $B$  is material dependent, the electrons and holes concentration can be increased by engineering of structures, such as double heterostructures or quantum wells (QW), that allow carrier confinement. A double heterostructure consists of a small bandgap active region between two large bandgap barrier regions. The heterostructure barriers are heavily doped ( $\sim 10^{18} \text{ cm}^{-3}$ ), while the active region is usually left undoped (intrinsic), forming a p-i-n structure. As shown in Fig. 1.10(b), the carriers are confined in the active layer of the p-i-n structure, therefore increasing the carrier concentration and the recombination rate. In this case, the carriers recombine emitting photons of energy equal to the active layer bandgap [3].

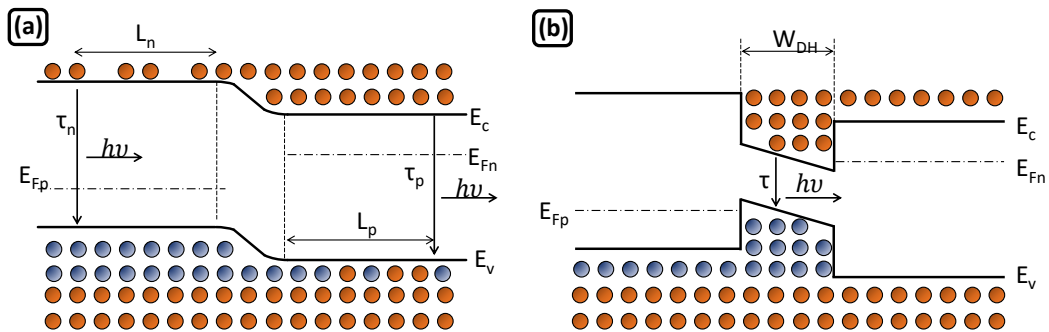


FIGURE 1.10: Schematic drawing of (a) homojunction and (b) a double heterostructure both under forward bias (adapted from [3]). The horizontal axis is distance through the structure.

When the width of the active layer ( $W_{DH}$ ) is comparable to the de Broglie wavelength for thermal motion<sup>¶</sup> (Eq. 1.10), quantum size effects become important [30].

$$\lambda_{dB} = \frac{h}{p} = \frac{h}{\sqrt{2m^*E}} = \frac{h}{\sqrt{2m^*kT}} \quad (1.10)$$

<sup>¶</sup>Calculated assuming a thermal energy of  $E = kT$ .

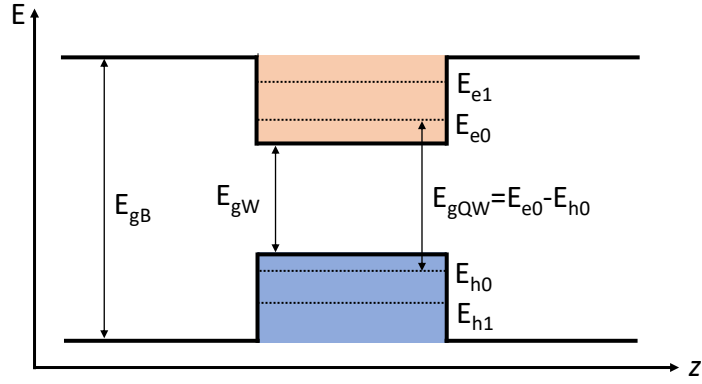


FIGURE 1.11: Schematic band diagram of a quantum well (QW) structure showing the energy difference between the QW ground states ( $E_{e0}$  and  $E_{h0}$ ). The  $E$  and  $z$  axes represent energy and growth direction, respectively (adapted from [30]).

Here  $p$  and  $m^*$  are the carrier momentum and effective mass, respectively. For GaN, which has an electron effective mass of  $0.2m_0$  (with  $m_0$  being the electron mass),  $\lambda_{dB} \approx 17$  nm, meaning that, for active layers thinner than  $\sim 17$  nm, quantum effects are observed and the active layer is called a quantum well. In the quantum well, the carriers are confined in the growth direction ( $z$ ). In this case, and contrary to a bulk semiconductor where the carriers occupy a continuous band, the allowed energy levels become quantized and discrete. Assuming infinite barriers for the quantum well the allowed energy levels are given by [28]:

$$E_n = \frac{\hbar^2 \pi^2}{2m^* L^2} n^2, \quad n = 1, 2, 3, \dots \quad (1.11)$$

where  $L$  is the width of the quantum well and  $n$  is the integer number of levels. The ground and first excited energy levels for electrons and holes inside a quantum well structure are shown schematically in Fig. 1.11. In this case, the emitted photon energy is given by the separation of the QW energy levels, e.g. for a transition between the QW ground states the photon has an energy equal to  $E_{e0} - E_{h0}$ . As such, the LED emission wavelength can be tuned by selecting an active layer with an appropriate bandgap and by optimising the QW composition and width. In addition, as QW active regions provide additional carrier confinement, high efficiency LEDs are based on QW and multiple QW structures (where the QW structure is repeated for a certain period) [3, 30].

#### 1.2.4 III-nitride LEDs

The LEDs described in this thesis with wavelengths spanning from the violet to the green are fabricated from LED wafers based on III-nitride materials. The violet and green LED (shown in Chapter 3) epitaxial structures are grown on conventional patterned

TABLE 1.1: Important properties of the AlGaInN binary alloys (in wurtzite phase) at room temperature (retrieved from [3]).

Parameter	AlN	GaN	InN
Lattice constant $a_0$ (Å)	3.112	3.191	3.545
Lattice constant $c_0$ (Å)	4.982	5.185	5.703
Bandgap energy $E_g$ (eV)	6.28	3.425	0.77
Electron mobility $\mu_n$ (cm <sup>2</sup> /Vs)	300	1500	3200
Hole mobility $\mu_p$ (cm <sup>2</sup> /Vs)	14	30	-

sapphire substrates. The blue LED (shown in Chapters 3-5) epitaxial structures are grown on (111)-oriented silicon wafers, and are commercially available through Plessey Semiconductors Ltd.

The III-nitride materials have three basic binary alloys: AlN, GaN, and InN. Their stable crystal structure under normal conditions is the hexagonal wurtzite phase (inset of Fig. 1.12), however, the cubic zinc blende phase can be obtained under special conditions [31]. Table 1.1 summarises important properties (in the context of light-emitting applications) of the binary alloys in the wurtzite phase at room temperature [3].

The III-nitrides' isomorphous nature means that the wurtzite structure is maintained during the formation of ternary and quaternary alloys. This means that the bandgap of these ternary alloys can be engineered to any chosen value between the bandgaps of the constituent binaries. The bandgap *vs* lattice constant of the AlGaInN material system (in the wurtzite phase) is shown in Fig. 1.12. The AlGaInN alloys are direct bandgap materials throughout the deep and near UV, visible and near infrared (NIR) spectral range, which makes them desirable for light emitting applications in a wide range of wavelengths. Of particular interest for this thesis is the  $\text{In}_x\text{Ga}_{1-x}\text{N}$  alloy, which, for In concentrations of typically  $\sim 9\%$ ,  $\sim 17\%$ , and  $\sim 30\%$ , yields violet, blue, and green emission, respectively [32].

The majority of III-nitride LEDs are grown by metal-organic chemical vapour deposition (MOCVD). During MOCVD, metal alkyl and ammonia precursors are transported in vapour form to a heated substrate, where they react forming epitaxial films of the desired material. Typically in GaN growth very high temperatures ( $\sim 1000$  °C) are required because of the high bond-strength of N-H bond in ammonia precursors [34]. This high deposition temperature limits the choice of growth substrate, as it has to be chemically and mechanically stable under these conditions. Sapphire is the most common

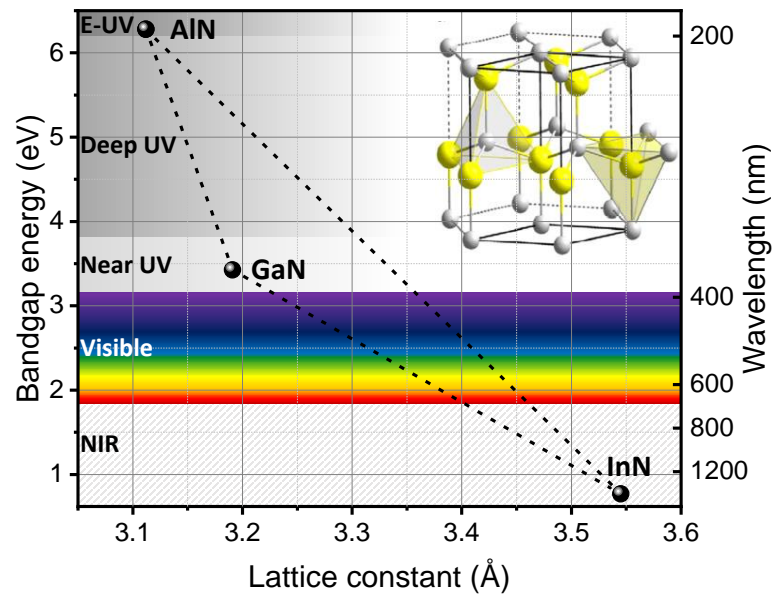


FIGURE 1.12: Bandgap energy *vs* lattice constant of the AlGaInN material system in wurtzite crystal structure ( $E_g$  and  $a_0$  values retrieved from [3]); inset shows a representation of the wurtzite crystal structure (retrieved from [33]).

substrate<sup>†</sup>, although less common, Si and SiC substrates are also used for the growth of III-nitrides [35]. Figures 1.13(a)-1.13(c) show the epitaxy relationship between *c*-plane GaN and *c*-plane sapphire, 111-oriented Si and 6H-SiC, respectively.

Table 1.2 summarises important properties of the growth substrates. The lattice mismatch between GaN and the different substrates results in a high density of misfit dislocations at the GaN/substrate interface. Although III-nitrides are much more tolerant to defects than other conventional III-V materials, great effort has been made to reduce the misfit and threading dislocations (TD) density. The coefficient of thermal expansion (CTE) mismatch leads to a strained film, which is prejudicial as it can lead

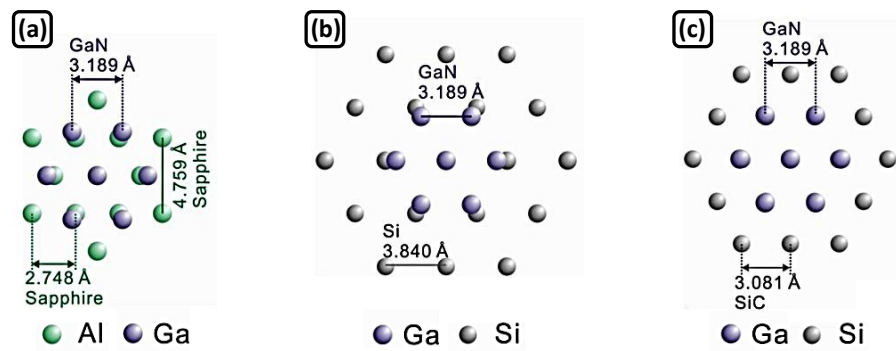


FIGURE 1.13: Epitaxy relationship between *c*-plane GaN and (a) *c*-plane sapphire, (b) Si(111) and (c) 6H-SiC (adapted from [36]).

<sup>†</sup>Historically, sapphire was one of the few available materials stable under MOCVD growth conditions (1000 °C and  $\text{NH}_3$  atmosphere) and with crystal symmetry similar to GaN [12])

TABLE 1.2: Comparison of  $c$ -plane sapphire, Si(111), and 6H-SiC as growth substrates for  $c$ -plane GaN (retrieved from [37, 38]).

Parameter	$c$ -plane sapphire	Si(111)	6H-SiC
Lattice mismatch (%)	+16	-17	+3.5
TD density ( $\text{cm}^{-2}$ )	$1.8 \times 10^{13}$	$2.8 \times 10^{13}$	$1.1 \times 10^{12}$
CTE mismatch (%)	-34	+54	+25
Cost per 2-inch wafer (Euro)	20	10	100
Cost per 6-inch wafer (Euro)	500	20	-

The cost per 2- and 6-inch wafer refers to the year 2012.

to cracking of the film (to be discussed). Also important is the cost of the substrates, which clearly illustrates why SiC, which has the smallest lattice mismatch, is not the most substrate used for the growth of III-nitrides. Due to their relevance to this work, the growth of III-nitrides on sapphire and silicon substrates will be discussed in more depth in the following sections.

Conventionally, III-nitride based devices are grown on polar (0001)  $c$ -plane of the wurtzite crystal structure (Fig. 1.14(a)). This leads to the formation of strong polarisation fields pointing along the [0001] axis. These fields reduce the overlap of the

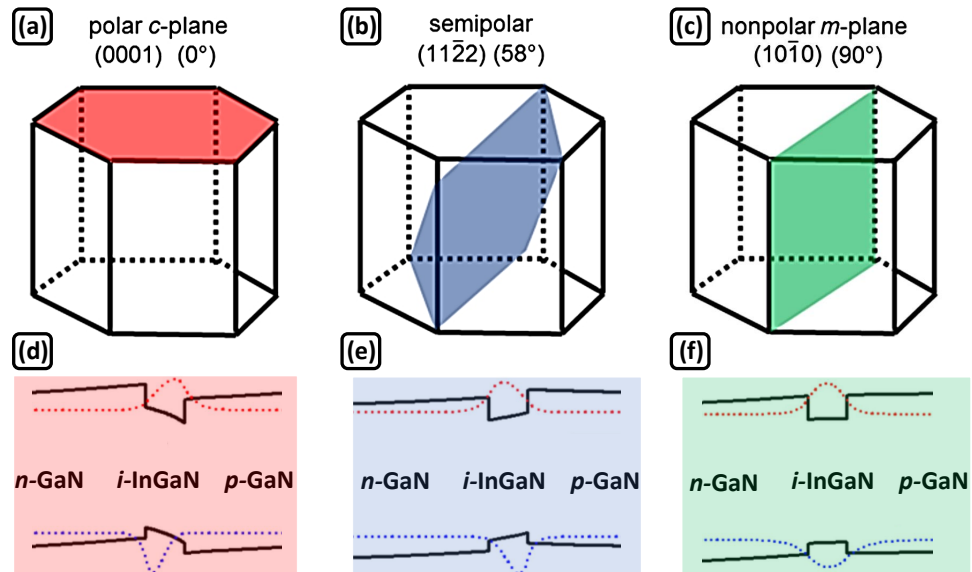


FIGURE 1.14: Schematics of (a) polar ( $c$ -plane), (b) semipolar  $(11\bar{2}2)$ , and (c) nonpolar plane ( $m$ -plane) of III-nitride wurtzite crystal structure; (d)-(f) simulated band diagram for  $\text{In}_{0.2}\text{Ga}_{0.8}\text{N}(3 \text{ nm})/\text{GaN}(15 \text{ nm})$  QW grown on  $c$ -plane, semipolar  $(11\bar{2}2)$  and nonpolar ( $m$ )-plane, respectively (adapted from [39]). The vertical axis in (d)-(f) is energy and the horizontal axis is distance through the heterostructure.



electron and hole wavefunctions inside the QWs (Fig. 1.14(d)), thus reducing the radiative recombination rate and, ultimately the IQE. By growing III-nitrides in semipolar (e.g. orientation  $11\bar{2}2$  - Fig. 1.14(b)) and nonpolar (e.g. orientation  $10\bar{1}0$  - Fig. 1.14(c)) growth planes, these fields can be significantly reduced or even eliminated. This has tremendous consequences in the QWs' electronic bands and on the carriers wavefunctions, as shown in Figs. 1.14(e) and 1.14(f) [40].

#### 1.2.4.1 Growth on sapphire

As mentioned above, nowadays sapphire is the most common substrate for growth of III-nitrides. Sapphire is transparent in the visible range ( $E_g=8.1-8.6$  eV), chemically and thermally very stable (melting temperature of 2050 °C), and the technology of growth of nitrides on sapphire is quite mature. The III-nitride materials' unit cell is rotated 30° about the  $c$  axis with respect to the sapphire unit cell to ensure both materials crystal orientations are parallel. Nevertheless, the lattice mismatch between GaN and sapphire is around 16%. Due to the large lattice and thermal mismatch, the quality of GaN films grown directly on sapphire is poor. GaN films grown directly on sapphire exhibit a large number of dislocations, hillocks, and strong deep level yellow luminescence [35, 41].

Amano *et al.* [8] discovered that optically flat and crack free GaN films could be epitaxially grown by MOCVD on a sapphire substrate, by depositing a low temperature AlN buffer layer between the substrate and the GaN film. This method, often called two-step strained heteroepitaxy, is crucial in the growth of high quality III-nitride films, as it is still used nowadays. The two-step strain heteroepitaxy consists of two steps: (1) growth of a low-temperature (500-550 °C) AlN or GaN\*\* 10-100 nm thick buffer layer; (2) growth of thick ( $>1 \mu\text{m}$ ) high-temperature GaN layer typically at 1000-1060 °C. The growth mechanism of GaN grown on sapphire by MOCVD using a AlN buffer layer was analysed by Kiramatsu *et al.* [43] and consists of the following stages: (1) high-density nucleation of GaN on top of the AlN buffer; (2) geometric selection arranging the crystallographic direction of the GaN columnar crystals; and (3) highly lateral growth velocity of the trapezoid islands. Even with this method the threading dislocation density in the epitaxial materials is on the order of  $10^8-10^9 \text{ cm}^{-2}$ . While the high dislocation density of a III-nitride epitaxial structure does not prevent the device from working as a light emitter (to be discussed after), it limits its full potential as these defects act as current leakage path and carrier traps providing routes for non-radiative recombination [44, 45].

---

\*\*In 1991, Nakamura *et al.* [42] reported a two-step epitaxial growth of GaN on sapphire using a low temperature GaN buffer layer.

The dislocation density in III-nitrides grown on sapphire has been reduced using advanced growth techniques, such as epitaxial lateral overgrowth (ELO) [45] and patterned sapphire substrates (PSS) [46]. The ELO techniques allow reduction in the threading dislocation density to  $10^4$ - $10^5$   $\text{cm}^{-2}$ , however, due to their complexity and longer turn-around time, this technique is often reserved for laser diode applications. On the other hand, using PSS for III-nitride growth not only reduces the dislocation density to  $\sim 10^7$   $\text{cm}^{-2}$  [47] (increasing the IQE) but also increases the LEE, thus improving the EQE of GaN-based LEDs. An oblique view scanning electron microscopy micrograph of PSS is shown in Fig. 1.15(a). Due to this structure, nucleation of GaN only occurs at the etched flat  $c$ -plane and not on the sidewalls. Fig. 1.15(b) shows that because GaN does not nucleate on the sidewall of the cone structure no dislocations are generated at this interface. Dislocations are generated at the interface of GaN with the flat etched  $c$ -plane and at the top of the cone. This reduction of dislocations mitigates non-radiative recombination, increasing the LED structure IQE. The mechanism for improved light extraction efficiency is shown in Figs. 1.15(c) and 1.15(d). Due to the high refractive index contrast between air and the semiconductor die, in a flat surface sapphire LED a large portion of the emitted photons undergo total internal reflection, being trapped inside the semiconductor die (Fig. 1.15(c)). In the case of PSS, the inclined sidewalls effectively scatter photons, increasing their probability of escaping from the die - in other words, increasing the light extraction efficiency and EQE [46].

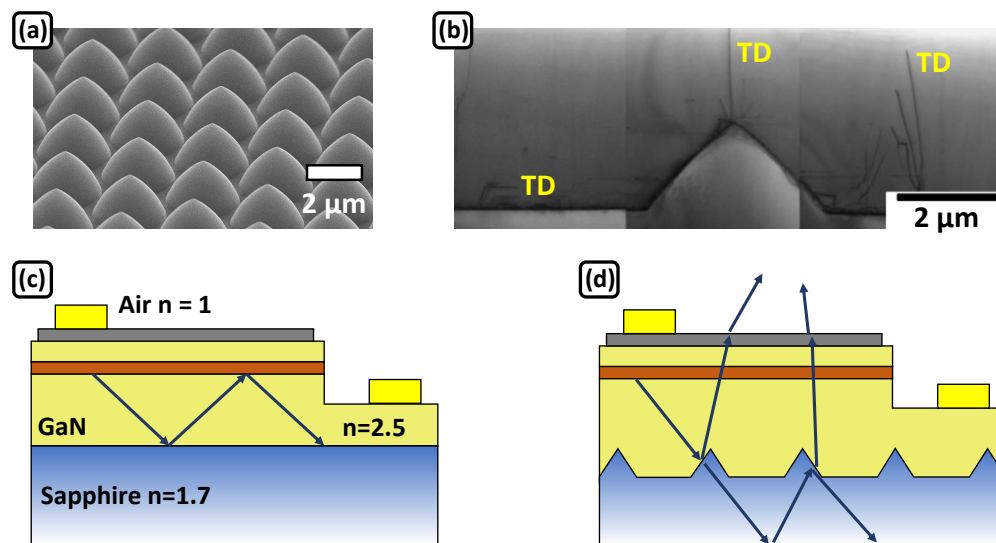


FIGURE 1.15: (a) Scanning electron microscopy micrograph of patterned sapphire substrate (PSS) [48]; (b) cross-sectional transmission electron microscopy of GaN grown on random-cone PSS (dislocations identified in yellow) [49]; (c) and (d) schematic cross-sectional LED structure and photon trajectories of an LED fabricated in flat substrate sapphire and in PSS, respectively (adapted from [46]).

### 1.2.4.2 Growth on silicon

Silicon is the workhorse of microfabrication, being present in virtually every electronic device. Silicon, as a growth substrate for III-nitrides, is interesting due to (1) the availability of Si substrates in large sizes (up to 450 mm diameter) at low cost and high quality, (2) Si's high thermal and electrical conductivity, and (3) the possibility of integration with other devices on the Si substrate. Despite these advantages, the growth of III-nitrides (in particular GaN) on Si substrates is more challenging than the growth on sapphire.

For the growth of wurtzite nitrides, Si(111) is the most favoured orientation due to the threefold symmetry at the surface, which gives a good rotation matching to the growth seeding layer<sup>††</sup> [50]. Similarly to the growth on sapphire, the large lattice mismatch (17%) between GaN and Si(111) leads to a large density of threading dislocations ( $>10^{10}$  cm<sup>-2</sup>) in the epitaxial film (Fig. 1.16(a)). While for sapphire this problem is mitigated by the growth of a low-temperature GaN buffer, such approach is not suitable for Si. At normal growth conditions for GaN, Ga reacts with silicon initiating a strong and fast etching reaction, usually referred to as melt-back etching. Figure 1.16(b) shows the hole etched by the gallium atoms into the Si and the film roughness. Due to the large thermal mismatch, if GaN films could be grown directly on Si they would be in tension, as a consequence of the tensile stress introduced upon cooling from the growth temperature. This leads to strong cracking of the GaN film surface, resulting in non-uniform illumination pattern (Figs. 1.16(c) and 1.16(d)) and wafer bowing. In addition, to achieve a good film quality the Si amorphous native oxide must be removed before the growth [36, 51].

This native oxide can be easily removed, inside the growth chamber, by heating the substrate to temperatures of 1100 °C in a hydrogen atmosphere. To prevent the melt-back etching, the growth of GaN on Si is initiated with deposition of a high temperature AlN layer. This layer not only avoids melt-back etching but also minimizes the crystal misorientation and defect density of the GaN grown on top. The quality of the AlN and subsequent GaN layer largely depend on the structural and chemical properties at the interface of AlN with Si(111). The first 2-3 nm of this interface were found to be amorphous SiN<sub>x</sub>, that formed unintentionally prior to the AlN growth. Inadvertently, the thin SiN<sub>x</sub> layer, which does not affect the epitaxial growth of AlN, plays an important role in the transfer of III-nitride devices to foreign substrates (see Chapter 2) [36].

GaN structures grown on Si substrates are under large tensile growth stress and thermal stress introduced upon cooling, which makes them susceptible to cracking. The

---

<sup>††</sup>Nevertheless, III-nitrides can also be grown on (100)- and (001)-oriented Si substrates, albeit with lower crystalline quality [36, 50].

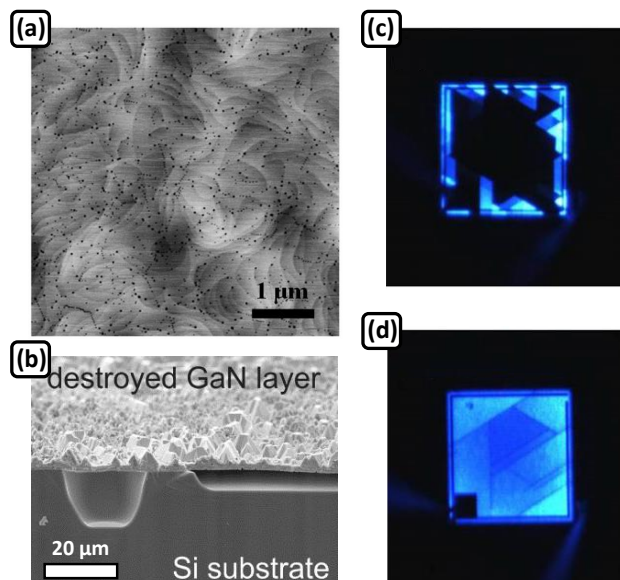


FIGURE 1.16: (a) Atomic force microscopy micrograph of a typical surface of a GaN epilayer grown on a Si substrate, in which each dark spot corresponds to a threading dislocation [36]; (b) GaN on Si after melt-back etching [51]; (c) and (d) examples of cracked GaN LEDs on Si under EL test, showing a non-uniform illumination pattern [36].

critical thickness of a crack free GaN film grown directly on a high temperature AlN buffer layer is only 250 nm. This tensile stress can be compensated by introducing compressive stress into the epilayer during growth. This can be achieved by growing graded  $\text{Al}_x\text{Ga}_{1-x}\text{N}$  intermediate layers [52], low temperature AlN [53] or AlGaIn/GaN superlattices [54]. Figure 1.17(a) shows the effect of the graded  $\text{Al}_x\text{Ga}_{1-x}\text{N}$  compressive layer in the curvature of GaN structures grown on 6-inch Si substrates. Due to the larger in-plane lattice parameter of GaN compared to AlN (Table 1.1), an  $\text{Al}_x\text{Ga}_{1-x}\text{N}$  layer will be under compression when it is grown on relaxed AlN. The compressive stress in the  $\text{Al}_x\text{Ga}_{1-x}\text{N}$  layer will cause convex bowing at the growth temperature (Fig. 1.17(a) LED1 orange shaded region), thus counteracting the concave wafer bow which occurs as a result of the tensile stress introduced during cooling to room temperature (Fig. 1.17(a) LED1 blue shaded region). Figures 1.17(b) and 1.17(c) show that by using a stress management  $\text{Al}_x\text{Ga}_{1-x}\text{N}$  layer it is possible to grow crack free flat GaN LED structures on Si substrates [36].

The large lattice mismatch between Si and AlGaIn, GaN structures leads to a high initial dislocation density. Similarly to the sapphire case, epitaxial lateral overgrowth is also an effective TD reduction method for GaN grown on Si [56]. A more conventional method is the growth of a  $\text{SiN}_x$  interlayer into the GaN layer, which acts as nano-ELO. The thin  $\text{SiN}_x$  interlayer constitutes a mask containing random holes through which small faceted GaN islands form on regrowth, causing the TD to bend laterally and annihilate themselves. Employing the methods show above it is possible to grow flat,

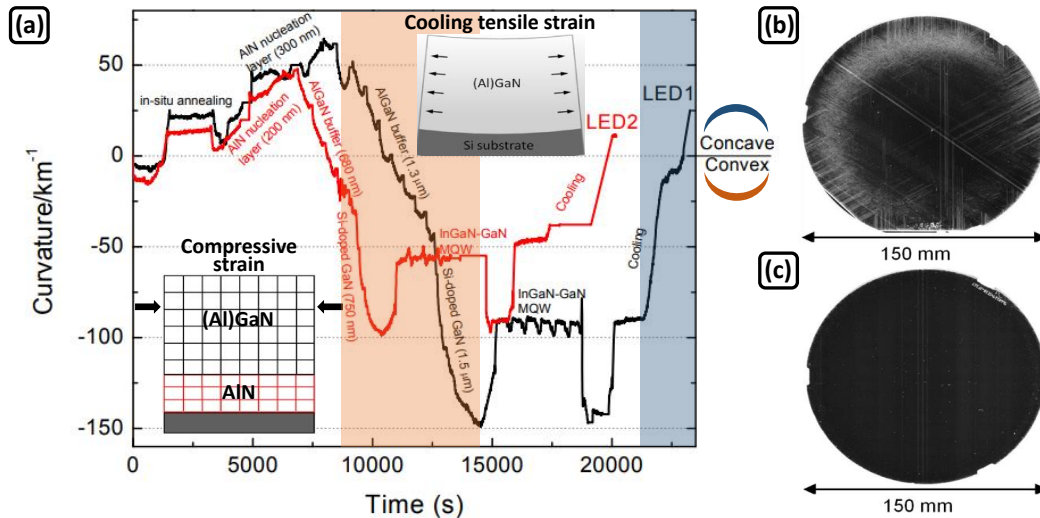


FIGURE 1.17: (a) *In-situ* wafer curvature measured during growth of complete  $2.8 \mu\text{m}$  (LED1) and  $1.8 \mu\text{m}$  (LED2) thick LED structures on 6-inch Si substrates (adapted from [55]); (b) and (c) optical images of a badly cracked and a crack free GaN layer on 6 inch Si, respectively [36].

thick, crack-free GaN films on Si substrates with threading dislocation densities below  $10^9 \text{ cm}^{-2}$ , or even with TD densities comparable to the ones seen on GaN on sapphire ( $2\text{-}3 \times 10^8 \text{ cm}^{-2}$  [57]).

#### 1.2.4.3 Dislocations in III-nitrides

As mentioned above III-nitrides, in particular GaN, exhibit threading dislocation densities on the order of  $10^8\text{-}10^9 \text{ cm}^{-2}$ . The dislocations create energy levels inside the forbidden gap, which are a pathway for non-radiative recombination of the charge carriers [3]. These mechanisms reduce the radiative efficiency of light emitters, and, in fact for GaAs, if the dislocation density exceeds  $10^3 \text{ cm}^{-2}$  the emission is quenched [36]. However, the question of how can III-nitrides be so highly radiative efficient (IQE > 70%), while exhibiting such a high density of dislocations, is still open to debate.

One possible explanation is that the electronic states of the dislocation do not lie inside the forbidden gap, but outside the forbidden gap, i.e. within the conduction and valence bands of the semiconductor (Figs. 1.18(a) and 1.18(b)). This hypothesis is based on an incomplete screening of the dislocation potential, which results in the repulsion of either electron or holes, and thus in the absence of non-radiative recombination [3].

Another explanation is that compositional alloy fluctuations, alloy clustering effects (specifically in In-rich GaInN clusters), and phase separation effects result in a variation of the bandgap energy and lead to local potential minima, which in turn can attract and confine carriers. Figure 1.18(c) shows how an In-rich cluster potential minima can

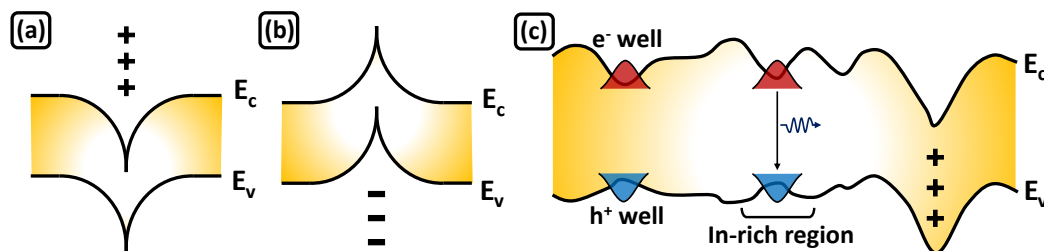


FIGURE 1.18: Band diagram of dislocation (a) donor states in conduction band and (b) acceptor states in the valence band; (c) band diagram of GaInN with In rich regions (adapted from [3]).

trap and localise carriers, preventing them from diffusing to a nearby dislocation, where non-radiative recombination can happen. However, it has been suggested that In-rich clusters are caused by the imaging method (damage of the InGaN QWs by electron beam) and that localisation of the carriers is due to alloy fluctuations [58].

#### 1.2.4.4 Doping

The realisation of efficient light emitters not only depends on good crystalline quality but also on achieving effective  $n$  and  $p$  doping. Non-intentionally doped GaN is  $n$ -doped with carrier concentration  $\sim 10^{16} \text{ cm}^{-3}$ . This high  $n$ -type background carrier density has been attributed to nitrogen vacancies and Si and/or oxygen impurities, however the origin of this  $n$  doping is still controversial. As mentioned before, high-quality III-nitrides are grown by MOCVD. This technique allows a precise control of the composition, thickness, and doping of the epitaxial films. The dopants are introduced, during the growth, as a gas and the doping concentration controlled by the gas flow rate [41, 59].

Silicon is the most used dopant for  $n$ -type conductivity in GaN, although, germanium can also be used. Si mainly substitutes at the gallium site due to the low covalent radii difference between Si and Ga, compared with the radii difference with nitrogen, forming shallow donors. The most popular Si doping sources are  $\text{SiH}_4$  and  $\text{Si}_2\text{H}_6$  in MOCVD growth. Using  $\text{SiH}_4$ , Nakamura *et al.* [60] showed that GaN could be grown without cracks or pits on the surface with carrier concentrations up to  $2 \times 10^{19} \text{ cm}^{-3}$ , with an associated mobility of  $100 \text{ cm}^2/\text{Vs}$ . The activation energy for ionization of Si donors in GaN is estimated to be between 12-17 meV [61], which explains the high ionization efficiency at room temperature [41, 59].

Historically, efficient  $p$ -doping in III-nitrides has always been challenging and the main obstacle towards the realisation of GaN-based  $pn$  junction LEDs. Acceptors in III-nitrides can be chemically passivated by hydrogen atoms, which provide the electron that acceptors tend to accept from the valence band, thereby passivating the acceptor.

In addition, acceptors in III-nitrides have a high thermal activation energy, and, as a result, only a small percentage of acceptors, typically less than 10%, are ionized at room temperature [3].

The most common used acceptor in GaN is magnesium (Mg), which substitutes the Ga atom thereby forming a substitutional acceptor. Generally, Mg-doped GaN grown by MOCVD (using  $\text{Cp}_2\text{Mg}$  gas) exhibits a semi-insulating behaviour. It was thought that hydrogen<sup>††</sup>, generated during the epitaxial growth of GaN, behaves as a donor compensating the acceptors, thus forming neutral Mg-H complexes. Amano *et al.* [9] discovered that the acceptor dopants can be activated by post-growth LEEBI, thus achieving Mg-doped GaN *p* conductivity (hole concentration and mobility of  $2 \times 10^{16} \text{ cm}^{-3}$  and  $8 \text{ cm}^2/\text{Vs}$ , respectively). Subsequently, Nakamura *et al.* [62] demonstrated that low resistivity p-type Mg-doped GaN films can be obtained by thermal annealing at  $700 \text{ }^\circ\text{C}$  in a  $\text{N}_2$  atmosphere (hole concentration and mobility of  $3 \times 10^{17} \text{ cm}^{-3}$  and  $10 \text{ cm}^2/\text{Vs}$ , respectively). During thermal annealing the H-N bond is broken and the H atoms are driven out of the epitaxial film. The heating caused by the LEEBI is believed to have this same effect. However, thermal annealing ( $675\text{-}725 \text{ }^\circ\text{C}$  for 5 minutes in a  $\text{N}_2$  atmosphere) is the preferred method to activate the Mg acceptors, as it is an easy, reliable, *in-situ* mass production process [3, 59].

In GaN, the Mg acceptor level is located about 200 meV above the valence band. Because of the deep nature of the Mg acceptor, very high doping levels of  $\sim 10^{19} \text{ cm}^{-3}$  are frequently used in device applications. However, at this high concentration Mg atoms can occupy interstitial sites, leading to the formation of defects, instead of substituting the Ga atom. These factors limit the typical hole concentrations in highly Mg doped GaN films to  $\sim 10^{17} \text{ cm}^{-3}$  [3, 59].

#### 1.2.4.5 Polarisation effects

As previously mentioned, wurtzite III-nitrides are strongly polarised along the *c*-axis, exhibiting spontaneous and piezoelectric polarisation.

The spontaneous polarisation originates from a deviation from an ideal tetrahedral coordination along the (0001) axis and the ionicity of the crystal. The high electronegativity of the nitrogen atoms creates a strong dipole in the metal (Al, Ga, In) nitrogen bond, which, due to the deviation from the ideal tetrahedral configuration, results in non-zero dipole moment. As the wurtzite III-nitrides lack inversion symmetry, the crystal has two

---

<sup>††</sup>Sources of H atoms and H passivation include the methyl and ethyl groups of the organo-metallics, ammonia, as well as hydrogen from the  $\text{H}_2$  carrier gas [3].

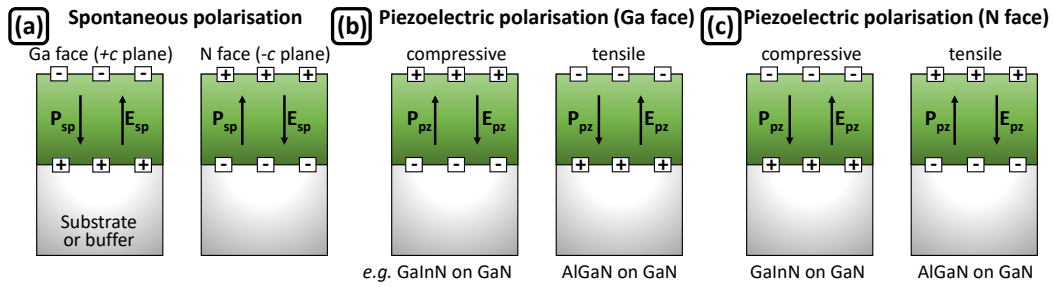


FIGURE 1.19: Schematic cross-section views of surface charges and direction of electric field and polarisation field for spontaneous (sp) and piezoelectric (pz) polarisation in III-nitrides for Ga and N face orientation (adapted from [3]).

polar surfaces, one terminated with metal atoms and the other N-face. The spontaneous polarisation for Ga and N face terminated GaN is shown in Fig. 1.19(a) [40, 63].

The piezoelectric polarisation arises from the hetero-epitaxially growth of III-nitride devices, for example the active region of an LED consists of several few-nanometre-thick InGaN QWs between GaN or InGaN barriers. The in-plane lattice constant mismatches with the underlying layer results in the expansion or contraction of the III-nitride film. For example, InGaN is compressively strain when grown on a thick relaxed GaN buffer layer. In a similar fashion, AlGaIn is under tensile strain when grown on a thick relaxed GaN buffer layer (Figs. 1.19(b) and 1.19(c)) [3, 40].

The piezoelectric polarisation constants in III-nitrides are up to ten times larger than in conventional III-V and II-VI semiconductor alloys [65]. As a result the InGaIn

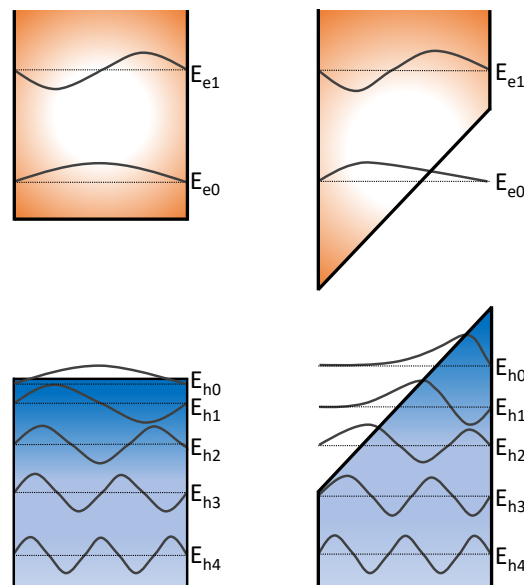


FIGURE 1.20: Electronic band structure of a quantum well structure showing (left) no QCSE and exhibiting (right) QCSE, resulting in effective bandgap narrowing and spatial separation of electron and hole wavefunctions (adapted from [64]).



QW structures, employed in visible LEDs, experience large internal fields that bend the conduction and valence bands of the QWs. Consequently, the electron and holes are spatially separated (reducing the radiative recombination<sup>§§</sup>) and the energy of the radiative transition is lowered (red-shifted). The lower efficiency and lower emission energy are collectively referred to as the quantum-confined Stark effect (QCSE) - Fig. 1.20 [3, 64].

This effect can be mitigated by reducing the QWs thicknesses down to 2-3 nm, thus decreasing the electron and hole separation. Nevertheless, InGaN/GaN QWs are still affected by QCSE, which causes their emission to blue-shift with increasing current density (due to carrier screening effects) [3, 40].

### 1.2.5 AlGaInP-based LEDs

The red (630 nm) LEDs described in Chapter 4 are fabricated from LED wafers based on AlGaInP materials. These LEDs were acquired through a collaboration with a confidential company, with the help of Dr. Erdan Gu. The LEDs were fabricated by the company, as such a detailed explanation of the fabrication workflow was not provided. Nevertheless, a brief explanation of the LEDs structure and overview of the fabrication process workflow are shown in Chapter 4.

The quaternary AlGaInP alloy system, grown on lattice matched GaAs substrates, is important for high performance LEDs and lasers operating in the orange and red regions of the visible spectrum. This quaternary alloy was first developed in the 1980s for double heterostructure lasers operating in the 680 nm range [66, 67]. Following the success of the AlGaInP lasers, the first AlGaInP LEDs, with emission wavelength extending from  $\sim 560$ -620 nm, were reported [5, 68]. AlGaInP and the binary alloys AlP, GaP, and InP crystallize in the zinc blend structure at room temperature. Table 1.3

TABLE 1.3: Important properties of III-V phosphides and GaAs at room temperature (retrieved from [3]).

Parameter	AlP	GaP	InP	GaAs
Lattice constant $a_0$ (Å)	5.4635	5.4512	5.8686	5.6533
Bandgap energy $E_g$ (eV)	2.45	2.26	1.35	1.42
Electron mobility $\mu_n$ (cm <sup>2</sup> /Vs)	60	110	4600	8500
Hole mobility $\mu_p$ (cm <sup>2</sup> /Vs)	450	75	150	400

<sup>§§</sup>The radiative recombination is proportional to the absolute square of the overlap integral of electron and hole wavefunctions. Due to the spatial separation of the carriers, their wavefunctions overlap is reduced, thereby the radiative recombination rate [40].

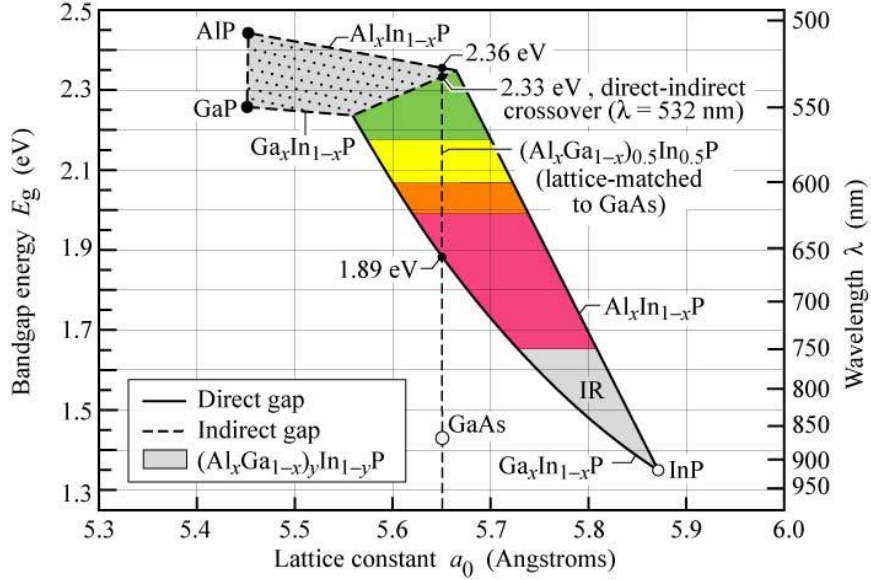


FIGURE 1.21: Bandgap energy and corresponding wavelength *vs* lattice constant of  $(\text{Al}_x\text{Ga}_{1-x})_y\text{In}_{1-y}\text{P}$  at 300 K. The dashed vertical line shows  $(\text{Al}_x\text{Ga}_{1-x})_{0.5}\text{In}_{0.5}\text{P}$  lattice matched to GaAs (retrieved from [3]).

summarises important parameters of the III-V phosphides binary alloys and of the GaAs substrate [3].

At the molar indium composition of 50%,  $(\text{Al}_x\text{Ga}_{1-x})_{0.5}\text{In}_{0.5}\text{P}$  is lattice matched to GaAs (as shown in Fig. 1.21). The bandgap energy of lattice matched GaInP ( $x = 0$ ) is approximately 1.9 eV (650 nm). The addition of Al to GaInP allows one to shift the emission towards shorter emission wavelengths. However,  $(\text{Al}_x\text{Ga}_{1-x})_{0.5}\text{In}_{0.5}\text{P}$  becomes an indirect bandgap semiconductor at Al mole fractions of  $\sim 0.53$ , which translates into a emission wavelength at the direct-indirect crossover point of approximately 555 nm. Below this value the radiative efficiency strongly decreases and this material is no longer suitable for light emitting applications [3].

### 1.2.5.1 Growth on GaAs

AlGaInP is heteroepitaxially grown on (100) GaAs substrates by MOCVD at temperatures between 650 and 800 °C. Commonly before the epitaxy of the AlGaInP layer, GaInP and AlInP materials are firstly deposited on the lattice matched GaAs substrates, respectively, following the linear interpolation method. The *p* and *n*  $(\text{Al}_x\text{Ga}_{1-x})_{0.5}\text{In}_{0.5}\text{P}$ , with  $0.6 \leq x \leq 1$ , confinement layers and the  $(\text{Al}_x\text{Ga}_{1-x})_{0.5}\text{In}_{0.5}\text{P}$  active layer are lattice matched to the GaAs substrate during the growth at high temperature. The lattice matched growth on GaAs results in high quality films, however, due to CTE mismatch between GaAs and AlGaInP, the epitaxial film is under compressive strain at room temperature [69, 70].

Although AlGaInP is perfectly lattice matched to GaAs, the growth of AlGaInP still proved challenging due to oxygen incorporation and ordering effects. Aluminium is highly reactive and binds easily to oxygen impurities present in the chamber or in the source gases. These impurities form deep-level donor states that act as nonradiative centres and compensate shallow acceptors, which is detrimental to a device's performance. The ordering of Ga and In atoms along the (111) planes lowers the bandgap energy of AlGaInP. As a result, the emission wavelength varies as the degree of ordering changes. Oxygen incorporation and ordering effects can be minimised by optimising the growth conditions (high temperature and high V-III ratio) and the orientation of the growth substrate [69].

### 1.2.5.2 Doping

Light emitting applications require the intentional doping of both *n*- and *p*-type confinement layers ( $(\text{Al}_x\text{Ga}_{1-x})_{0.5}\text{In}_{0.5}\text{P}$ , with  $0.6 \leq x \leq 1$ ). Early attempts to dope high Al-content AlGaInP alloys were not very successful, especially for *p*-type alloys. These early difficulties were due to: (1) high oxygen content in the early AlGaInP materials which electrically compensated the shallow acceptors; (2) increase of the acceptor ionization energy with increasing Al content, reducing free hole concentrations; and (3) hydrogen passivation of the acceptor impurities (similar to III-nitrides) [71, 72].

$\text{Si}_2\text{H}_6$  or  $\text{SiH}_4$  are commonly used as source gases for *n*-type Si doped AlGaInP. The doping concentration is controlled by adjusting the dopant flux, and it is commonly in the range of  $2 \times 10^{17}$  to  $5 \times 10^{18} \text{ cm}^{-3}$ . The most common *p*-type dopants for AlGaInP are zinc (Zn) and magnesium, however Mg is usually preferred as it has a smaller ionization energy than Zn. The doping density for the *p*-type confinement layer is in the range of  $4 \times 10^{17}$  and  $2 \times 10^{18} \text{ cm}^{-3}$ , and can be controlled by adjusting the flux of  $\text{Cp}_2\text{Mg}$  during growth. Reactivation of the passivated acceptors can be achieved by post-growth annealing in  $\text{H}_2$  or  $\text{N}_2$  ambient at temperatures above 400-500 °C [73]. For AlGaInP hole and electron mobilities are usually  $\sim 10 \text{ cm}^2/\text{Vs}$  and  $\sim 50$  to  $500 \text{ cm}^2/\text{Vs}$ , respectively [71, 72].

### 1.2.6 LED efficiency droop

Ideally the optical power emitted by an LED would increase linearly with the injected current, and thus the efficiency would be constant, independent of the current. However, in real LEDs the efficiency peaks at relatively low current and then gradually decreases with increasing current. This phenomena is known as efficiency droop and it is shown in Figs. 1.22(a) and 1.22(b) for AlGaInP-based and GaN-based LEDs, respectively [3].

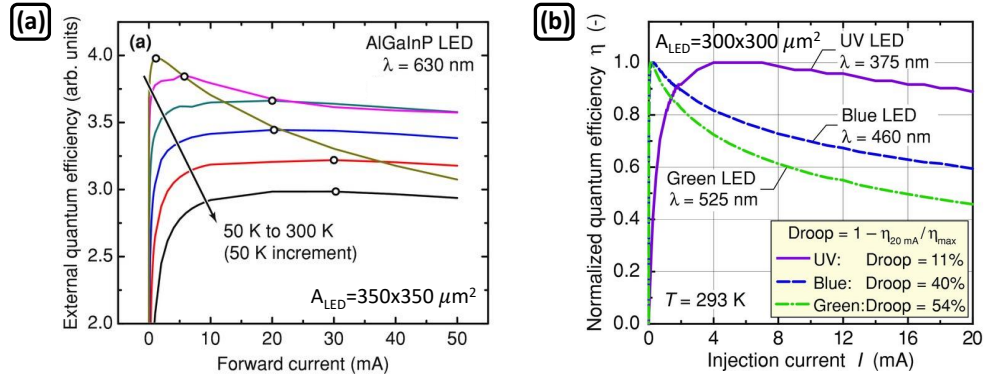


FIGURE 1.22: (a) EQE *vs* current of a AlGaInP-based LED at different temperatures (open black circles indicate the peak position of each curve); (b) efficiency *vs* current curves of GaN-based UV, blue, and green LEDs at 293 K; - retrieved from [32].

AlGaInP-based LEDs exhibit strong efficiency droop at cryogenic temperatures, however, at room temperature the efficiency droop is close to zero, thus not posing an obstacle in practical high-brightness applications. It has been suggested that for AlGaInP-based LEDs, the efficiency droop occurs due to an increase in non-radiative recombination via traps and due to electron leakage out of the active region [3, 74]. For GaN-based LEDs the efficiency peak occurs at relatively low current density (0.1-10 A/cm<sup>2</sup>) and the efficiency droop increases with increasing wavelength (from UV to green), posing a bigger obstacle for high-power applications than AlGaInP-based LEDs. For GaN-based devices the origin of the efficiency droop is not fully understood and several mechanisms have been proposed, with Auger recombination and carrier leakage being the most discussed [32, 75, 76].

In the Auger process, an electron recombines with a hole, transferring the released energy for exciting a third carrier (electron or hole) rather than emitting a photon. When analysing the influence of Auger recombination on the efficiency droop, carrier leakage is neglected and, as such, the IQE is given by the *ABC* model:

$$IQE = \frac{Bn^2}{An + Bn^2 + Cn^3} \quad (1.12)$$

where  $n$  is the carrier density and  $A$ ,  $B$ , and  $C$  are the SRH non-radiative, radiative, and Auger non-radiative recombination coefficients. Shen *et al.* [77] were the first to suggest that Auger recombination could be the primary non-radiative path for carriers at typical LED operating currents, and the reason behind the efficiency droop. The measured Auger coefficient varied between  $1.4 \times 10^{-30}$  and  $2.0 \times 10^{-30}$  cm<sup>6</sup>s<sup>-1</sup>, which accordingly to the limit set by Piprek [75] ( $C \geq 10^{-31}$  cm<sup>6</sup>s<sup>-1</sup>), is enough to cause significant efficiency droop. Iveland *et al.* [78] reported direct measurement of Auger electrons emitted by a LED under current injection, and showed a linear correlation between the emitted electron and the efficiency droop. Nevertheless, this work has been contested by others [79],

who have commented that the LED structure used in [78] is unsuitable to retrieve an Auger signature.

Carrier leakage has also been proposed as the main mechanism behind the efficiency droop. In this case, as the carrier concentration increases, an increasing number of carriers may not be captured by the active region or may escape from the active region. In this case an extra term, that accounts for the carriers that recombine outside the active region, is added to the denominator of Eq. 1.12 (*ABC* model). A common cause of carrier leakage in GaN-based LEDs, is when an electron fails to be captured by MQW structure and eventually recombines with holes in the *p*-type GaN or at the *p*-type contact electrode. To mitigate this problem, an AlGaIn electron blocking layer (EBL) is grown on the *p*-side of the MQW structure. However, the EBL is unable to completely stop electron leakage in nitride LEDs, and a direct connection between the efficiency droop and electron leakage has been proposed [80]. In nitride LEDs, polarisation effects are believed to be one of the possible reasons for electron leakage. With the typical Ga-polar growth of nitride LEDs, the polarisation charges at the MQW-EBL interface are positive, which leads to electron accumulation at this interface and strong negative band bending [3, 32, 75].

### 1.3 Micro-LEDs

Micron-sized LEDs (micro-LEDs) are, by convention, defined as LEDs with an emission area of less than 100  $\mu\text{m}$  in each dimension [81]. The first micro-LED (12  $\mu\text{m}$  diameter disk - Figs. 1.23(a) and 1.23(b)) was reported in 2000 by Jin *et al.* [82], who showed that, for an identical area, the external quantum efficiency of micro-LED is enhanced over conventional broad area LEDs. Later, in 2001, the same group [83] demonstrated a 10x10 blue nitride microdisplay (Fig. 1.23(c)), highlighting “*that III-nitride microdisplays have an unsurpassed ability to provide high-brightness/resolution/contrast, ..., long life, high speed, and low-power consumption*”.

Micro-LEDs can deliver higher power density and sustain higher current density operation (up to several  $\text{kA}/\text{cm}^2$ ) than conventional broad area LEDs. This has been attributed to better thermal management [84], less current crowding [85] and enhanced light extraction efficiency [86] in micro-LEDs. In addition, due to their size the modulation bandwidth of micro-LEDs is no longer limited by the *RC* constant but instead by the differential carrier lifetime, which accordingly to the *ABC* model is inversely proportional to the carrier density. This results in extremely high modulation bandwidths

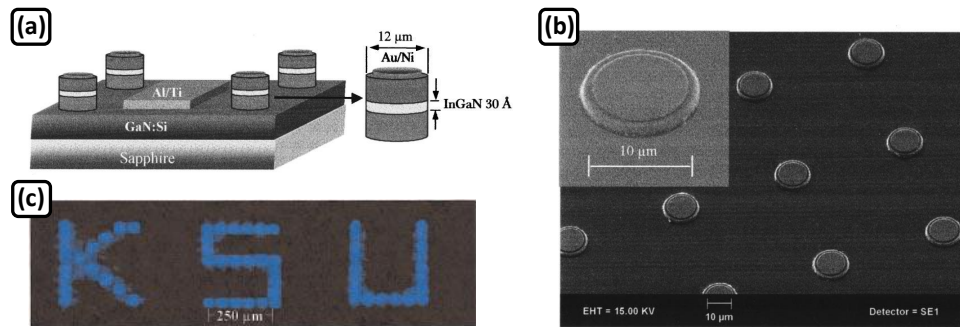


FIGURE 1.23: (a) Schematic drawing and (b) scanning electron microscopy micrograph of InGaN/GaN QW micro-LEDs [82]; (c) first III-nitride blue microdisplay [83].

of up to 830 MHz<sup>¶¶</sup> for a single colour micro LED at 16 kA/cm<sup>2</sup> [87]. Nowadays, micro-LEDs are regarded as the next-generation of self-emissive displays<sup>\*\*\*</sup> (Figs. 1.24(a) and 1.24(b)) [81, 91, 92], and can be found in a wide range of applications, such as visible light communication (VLC - Fig. 1.24(c)) and optogenetics (Fig. 1.24(d)) [93, 94].

In VLC, data is transmitted by modulating visible light at rates unperceived by the human eye. This technology uses the existing lighting infrastructure and highly energy efficient LEDs to exploit the license-free and virtually unlimited bandwidth of the THz-frequency visible spectrum [93]. The upper bound of data transmission in a VLC channel

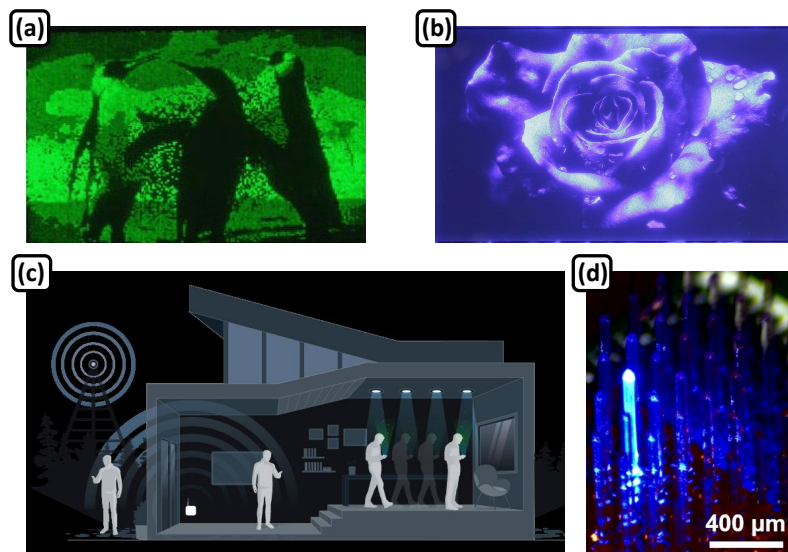


FIGURE 1.24: Monolithic (a) green [92] and (b) blue [91] micro-LED microdisplays; illustration of the LiFi concept [95]; micro-LED array integrated with a micro-needle array for neural interfacing [94].

<sup>¶¶</sup>Putting this value into perspective, conventional broad area LEDs bandwidth is around 20 MHz.

<sup>\*\*\*</sup>With companies such as Samsung [88], Apple [89], and Facebook [90] pushing towards commercialisation.

(capacity of the channel -  $C$ ) is given by the Shannon theorem - Eq. 1.13 [96]:

$$C = B \cdot \log_2(1 + S/N) \quad (1.13)$$

where  $B$  is the modulation bandwidth,  $S$  is the power of the signal, and  $N$  is the power of the noise. From Eq. 1.13 it is obvious that the channel capacity increases with the bandwidth and optical power of LEDs. Early studies showed that commercial broad area LEDs are capable of achieving VLC data rates in the range of 100 Mbps [97, 98]. Employing more advanced modulation schemes and equalisation techniques data rates of a few Gbps have been demonstrated [99, 100]. Nevertheless, the inherently low bandwidth of commercial LEDs ( $\sim 20$  MHz) is an obstacle towards high-speed VLC systems. On the other hand, micro-LEDs extremely high modulation bandwidth and compatibility with commercial LED growth and fabrication processes makes them a perfect candidate for high-speed VLC applications. In fact, due to the 100's MHz bandwidth of micro-LEDs and the development of highly spectral efficient modulation schemes, such as orthogonal frequency division multiplexing (OFDM), VLC data rates of 10 Gbps have been achieved by a single violet micro-LED [101]. Although the low absolute optical power of micro-LEDs seems to set a practical limitation on the employment of micro-LEDs in VLC, it has been recently demonstrated that, using in-series connected micro-LED arrays, several Gbps data rates can be achieved at long distances (e.g. 6.58 Gbps at 10 m) [102].

The concept of VLC has also been extended to underwater wireless optical communication (UWOC), with reports of LED-based transmitters achieving 2.28 Mbps in 50 m [103] and 14.6 Gbps in 1.2 m [104] of tap water. Light sources operating in the visible range take advantage of water's transparency window in that wavelength range. More recently, micro-LEDs have also been employed in underwater media for communication. Tian *et al.* [105] reported a data rate of 800 Mbps in 0.6 m of tap water, using a single blue micro-LED. Using an in-series connected blue micro-LED array Arvanitakis *et al.* [106] achieved 4.92 Gbps in 1.5 m of tap water.

LEDs have also made an impact in the field of optogenetics, which uses light to stimulate/inhibit neuron function [107]. One of the main challenges in *in-vivo* optogenetics is how to deliver light into the brain without damaging the surrounding tissue, whilst keeping high spatio-temporal resolution and freedom of movement of the subject. A common approach is to use an optical fibre to guide light from an external light source into the brain. In this case, commercial LEDs can be used as the external light source [108], and specific optogenetics LED modules can be acquired from Thorlabs [109]. However, in fibre-based approached spatial resolution is compromised and the requirement for a

light source with an external physical connection also hinders wireless solutions. Alternatively, micro-LED arrays can be fabricated into a probe shape, which is then inserted directly into the subject's brain, thus eliminating the need for external light sources and enabling unique spatial resolution. Following this approach several reports have emerged in the past years [110–113].

## 1.4 Micro-transfer printing

Micro-transfer printing offers advanced capabilities in the manipulation of solid micro/nano structures via their selective transfer from one substrate (the donor substrate) to another substrate (the receiver substrate) using a soft, elastomeric stamp. This technique relies on strategies to fabricate suspended platelets of material still tethered to the growth substrate, on the successful transfer of individual or arrays of these platelets onto a receiving substrate, and efficient encapsulation and electrical addressing of the aforementioned platelets. By separating the fabrication substrate from the application substrate, it bypasses the incompatibility problem of delicate substrates (e.g. flexible polymers, CMOS, amongst others) with conventional fabrication technologies which have a mature and established commercial infrastructure (e.g. III-nitrides MOCVD growth). This process enables massive parallel assembly of diverse materials in various structural forms (i.e. wires and membranes with dimensions from a few nanometres to macroscopic scales), with throughputs that correspond to millions of objects per hour, into spatially organised, functional arrangements with two or three-dimensional (3D) layouts [114–116].

Micro-transfer printing has been used to realise flexible arrays of inorganic micro-LEDs (Figs. 1.25(a) and 1.25(b)), flexible micro-LED neuroprobes (Fig. 1.25(c)), active- and passive-matrix addressable micro-LED microdisplays (Figs. 1.25(d) and 1.25(e)), as well as complex 3D structures (Figs. 1.25(f) and 1.25(g)).



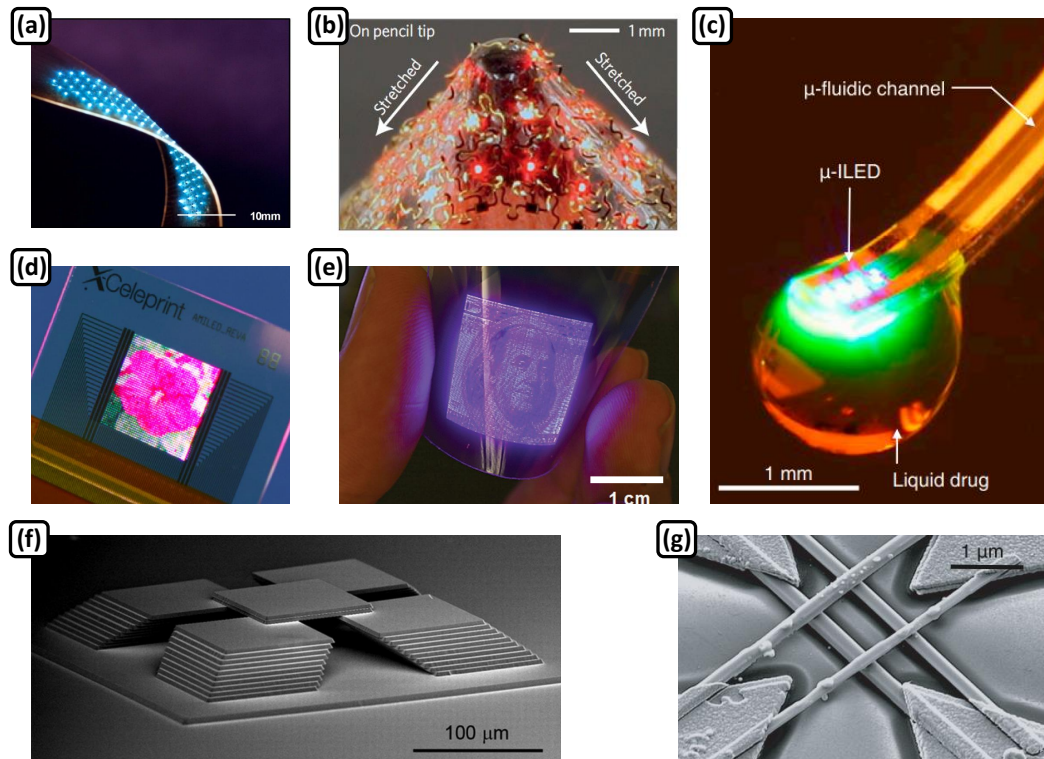


FIGURE 1.25: (a) Optical image of a flexible GaN-based micro-LED array [117]; (b) optical image of an array of AlGaInP-based micro-LEDs (6x6) tightly stretched on the sharp tip of a pencil [118]; (c) optofluidic neural probe during simultaneous drug delivery and photostimulation [119]; (d) photograph of a 127 ppi full-colour active matrix display on glass in operation [120]; (e) passive-matrix micro-LED display on a flexible substrate [121]; (f) scanning electron microscopy (SEM) micrograph of silicon platelets assembled by micro-transfer printing [122]; SEM micrograph of a polarisation-sensitive cross-nanowire THz detector [123].

## 1.5 Summary

This chapter has given a brief and largely historical overview of the development of light emitting diodes and a theoretical background on semiconductors and on the operating principles of LEDs. The importance of heterostructures and later on of MQWs structures in achieving high-efficiency solid state emitters has been discussed. Due to their relevance to this work, the growth of high-quality and efficient  $n$ - and  $p$ -type doping of III-nitride and AlGaInP-based LEDs have been described in further detail. The LED efficiency droop phenomena and possible mechanisms behind it have been discussed. The high-brightness and high-bandwidth of micro-LEDs and their application in visible light communication has been presented. To conclude, the technique of micro-transfer printing and its suitability for the emerging field of hybrid optoelectronic devices was briefly introduced.

## Bibliography

- [1] H. J. Round. *A Note on Carborundum*, pages 879–879. Electrical World, 1907.
- [2] Nick Holonyak and S. F. Bevacqua. Coherent (visible) light emission from Ga(As<sub>1-x</sub>P<sub>x</sub>) junctions. *Applied Physics Letters*, 1(4):82–83, 1962.
- [3] E. Fred Schubert. *Light-Emitting Diodes - 3<sup>rd</sup> Edition*. Cambridge University Press, 2018.
- [4] R. A. Logan, H. G. White, and W. Wiegmann. Efficient green electroluminescence in nitrogen-doped GaP p-n junctions. *Applied Physics Letters*, 13(4):139–141, 1968.
- [5] C. P. Kuo, R. M. Fletcher, T. D. Osentowski, M. C. Lardizabal, M. G. Craford, and V. M. Robbins. High performance AlGaInP visible light-emitting diodes. *Applied Physics Letters*, 57(27):2937–2939, 1990.
- [6] J.I. Pankove, E.A. Miller, and J.E. Berkeyheiser. GaN blue light-emitting diodes. *Journal of Luminescence*, 5(1):84–86, 1972.
- [7] S. Nakamura and M. R. Krames. History of Gallium–Nitride–Based Light-Emitting Diodes for Illumination. *Proceedings of the IEEE*, 101(10):2211–2220, 2013.
- [8] H. Amano, N. Sawaki, I. Akasaki, and Y. Toyoda. Metalorganic vapor phase epitaxial growth of a high quality GaN film using an AlN buffer layer. *Applied Physics Letters*, 48(5):353–355, 1986.
- [9] Hiroshi Amano, Masahiro Kito, Kazumasa Hiramatsu, and Isamu Akasaki. P-Type Conduction in Mg-Doped GaN Treated with Low-Energy Electron Beam Irradiation (LEEBI). *Japanese Journal of Applied Physics*, 28(Part 2, No. 12):L2112–L2114, dec 1989.
- [10] Shuji Nakamura, Masayuki Senoh, Naruhito Iwasa, and Shin ichi Nagahama. High-brightness In-GaN blue, green and yellow light-emitting diodes with quantum well structures. *Japanese Journal of Applied Physics*, 34(Part 2, No. 7A):L797–L799, jul 1995.
- [11] M. G. Craford, R. D. Dupuis, M. Feng, F. A. Kish, and J. Laskar. 50th Anniversary of the Light-Emitting Diode (LED): An Ultimate Lamp [Scanning the Issue]. *Proceedings of the IEEE*, 101(10):2154–2157, 2013.
- [12] I. Akasaki. GaN-Based p–n Junction Blue-Light-Emitting Devices. *Proceedings of the IEEE*, 101(10):2200–2210, 2013.
- [13] Elison Matioli and Claude Weisbuch. *Active Region Part A. Internal Quantum Efficiency in LEDs*, pages 121–152. Springer Netherlands, Dordrecht, 2013.
- [14] P. Altieri, A. Jaeger, R. Windisch, N. Linder, P. Stauss, R. Oberschmid, and K. Streubel. Internal quantum efficiency of high-brightness AlGaInP light-emitting devices. *Journal of Applied Physics*, 98(8):086101, 2005.
- [15] I. E. Titkov, S. Y. Karpov, A. Yadav, V. L. Zerova, M. Zulonas, B. Galler, M. Strassburg, I. Pietzonka, H. Lugauer, and E. U. Rafailov. Temperature-dependent internal quantum efficiency of blue high-brightness light-emitting diodes. *IEEE Journal of Quantum Electronics*, 50(11):911–920, Nov 2014.

- [16] Claude Weisbuch. Review—On The Search for Efficient Solid State Light Emitters: Past, Present, Future. *ECS Journal of Solid State Science and Technology*, 9(1):016022, jan 2020.
- [17] Matthias Auf der Maur, Alessandro Pecchia, Gabriele Penazzi, Walter Rodrigues, and Aldo Di Carlo. Efficiency Drop in Green InGaN/GaN Light Emitting Diodes: The Role of Random Alloy Fluctuations. *Phys. Rev. Lett.*, 116:027401, Jan 2016.
- [18] LED bulb. [https://www.vippng.com/preview/iiwThhi\\_led-bulbs/](https://www.vippng.com/preview/iiwThhi_led-bulbs/), Accessed 2020-04-30.
- [19] LED traffic light. [https://www.alibaba.com/product-detail/New-design-flashing-light-led-lights\\_60538229641.html](https://www.alibaba.com/product-detail/New-design-flashing-light-led-lights_60538229641.html), Accessed 2020-04-30.
- [20] First Fully Electronical Controlled Adaptive All-LED Headlamp. <https://www.al-lighting.com/company/history/>, Accessed 2020-04-30.
- [21] Fitbit Charge HR review: the fitness tracker with an always-on heart-rate monitor. <http://lamababreview.blogspot.com/2016/05/fitbit-charge-hr-review-fitness-tracker.html>, Accessed 2020-04-30.
- [22] Press release: New light to illuminate the world. <https://www.nobelprize.org/prizes/physics/2014/press-release/>, Accessed 2020-04-30.
- [23] Claude Weisbuch. Historical perspective on the physics of artificial lighting. *Comptes Rendus Physique*, 19(3):89 – 112, 2018. LEDs: The new revolution in lighting / Les LED : la nouvelle révolution de l'éclairage.
- [24] Jong Kyu Kim and E. Fred Schubert. Transcending the replacement paradigm of solid-state lighting. *Opt. Express*, 16(26):21835–21842, Dec 2008.
- [25] Lumileds - High Power LEDs. <https://www.lumileds.com/products/high-power-leds>, Accessed 2020-05-01.
- [26] Lumileds talks LED packaging – interview. <https://www.electronicweeky.com/news/products/led/lumileds-talks-led-packaging-interview-2008-03/>, Accessed 2020-05-01.
- [27] S. M. Sze and Kwok K. Ng. *Physics of Semiconductor Devices: Third Edition*. John Wiley & Sons, Inc., 2006.
- [28] Peter Yu and Manuel Cardona. *Fundamentals of Semiconductors, Physics and Materials Properties*. Springer-Verlag Berlin Heidelberg, 2010.
- [29] Donald A. Neamen. *Semiconductor Physics and Devices, Basic Principles*. McGraw-Hill, 2011.
- [30] Mark Fox. *Optical Properties of Solids*. Oxford University Press, 2010.
- [31] Ian M. Watson. Metal organic vapour phase epitaxy of AlN, GaN, InN and their alloys: A key chemical technology for advanced device applications. *Coordination Chemistry Reviews*, 257(13):2120 – 2141, 2013. Chemistry and Applications of Metal Nitrides.
- [32] Jaehee Cho, E. Fred Schubert, and Jong Kyu Kim. Efficiency droop in light-emitting diodes: Challenges and countermeasures. *Laser & Photonics Reviews*, 7(3):408–421, 2012.
- [33] Thobeka Kente and Sabelo Dalton Mhlanga. Gallium nitride nanostructures: Synthesis, characterization and applications. *Journal of Crystal Growth*, 444:55 – 72, 2016.

- [34] S.P. DenBaars and S. Keller. Chapter 2 Metalorganic Chemical Vapor Deposition (MOCVD) of Group III Nitrides. In Jacques I. Pankove and Theodore D. Moustakas, editors, *Gallium Nitride (GaN) I*, volume 50 of *Semiconductors and Semimetals*, pages 11 – 37. Elsevier, 1997.
- [35] Guoqiang Li, Wenliang Wang, Weijia Yang, Yunhao Lin, Haiyan Wang, Zhiting Lin, and Shizhong Zhou. GaN-based light-emitting diodes on various substrates: a critical review. *Reports on Progress in Physics*, 79(5):056501, apr 2016.
- [36] D Zhu, D J Wallis, and C J Humphreys. Prospects of III-nitride optoelectronics grown on Si. *Reports on Progress in Physics*, 76(10):106501, oct 2013.
- [37] A. Dadgar, A. Strittmatter, J. Bläsing, M. Poschenrieder, O. Contreras, P. Veit, T. Riemann, F. Bertram, A. Reiher, A. Krtischil, A. Diez, T. Hempel, T. Finger, A. Kasic, M. Schubert, D. Bimberg, F. A. Ponce, J. Christen, and A. Krost. Metalorganic chemical vapor phase epitaxy of gallium-nitride on silicon. *physica status solidi (c)*, n/a(6):1583–1606, 2003.
- [38] D. Zhu, C. McAleese, M. Häberlen, M. J. Kappers, N. Hylton, P. Dawson, G. Radtke, M. Couillard, G. A. Botton, S.-L. Sahonta, and C. J. Humphreys. High-efficiency InGaN/GaN quantum well structures on large area silicon substrates. *physica status solidi (a)*, 209(1):13–16, 2012.
- [39] Yuji Zhao, Houqiang Fu, George T. Wang, and Shuji Nakamura. Toward ultimate efficiency: progress and prospects on planar and 3D nanostructured nonpolar and semipolar InGaN light-emitting diodes. *Adv. Opt. Photon.*, 10(1):246–308, Mar 2018.
- [40] Michael Kneissl, Jens Rass, Lukas Schade, and Ulrich T. Schwarz. *Growth and Optical Properties of GaN-Based Non- and Semipolar LEDs*, pages 83–119. Springer Netherlands, Dordrecht, 2013.
- [41] S. C. Jain, M. Willander, J. Narayan, and R. Van Overstraeten. III-nitrides: Growth, characterization, and properties. *Journal of Applied Physics*, 87(3):965–1006, 2000.
- [42] Shuji Nakamura. GaN growth using GaN buffer layer. *Japanese Journal of Applied Physics*, 30(Part 2, No. 10A):L1705–L1707, oct 1991.
- [43] K. Hiramatsu, S. Itoh, H. Amano, I. Akasaki, N. Kuwano, T. Shiraishi, and K. Oki. Growth mechanism of GaN grown on sapphire with AlN buffer layer by MOVPE. *Journal of Crystal Growth*, 115(1):628 – 633, 1991.
- [44] Tomoya Sugahara, Hisao Sato, Maosheng Hao, Yoshiki Naoi, Satoshi Kurai, Satoru Tottori, Kenji Yamashita, Katsushi Nishino, Linda T. Romano, and Shiro Sakai. Direct evidence that dislocations are non-radiative recombination centers in GaN. *Japanese Journal of Applied Physics*, 37(Part 2, No. 4A):L398–L400, apr 1998.
- [45] Shuji Nakamura. InGaN-based blue light-emitting diodes and laser diodes. *Journal of Crystal Growth*, 201-202:290 – 295, 1999.
- [46] Kazuyuki Tadatomo. *Epitaxy Part B. Epitaxial Growth of GaN on Patterned Sapphire Substrates*, pages 59–81. Springer Netherlands, Dordrecht, 2013.
- [47] Shizhong Zhou, Zhiting Lin, Haiyan Wang, Tian Qiao, Liyi Zhong, Yunhao Lin, Wenliang Wang, Weijia Yang, and Guoqiang Li. Nucleation mechanism for epitaxial growth of GaN on patterned sapphire substrates. *Journal of Alloys and Compounds*, 610:498 – 505, 2014.
- [48] Micro-Patterned Sapphire Substrate, MPSS. <https://www.aurotek.com.tw/en/product/product-detail/c04/154/611>, Accessed 2020-05-11.

- [49] Narihito Okada, Tohru Murata, Kazuyuki Tadatomo, Huang C. Chang, and Kazuhiro Watanabe. Growth of GaN layer and characterization of light-emitting diode using random-cone patterned sapphire substrate. *Japanese Journal of Applied Physics*, 48(12):122103, dec 2009.
- [50] A Dadgar, F Schulze, M Wienecke, A Gadanez, J Bläsing, P Veit, T Hempel, A Diez, J Christen, and A Krost. Epitaxy of GaN on silicon—impact of symmetry and surface reconstruction. *New Journal of Physics*, 9(10):389–389, oct 2007.
- [51] A. Dadgar, M. Poschenrieder, J. Bläsing, O. Contreras, F. Bertram, T. Riemann, A. Reiher, M. Kunze, I. Daumiller, A. Krtschil, A. Diez, A. Kaluza, A. Modlich, M. Kamp, J. Christen, F.A. Ponce, E. Kohn, and A. Krost. MOVPE growth of GaN on Si(111) substrates. *Journal of Crystal Growth*, 248:556 – 562, 2003. Proceedings of the eleventh international conference on Metalorganic Vapor Phase Epitaxy.
- [52] Min-Ho Kim, Young-Gu Do, Hyon Chol Kang, Do Young Noh, and Seong-Ju Park. Effects of step-graded  $\text{Al}_x\text{Ga}_{1-x}\text{N}$  interlayer on properties of GaN grown on Si(111) using ultrahigh vacuum chemical vapor deposition. *Applied Physics Letters*, 79(17):2713–2715, 2001.
- [53] A. Dadgar, M. Poschenrieder, J. Bläsing, K. Fehse, A. Diez, and A. Krost. Thick, crack-free blue light-emitting diodes on Si(111) using low-temperature AlN interlayers and in situ  $\text{Si}_x\text{N}_y$  masking. *Applied Physics Letters*, 80(20):3670–3672, 2002.
- [54] Eric Feltin, B. Beaumont, M. Laügt, P. de Mierry, P. Vennéguès, H. Lahrèche, M. Leroux, and P. Gibart. Stress control in GaN grown on silicon (111) by metalorganic vapor phase epitaxy. *Applied Physics Letters*, 79(20):3230–3232, 2001.
- [55] D. Zhu, C. McAleese, K. K. McLaughlin, M. Häberlen, C. O. Salcianu, E. J. Thrush, M. J. Kappers, W. A. Phillips, P. Lane, D. J. Wallis, T. Martin, M. Astles, S. Thomas, A. Pakes, M. Heuken, and C. J. Humphreys. GaN-based LEDs grown on 6-inch diameter Si (111) substrates by MOVPE. In Klaus P. Streubel, Heonsu Jeon, and Li-Wei Tu, editors, *Light-Emitting Diodes: Materials, Devices, and Applications for Solid State Lighting XIII*, volume 7231, pages 164 – 174. International Society for Optics and Photonics, SPIE, 2009.
- [56] E. Feltin, B. Beaumont, P. Vennéguès, M. Vaille, P. Gibart, T. Riemann, J. Christen, L. Dobos, and B. Pécz. Epitaxial lateral overgrowth of GaN on Si (111). *Journal of Applied Physics*, 93(1):182–185, 2003.
- [57] Jun-Youn Kim, Yongjo Tak, Hyun-Gi Hong, Suhee Chae, Jae Won Lee, Hyoji Choi, Jae Kyun Kim, Bokki Min, Youngsoo Park, U-In Chung, Minh Kim, Seongsuk Lee, Namgoo Cha, Yoonhee Shin, Cheolsoo Sone, Jong-Ryeol Kim, and Jong-In Shim. Highly efficient InGaN/GaN blue LEDs on large diameter Si (111) substrates comparable to those on sapphire. In Matthew H. Kane, Christian Wetzel, and Jian-Jang Huang, editors, *Eleventh International Conference on Solid State Lighting*, volume 8123, pages 87 – 92. International Society for Optics and Photonics, SPIE, 2011.
- [58] C. J. Humphreys. Does In form In-rich clusters in InGaN quantum wells? *Philosophical Magazine*, 87(13):1971–1982, 2007.
- [59] J K Sheu and G C Chi. The doping process and dopant characteristics of GaN. *Journal of Physics: Condensed Matter*, 14(22):R657–R702, may 2002.
- [60] Shuji Nakamura, Takashi Mukai, and Masayuki Senoh. Si- and Ge-Doped GaN Films Grown with GaN Buffer Layers. *Japanese Journal of Applied Physics*, 31(Part 1, No. 9A):2883–2888, sep 1992.

- [61] W. Götz, N. M. Johnson, C. Chen, H. Liu, C. Kuo, and W. Imler. Activation energies of Si donors in GaN. *Applied Physics Letters*, 68(22):3144–3146, 1996.
- [62] Shuji Nakamura, Takashi Mukai, Masayuki Senoh, and Naruhito Iwasa. Thermal Annealing Effects on P-Type Mg-Doped GaN Films. *Japanese Journal of Applied Physics*, 31(Part 2, No. 2B):L139–L142, feb 1992.
- [63] C. X. Ren. Polarisation fields in III-nitrides: effects and control. *Materials Science and Technology*, 32(5):418–433, 2016.
- [64] J. Ryou, P. D. Yoder, J. Liu, Z. Lochner, H. Kim, S. Choi, H. J. Kim, and R. D. Dupuis. Control of Quantum-Confined Stark Effect in InGa<sub>N</sub>-Based Quantum Wells. *IEEE Journal of Selected Topics in Quantum Electronics*, 15(4):1080–1091, July 2009.
- [65] E. T. Yu, X. Z. Dang, P. M. Asbeck, S. S. Lau, and G. J. Sullivan. Spontaneous and piezoelectric polarization effects in III-V nitride heterostructures. *Journal of Vacuum Science & Technology B: Microelectronics and Nanometer Structures Processing, Measurement, and Phenomena*, 17(4):1742–1749, 1999.
- [66] I. Hino, A. Gomyo, K. Kobayashi, and T. Suzuki. Room temperature pulsed operation of AlGaInP/GaInP double heterostructure visible light lasers grown by MOCVD. In *1983 International Electron Devices Meeting*, pages 308–310, Dec 1983.
- [67] K. Kobayashi, S. Kawata, A. Gomyo, I. Hino, and T. Suzuki. Room-temperature CW operation of AlGaInP double-heterostructure visible lasers. *Electronics Letters*, 21(20):931–932, Sep. 1985.
- [68] H. Sugawara, M. Ishikawa, and G. Hatakoshi. High-efficiency InGaAlP/GaAs visible light-emitting diodes. *Applied Physics Letters*, 58(10):1010–1012, 1991.
- [69] Mariko Suzuki, Kazuhiko Itaya, Yukie Nishikawa, Hideto Sugawara, and Masaki Okajima. Reduction of residual oxygen incorporation and deep levels by substrate misorientation in InGaAlP alloys. *Journal of Crystal Growth*, 133(3):303 – 308, 1993.
- [70] Guohong Wang, Xiaoyan Yi, Teng Zhan, and Yang Huang. *The AlGaInP/AlGaAs Material System and Red/Yellow LED*, pages 171–202. Springer International Publishing, Cham, 2019.
- [71] H. Chui, N.F. Gardner, P.N. Grillo, J.W. Huang, M.R. Krames, and S.A. Maranowski. Chapter 2 High-Efficiency AlGaInP Light-Emitting Diodes. In Gerd Mueller, editor, *Electroluminescence I*, volume 64 of *Semiconductors and Semimetals*, pages 49 – 128. Elsevier, 1999.
- [72] C.H. Chen, S.A. Stockman, M.J. Peanasky, and C.P. Kuo. Chapter 4 OMVPE Growth of AlGaInP for High-Efficiency Visible Light-Emitting Diodes. volume 48 of *Semiconductors and Semimetals*, pages 97 – 148. Elsevier, 1997.
- [73] S. Minagawa, M. Kondow, H. Yanagisawa, and T. Tanaka. Effect of cap layer and cooling atmosphere on the hole concentration of p(Zn)-AlGaInP grown by organometallic vapor phase epitaxy. *Journal of Crystal Growth*, 118(3):425 – 429, 1992.
- [74] Jong-In Shim, Dong-Pyo Han, Hyunsung Kim, Dong-Soo Shin, Guan-Bo Lin, David S. Meyaard, Qifeng Shan, Jaehee Cho, E. Fred Schubert, Hyunwook Shim, and Cheolsoo Sone. Efficiency droop in AlGaInP and GaInN light-emitting diodes. *Applied Physics Letters*, 100(11):111106, 2012.
- [75] Joachim Piprek. Efficiency droop in nitride-based light-emitting diodes. *physica status solidi (a)*, 207(10):2217–2225, 2010.

- [76] Giovanni Verzellesi, Davide Saguatti, Matteo Meneghini, Francesco Bertazzi, Michele Goano, Gaudenzio Meneghesso, and Enrico Zanoni. Efficiency droop in InGaN/GaN blue light-emitting diodes: Physical mechanisms and remedies. *Journal of Applied Physics*, 114(7):071101, 2013.
- [77] Y. C. Shen, G. O. Mueller, S. Watanabe, N. F. Gardner, A. Munkholm, and M. R. Krames. Auger recombination in InGaN measured by photoluminescence. *Applied Physics Letters*, 91(14):141101, 2007.
- [78] Justin Iveland, Lucio Martinelli, Jacques Peretti, James S. Speck, and Claude Weisbuch. Direct Measurement of Auger Electrons Emitted from a Semiconductor Light-Emitting Diode under Electrical Injection: Identification of the Dominant Mechanism for Efficiency Droop. *Phys. Rev. Lett.*, 110:177406, Apr 2013.
- [79] Francesco Bertazzi, Michele Goano, Xiangyu Zhou, Marco Calciati, Giovanni Ghione, Masahiko Matsubara, and Enrico Bellotti. Comment on "Direct Measurement of Auger Electrons Emitted from a Semiconductor Light-Emitting Diode under Electrical Injection: Identification of the Dominant Mechanism for Efficiency Droop" [Phys. Rev. Lett. 110, 177406 (2013)], 2013.
- [80] Kenneth J. Vampola, Michael Iza, Stacia Keller, Steven P. DenBaars, and Shuji Nakamura. Measurement of electron overflow in 450 nm InGaN light-emitting diode structures. *Applied Physics Letters*, 94(6):061116, 2009.
- [81] Tingzhu Wu, Chin-Wei Sher, Yue Lin, Chun-Fu Lee, Shijie Liang, Yijun Lu, Sung-Wen Huang Chen, Weijie Guo, Hao-Chung Kuo, and Zhong Chen. Mini-LED and Micro-LED: Promising Candidates for the Next Generation Display Technology. *Applied Sciences*, 8(9):1557, 2018.
- [82] S. X. Jin, J. Li, J. Z. Li, J. Y. Lin, and H. X. Jiang. GaN microdisk light emitting diodes. *Applied Physics Letters*, 76(5):631–633, 2000.
- [83] H. X. Jiang, S. X. Jin, J. Li, J. Shakya, and J. Y. Lin. III-nitride blue microdisplays. *Applied Physics Letters*, 78(9):1303–1305, 2001.
- [84] Zheng Gong, Shirong Jin, Yujie Chen, Jonathan McKendry, David Massoubre, Ian. M. Watson, Erdan Gu, and Martin D. Dawson. Size-dependent light output, spectral shift, and self-heating of 400 nm InGaN light-emitting diodes. *Journal of Applied Physics*, 107(1):013103, 2010.
- [85] X. Guo and E. F. Schubert. Current crowding and optical saturation effects in GaInN/GaN light-emitting diodes grown on insulating substrates. *Applied Physics Letters*, 78(21):3337–3339, 2001.
- [86] H. W. Choi, C. W. Jeon, M. D. Dawson, P. R. Edwards, R. W. Martin, and S. Tripathy. Mechanism of enhanced light output efficiency in InGaN-based microlight emitting diodes. *Journal of Applied Physics*, 93(10):5978–5982, 2003.
- [87] R. X. G. Ferreira, E. Xie, J. J. D. McKendry, S. Rajbhandari, H. Chun, G. Faulkner, S. Watson, A. E. Kelly, E. Gu, R. V. Penty, I. H. White, D. C. O'Brien, and M. D. Dawson. High Bandwidth GaN-Based Micro-LEDs for Multi-Gb/s Visible Light Communications. *IEEE Photonics Technology Letters*, 28(19):2023–2026, Oct 2016.
- [88] Samsung - The Wall. <https://www.samsung.com/us/business/products/displays/direct-view-led/the-wall/>, Accessed 2020-05-22.
- [89] MicroLED-info - Apple. <https://www.microled-info.com/apple>, Accessed 2020-05-22.

- [90] MicroLED display developer Plessey to work with Facebook. <https://optics.org/news/11/4/6>, Accessed 2020-05-22.
- [91] François Templier, Ludovic Dupré, Bertrand Dupont, Anis Daami, Bernard Aventurier, Franck Henry, Denis Sarrasin, Sébastien Renet, Frédéric Berger, François Olivier, and Lydie Mathieu. High-resolution active-matrix 10  $\mu\text{m}$  pixel-pitch GaN LED microdisplays for augmented reality applications. In Liang-Chy Chien, Tae-Hoon Yoon, and Qiong-Hua Wang, editors, *Advances in Display Technologies VIII*, volume 10556, pages 100 – 105. International Society for Optics and Photonics, SPIE, 2018.
- [92] Jacob Day, J. Li, D. Y. C. Lie, Charles Bradford, J. Y. Lin, and H. X. Jiang. III-Nitride full-scale high-resolution microdisplays. *Applied Physics Letters*, 99(3):031116, 2011.
- [93] Sujan Rajbhandari, Jonathan J D McKendry, Johannes Herrnsdorf, Hyunchae Chun, Grahame Faulkner, Harald Haas, Ian M Watson, Dominic O’Brien, and Martin D Dawson. A review of gallium nitride LEDs for multi-gigabit-per-second visible light data communications. *Semiconductor Science and Technology*, 32(2):023001, jan 2017.
- [94] Niall McAlinden, Yunzhou Cheng, Robert Scharf, Enyuan Xie, Erdan Gu, Christopher F. Reiche, Rohit Sharma, Prashant Tathireddy, Prashant Tathireddy, Loren Rieth, Steve Blair, and Keith Mathieson. Multisite microLED optrode array for neural interfacing. *Neurophotonics*, 6(3):1 – 9, 2019.
- [95] What is LiFi? - Purelifi. <https://purelifi.com/lifi-technology/>, Accessed 2020-05-22.
- [96] C. E. Shannon. Communication in the presence of noise. *Proceedings of the IRE*, 37(1):10–21, Jan 1949.
- [97] H. Le Minh, D. O’Brien, G. Faulkner, L. Zeng, K. Lee, D. Jung, Y. Oh, and E. T. Won. 100-Mb/s NRZ Visible Light Communications Using a Postequalized White LED. *IEEE Photonics Technology Letters*, 21(15):1063–1065, 2009.
- [98] J. Grubor, S. C. J. Lee, K. Langer, T. Koonen, and J. W. Walewski. Wireless High-Speed Data Transmission with Phosphorescent White-Light LEDs. In *33rd European Conference and Exhibition of Optical Communication - Post-Deadline Papers (published 2008)*, pages 1–2, 2007.
- [99] A. H. Azhar, T. Tran, and D. O’Brien. A Gigabit/s Indoor Wireless Transmission Using MIMO-OFDM Visible-Light Communications. *IEEE Photonics Technology Letters*, 25(2):171–174, 2013.
- [100] G. Cossu, A. M. Khalid, P. Choudhury, R. Corsini, and E. Ciaramella. 3.4 Gbit/s visible optical wireless transmission based on RGB LED. *Opt. Express*, 20(26):B501–B506, Dec 2012.
- [101] Mohamed Sufyan Islim, Ricardo X. Ferreira, Xiangyu He, Enyuan Xie, Stefan Videv, Shaun Viola, Scott Watson, Nikolaos Bamiedakis, Richard V. Penty, Ian H. White, Anthony E. Kelly, Erdan Gu, Harald Haas, and Martin D. Dawson. Towards 10 Gb/s orthogonal frequency division multiplexing-based visible light communication using a GaN violet micro-LED. *Photon. Res.*, 5(2):A35–A43, Apr 2017.
- [102] E. Xie, R. Bian, X. He, M. S. Islim, C. Chen, J. J. D. McKendry, E. Gu, H. Haas, and M. D. Dawson. Over 10 Gbps VLC for Long-Distance Applications Using a GaN-Based Series-Biased Micro-LED Array. *IEEE Photonics Technology Letters*, 32(9):499–502, May 2020.



- [103] M. Doniec and D. Rus. BiDirectional optical communication with AquaOptical II. In *2010 IEEE International Conference on Communication Systems*, pages 390–394, 2010.
- [104] Jianyang Shi, Xin Zhu, Fumin Wang, Peng Zou, Yingjun Zhou, Junlin Liu, Fengyi Jiang, and Nan Chi. Net data rate of 14.6 Gbit/s Underwater VLC utilizing Silicon Substrate Common-Anode Five Primary Colors LED. In *Optical Fiber Communication Conference (OFC) 2019*, page M3I.5. Optical Society of America, 2019.
- [105] Pengfei Tian, Xiaoyan Liu, Suyu Yi, Yuxin Huang, Shuailong Zhang, Xiaolin Zhou, Laigui Hu, Lirong Zheng, and Ran Liu. High-speed underwater optical wireless communication using a blue GaN-based micro-LED. *Opt. Express*, 25(2):1193–1201, Jan 2017.
- [106] G. N. Arvanitakis, R. Bian, J. J. D. McKendry, C. Cheng, E. Xie, X. He, G. Yang, M. S. Islam, A. A. Purwita, E. Gu, H. Haas, and M. D. Dawson. Gb/s Underwater Wireless Optical Communications Using Series-Connected GaN Micro-LED Arrays. *IEEE Photonics Journal*, 12(2):1–10, 2020.
- [107] S B Goncalves, J F Ribeiro, A F Silva, R M Costa, and J H Correia. Design and manufacturing challenges of optogenetic neural interfaces: a review. *Journal of Neural Engineering*, 14(4):041001, may 2017.
- [108] Jacob Gold Bernstein, Brian Douglas Allen, Alexander A. Guerra, and Edward Stuart Boyden. Processes for design, construction and utilisation of arrays of light-emitting diodes and light-emitting diode-coupled optical fibres for multi-site brain light delivery. *The Journal of Engineering*, 2015:177–184(7), May 2015.
- [109] Fiber-Coupled LEDs for Optogenetics. [https://www.thorlabs.com/newgrouppage9.cfm?objectgroup\\_id=10797](https://www.thorlabs.com/newgrouppage9.cfm?objectgroup_id=10797), Accessed 2020-08-27.
- [110] H. Cao, L. Gu, S. K. Mohanty, and J. . Chiao. An Integrated LED Optrode for Optogenetic Stimulation and Electrical Recording. *IEEE Transactions on Biomedical Engineering*, 60(1):225–229, 2013.
- [111] Niall McAlinden, Erdan Gu, Martin D. Dawson, Shuzo Sakata, and Keith Mathieson. Optogenetic activation of neocortical neurons in vivo with a sapphire-based micro-scale LED probe. *Frontiers in Neural Circuits*, 9:25, 2015.
- [112] Fan Wu, Eran Stark, Pei-Cheng Ku, Kensall D. Wise, György Buzsáki, and Euisik Yoon. Monolithically Integrated LEDs on Silicon Neural Probes for High-Resolution Optogenetic Studies in Behaving Animals. *Neuron*, 88(6):1136 – 1148, 2015.
- [113] Tae-il Kim, Jordan G. McCall, Yei Hwan Jung, Xian Huang, Edward R. Siuda, Yuhang Li, Jizhou Song, Young Min Song, Hsuan An Pao, Rak-Hwan Kim, Chaofeng Lu, Sung Dan Lee, Il-Sun Song, GunChul Shin, Ream Al-Hasani, Stanley Kim, Meng Peun Tan, Yonggang Huang, Fiorenzo G. Omenetto, John A. Rogers, and Michael R. Bruchas. Injectable, Cellular-Scale Optoelectronics with Applications for Wireless Optogenetics. *Science*, 340(6129):211–216, 2013.
- [114] Andrew Carlson, Audrey M. Bowen, Yonggang Huang, Ralph G. Nuzzo, and John A. Rogers. Transfer Printing Techniques for Materials Assembly and Micro/Nanodevice Fabrication. *Advanced Materials*, 24(39):5284–5318, 2012.
- [115] Hao Zhang and John A. Rogers. Recent Advances in Flexible Inorganic Light Emitting Diodes: From Materials Design to Integrated Optoelectronic Platforms. *Advanced Optical Materials*, 7(2):1800936, 2019.

- [116] Changhong Linghu, Shun Zhang, Chengjun Wang, and Jizhou Song. Transfer printing techniques for flexible and stretchable inorganic electronics. *Advanced Optical Materials*, 2(26):npj Flexible Electronics, 2018.
- [117] Hoon-sik Kim, Eric Brueckner, Jizhou Song, Yuhang Li, Seok Kim, Chaofeng Lu, Joshua Sulkin, Kent Choquette, Yonggang Huang, Ralph G. Nuzzo, and John A. Rogers. Unusual strategies for using indium gallium nitride grown on silicon (111) for solid-state lighting. *Proceedings of the National Academy of Sciences*, 108(25):10072–10077, 2011.
- [118] Rak-Hwan Kim, Dae-Hyeong Kim, Jianliang Xiao, Bong Hoon Kim, Sang-Il Park, Bruce Panilaitis, Roozbeh Ghaffari, Jimin Yao, Ming Li, Zhuangjian Liu, Viktor Malyarchuk, Dae Gon Kim, An-Phong Le, Ralph G. Nuzzo, David L. Kaplan, Fiorenzo G. Omenetto, Yonggang Huang, Zhan Kang, and John A. Rogers. Waterproof AllInGaP optoelectronics on stretchable substrates with applications in biomedicine and robotics. *Nature Materials*, 9:929–937, 2011.
- [119] Jae-Woong Jeong, Jordan G McCall, Gunchul Shin, Yihui Zhang, Ream Al-Hasani, Minku Kim, Shuo Li, Joo Yong Sim, Kyung-In Jang, Yan Shi, Daniel Y Hong, Yuhao Liu, Gavin P Schmitz, Li Xia, Zhubin He, Paul Gamble, Wilson Z Ray, Yonggang Huang, Michael R Bruchas, and John A Rogers. Wireless Optofluidic Systems for Programmable In Vivo Pharmacology and Optogenetics. *Cell*, 162(3):662–674, 2015.
- [120] Christopher A. Bower, Matthew A. Meitl, Brook Raymond, Erich Radauscher, Ronald Cok, Salvatore Bonafede, David Gomez, Tanya Moore, Carl Prevatte, Brent Fisher, Robert Rotzoll, George A. Melnik, Alin Fecioru, and António José Trindade. Emissive displays with transfer-printed assemblies of  $8\ \mu\text{m} \times 15\ \mu\text{m}$  inorganic light-emitting diodes. *Photon. Res.*, 5(2):A23–A29, Apr 2017.
- [121] Ronald S. Cok, Matthew Meitl, Robert Rotzoll, George Melnik, Alin Fecioru, Antonio Jose Trindade, Brook Raymond, Salvatore Bonafede, David Gomez, Tanya Moore, Carl Prevatte, Erich Radauscher, Scott Goodwin, Paul Hines, and Christopher A. Bower. Inorganic light-emitting diode displays using micro-transfer printing. *Journal of the Society for Information Display*, 25(10):589–609, 2017.
- [122] Seok Kim, Jian Wu, Andrew Carlson, Sung Hun Jin, Anton Kovalsky, Paul Glass, Zhuangjian Liu, Numair Ahmed, Steven L. Elgan, Weiqiu Chen, Placid M. Ferreira, Metin Sitti, Yonggang Huang, and John A. Rogers. Microstructured elastomeric surfaces with reversible adhesion and examples of their use in deterministic assembly by transfer printing. *Proceedings of the National Academy of Sciences*, 107(40):17095–17100, 2010.
- [123] Kun Peng, Dimitars Jevtics, Fanlu Zhang, Sabrina Sterzl, Djamshid A. Damry, Mathias U. Rothmann, Benoit Guilhabert, Michael J. Strain, Hark H. Tan, Laura M. Herz, Lan Fu, Martin D. Dawson, Antonio Hurtado, Chennupati Jagadish, and Michael B. Johnston. Three-dimensional cross-nanowire networks recover full terahertz state. *Science*, 368(6490):510–513, 2020.

## Chapter 2

# Experimental techniques for fabrication of micro light emitting diodes for transfer printing applications

Fabrication of releasable suspended micron-sized light emitting diodes (micro-LEDs) requires highly specific equipment and processes. In this chapter, the main techniques used for fabrication and transfer of micro-LEDs are reviewed and discussed. This chapter is divided into two sections. In section one, the main micro-LED fabrication processes and techniques are presented. In section two, the assembly of micro-LEDs onto non-native substrates by transfer printing is described.

### 2.1 Fabrication of micro-LEDs for transfer printing applications

The typical fabrication process of suspended GaN-based micro-LED platelets is schematically shown in Fig. 2.1. The fabrication process is similar to the one followed for the fabrication of commercial LEDs, with the main exceptions being the smaller pixel size and underetching for suspension of platelets on their growth substrate. In this section, the techniques and processes required for the fabrication of suspended micro-LED platelets are described. These techniques and processes have been grouped into pattern definition, pattern transfer and formation of metal contacts.

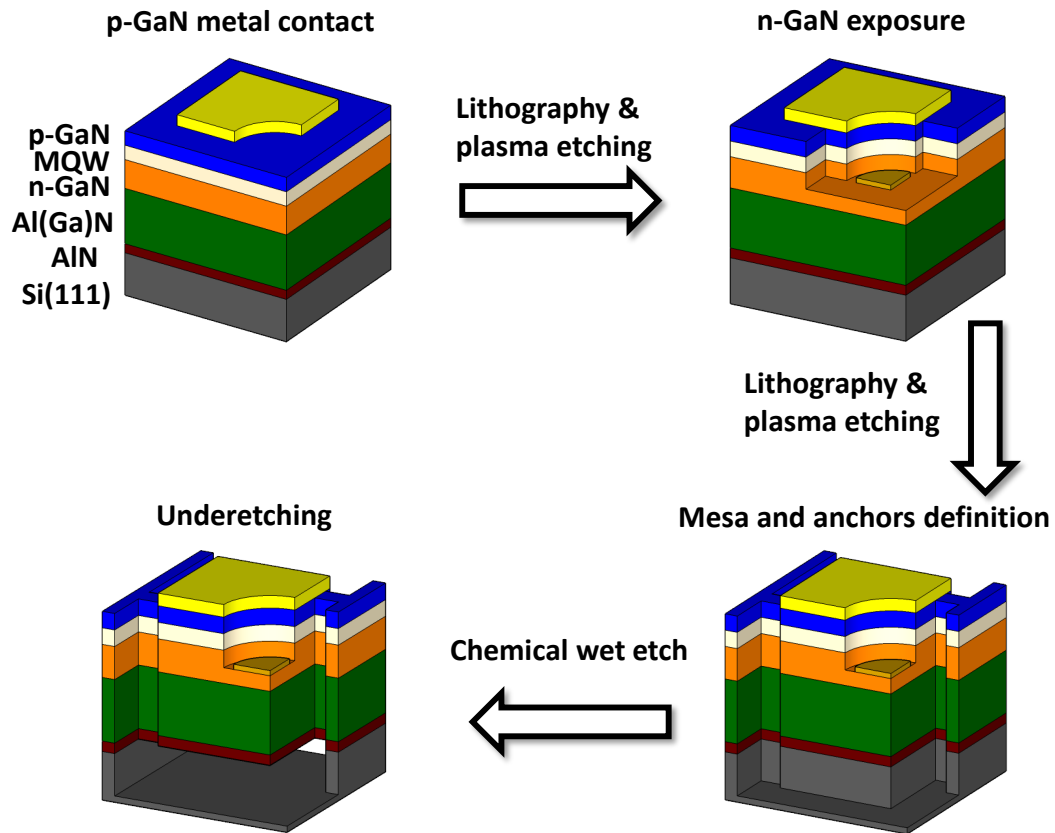


FIGURE 2.1: Schematic process flow for the fabrication of suspended GaN-based micro-LEDs.

## 2.1.1 Pattern definition

### 2.1.1.1 Photolithography

Photolithography is the process of transferring patterns on a mask to a thin layer of photosensitive material (called photoresist - PR) by light exposure (usually ultraviolet-UV). The transferred PR pattern acts as mask in subsequent etching processes that remove material from unmasked portions of the sample. The photolithography process starts with coating of the sample with a thin layer of PR. Next, the sample is exposed to UV light through apertures previously defined on the mask. This step activates the photo active compounds (PACs) in the PR, changing its chemistry. In the case of a positive PR, the exposed PR becomes soluble in developer and it is removed, while for a negative PR, the exposed PR becomes insoluble in developer and non-exposed PR is washed away. Thus, with a positive PR the obtained pattern corresponds to the mask pattern, while with a negative PR the obtained pattern is the negative of the mask [1]. This process is illustrated in Fig. 2.2.

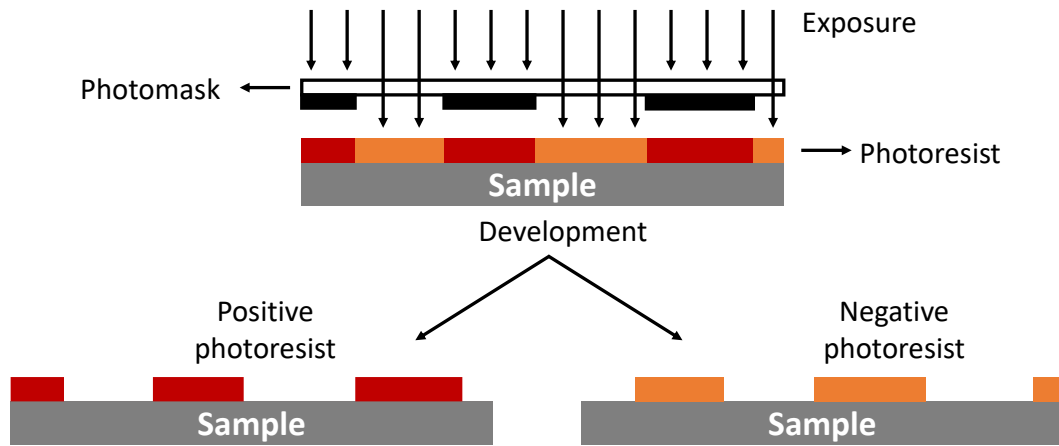


FIGURE 2.2: Schematic photolithography process for positive and negative photoresists, respectively.

In this work, alignment and exposure were performed in a Karl Suss MA6 Mask Aligner system (Fig. 2.3(a)). The main features of this system are the lamp housing, microscope, alignment stage, and mask holder. The lamp house holds a high-pressure short-arc mercury lamp (Hg UV400), which emits wavelengths primarily between 365 and 436 nm (Fig. 2.3(b)). The alignment stage allows precise translation ( $x$ - $y$ ) and rotation control. The microscope and alignment stage allow one to align the sample with the mask patterns. To allow for free movement of the sample during this step, a  $30\ \mu\text{m}$  gap between the sample and the mask is used. When aligned, the sample is brought into contact with the mask to ensure the highest resolution possible. The exposure time and dose are determined by the PR properties and thickness.

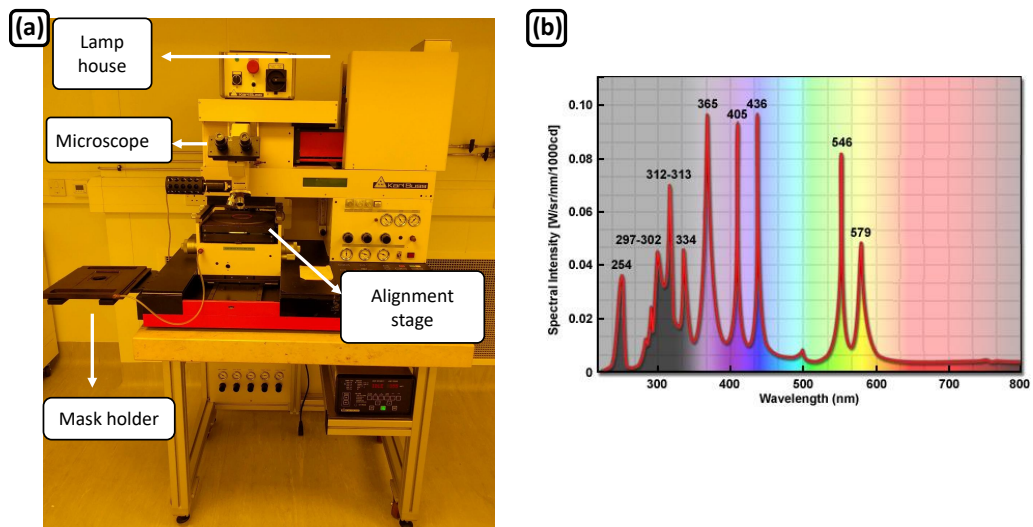


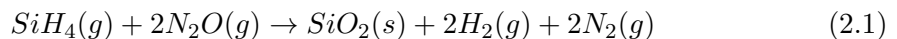
FIGURE 2.3: (a) Photograph of the mask aligner system used in this work with main features identified; (b) high-pressure mercury lamp typical emission spectrum (from [2]).

### 2.1.2 Pattern transfer

The pattern transfer process is initiated with the lithographic pattern definition step (introduced in the previous section) and finalised with the subsequent etching of the underlying material. In the etching process material is chemically and/or physically attacked and eroded in the PR unprotected areas. However, in many etching processes hard masks are required, as resists are simply not tolerant enough under harsh etching conditions. Generally, etching can be classified into dry etching and wet etching. In this section, the concept of hard masks and related processes are firstly introduced. Then, both types of etching and related techniques/processes are reviewed.

#### 2.1.2.1 Hard masks by plasma-enhanced chemical vapour deposition

As mentioned in the previous section, photolithography allows the creation of PR patterns that act as a mask during etching. However, some of the etching processes used in this work are not compatible with the use of PR (e.g. potassium hydroxide (KOH) wet etchant). A common solution to this problem is to use silicon dioxide ( $\text{SiO}_2$ ) as a hard-mask, which offers better etching resistance. This hard-mask is defined by transferring the PR pattern onto the  $\text{SiO}_2$  layer through dry etching (to be discussed in following subsection). In this work,  $\text{SiO}_2$  is deposited by plasma-enhanced chemical vapour deposition (PE-CVD) in an Oxford Plasma 80 Plus system (Fig. 2.4(a)). Figure 2.4(b) shows a schematic drawing of a PE-CVD deposition chamber. The sample is placed on the heated electrode (300 °C) and the source gases (silane ( $\text{SiH}_4$ ) and nitrous oxide ( $\text{N}_2\text{O}$ )) are introduced from the top. The source gases are activated in the plasma and diffuse to the sample surface, where they react to form a thin  $\text{SiO}_2$  film:



By using a plasma it is possible to decrease the deposition temperature while maintaining competitive deposition rates (0.1-10 nm/s) [1]. By comparison plasma-free  $\text{SiO}_2$  can also be grown by dry thermal oxidation at 900 °C and at rates of 0.5 nm/min [1].

In this work,  $\text{SiO}_2$  was deposited at a rate of 34 nm/min under the following conditions: gas flows of 170 sccm of silane and 710 sccm of nitrous oxide, 70 W of radio frequency (RF) power and substrate temperature of 300 °C.

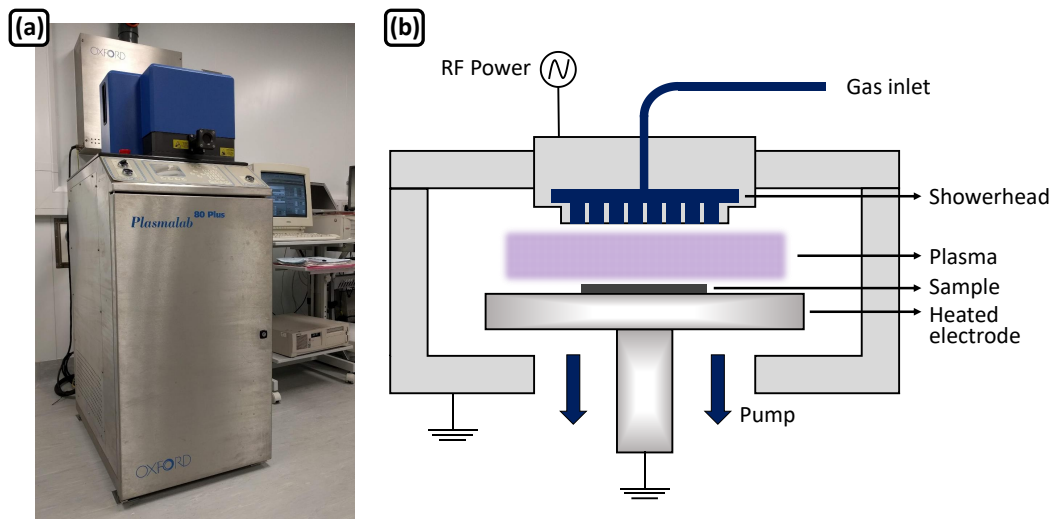


FIGURE 2.4: (a) Photograph of an Oxford Plasma 80 Plus plasma-enhanced chemical vapour deposition (PE-CVD) system; (b) schematic drawing of the PE-CVD chamber (adapted from [1]).

### 2.1.2.2 Dry etching

The term dry etching is usually used as a synonym of plasma etching, however, plasma-free dry etching processes exist. An example of such is the hydrogen fluoride (HF) vapour phase etching of  $\text{SiO}_2$ . In this work, all the dry etching processes are plasma etching processes. A plasma can be defined as a fully or partially ionized gas composed of equal numbers of positive and negative charges and a different number of unionised molecules [3]. Most microfabrication techniques use RF-excited (usually 13.56 MHz) low-temperature and low-density plasmas contained in a vacuum chamber. The plasma is initiated by the gas free electrons, which, due to the RF field, gain kinetic energy and collide with the gas molecules, ionising them. These energetic electrons can also

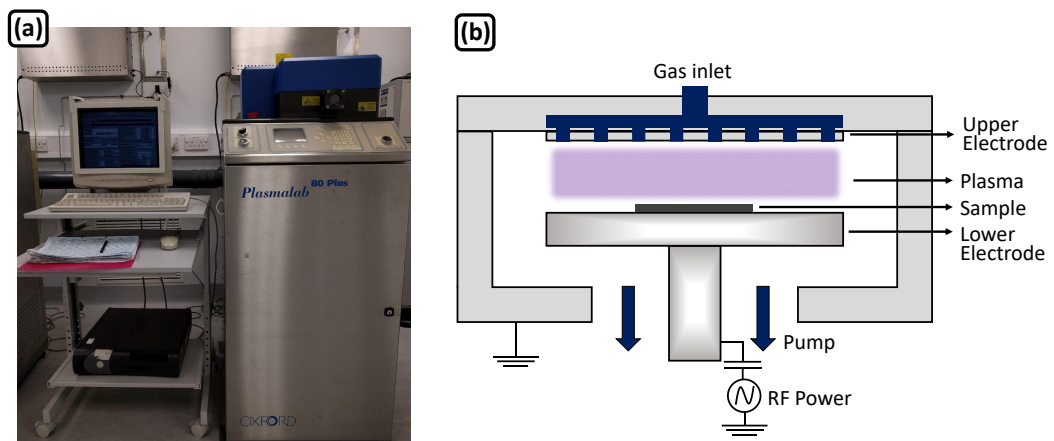


FIGURE 2.5: (a) Photograph of an Oxford Plasma 80 Plus reactive ion etching (RIE) system; (b) schematic drawing of an RIE chamber (adapted from [1]).

generate reactive radicals and enhance chemical reactions. Most plasma processes use both the energetic ions and the reactive radical for material removal, a process called reactive ion etching (RIE). In RIE ionic species accelerated by the RF field impart energy directionally to the surface, while highly reactive radicals react with the sample yielding volatile byproducts. This technique is associated with the production of vertical sidewalls and highly accurate reproduction of the PR dimensions (minimal undercut) [1, 3].

A photograph of the RIE system used in this thesis and a schematic drawing of its chamber are shown in Figs. 2.5(a) and 2.5(b), respectively. The reactive gases are fed through the top gas inlet and the plasma initiated and maintained by the RF field. The sample to be etched is placed on the lower electrode, which, being reverse biased, is strongly attacked by energetic ions and neutral radicals. In an RIE system the plasma density ( $\sim 10^9 \text{ cm}^{-3}$ ) and the bombardment energy are dependent on each other and cannot be controlled independently [1, 3]. In this work, the RIE system was mainly used to etch PR patterned  $\text{SiO}_2$ . The  $\text{SiO}_2$  was etched at a rate of 28 nm/min under the following conditions: gas flow of 5 sccm of fluoroform ( $\text{CHF}_3$ ) and 15 sccm of argon (Ar), 120 W of RF power at a pressure of 0.03 Torr.

An inductively coupled plasma (ICP) dry etching system is a modified RIE system in which plasma generation and biasing are separated (shown in Fig. 2.6). ICP systems use a set of RF-powered coils, physically separated from the gas through a dielectric window, to generate a high density plasma ( $\sim 10^{11}\text{-}10^{12} \text{ cm}^{-3}$ ). The samples are placed on the platen electrode and the ion bombardment controlled by platen RF power. As separate sources are used for plasma generation and ion acceleration, higher etch rates and higher selectivity can be achieved [1, 3]. In this work, the ICP system was used to etch GaN-based materials. An etch rate of 340 nm/min is achieved under the following

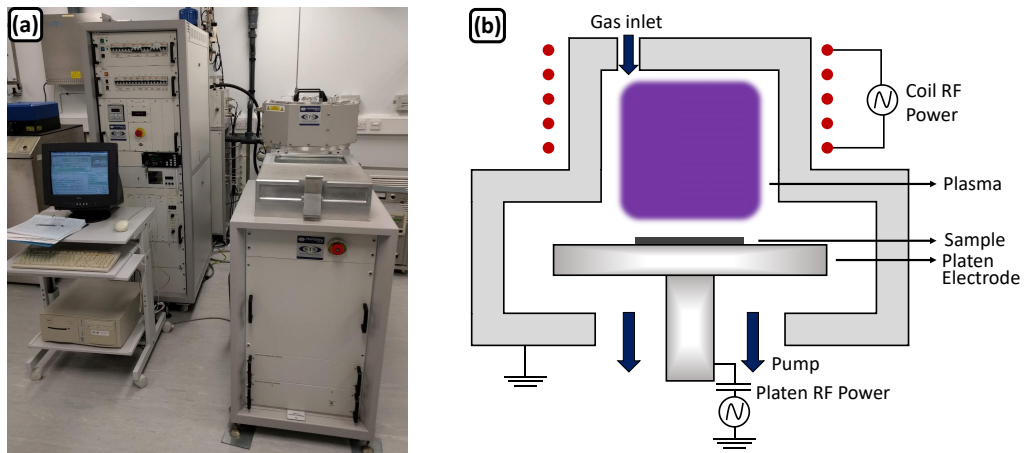


FIGURE 2.6: (a) Photograph of the inductively coupled plasma (ICP) deep reactive ion etching system used in this work; (b) schematic drawing of an ICP chamber (adapted from [1]).



conditions: Ar flow of 10 sccm, chlorine (Cl<sub>2</sub>) flow of 30 sccm, coil power of 400 W, platen power of 200 W and chamber pressure of 20 mTorr.

### 2.1.2.3 Wet etching

In wet etching, liquid chemical baths are used to etch away materials. The mechanisms for wet etching involve three essential steps: transport of reactants to the reacting surface, occurrence of chemical surface reactions generating soluble products, and transport of the products away from the surface. While plasma dry etching processes are characterised for their directionality, most of the wet etching processes are isotropic. A notable exception is the wet etching of silicon in alkaline aqueous solutions (such as KOH), which is strongly anisotropic along preferred crystalline directions [1, 3]. Silicon crystallises in the cubic diamond crystal structure. This structure belongs to the face-centred cubic (fcc) crystal family and its unit cell can be thought of as two interpenetrating fcc lattices with their origins at (0,0,0) and (1/4,1/4,1/4). Figure 2.7 shows the silicon crystal planes and crystallographic directions (a) (100) and  $\langle 100 \rangle$ , (b) (110) and  $\langle 110 \rangle$ , and (c) (111) and  $\langle 111 \rangle$ . The angle between two planes ( $\theta$ ) can be calculated from the scalar product of the normal vectors:

$$\mathbf{a} \cdot \mathbf{b} = |\mathbf{a}||\mathbf{b}|\cos(\theta) \quad (2.2)$$

Plane (100) intersects the plane (110) at 45° and the plane (111) at 54.7°. Crystallographic dependent etching of silicon relies on aligning mask openings with the Si wafer crystal planes. The wafer orientation is labelled according to the surface plane and respective normal vector. For example, the surface of a Si (111)-oriented wafer is a (111) plane with [111] surface normal vector.

One important parameter in crystallographic dependent etching of silicon is the atomic lattice packing density and available bonds in the crystallographic plane [4]. The highest atomic packing density occurs along direction  $\langle 111 \rangle$  in plane (111) (Fig. 2.7(c)). Direction  $\langle 100 \rangle$  shows a less dense atomic packing in the (100) plane (Fig. 2.7(a)). And direction  $\langle 110 \rangle$  exhibits a very low atomic packing density in the (110) plane, when compared to (111) and (100) planes. Taking this into account, one would expect the etch rate to be considerably faster in the  $\langle 110 \rangle$  direction than in the  $\langle 100 \rangle$  direction and even more so than in the  $\langle 111 \rangle$  direction. This assumption is confirmed by experimental etch rates for Si along the aforementioned planes. Table 2.1 shows the etch rate for the Si(100), Si(110), and Si(111) planes in a 30% KOH solution at 70 °C [5]. It immediately stands out that the plane Si(110) is etched faster than the plane Si(100), and the

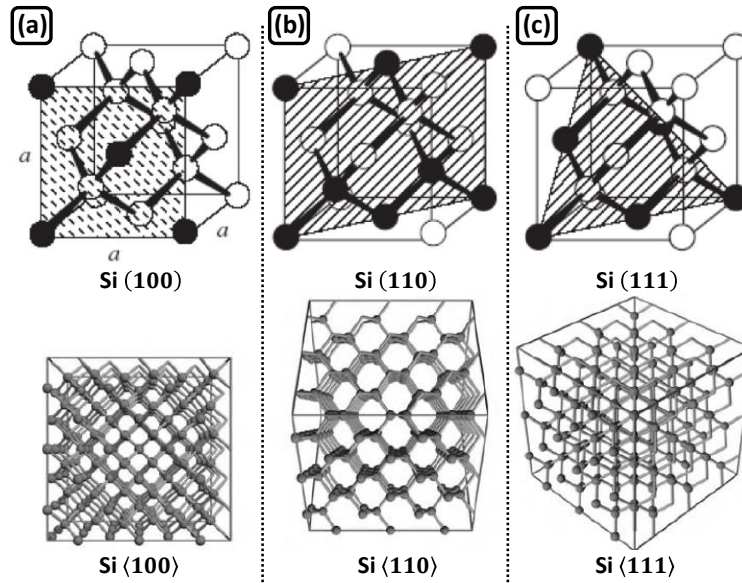


FIGURE 2.7: Silicon crystal planes and crystallographic directions for (a) (100), (b) (110), and (c) (111) Miller indices (adapted from [1]).

plane Si(111) is barely etched, confirming the theoretical prediction based on the atomic packing density.

In this work, crystallographic dependent KOH wet etching was used to create pyramidal protrusions on Si(100)-oriented wafers and to underetch the planes (110) on Si(111)-oriented wafers. The former is used to fabricate stamps for transfer printing and the latter to suspend and release micro-LED platelets from their Si(111) growth substrate (left bottom corner of Fig. 2.1). In both of these processes, PE-CVD deposited SiO<sub>2</sub> had to be used as a mask, as PR is severely attacked in KOH solutions. PE-CVD deposited SiO<sub>2</sub> is etched at 15 nm/min in a 30% KOH solution at 80 °C. Silicon nitride is commonly used in industry as it offers better resistivity to KOH (0.67 nm/min) [6]. However, the deposition of high quality SiN<sub>x</sub> films is quite challenging in our current PE-CVD system. As such, in this work, and despite its faster etching rate, SiO<sub>2</sub> masks are used in KOH wet etching processes. Figure 2.8 shows a schematic drawing of the KOH etched features used in this work for Si(100) and Si(111) wafers. In Fig. 2.8(a) a SiO<sub>2</sub> mask with a square opening (aligned with the primary flat) is RIE defined on

TABLE 2.1: Orientation dependent etch rate ( $\mu\text{m}/\text{min}$ ) for a 30% concentration KOH solution at 70 °C [5].

Direction	Etch rate ( $\mu\text{m}/\text{min}$ )	Etch rate normalised to plane Si(110)
Si(100)	0.797	0.548
Si(110)	1.455	1.000
Si(111)	0.005	0.004

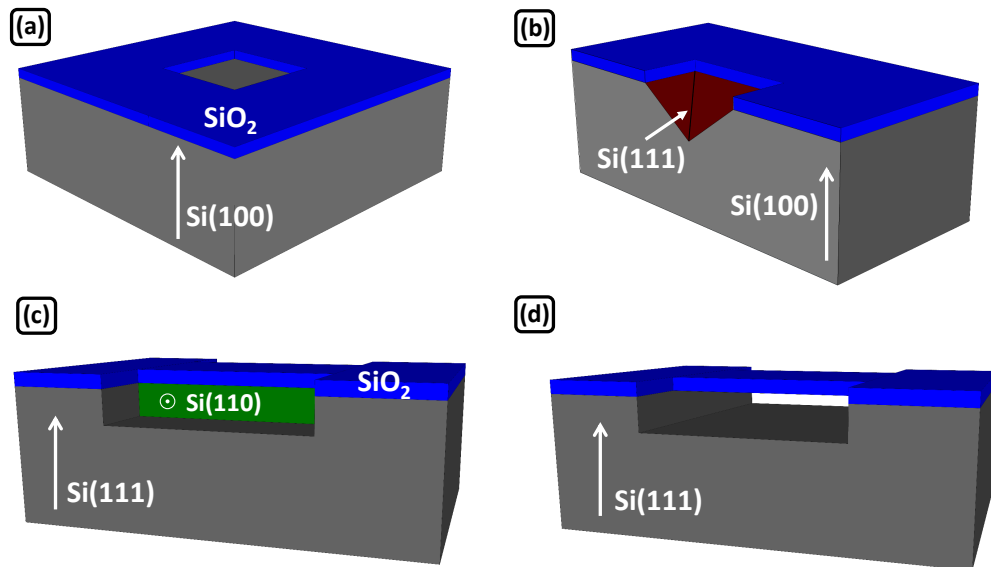


FIGURE 2.8: Schematic of (a) and (b) Si(100) wafer with a SiO<sub>2</sub> square mask opening before and after KOH etching (which exposes the Si(111) planes (identified in red)), respectively; (c) and (d) Si(111) wafer with Si(110) planes exposed (identified in green) before and after KOH etching (which etches the Si(110) plane), respectively (adapted from [1]).

top of a Si(100) sample. Figure 2.8(b) shows an inside cut of the sample after KOH wet etching. The Si(100) planes are etched while the Si(111), identified in red, are practically unetched. This etching process is said to be self limiting as it terminates when the slow etching Si(111) planes meet. As the planes (111) intersect the planes (100) at 54.7° the obtained etching feature is a square based pyramid. Figure 2.8(c) shows a SiO<sub>2</sub> bridge feature etched down to the Si(111) substrate. An additional dry etching step exposes the Si(110) planes - identified in green. The planes Si(110) are fast etched in KOH, while the Si(111) are practically not affected. As the etch removes the planes underneath a structure (in this case, the SiO<sub>2</sub> bridge) it is usually referred as an underetch. After completion of the underetch the SiO<sub>2</sub> bridge is left suspended (Fig. 2.8(d)).

The principle shown in Figs. 2.8(c) and 2.8(d) is applied in the fabrication of suspended micro-LED platelets from GaN on Si. In this case, the micro-LED platelets are tethered to the Si(111) substrate by sacrificial anchors (which are defined by dry etching) and the Si(110) planes underneath the platelet are removed in KOH wet etching. Optical pictures taken at different stages of etching process show the etch front progression underneath a GaN platelet (Fig. 2.9).

KOH aqueous solutions are known to anisotropically etch N-polar GaN and AlN [7]. The N-polar GaN etching results in nanotip pyramids structures [8], which can lead to considerable sidewall roughness of the micro-LED mesa structure. In order to mitigate this effect a thick layer of SiO<sub>2</sub> is PE-CVD deposited, before the KOH etching, for

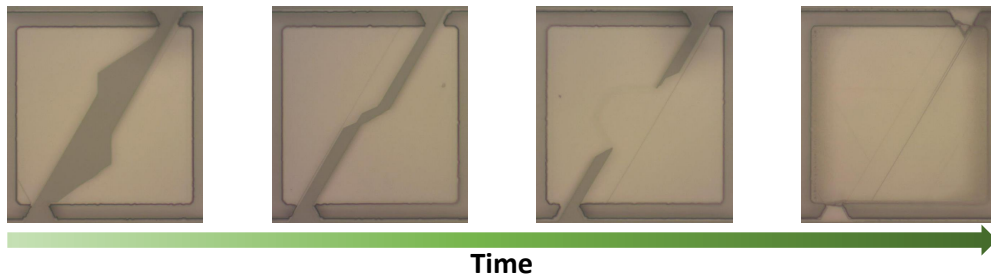


FIGURE 2.9: Plan-view optical microscope images of the KOH etch front progression over time of the planes underneath a GaN platelet. The platelet is  $100 \times 100 \mu\text{m}^2$ .

sidewall protection during the process. As the backside of the micro-LED structure is also exposed to KOH during the underetching, roughening of the micro-LED backside is expected. This roughness can play a huge role in transfer printing as it reduces the contact area between the micro-LED backside and a receiving substrate. Fortunately, the micro-LED platelet backside is protected from KOH by a thin layer of  $\text{SiN}_x^*$ , which forms between the Si(111) substrate and the buffer layer during the epitaxial growth of the LED structure [9].

### 2.1.3 Metal contacts

A crucial step in the fabrication of LEDs is the formation of metal contacts to both  $p$ - and  $n$ -GaN. In this work, different metals were deposited, by physical vapour deposition (PVD)<sup>†</sup> methods, onto the GaN surface to form metal-semiconductor contacts. In addition, in order to achieve a low specific contact resistivity, a thermal annealing process is applied to the  $p$ -GaN metal contact. The following section describes the techniques used for metal deposition and thermal annealing.

#### 2.1.3.1 Metal deposition by electron beam evaporation

In this work, the  $p$ -GaN metal contact was deposited in an electron beam (e-beam) evaporation system. Depending on the micro-LED being top-emitting or flip-chip emitting different metal were used. Top-emitting micro-LEDs required a nickel/gold (Ni/Au) 10/20 nm thick bilayer, while flip-chip micro-LEDs required a 100 nm thick palladium (Pd) metallic film.

Figures 2.10(a) and 2.10(b) show a photograph of the e-beam evaporator used in this work and a schematic drawing of its chamber, respectively. The deposition process is

\*As mentioned before,  $\text{SiN}_x$  exhibits high resistance to KOH aqueous wet etching.

<sup>†</sup>In PVD, material is ejected from a solid target material, transported in a vacuum to a sample surface where film deposition takes place.

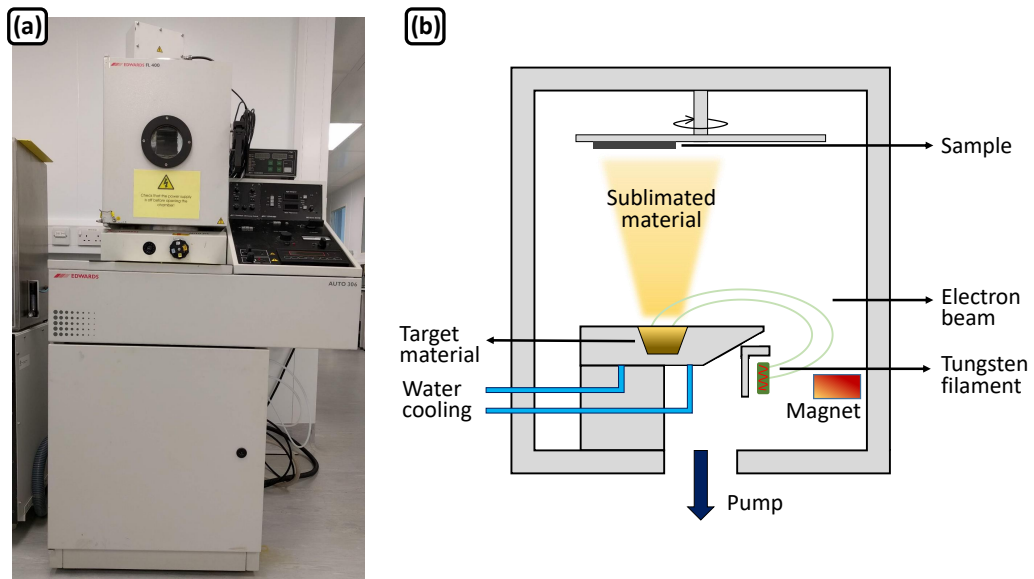


FIGURE 2.10: (a) Photograph of the e-beam metal deposition system used in this work; (b) schematic drawing of an e-beam deposition chamber (adapted from [1]).

performed in a vacuum chamber at pressures lower than  $2 \times 10^{-5}$ , which ensures a mean free path larger than the chamber size. An electron beam is generated by a passing a high electric current (in the order of 40 mA for Pd deposition) through a tungsten filament. This electron beam is redirected by a magnetic field towards a crucible that contains the desired target material. The electrons' kinetic energy is converted into thermal energy which causes the target material to melt, forming a plume of sublimated material. This plume of sublimated material travels until it reaches the sample surface, where it condenses to form a solid thin film. The target material atoms arrive at thermal speeds, which results in basically room temperature deposition. Low deposition temperature combined with line-of-sight transport means that evaporated films will not coat sidewalls or holes well, however planar surfaces exhibit good film quality [1].

### 2.1.3.2 Metal deposition by sputtering

In this work, a titanium/gold bilayer (100/200 nm thick) was used as metal contact to the *n*-GaN and to define the metal tracks. Both of these metals were deposited in a magnetron sputtering system. Figures 2.11(a) and 2.11(b) show a photograph of the magnetron sputtering system used and a schematic drawing of its chamber, respectively. In this technique, argon ions ( $\text{Ar}^+$ ), from a glow discharge plasma, hit the negatively biased target and eject target atoms. The magnet behind the target creates a field which confines electron movement, leading to a higher ionisation density, and therefore high deposition rates (1-10 nm/s). The ejected target atoms are transported in a vacuum to the sample surface where they deposit forming a thin film. Because sputtering pressures

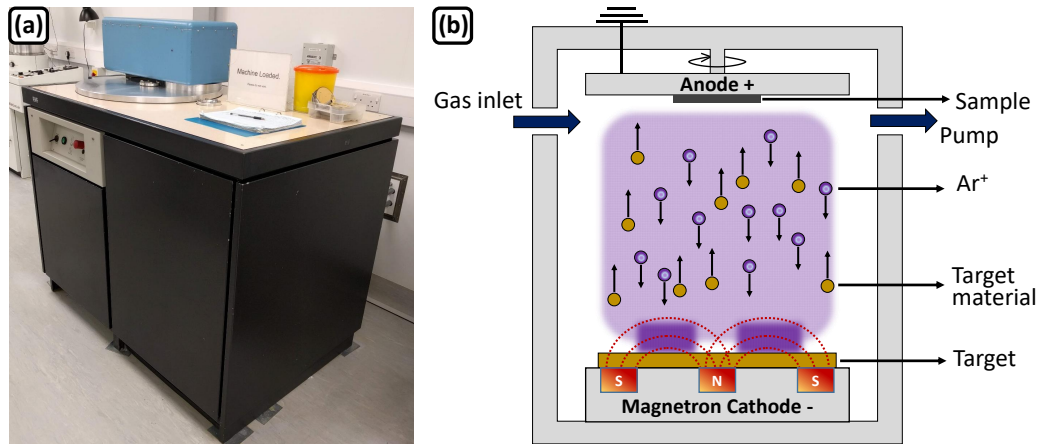


FIGURE 2.11: (a) Photograph of the sputter metal deposition system used in this work; (b) schematic drawing of a sputter deposition chamber (adapted from [1]).

are quite high, 1-10 mTorr, sputtered atoms will experience many collisions before reaching the sample surface. Therefore they deposit on the surface with random incidence angles, which results in good step coverage [1].

### 2.1.3.3 Thermal annealing

Thermal annealing of the  $p$ -GaN metal contact is known to reduce the specific contact resistance between the  $p$ -GaN and its metal contact (Ni/Au and Pd). For example, a as-deposited Ni/Au contact to  $p$ -GaN exhibits nonlinear characteristics, indicating a Schottky-type barrier between the metal and the  $p$ -GaN. Annealing at 500 °C of the Ni/Au metal contact can result in a specific contact resistance as low as  $4 \times 10^{-6} \Omega/\text{cm}^2$  and thus a good ohmic contact to  $p$ -GaN [10]. In this work, the thermal annealing was performed in a rapid thermal annealing (RTA) system. Figures 2.12(a) and 2.12(b) show a photograph of the RTA system used and a schematic drawing of its chamber, respectively. Compared to furnaces, RTA systems are single wafer tools capable of achieving ramp rates on the order of 50 to 300 °C/s, 1000 times higher than horizontal furnaces [1]. Such rapid heating rates are performed by high intensity tungsten-halogen lamps controlled by pyrometer and thermocouples<sup>‡</sup> that measure the sample temperature [11]. The gas inlet allows the introduction of different gases, such as, N<sub>2</sub> and air, so the sample can be annealed in different atmospheres. In this work, the flip-chip Pd-based micro-LEDs were annealed at 300 °C in a N<sub>2</sub> atmosphere, while the top-emitting Ni/Au-based micro-LEDs were annealed at 510 °C in an air atmosphere.

<sup>‡</sup>Thermocouples are usually used for process temperature below 600 °C [1].



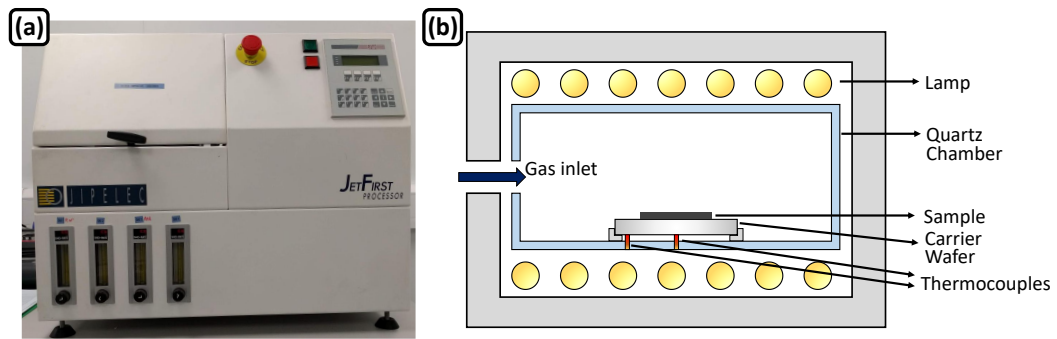


FIGURE 2.12: (a) Photograph of the rapid thermal annealing (RTA) system used in this work; (b) schematic drawing of a RTA chamber (adapted from [1]).

## 2.2 Mechanics of elastomeric transfer printing

In this work,  $100 \times 100 \mu\text{m}^2$  mesa size suspended ultra-thin micro-LED platelets were fabricated following the procedures described above. Figure 2.13(a) shows a scanning electron microscopy (SEM) micrograph of an array of suspended micro-LED platelets. Figure 2.13(b) shows a coloured SEM micrograph of a single micro-LED platelet, the pixel, *n*-GaN metal contact, LED mesa, and anchors are identified in blue, orange, yellow, and green, respectively.

Conventional assembly techniques, relying on robotic systems, cannot support assembly of such ultra-small ( $< 200 \times 200 \mu\text{m}^2$ ) and ultra-thin ( $< 50 \mu\text{m}$ ) micro-LED platelets into addressable arrays with high spatial resolution [12]. An alternative technique is elastomeric micro-transfer printing<sup>§</sup> (micro-TP), in which a stamp, made of an elastomer called polydimethylsiloxane (PDMS), is used to retrieve (“pick”) the suspended micro-LED platelets and release (“place”) them onto non-native and unconventional substrates [14].

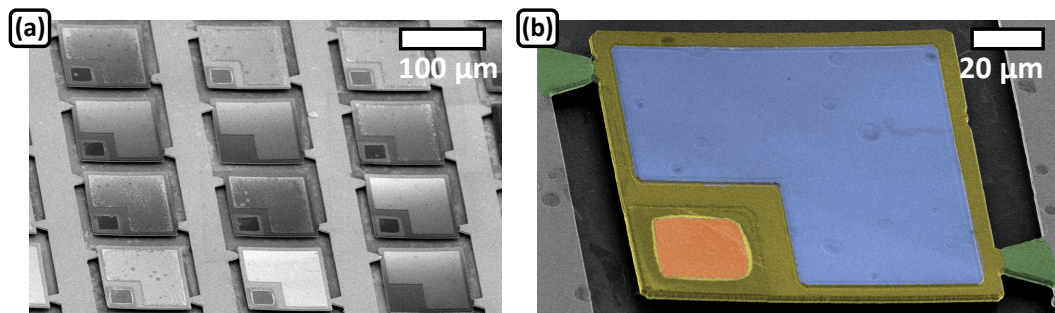


FIGURE 2.13: (a) Scanning electron microscopy (SEM) micrograph of an array of suspended micro-LED platelets; (b) coloured SEM of a single micro-LED platelet.

<sup>§</sup>While transfer printing is commonly used as a synonymy for elastomeric transfer printing, it should be noted that there are other mass-transfer techniques, such as electrostatic and electromagnetic transfer, that also involve the use of a “stamp” and are sometimes referred to as transfer printing [13].

### 2.2.1 Physical concepts

Contacting the soft PDMS stamp against solid thin-film objects (shown in green in Fig. 2.14(a)) leads to conformal contact, driven by generalised adhesion forces, which are typically dominated by van der Waals' interactions. The adhesion between the solid objects and the stamp is kinetically controllable owing to the viscoelastic behaviour of the elastomer<sup>¶</sup>. Pulling the stamp away from the donor substrate with sufficiently high peel velocity (typically 10 cm/s) leads to adhesion that is strong enough so that the solid objects adhere preferentially to the stamp, lifting them away from the substrate (Fig. 2.14(a)). The stamp is then brought into contact with a receiving substrate. Removing the stamp with sufficiently low peel velocity ( $\sim 1$  mm/s) causes the objects to adhere preferentially to the receiving substrate and separate from the stamp (Fig. 2.14(b)) [14].

The interfacial adhesive strength ( $G$ ) between the stamp and its contacting substrate depends on the stamp width and the force applied to the stamp in the normal direction. Assuming the donor and receiver substrate are the same, separation at either the stamp/film or film/substrate interface corresponds to a  $G_c^{stamp/film}$  and  $G_c^{film/substrate}$ , respectively, leading to the simple relations [16]:

$$G_c^{stamp/film} > G_c^{film/substrate} \quad \text{for retrieval} \quad (2.3)$$

$$G_c^{stamp/film} < G_c^{film/substrate} \quad \text{for printing} \quad (2.4)$$

The elastic nature of both the rigid film and the substrate implies that  $G_c^{film/substrate}$  is independent of the stamp peeling velocity. On the other hand, due to the viscoelastic properties of the stamp, the stamp energy release rate depends on the velocity and can

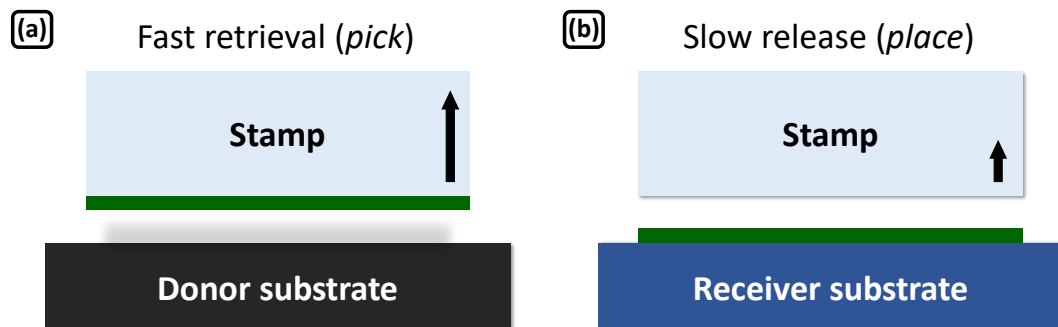


FIGURE 2.14: Side-view schematic drawing of the generic process flow for kinetically-controlled transfer printing during (a) retrieval and (b) releasing (adapted from [14]).

<sup>¶</sup>Certain polymers, such as PDMS, exhibit viscoelasticity; this is they exhibit both elastic and viscous behaviour when subjected to stress. On release of such stress, the material molecules slowly recover their former spatial arrangement and the strain slowly returns to zero. The polymer is elastic, in that it recovers, but also viscous, in that it exhibits a time-dependent strain [15].



be expressed by [16]:

$$G_c^{stamp/film}(v) = G_0 \left[ 1 + \left( \frac{v}{v_0} \right)^n \right] \quad (2.5)$$

where  $G_0$  is the zero-velocity energy release rate,  $v$  is the peeling velocity,  $v_0$  a reference velocity associated with  $G_0$ , and  $n$  is a scaling parameter that can be determined experimentally. Figure 2.15 shows a schematic diagram of the critical energy release rate for the stamp/film (black curve) and film/substrate (red line) interfaces. These two curves intersect at the critical peeling velocity; at peeling velocities  $v > v_c$ ,  $G_c^{film/substrate} < G_c^{stamp/film}$  and the film is retrieved from the substrate (pick-up); at peeling velocities  $v < v_c$ ,  $G_c^{film/substrate} > G_c^{stamp/film}$  and the film remains on the substrate (printing). For the limit of a very weak film/substrate interface (Fig. 2.15 green line), the film is always retrieved regardless of the peel velocity and therefore cannot be printed on the substrate. For case of a very strong film/substrate interface (Fig. 2.15 black line), the film is never retrieved.

This technique has proven to be efficient (up to 99.5% yield) and largely independent of chemical composition or surface energy of the receiving substrate, when the surface roughness is less than 3 nm over  $1 \mu\text{m}^2$  [14]. Such printing can be challenging when the contact area between the film and the receiving substrate is smaller than the contact area between the film and the soft, conformal stamp. Although the adhesion to the receiving substrate can be increased by using adhesive polymer layers, the fact that these materials are known to be electrical insulators and poor thermal conductors can pose an obstacle towards high-performance devices.

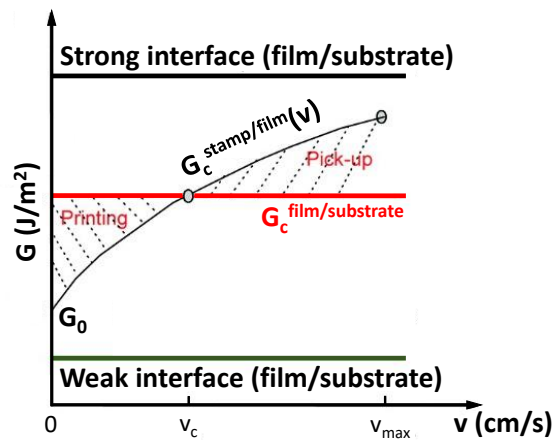


FIGURE 2.15: Schematic diagram of critical energy release rates for the stamp/film and film/substrate interfaces. The intersection of the horizontal line with the monotonically increasing curve represents the critical peel velocity ( $v_c$ ) for kinetically controlled transfer printing. The horizontal lines at the bottom and top represent very weak and very strong film/substrate interfaces, respectively, corresponding to conditions for which only retrieval and printing can be realised (adapted from [14]).

An alternative is to use microstructured stamps for kinetically controlled, adhesive-less transfer printing onto rough or non-adhesive substrates [17, 18]. These stamps have relief structures which allow one to minimise the contact area between the stamp and the film, in a manner that can reduce the adhesive strength and facilitate printing. A popular microstructured stamp design is the four pyramidal protrusions (microtips) on the corners of a square post stamp, developed by Rogers' group for transfer printing of discrete microstructures [18]. A schematic drawing (with the main dimensions identified) and a SEM micrograph (showing in detail the microtip) of such stamp are shown in Figs. 2.16(a) and 2.16(b), respectively. During retrieval (pick-up), downward force mechanically collapses the region between the microtips (this effect is known as *roof collapse*), maximising the contact area, and thus the strength of adhesion between the stamp and the microstructure (hereby referred to as platelet). When in full contact, the compressed stamp has a strong rate-dependent behaviour due to the viscoelastic nature of the stamp. Quick retraction of the stamp maintains the roof collapsed, maximising the adhesion strength between the stamp and the platelet, and thus retrieving it from its donor substrate. Figure 2.16(c) shows a colourised SEM micrograph of the stamp (identified in blue) with the roof collapsed and the retrieved platelet (identified in green). The deformation of the microtip is shown in further detail. Immediately after retraction, elastic restoring forces bring the stamp back to its original shape; the *roof de-collapses* leaving contact only at the sharp points of the microtips (Fig. 2.16(d)). During printing, the stamp is pressed against a receiver surface such that the platelet backside comes into full contact, but the stamp roof does not collapse. Slow retraction minimises the adhesion strength associated to the microtip viscoelasticity, thus facilitating release. Inspection of the effective contact areas during the collapsed and uncollapsed states, by SEM and optical images, show that the projected contacts areas are  $\sim 80\%$  and  $\sim 0.07\%$ , respectively. The ratio of these areas suggests an expected difference in adhesion of more than 1000 times between retrieval and release (Fig. 2.16(e)).

The important parameters in this four corner microtips stamp design are the stamp width ( $W_{stamp}$ ) and the microtip height ( $h_{microtip}$ ) and width ( $W_{microtip}$ ). The microtip height depends on its width accordingly to the following expression  $h_{microtip} = W_{microtip}/\sqrt{2}$ . There exists a minimum height,  $h_{min}$ , below which the elastic restoring force is too small to *de-collapse the roof*, thus failing to release the platelet. There also exists a maximum height,  $h_{max}$ , above which the elastic restoring force associated with compression of the microtips is so large that the stamp rapidly delaminates from the platelet after the pull-off force is applied. Kim *et al.* [18] have numerically calculated  $h_{min}=8.44 \mu\text{m}$  and  $h_{max}=13.3 \mu\text{m}$  for the case of silicon platelets ( $100 \times 100 \times 3 \mu\text{m}^3$ ) and  $100 \mu\text{m}$  wide four corner microtips stamps. In addition, Wu *et al.* [20] have proposed analytic expressions for the microtip minimum and maximum height, which can assist in

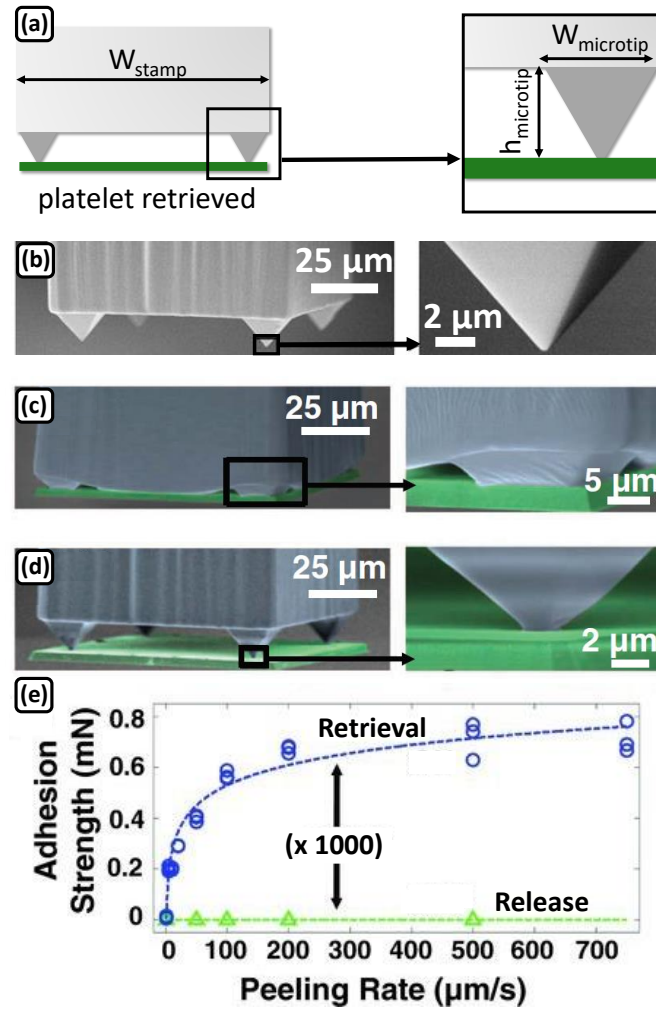


FIGURE 2.16: (a) Schematic drawing of the four corner pyramidal protrusions (microtips) stamp; scanning electron microscopy (SEM) micrographs of the stamp during (b) no contact, (c) roof collapse, and (d) roof de-collapse; (e) adhesion strength as a function of delamination velocity during retrieval (blue curve, stamp in full contact under 1.5 mN preload) and release (green curve, only microtips in contact under 0.2 mN preload) - adapted from [18, 19].

the stamp design for reversible adhesion. In this work, a variation of the four corner microtips stamp, previously described, was used for micro-transfer printing of micro-LED platelets.

### 2.2.2 Stamp fabrication process

The stamp fabrication process flow is shown in Fig. 2.17. Fabrication starts with PECVD of a  $SiO_2$  layer (shown in blue in Fig. 2.17(a)) on a Si(100) wafer. Next, square openings, aligned with the wafer flat, on the  $SiO_2$  are defined by RIE (Fig. 2.17(a)). A 30% KOH solution at 80  $^{\circ}C$  was used to expose the 54.7 $^{\circ}$  angled Si(111) planes and the remaining  $SiO_2$  was removed in buffered oxide etch (the Si(111) planes are identified in

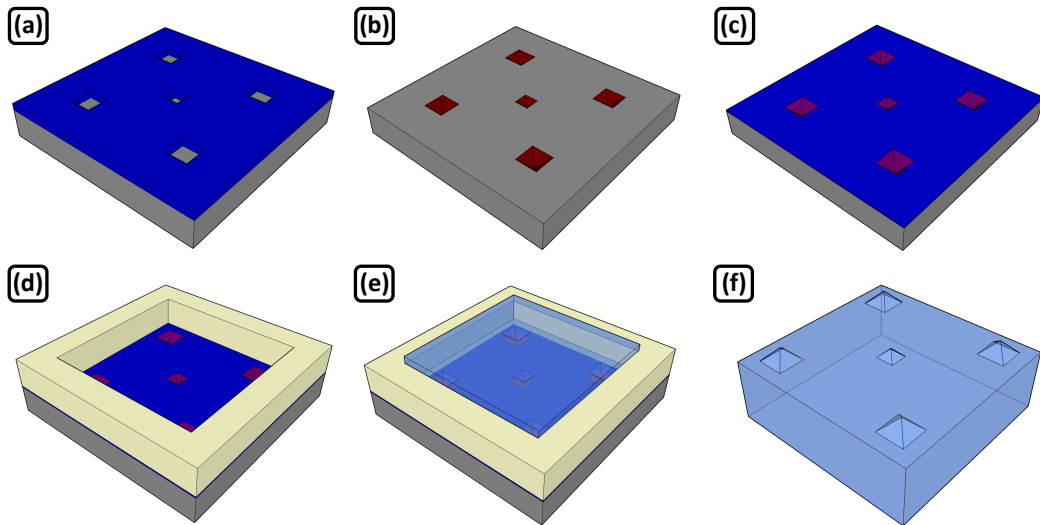


FIGURE 2.17: Schematic drawing of the elastomer stamp fabrication process flow: (a)  $\text{SiO}_2$  deposition on a Si(100) wafer and definition of square openings; (b) definition of pyramidal protrusions by anisotropic wet etching; (c)  $\text{SiO}_2$  deposition; (d) definition of the body of the stamp using thick SU-8; (e) pouring of PDMS; (f) PDMS stamp after being peeled-away from the Si(100) mould.

dark red in Fig. 2.17(b)). This step allows one to create the pyramidal microtips. In this stamp design, 4 corner microtips ( $h_{\text{corner}} = 10.6 \mu\text{m}$ ) and 1 central microtip ( $h_{\text{central}} = 9.2 \mu\text{m}$ ) were employed. The smaller central microtip facilitates the *roof de-collapse* of the stamp, and after full relaxation of the stamp, only the four corner pyramids are in contact with the retrieved platelet. Next, a thin layer of  $\text{SiO}_2$  is deposited, smoothing the Si surface, which facilitates the peeling of the PDMS (Fig. 2.17(c)). The body of the stamp is made by spin-coating and patterning a thick SU-8 (MicroChem 2100) layer (shown in yellow in Fig. 2.17(d)). The PDMS is prepared by mixing a pre-polymer base with a cross-linking curing agent in ratio of 8:1 (Sylgard 184). This mixture was degassed in a vacuum dessicator at low pressure using a roughing pump, poured into to the mould and left to cure at room temperature for 24 hours (Fig. 2.17(e)). The PDMS stamp is then peeled away from the mould (Fig. 2.17(f)) and wax-bonded to a glass cover.

### 2.2.3 Adapted NanoInk NLP 2000 system for micro-transfer printing

Figure 2.18(a) shows a photograph of an adapted NanoInk NLP 2000 system for micro-transfer printing. This system is a commercially available dip-pen nanolithography instrument capable of depositing a wide variety of materials (e.g. polymers, proteins, nanoparticles, etc.) with sub-micron accuracy and precision [21]. This system uses sets of individual or arrayed “pen” tips to create multi-component patterns with 1-10 microns feature sizes. The NLP 2000 system employs a 5 axis system consisting of

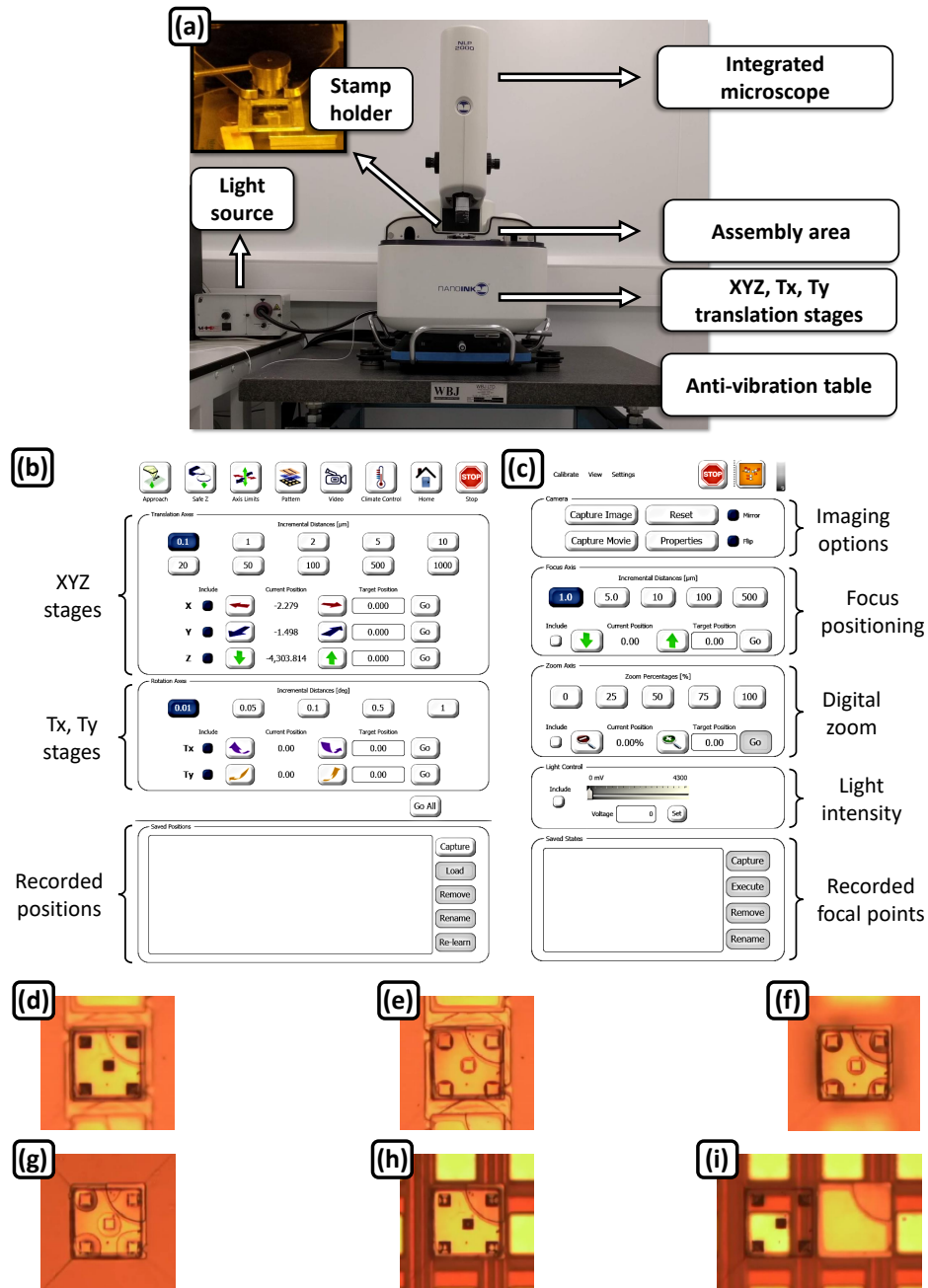


FIGURE 2.18: (a) Photograph of the adapted NanoInk NLP 2000 system for micro-transfer printing; (b) and (c) software interface for the stage motion control and imaging options, respectively; (d)-(i) plan-view (through stamp) optical images acquired with the NLP 2000 system integrated microscope of a micro-LED platelet being transfer printed from its silicon growth substrate onto a rigid substrate without any adhesion enhancement layer.

$xyz$  piezo-driven linear stages and  $T_x, T_y$  encoded goniometer stages, with accuracies of  $\pm 25$  nm and  $\pm 0.00025^\circ$ , respectively. This allows for automated and precise patterning of areas as large as  $10 \times 10$  cm<sup>2</sup>. This system was further adapted for micro-transfer printing applications by replacing the “pen” tips by a stamp holder, shown as an inset

in Fig. 2.18(a), and by replacing the ink reservoir by arrays of suspended platelets suitable for transfer printing applications.

The software interfaces for the stage motion control and imaging options are shown in Figs. 2.18(b) and 2.18(c), respectively. The stage motion can be controlled in  $xyz$ -directions and tilted in  $x$  and  $y$ . The donor and receiver substrate can be recorded, allowing fast and precise alignment of the stamp with the donor or receiver substrate. The imaging software interface allows for control of the focus positioning, digital zoom, and light intensity. It also allows to save and record focal points, which is useful to toggle between different image planes.

Facilitated by the optical transparency of the stamp Figs. 2.18(d)-2.18(i) show optical images acquired by the NanoInk microscope during micro-transfer printing of a GaN micro-LED platelet onto a rigid substrate without any adhesion enhancement layer. First, the 5 microtips' design of elastomeric stamp (delimited by the black square) is aligned with the micro-LED platelet suspended on its Si substrate (Fig. 2.18(d)). Next, the stamp is pressed against the platelet, collapsing the stamp *roof*, and thus maximising the adhesion strength between platelet and stamp (Fig. 2.18(e)). Quick retraction of the stamp maintains the *roof collapsed* and the platelet is retrieved from its Si substrate, which in Fig. 2.18(f) is in a different focal plane than the platelet. The stage then moves to a pre-recorded position on the receiver substrate, while at the same time, the stamp recovers its initial shape (Fig. 2.18(g)). When the stamp is fully relaxed (*roof de-collapses*) the platelet is then brought into contact with the receiving substrate, and only the four corner microtips are being pressed against the platelet (Fig. 2.18(h)). Slow retraction of the stamp, minimises the adhesion strength between the stamp microtips and the platelet, thus releasing it onto the receiving substrate with great accuracy and repeatability (Fig. 2.18(i)).

After micro-TP, the micro-LED platelets are not functional as they need to be electrically insulated and electrical connected to existing bonding pads on the receiving substrate. The next subsection, describes the techniques used for efficient encapsulation and electrical insulation of micro-LED pixels after micro-TP.

#### 2.2.4 Pixel encapsulation after micro-TP

Figure 2.19(a) shows a 45° tilted SEM micrograph of a micro-LED transfer printed onto the edge of a rigid substrate. Perhaps not obvious at first sight but easily seen in the larger magnification inset, is that the micro-LED platelet is bowed. This arises from the compressive strain introduced in the epitaxial structure during growth, which was

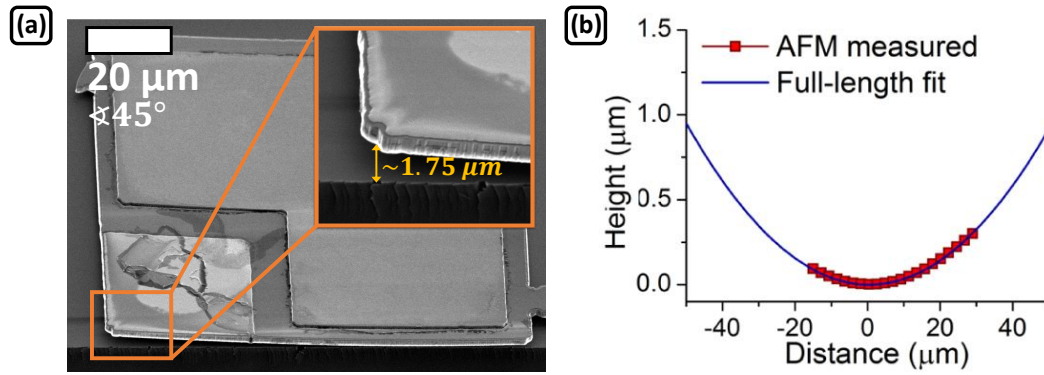


FIGURE 2.19: (a) Scanning electron microscopy micrograph of a micro-LED transfer printed onto the edge of a rigid substrate (the inset shows in further detail the micro-LED curved edges); (b) atomic force microscopy line scan over the central area of an unbonded micro-LED die and full-length parabolic fit (reproduced from [22]).

necessary to balance the tensile stress occurring during cooldown. From the SEM micrograph the distance between the flat rigid substrate and the micro-LED edge corner was estimated to be approximately  $1.75 \mu\text{m}$ . Trindade *et al.* [22] investigated the curvature of such micro-LED platelets by taking an AFM line scan over the central area of an unbonded micro-LED backside (Fig. 2.19(b)). A full length parabolic fit of the AFM results shows an height of  $1 \mu\text{m}$  at the edge of the platelet. This concave curvature of the micro-LED platelets combined with micro-LED roughened sidewalls (occurring during the KOH underteching step [23]) prevent an efficient pixel electrical insulation by conventional inorganic thin layers, such as  $\text{SiO}_2$  or  $\text{SiN}_x$ . Furthermore, Trindade *et al.* also reported that the micro-LED backside exhibited a root-mean-square roughness of  $\sim 1 \text{ nm}$ , which was attributed to the protective  $\text{SiN}_x$  layer formed between the Si substrate and the AlN growth initiation layer (see Chapter 1).

A common alternative to  $\text{SiO}_2$  to insulate and encapsulate transfer printed optoelectronic devices is the use of thick polymers, such as SU-8 [22, 24] or benzocyclobutene (BCB) [25, 26]. One of the big advantages of using SU-8 or BCB is that, as these materials are photosensitive, apertures (that allow access to the printed device electrical contacts) can be defined in a single photolithography step. One major drawback is that these thick polymers are applied by spin-coating, which can displace devices that are not strongly bonded to their receiving substrate and result in non-uniform coverage of the devices sidewall. This led us to investigate if these problems could be mitigated by using Parylene-C (Pa-C) instead of SU-8 as an insulation layer.

Pa-C was chosen due its excellent chemical stability and electrical insulation properties. A photograph of the Parylene-C (Pa-C) deposition system and a schematic drawing of the deposition process are shown in Figs. 2.20(a) and 2.20(b), respectively. Pa-C is deposited by CVD, in a process called the Gorham process after William Gorham [27].



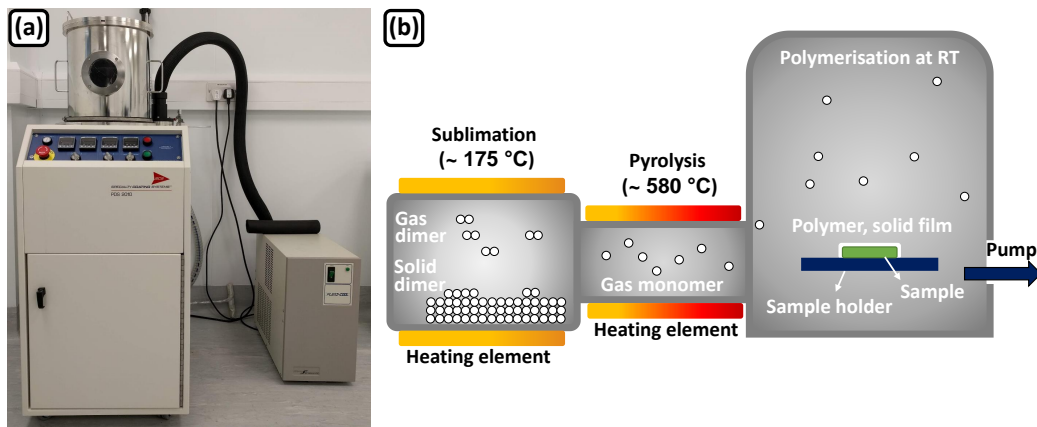


FIGURE 2.20: (a) Photograph of the Parylene-C deposition system used in this work; (b) schematic drawing of the Parylene-C deposition system chamber (adapted from [30]).

The deposition process is carried out under vacuum ( $\sim 0.1$  torr) and begins with a granular dimer precursor. Sublimation of the dimer, at around  $175^\circ\text{C}$ , followed by pyrolysis, at around  $580^\circ\text{C}$ , cleaves the dimer into its reactive radical monomer. Within the deposition chamber (at room temperature), the reactive monomer adsorbs to all exposed surfaces and begins to spontaneously polymerise, forming conformal films [28]. An extensive review of the deposition process and properties of Parylenes can be found in [29]. In this work, Pa-C films were deposited on a Speciality Coating Systems PDS 2010 system at a rate of  $0.57\ \mu\text{m}$  per gram of dimer.

Contrary to SU-8, as Pa-C is not photosensitive, patterning of Pa-C film is done by dry plasma etching. Being a polymer, Pa-C is readily removed in oxygen-based plasmas. The etching mechanism for Pa-C is believed to be similar to that of Parylene-N (Pa-N), which is different only by the absence of a chlorine atom (Pa-C and Pa-N chemical structures shown in Figs. 2.21(a) and 2.21(b), respectively). Plasma removal of Pa-N involves benzene ring opening using reactive oxygen radicals to form volatile carbon dioxide or carbon monoxide products [28, 31]. A comprehensive explanation of the etching mechanism can be found in [32]. In this work, Pa-C was etched in an RIE system at the rate of  $320\ \text{nm}/\text{min}$  under the following conditions: gas flow of  $50\ \text{sccm}$  of  $\text{O}_2$ ,  $200\ \text{W}$  of RF power at a pressure of  $0.08\ \text{Torr}$ . The next subsection, compares the use of SU-8 2005 and Pa-C as a pixel insulation/encapsulation layer.



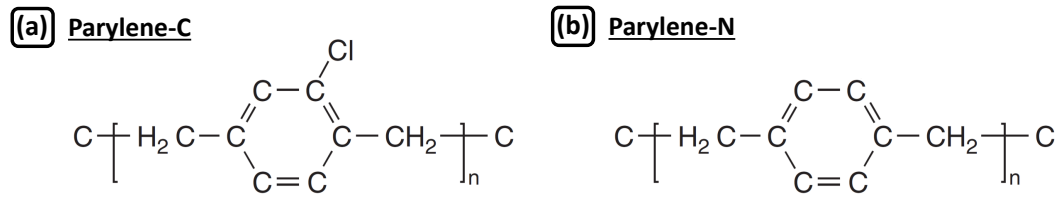


FIGURE 2.21: Chemical structures of (a) Pa-C and (b) Pa-N [1].

### 2.2.4.1 SU-8 vs Parylene-C

In order to investigate the insulation properties of both polymers, two identical samples, employing either SU-8 or Pa-C, were fabricated by sequentially transfer printing a 2x4 array of micro-LEDs onto SU-8 coated patterned sapphire substrates. Next, for the SU-8 sample, a 4.5  $\mu\text{m}$  thick SU-8 layer was prepared by spin-coating SU-8 2005 for 60 s at 3000 rpm, soft-bake for 5 minutes at 95  $^{\circ}\text{C}$ , UV-expose for 12 s, post-exposure bake for 1 minute at 95  $^{\circ}\text{C}$ , develop for 1 minute in propylene glycol methyl ether acetate (PGMEA), and hard-bake for 30 minutes at 150  $^{\circ}\text{C}$ . For the Pa-C sample, a 4.5  $\mu\text{m}$  thick Pa-C film was deposited in a Specialty Coating Systems PDS 2010 Parylene Coater. Afterwards, for both samples, 40  $\mu\text{m}$  wide titanium/gold (Ti/Au, 100/200 nm thick) tracks were lithographically defined, contacting the micro-LED platelet through localised apertures in both insulation layers. Figures 2.22(a) and 2.22(d) show plan-view photographs of a micro-LED using SU-8 and Pa-C as insulation layer, respectively. It

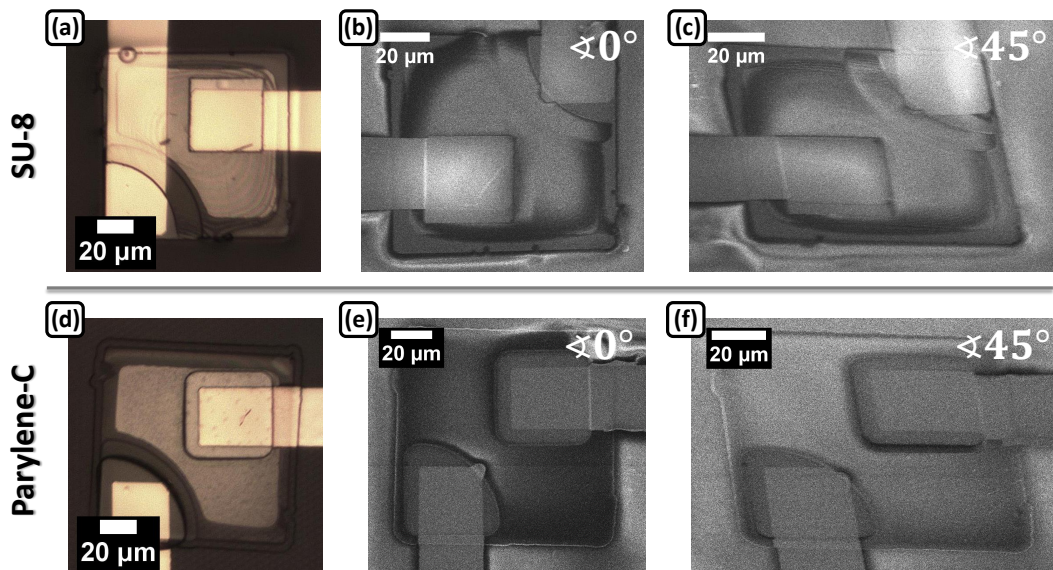


FIGURE 2.22: Plan-view photographs of a transfer printed micro-LED insulated with (a) SU-8 and (d) Pa-C; (b) and (e) SEM micrographs of a transfer printed micro-LED insulated SU-8 and Pa-C, respectively; (c) and (f) 45 $^{\circ}$ tilted SEM micrographs of a transfer printed micro-LED insulated with SU-8 and Pa-C, respectively.

can be observed that the SU-8 film shows interference fringes, when illuminated with the microscope light, suggesting thickness variation across the platelet. In addition, the SU-8 layer does not cover the full platelet. Neither fringes or discontinuities are observed for the Pa-C insulated platelet, suggesting that the Pa-C is a continuous uniform film. Plan-view SEM micrographs of the micro-LEDs (Fig. 2.22(b) for SU-8 and Fig. 2.22(e) for Pa-C) confirm the optical microscope results. By tilting the samples inside the SEM chamber it can be observed that the SU-8 layer fails to completely cover the pixel (Fig. 2.22(c)), leaving the sidewalls exposed, which can lead to electrical shortage between the  $p$ -GaN and  $n$ -GaN epilayers of the LED structure. On the other hand, the Pa-C layer perfectly conforms to the micro-LED sidewall (Fig. 2.22(f)), fully insulating and encapsulating the micro-LED platelet.

Figures 2.23(a) and 2.23(b) show the voltage *vs* current density (JV) and optical power density *vs* current density (LJ) curves, respectively, of the best performing transfer printed micro-LED insulated with SU-8 (blue squares) and Pa-C (grey triangles). The JV characteristic was measured by a voltage source, through scanning each data point under direct current (DC) conditions (Yokogawa GS610). The LJ characteristic was measured using a calibrated Si photodiode detector (Thorlabs PM100D) placed in close proximity to the micro-LED backside. The forward diode voltage of commercial LEDs (250x250  $\mu\text{m}^2$  size) is usually defined at 20 mA, corresponding to a current density of 32 A/cm<sup>2</sup> [33]. At this current density the SU-8 and Pa-C insulated micro-LEDs exhibit a forward voltage of 4.5 V and 4 V, respectively. The SU-8 insulated device also exhibits a larger series resistance ( $413 \pm 6 \Omega$ ) than the Pa-C insulated device ( $150 \pm 10 \Omega$ ). The lower forward diode voltage and series resistance suggest that using Pa-C as an insulation layer results in a better ohmic contact, which might be due to undeveloped residues of SU-8 in the micro-LED vias. In terms of optical power density, at 120 A/cm<sup>2</sup> the SU-8 and Pa-C insulated micro-LEDs achieve similar values (6.6 W/cm<sup>2</sup> and 7.6 W/cm<sup>2</sup>, respectively).

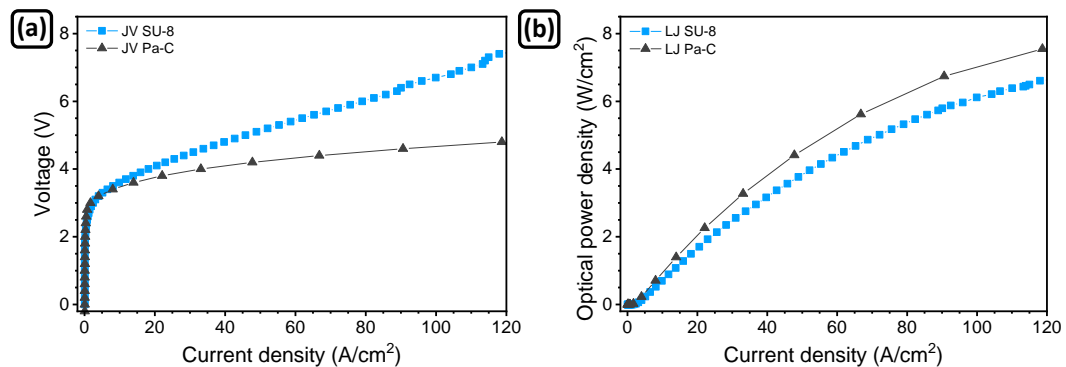


FIGURE 2.23: (a) Voltage *vs* current density (JV) curve and (b) optical power density *vs* current density (LJ) curve of the best performing transfer printed micro-LED insulated with SU-8 (blue squares) and with Pa-C (grey triangles).

The big advantage of using Pa-C over SU-8 as an insulation layer is shown in Fig. 2.24. Figure 2.24 shows the distribution of voltages at 1 mA and power density at 50 A/cm<sup>2</sup> of the 2x4 array of transfer printed micro-LEDs insulated with (a) SU-8 and (b) Pa-C. Due to SU-8 non-uniform film thickness the micro-LEDs voltage at 1 mA varies between 3.73 and 7.36 V, with some of the micro-LEDs exhibiting no optical power at 50 A/cm<sup>2</sup>. On the other hand, Pa-C film high conformity and uniformity leads to a smaller variation of voltage (between 3.2 and 5.3 V), as well as, in power density (from 3.9 to 4.9 W/cm<sup>2</sup>).

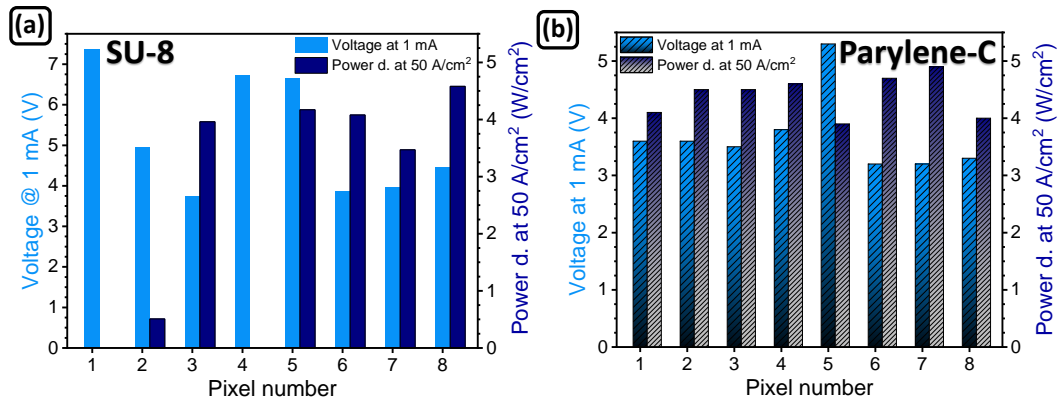


FIGURE 2.24: Distribution of voltage at 1 mA and power density at 50 A/cm<sup>2</sup> of a 2x4 array of transfer printed micro-LEDs insulated with (a) SU-8 and (b) Pa-C.

### 2.3 Summary

This chapter presented the different techniques and systems used to fabricate GaN-based suspended micro-LED platelets on their Si growth substrate. Elastomeric transfer printing was introduced as a technique which allows one to transfer such suspended micro-LED platelets onto non-native substrates with high accuracy and yield. In addition, micro-LED encapsulation after micro-transfer printing was discussed and the suitability of Parylene-C as an insulation/encapsulation layer demonstrated.

## Bibliography

- [1] Sami Franssila. *Introduction to Microfabrication Second Edition*. John Wiley & Sons, Ltd., 2010.
- [2] Education in Microscopy and Digital Imaging. <http://zeiss-campus.magnet.fsu.edu/articles/lightsources/mercuryarc.html>, Accessed 2019-08-09.
- [3] S. M. Sze and Kwok K. Ng. *Physics of Semiconductor Devices: Third Edition*. John Wiley & Sons, Inc., 2006.
- [4] K. E. Bean. Anisotropic etching of silicon. *IEEE Transactions on Electron Devices*, 25(10):1185–1193, Oct 1978.
- [5] Kazuo Sato, Mitsuhiro Shikida, Yoshihiro Matsushima, Takashi Yamashiro, Kazuo Asaumi, Yasuroh Iriye, and Masaharu Yamamoto. Characterization of orientation-dependent etching properties of single-crystal silicon: effects of KOH concentration. *Sensors and Actuators A: Physical*, 64(1):87–93, 1998. Tenth IEEE International Workshop on Micro Electro Mechanical Systems.
- [6] K. R. Williams, K. Gupta, and M. Wasilik. Etch rates for micromachining processing-Part II. *Journal of Microelectromechanical Systems*, 12(6):761–778, Dec 2003.
- [7] D. Zhuang and J.H. Edgar. Wet etching of GaN, AlN, and SiC: a review. *Materials Science and Engineering: R: Reports*, 48(1):1–46, 2005.
- [8] Hock M. Ng, Nils G. Weimann, and Aref Chowdhury. GaN nanotip pyramids formed by anisotropic etching. *Journal of Applied Physics*, 94(1):650–653, 2003.
- [9] D. Zhu, C. McAleese, M. Häberlen, M. J. Kappers, N. Hylton, P. Dawson, G. Radtke, M. Couillard, G. A. Botton, S.-L. Sahonta, and C. J. Humphreys. High-efficiency InGaN/GaN quantum well structures on large area silicon substrates. *physica status solidi (a)*, 209(1):13–16, 2012.
- [10] Jin-Kuo Ho, Charng-Shyang Jong, Chien C. Chiu, Chao-Nien Huang, Kwang-Kuo Shih, Li-Chien Chen, Fu-Rong Chen, and Ji-Jung Kai. Low-resistance ohmic contacts to p-type GaN achieved by the oxidation of Ni/Au films. *Journal of Applied Physics*, 86(8):4491–4497, 1999.
- [11] ECM USA inc Vacuum Furnaces. Jipelec RTP/RTA Furnaces. <http://www.ecm-usa.com/products/rtp-furnaces>, Accessed 2019-10-10.
- [12] Hoon-sik Kim, Eric Brueckner, Jizhou Song, Yuhang Li, Seok Kim, Chaofeng Lu, Joshua Sulkin, Kent Choquette, Yonggang Huang, Ralph G. Nuzzo, and John A. Rogers. Unusual strategies for using indium gallium nitride grown on silicon (111) for solid-state lighting. *Proceedings of the National Academy of Sciences*, 108(25):10072–10077, 2011.
- [13] Han Eol Lee, Jung Ho Shin, Jung Hwan Park, Seong Kwang Hong, Sang Hyun Park, Seung Hyung Lee, Jae Hee Lee, Il-Suk Kang, and Keon Jae Lee. Micro Light-Emitting Diodes for Display and Flexible Biomedical Applications. *Advanced Functional Materials*, 29(24):1808075, 2019.
- [14] Matthew A. Meitl, Zheng Tao Zhu, Vipin Kumar, Keon Jae Lee, Xue Feng, Yonggang Y. Huang, Ilesanmi Adesida, Ralph G. Nuzzo, and John A. Rogers. Transfer printing by kinetic control of adhesion to an elastomeric stamp. *Nature Materials*, 5(1):33–38, 1 2006.
- [15] N. G. McCrum, C. P. Buckley, and C. B. Bucknall. *Principles of Polymer Engineering*. Oxford University Press, 1997.

- [16] Xue Feng, Matthew A. Meitl, Audrey M. Bowen, Yonggang Huang, Ralph G. Nuzzo, and John A. Rogers. Competing Fracture in Kinetically Controlled Transfer Printing. *Langmuir*, 23(25):12555–12560, 2007. PMID: 17990898.
- [17] Tae-Ho Kim, Andrew Carlson, Jong-Hyun Ahn, Sang Min Won, Shuodao Wang, Yonggang Huang, and John A. Rogers. Kinetically controlled, adhesiveless transfer printing using microstructured stamps. *Applied Physics Letters*, 94(11):113502, 2009.
- [18] Seok Kim, Jian Wu, Andrew Carlson, Sung Hun Jin, Anton Kovalsky, Paul Glass, Zhuangjian Liu, Numair Ahmed, Steven L. Elgan, Weiqiu Chen, Placid M. Ferreira, Metin Sitti, Yonggang Huang, and John A. Rogers. Microstructured elastomeric surfaces with reversible adhesion and examples of their use in deterministic assembly by transfer printing. *Proceedings of the National Academy of Sciences*, 107(40):17095–17100, 2010.
- [19] Andrew Carlson, Audrey M. Bowen, Yonggang Huang, Ralph G. Nuzzo, and John A. Rogers. Transfer Printing Techniques for Materials Assembly and Micro/Nanodevice Fabrication. *Advanced Materials*, 24(39):5284–5318, 2012.
- [20] Jian Wu, Seok Kim, Weiqiu Chen, Andrew Carlson, Keh-Chih Hwang, Yonggang Huang, and John A. Rogers. Mechanics of reversible adhesion. *Soft Matter*, 7:8657–8662, 2011.
- [21] NanoInk NLP2000 system data sheet. [http://www.bnmfabrika.com/belgeler/Nanoink/DS\\_System\\_NLP2000.pdf](http://www.bnmfabrika.com/belgeler/Nanoink/DS_System_NLP2000.pdf), Accessed 2020-04-15.
- [22] A. J. Trindade, B. Guilhabert, E. Y. Xie, R. Ferreira, J. J. D. McKendry, D. Zhu, N. Laurand, E. Gu, D. J. Wallis, I. M. Watson, C. J. Humphreys, and M. D. Dawson. Heterogeneous integration of gallium nitride light-emitting diodes on diamond and silica by transfer printing. *Opt. Express*, 23(7):9329–9338, Apr 2015.
- [23] A. J. Trindade, B. Guilhabert, D. Massoubre, D. Zhu, N. Laurand, E. Gu, I. M. Watson, C. J. Humphreys, and M. D. Dawson. Nanoscale-accuracy transfer printing of ultra-thin AlInGaN light-emitting diodes onto mechanically flexible substrates. *Applied Physics Letters*, 103(25):253302, 2013.
- [24] K. Rae, P. P. Manousiadis, M. S. Islim, L. Yin, J. Carreira, J. J. D. Mckendry, B. Guilhabert, I. D. W. Samuel, G. A. Turnbull, N. Laurand, H. Haas, and M. D. Dawson. Transfer-printed micro-LED and polymer-based transceiver for visible light communications. *Opt. Express*, 26(24):31474–31483, Nov 2018.
- [25] Hoon-sik Kim, Eric Brueckner, Jizhou Song, Yuhang Li, Seok Kim, Chaofeng Lu, Joshua Sulkin, Kent Choquette, Yonggang Huang, Ralph G. Nuzzo, and John A. Rogers. Unusual strategies for using indium gallium nitride grown on silicon (111) for solid-state lighting. *Proceedings of the National Academy of Sciences*, 108(25):10072–10077, 2011.
- [26] Jing Zhang, Andreas De Groote, Amin Abbasi, Ruggero Loi, James O’Callaghan, Brian Corbett, António José Trindade, Christopher A. Bower, and Gunther Roelkens. Silicon photonics fiber-to-the-home transceiver array based on transfer-printing-based integration of III-V photodetectors. *Opt. Express*, 25(13):14290–14299, Jun 2017.
- [27] William F. Gorham. A New, General Synthetic Method for the Preparation of Linear Poly-p-xylylenes. *Journal of Polymer Science Part A-1: Polymer Chemistry*, 4(12):3027–3039, 1966.

- 
- [28] Brian J. Kim and Ellis Meng. Micromachining of Parylene C for bioMEMS. *Polymers for Advanced Technologies*, 27(5):564–576, 2016.
- [29] Jeffrey B. Fortin and Toh-Ming Lu. *Chemical Vapor Deposition Polymerization*. Springer US, 2004.
- [30] Comelec Parylene Coating. Comelec Parylene Coating Brochure. <http://www.comelec.ch/en/index.php>, Accessed 2019-10-10.
- [31] Ellis Meng, Po-Ying Li, and Yu-Chong Tai. Plasma removal of Parylene C. *Journal of Micromechanics and Microengineering*, 18(4):045004, feb 2008.
- [32] Russell R. A. Callahan, Gregory B. Raupp, and Stephen P. Beaudoin. Effects of gas pressure and substrate temperature on the etching of parylene-N using a remote microwave oxygen plasma. *Journal of Vacuum Science & Technology B: Microelectronics and Nanometer Structures Processing, Measurement, and Phenomena*, 19(3):725–731, 2001.
- [33] E. Fred Schubert. *Light-Emitting Diodes - 2<sup>nd</sup> Edition*. Cambridge University Press, 2006.

## Chapter 3

# On-chip dual-colour micro-LED arrays and their application in visible light communication and underwater wireless optical communication

This chapter presents the development of on-chip dual-colour micro-LED arrays and their application in visible light communication (VLC) and underwater wireless optical communication (UWOC). For this purpose, blue micro-LED platelets were printed onto the patterned sapphire substrate (PSS) of pre-fabricated violet and green micro-LEDs. Devices have been fabricated in two different layouts: individually addressable (blue-green and blue-violet) and in-series connected (blue-green). As shown below, individually addressable dual-colour micro-LED arrays allow tuning of the perceived colour and implementation of wavelength division multiplexing (WDM) schemes for gigabit per second (Gbps) VLC. On the other hand, the in-series connected dual-colour micro-LED array allows for a simpler electrical connecting scheme while maintaining Gbps VLC operation.

### 3.1 Introduction

The exceptional brightness, contrast, fast response time, long operation lifetime, and low power consumption of GaN-based micro-LEDs has led to their application in several fields, such as microdisplays [1] and free-space and underwater optical communications [2, 3]. Despite the huge success of monochromatic GaN-based micro-LEDs with different configurations for the aforementioned applications, a general thread common to many applications is the desire for different colour micro-emitters on a single chip platform. Multi-colour emission can be achieved by using colour converters to downshift the GaN-based micro-LED blue emission to longer wavelengths. However, due to the colour converters' lower efficiency, slow response time, and short lifespan, this solution is unsuitable for many applications [4]. Although possible, the growth of highly efficient inorganic red, green, and blue emitting materials on a single wafer is still in its early stages and is extremely challenging [5, 6]. Currently, highly efficient blue and green emitting LED structures are GaN-based, while efficient red emitters are AlGaInP-based (see Fig. 1.2(b)). An alternative is to fabricate blue, green, and red emitting micro-LEDs on their respective growth wafers and then, by transfer printing techniques, integrate the three different colour emitting micro-LEDs onto a common substrate.

Following this method, full-colour micro-LED microdisplays have been demonstrated (Fig. 3.1(a)). These arrays comprise several pixelated RGB micro-LEDs (Fig. 3.1(b)), with the blue and green emission being achieved by GaN-based LEDs and the AlGaInP material system being responsible for the red emission. Due to micro-LEDs' extremely high bandwidth, clusters of micro-LEDs in the microdisplay could be modulated at rates unperceived by the human eye and thus be used to transmit data (Fig. 3.1(c)). Such a smart microdisplay would act both as a display and as a high-speed VLC transmitter [9]. The data rate can be increased by employing wavelength division multiplexing techniques in which each different colour micro-LED would transmit a different data stream. This concept has already been implemented in a multi-Gbps VLC link using separate micro-LED chips of different colours [10], however it has not been explored in the concept

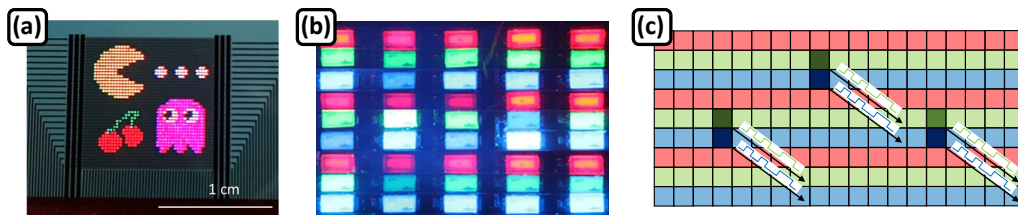


FIGURE 3.1: (a) Full-colour micro-LED display [7]; (b) close-up view of a 48x48 pixelated full-colour LED array, each chip is  $100 \times 250 \mu\text{m}^2$  in size [8]; (c) schematic drawing of a full-colour microdisplay with clusters of micro-LEDs acting as VLC transmitters.



of closely packaged on-chip multi-colour emitters. The results shown in this chapter demonstrate the potential of on-chip multi-colour micro-LED arrays, which are the basis of microdisplays, for high-speed WDM VLC.

A particular trend in VLC is underwater optical wireless communication. The development of high-speed underwater wireless communication channels is of paramount importance to the military, industry, and the scientific community, as it plays an important role in tactical surveillance, pollution monitoring, oil control and maintenance, offshore explorations, and oceanographic research, just to name a few. In particular, the emergence of automated unmanned vehicles (AUVs) for subsea exploration has created a demand for links capable of transmitting high-definition images in real time (Fig. 3.2(a)). While this can be achieved by tethered links, these can be impractical due to the challenging underwater environment. Underwater acoustics are the dominant technology in underwater wireless communication offering tens of km of range, however they suffer high latency and limited data rates of tens of kbps (Fig. 3.2(b1)). Radio frequency communication offers data rates up to Mbps, however this is attenuated by

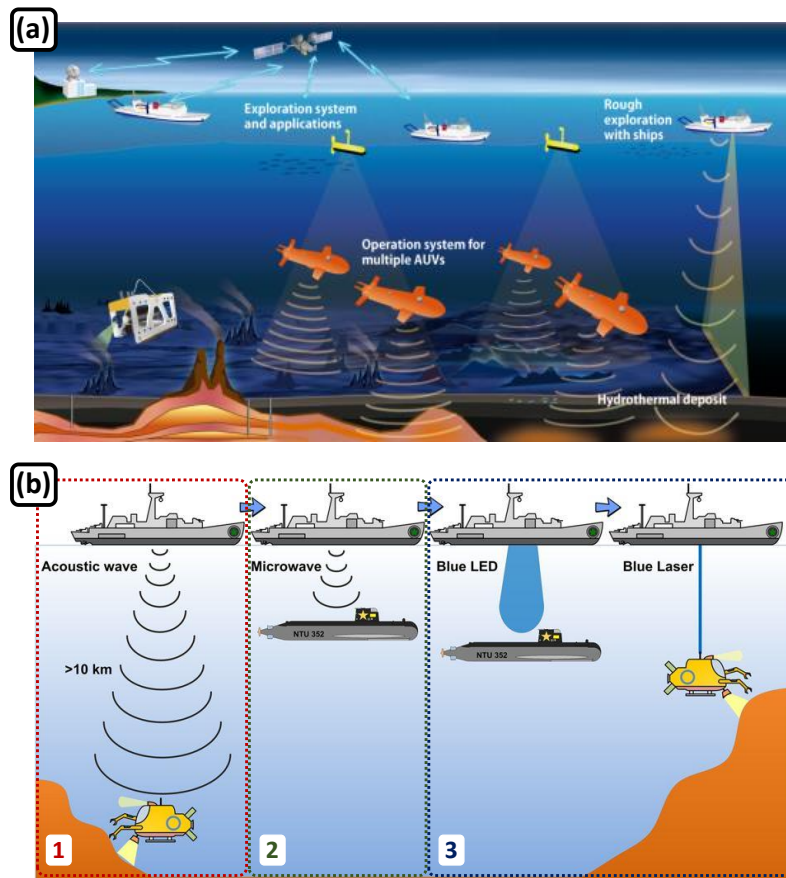


FIGURE 3.2: (a) Example of underwater wireless communication applications [11]; (b) schematic of (1) acoustic wave-, (2) microwave-, and (3) optical-based underwater communications [12].

seawater’s conductivity resulting in sub-metre ranges (Fig. 3.2(b2)). Optical devices operating at visible wavelengths can enable high-speed data transmission over tens of metres (Fig. 3.2(b3)) [3, 13, 14]. For instance, Doniec *et al.* [15] have demonstrated a 2.28 Mbps link over 50 m of clear water using an array of 18 LEDs. Arvanitakis *et al.* [16] reported data rates of 4.92 Gbps over 1.5 m of clear water using an in-series connected array of 6 micro-LEDs.

Optical signals in an underwater environment face several extreme challenges due to water absorption and/or scattering caused by suspended particles. Nevertheless, water’s lowest overall attenuation in the visible range (Fig. 3.3) results in a “transparency window”, where GaN-based LEDs are highly efficient. However, different bodies of water (varying from clear ocean to turbid harbour) exhibit different absorption/scattering properties. For example, in coastal ocean water the concentration of dissolved particles like salts, mineral components, and coloured dissolved organic matter is much higher than in clear ocean. This increase in turbidity causes the water’s transparency window shifts to longer wavelengths [3, 13, 14]. As such, wavelength-adaptable transmitters, consisting of multiple-colour LEDs, are highly desirable, not only due to their versatility but also due to the potential increase in data rates by using wavelength division multiplexing modulation schemes [17, 18].

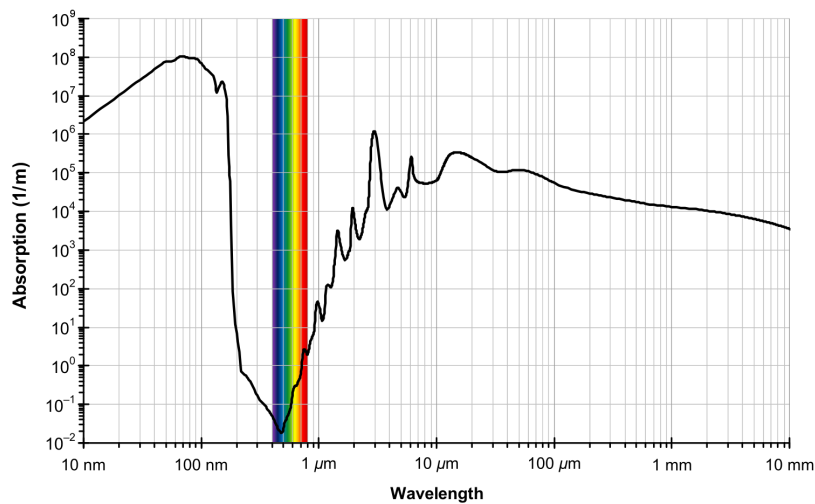


FIGURE 3.3: Water absorption spectrum (adapted from [19]).

## 3.2 Individually-addressable dual-colour micro-LED arrays

### 3.2.1 Device overview

#### 3.2.1.1 Violet and green micro-LEDs grown on sapphire

Violet and green emitting (405 nm and 520 nm, respectively) micro-LEDs in flip-chip configuration were fabricated from commercial InGaN epistuctures, grown on c-plane patterned sapphire substrates, following previously reported microfabrication procedures [20]. The violet LED epitaxial structure consisted of a 4.5  $\mu\text{m}$  GaN buffer layer, a 1.8  $\mu\text{m}$  thick *n*-doped GaN layer, a 116 nm thick active layer, a 85 nm magnesium-doped aluminium gallium nitride (AlGaIn:Mg) cladding layer, and finally a 25 nm thick *p*-doped GaN layer. The green LED epitaxial structure consisted of a 3  $\mu\text{m}$  undoped GaN buffer layer, 4  $\mu\text{m}$  of *n*-doped GaN, a 130 nm thick active layer, and was topped with a 300 nm thick *p*-doped GaN layer. In the first fabrication step, a *p*-GaN metal contact (palladium (Pd), thickness 100 nm) was electron-beam deposited, lithographically patterned, and annealed in a nitrogen environment at 300 °C (Fig. 3.4(a)). Inductively coupled plasma (ICP) etching was used to expose the underlying *n*-GaN layer defining a 20  $\mu\text{m}$  diameter pixel ( $3.15 \times 10^{-6} \text{ cm}^2$  active area) - Fig. 3.4(b). Another ICP etch step created a 90  $\mu\text{m}$  side square mesa down to the PSS, thus further reducing the micro-LEDs capacitance [21]. Then, a metal sputter deposition (titanium (Ti)/gold (Au), thicknesses 100/200 nm) defined the *n*-GaN metal contact layer (Fig. 3.4(c)). Next, a 300 nm silicon dioxide ( $\text{SiO}_2$ ) passivation layer was deposited by plasma-enhanced chemical vapour deposition (PE-CVD) and a  $\text{SiO}_2$  aperture on top of the *p*-GaN was defined by reactive ion etching (RIE). Finally, a second Ti/Au metallisation step defined the metal track (Fig. 3.4(d)).

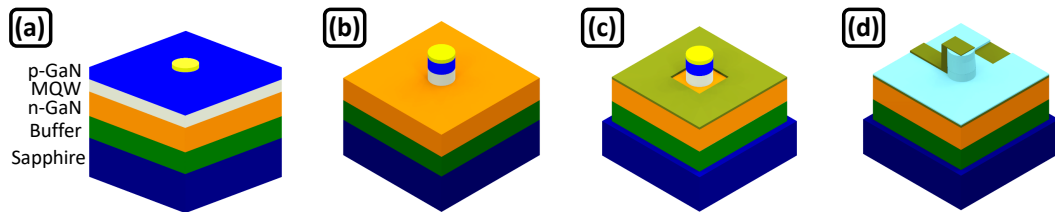


FIGURE 3.4: Schematic drawings of the sapphire substrate micro-LEDs' (violet and green) fabrication process (not to scale, see text for further details).

### 3.2.1.2 Suspended blue micro-LED platelets grown on silicon

Blue emitting (450 nm) micro-LED platelets with flip-chip configuration were fabricated from commercial InGaN epistuctures, grown on a silicon (Si) 111-oriented substrate. The blue LED epitaxial structure consisted of a 200 nm thick aluminium nitride (AlN) layer, followed by a 650 nm Al-graded GaN buffer layer, a 300 nm non-intentionally doped GaN layer, an 800 nm thick *n*-doped GaN, a 100 nm thick active layer, and a 140 nm thick *p*-doped GaN layer. An L-shaped pixel (active area of  $6.5 \times 10^{-5} \text{ cm}^2$ ) and a 100  $\mu\text{m}$  squared mesa were defined by the same processes as for the violet and green micro-LEDs. The blue TP micro-LED pixel size was chosen to be larger than the violet and green micro-LEDs in order to compensate for its lower operating optical power density. Additionally, in order to yield transferable micro-LED platelets, the following steps were undertaken. First, supporting “anchors” that tether the micro-LED platelet to the growth substrate were defined during the ICP mesa etching. Second, an additional etching step was used to expose the chemically preferentially etched Si(110) planes. Third, by wet etching (30% potassium hydroxide (KOH) solution at 80 °C) the Si(110) planes underneath the micro-LED platelets were removed. Upon completion of the underetch step, the blue micro-LED platelets are held suspended above an air gap (2  $\mu\text{m}$ ) by two diagonally opposed sacrificial anchors.

### 3.2.1.3 Heterogeneous integration by micro-transfer printing

Heterogeneous integration of the blue micro-LED platelets onto the sapphire substrate of respective violet and green micro-LEDs was enabled by micro-transfer printing (micro-TP). The elastomeric polydimethylsiloxane (PDMS) stamp show in Chapter 2 was used to pick-up the blue micro-LED platelets from their Si substrate and print them onto the PSS of the pre-prepared green and violet micro-LED chips. When printing, the adhesion force between the receiving substrate (in this case, PSS) and the micro-LED platelet backside must be larger than the adhesion force between the micro-LED platelet and the stamp. However, release of the micro-LED platelet onto to green and violet micro-LEDs' PSS is not a trivial task. Figures 3.5(a) and 3.5(b) show scanning electron microscope (SEM\* - 45 degrees tilted) and atomic force microscope (AFM<sup>†</sup>) micrographs of the PSS substrate, respectively. The SEM micrograph shows a highly dense cone-shaped periodically patterned surface. These features are also observed in AFM, from which a root-mean-square (RMS) roughness of 342 nm and maximum height feature of 1.9  $\mu\text{m}$  were extracted. The PSS roughness greatly reduces the effective contact area of the

---

\*SEM micrographs acquired using a tungsten low-vacuum JEOL JSM-IT100 InTouchScope.

<sup>†</sup>AFM micrographs using a Park systems AFM.

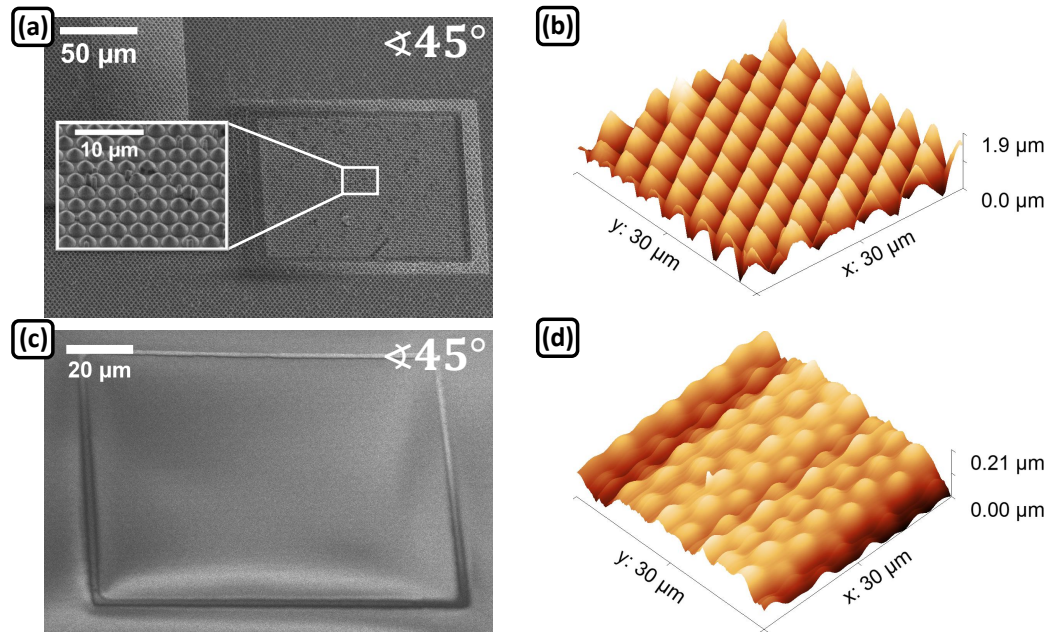


FIGURE 3.5: (a) and (b) 45 degrees tilted scanning electron microscope (SEM) and atomic force microscope (AFM) micrographs of the PSS, respectively; (c) and (d) 45 degrees tilted SEM and AFM micrographs of the PSS substrate after SU-8 planarisation, respectively.

micro-LED platelet backside with the receiving substrate, rendering the release of the micro-LED platelet from the stamp quite challenging.

In order to assist the release of the micro-LED platelet, the PSS was coated with an adhesion-enhancing layer of SU-8 epoxy-based photoresist (MicroChem SU-8 2005 - datasheet in [22]). SU-8 was chosen due to its high chemical, thermal and mechanical stability alongside its ability to render planar surfaces and high transparency at 450 nm ( $\sim 95\%$  after hard-bake) [22–24]. For this purpose, SU-8 2005 was spin-coated for 60 s at 3000 rpm, soft-baked for 5 minutes at 95 °C, UV-exposed for 12 s, post-exposure baked for 1 minute at 95 °C, developed for 1 minute in propylene glycol methyl ether acetate (PGMEA), and hard-baked for 30 minutes at 150 °C, yielding a 4.5 μm thick SU-8 layer.

This SU-8 layer effectively planarises the PSS surface, as shown by SEM and AFM (Figs. 3.5(c) and 3.5(d), respectively). The PSS RMS roughness and maximum height feature are down to 16.9 nm and 118 nm, respectively, which enabled a successful and repeatable release of the micro-LED platelet. The blue micro-LED was placed 50 μm apart from the violet or green micro-LED mesa. Next, a 4.5 μm thick Parylene-C (Pa-C) film was deposited as the insulation layer. Afterward, 40 μm wide metal tracks (Ti/Au, 100/200 nm thick) were lithographically defined, contacting the micro-LED platelet through, previously RIE defined, localized apertures in the Pa-C. Figures 3.6(a) and 3.6(b) show plan-view optical micrographs of the blue-green micro-LED array before and after micro-TP of the blue micro-LED platelet, respectively. The micro-LEDs in



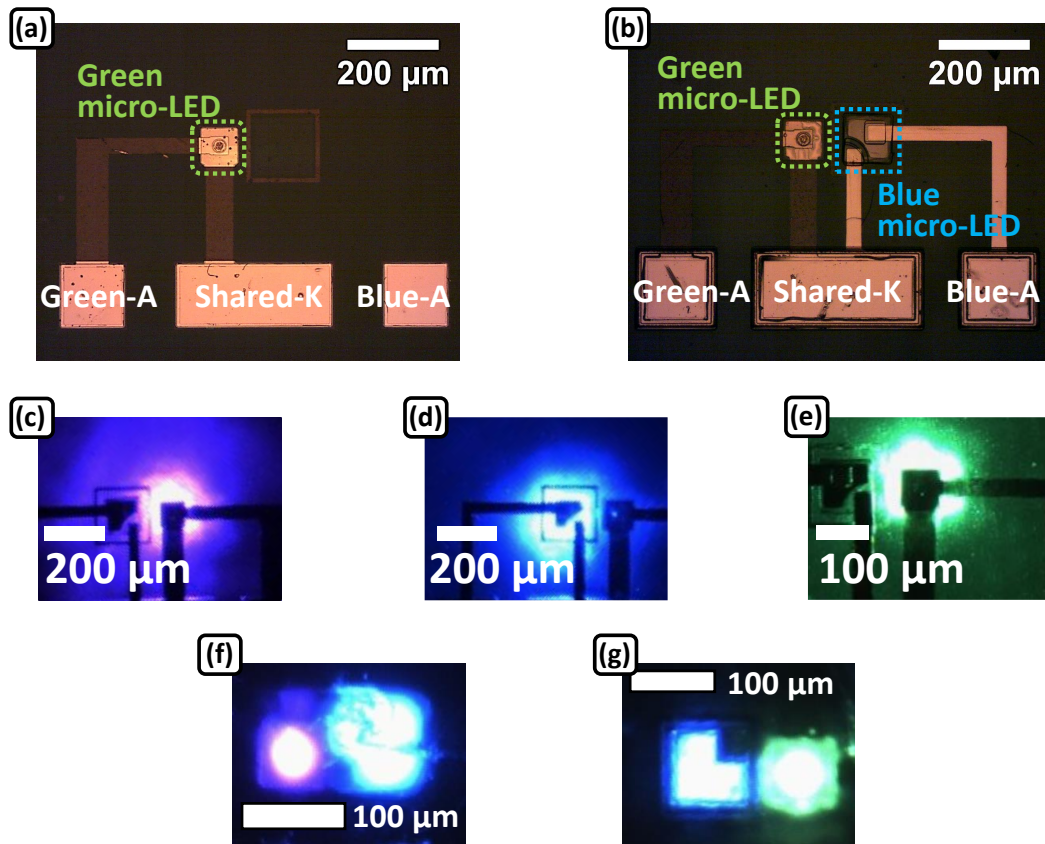


FIGURE 3.6: Plan-view optical micrographs of the blue-green micro-LED array (a) before and (b) after micro-TP of the blue micro-LED (A and K are the respective anode and common cathode contact pads); plan-view topside optical photograph of the (c) violet, (d) blue and (e) green micro-LEDs individually driven at the current density of  $318 \text{ A/cm}^2$ ,  $15 \text{ A/cm}^2$  and  $318 \text{ A/cm}^2$ , respectively; plan-view backside optical photographs of the (f) blue-violet and (g) blue-green micro-LED arrays simultaneously driven at  $318 \text{ A/cm}^2$  (green and violet) and  $15 \text{ A/cm}^2$  (blue).

this array are individually anode-addressable sharing a common cathode (K). The blue-violet micro-LED array follows the same layout. Plan-view topside optical micrographs of the individually driven violet (at  $318 \text{ A/cm}^2$ ), blue (at  $15 \text{ A/cm}^2$ ), and green (at  $318 \text{ A/cm}^2$ ) micro-LEDs are shown in Figs. 3.6(c)-3.6(e), respectively. In addition, plan-view backside optical photographs of the blue-violet and the blue-green micro-LED arrays simultaneously driven at  $318 \text{ A/cm}^2$  (green and violet) and  $15 \text{ A/cm}^2$  are shown in Figs. 3.6(f) and 3.6(g), respectively.

### 3.2.2 Electrical, optical and bandwidth performance of single-colour micro-LEDs

The room temperature (RT) voltage *vs* current density (JV) and optical power *vs* current density (LJ) performance of the violet, green, and blue micro-LEDs fabricated in

this work are shown in Figs. 3.7(a)-3.7(c), respectively. In addition, the electroluminescence (EL) spectra of the violet, green, and blue micro-LEDs, acquired at 318 A/cm<sup>2</sup> for the violet and green micro-LEDs and 15 A/cm<sup>2</sup> for the blue micro-LED, are presented in Figs. 3.7(d)-3.7(f), respectively. The JV characteristic was measured by a current source, through scanning each data point under direct current (DC) conditions (Yokogawa GS610). The LJ was measured using a calibrated Si photodiode detector (Thorlabs PM100D) in proximity to the backside of the micro-LEDs. The EL spectra were acquired by an optical fibre-coupled spectrometer (Avantes AvaSpec-2048L spectrometer). The violet and green micro-LEDs present a respective turn-on voltage (at 318 A/cm<sup>2</sup>) of 3.5 V and 5.4 V and, at 2.8 kA/cm<sup>2</sup>, their optical powers are 0.85 mW and 0.34 mW, respectively. At the current density of 318 A/cm<sup>2</sup>, the violet and green micro-LED EL spectra exhibit a broad peak centred at 400 and 512 nm, respectively.

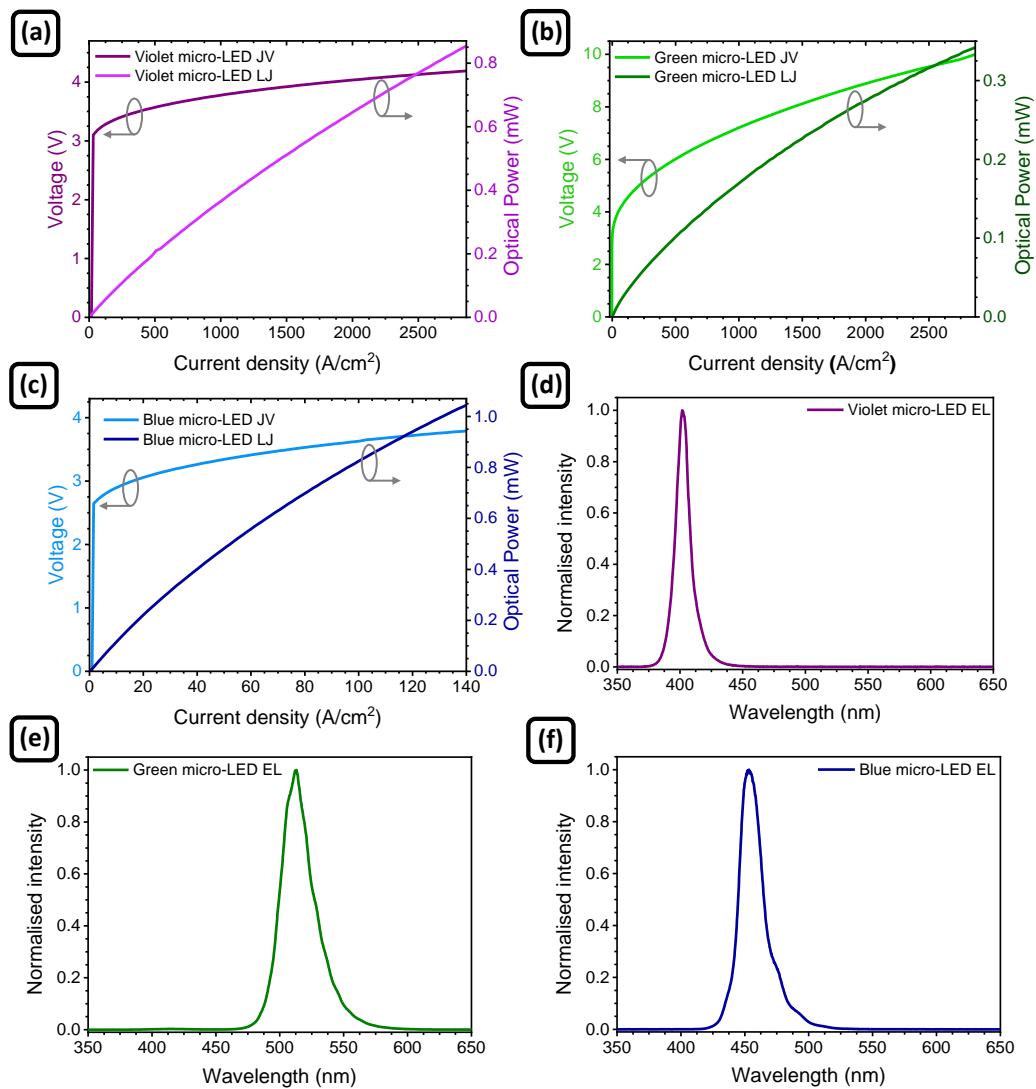


FIGURE 3.7: (a)-(c) Voltage *vs* current density (JV) and optical power *vs* current density (LJ) curves of the violet, green and blue micro-LEDs, respectively; (d)-(f) electroluminescence (EL) spectra of the violet, green, and blue micro-LEDs, respectively.

The blue micro-LED exhibits a turn-on voltage (at  $15 \text{ A/cm}^2$ ) and optical power (at  $138 \text{ A/cm}^2$ ) of  $3 \text{ V}$  and  $1.04 \text{ mW}$ , respectively. The lower current density operation of the micro-TP micro-LED is a direct consequence of its larger pixel size. At  $15 \text{ A/cm}^2$ , the blue micro-LED EL spectrum exhibits a broad peak centred at  $453 \text{ nm}$ . The micro-TP micro-LED exhibits a reverse leakage current, under dark conditions, of  $350 \text{ nA}$  at  $-3 \text{ V}$ . This value is lower than the one achieved by a similar device employing SU-8 as insulation layer, which upholds the superior capability of Pa-C as an electrical insulation layer for these transfer printed micro-LEDs. In addition, the low reverse leakage current is also a good indicator of the excellent JV performance shown by the TP micro-LED.

The modulation bandwidths of the different colour micro-LEDs were measured by applying a DC bias combined with a small-signal modulation from an HP8753ES network analyzer. The optical response was collected by a lens system and focused onto a fast photodiode (Femto HAS-X-S-1G4-SI bandwidth  $1.4 \text{ GHz}$ ). Figure 3.8(a) shows a schematic drawing of the experimental setup. The most widely adopted definition of bandwidth is the half power bandwidth, commonly known as  $-3 \text{ dB}$  bandwidth. It is defined as the frequency at which the AC power of the LED drops to half of the power in DC. As electrical power is proportional to the electrical current output of the

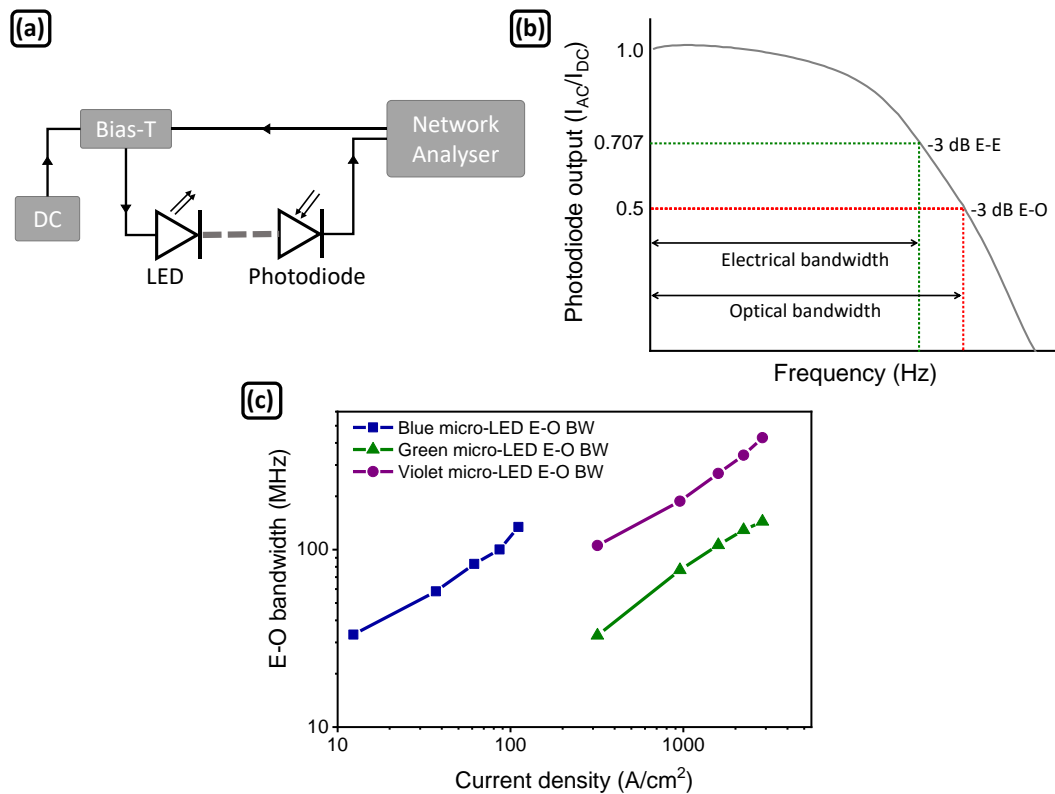


FIGURE 3.8: (a) Schematic drawing of the bandwidth measurement experimental setup; (b) photodiode response *vs* frequency curve (adapted from [25]); (c) E-O bandwidth *vs* current density curves of the violet, green, and blue micro-LEDs.



photodiode squared ( $I^2$ ), the -3 dB electrical-to-electrical (E-E) and the -3 dB electrical-to-optical (E-O) bandwidths occur at 0.707 and 0.5, respectively (Fig. 3.8(b)) [25]. The -3 dB E-O modulation bandwidths of each micro-LED, at different current densities, are shown in Fig. 3.8(c). The violet and green micro-LEDs exhibit E-O bandwidths up to 427 MHz and 144 MHz, respectively. The lower bandwidth and optical power of the green micro-LED, when compared to the violet micro-LED, can be attributed to its higher In content in the active region, and thus stronger quantum confined Stark effect [26]. Furthermore, the transfer printed blue micro-LED shows an E-O bandwidth up to 134 MHz. The lower value achieved by this micro-LED is related to its larger size and, thus, lower current density (and longer differential carrier lifetime) operation.

### 3.2.3 Colour properties of dual-colour micro-LED arrays

The assessment and quantification of colour is an important metric in LED characterisation. While many would argue that colour is subjective, the International Commission for Illumination (Commission Internationale de l'Eclairage, CIE) has standardized the measurement of colour by means of colour matching functions and the chromaticity diagram (CIE1931) [27].

CIE1931 colour coordinates of the blue-green and blue-violet micro-LED array on the colour-space chromaticity diagram are shown in Figs. 3.9(a) and 3.9(b), respectively. For the blue-green array, by increasing the current density of the blue micro-LED from 0 to 15 A/cm<sup>2</sup> and simultaneously decreasing the current density of the green micro-LED from 318 to 0 A/cm<sup>2</sup>, it is possible to tune the  $xy$  colour coordinates from (0.15, 0.04), for only the blue micro-LED, to (0.11, 0.71), for only the green micro-LED. The optical photographs in Fig. 3.9(a) show that the blue-green array is capable of efficient colour mixing (without any additional optic elements) under different bias conditions. The slightly violet appearance of the blue micro-LED, at 15 A/cm<sup>2</sup>, is a digital artifact due to the photographic camera detector. On the other hand, for the blue-violet array, varying the driving current of both micro-LEDs results in a small change of the CIE1931 colour coordinates. The enlarged inset shows, in further detail, how indistinguishable the CIE1931 colour coordinates of the blue-violet array are at different biases. This is due to the poorer human eye response in the violet-blue region, when compared to blue-green spectral region [27]. The typical blue-green and blue-violet array EL spectra, at different integrated area ratios of blue-green and blue-violet, respectively, correspond to the superposition of the individual spectra of each light source, as shown in Fig. 3.9(c).

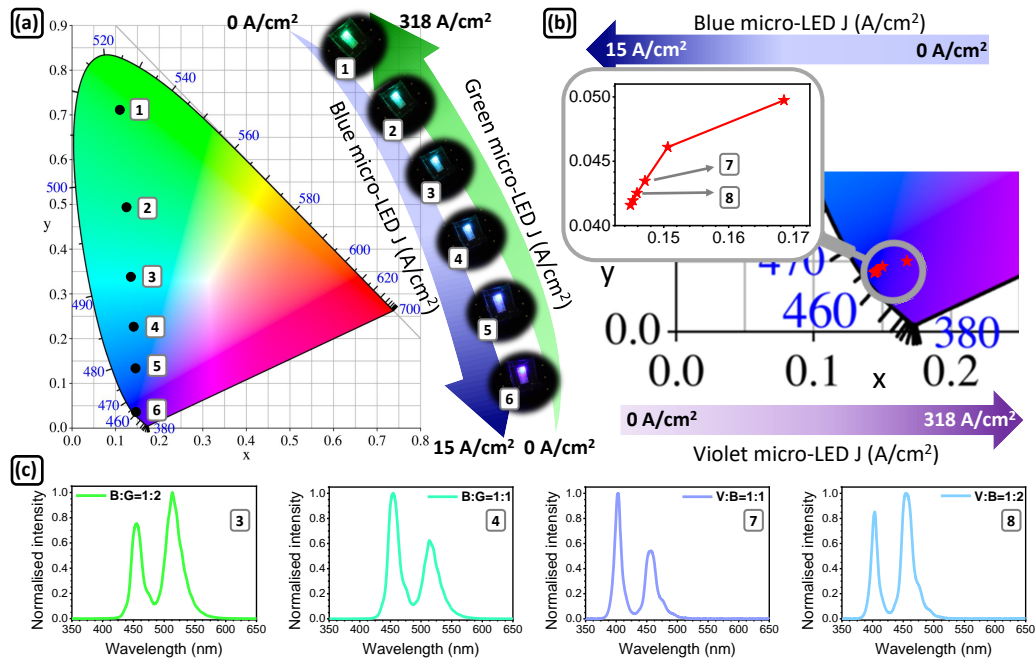


FIGURE 3.9: (a) Blue-green micro-LED array CIE1931 coordinates on the CIE1931 colour space chromaticity diagram and photographs of the device at different biases; (b) blue-violet micro-LED array CIE1931 colour coordinates at different biases; (c) electroluminescence spectra from the blue-green and blue-violet array at different integrated area ratios of blue-green and blue-violet, respectively (reproduced from [28]).

### 3.2.4 VLC application

#### 3.2.4.1 VLC modulation schemes

In optical wireless communication (OWC)<sup>‡</sup> systems the information is modulated in the instantaneous intensity of an optical carrier, and the receiver detects the optical intensity of the incoming signal, i.e. it operates in intensity modulation (IM) and direct detection (DD) mode [2, 30, 31]. The three main differences between OWC and RF technologies are summarised in Table 3.1.

VLC modulation schemes can be divided into: (1) single carrier modulation, which includes on-off keying (OOK), pulse amplitude modulation, pulse position modulation; and (2) multi-carrier modulation, which includes carrier-less amplitude and phase modulation and orthogonal frequency division multiplexing (OFDM) [2, 30, 31]. Due to their relevance to this work, OOK and OFDM will be discussed in further detail.

OOK is the simplest VLC modulation scheme, where data is transmitted by sequentially turning on and off the LED at a rapid speed. In the OOK non-return-to-zero

<sup>‡</sup>The term OWC refers to any optical transmission in an unguided media, with VLC being the common designation of OWC operating in the visible range [29].

TABLE 3.1: Comparison between OWC and RF, where  $P_{opt}$  and  $A_{RF}$  correspond to the optical power and amplitude of the RF carrier, respectively [2].

Parameter	OWC	RF
Information encoding	Amplitude	Amplitude and phase
Signal	Real-valued and unipolar	Complex-valued and bipolar
SNR	$\propto P_{opt}^2$	$\propto A_{RF}^2$

(OOK-NRZ) scheme, the bits 1 and 0 are represented by the presence or absence, respectively, of an optical pulse for the bit duration (Fig. 3.10(a)). OOK provides a good trade-off between system performance and implementation complexity, being the commonly used technology in digital optical transmission systems [2, 30, 31].

In OFDM parallel data streams are transmitted simultaneously through a collection of orthogonal subcarriers and complex equalisation can be omitted. The spectra of individual subcarriers overlap (Fig. 3.10(b)), however due to the orthogonality property, as long as the channel is linear, the subcarriers can be demodulated without interference. OFDM offers high spectral efficiency, ability to resist multipath interference, and dynamic subcarrier allocation technology to achieve the maximum bit rate [2, 30, 31].

A schematic block diagram of an OFDM signal generation and demodulation is shown in Fig. 3.10(c). The input bit streams are mapped onto complex numbers representing the quadrature amplitude modulation (QAM) constellation being used for transmission (constellations sizes from 4-QAM to 64-QAM are typically used). The sequence of complex numbers output from the constellation mapping are then serial-to-parallel (S/P) converted to form a vector. In order to generate a real signal (required for optical communications), Hermitian symmetry is imposed before applying the inverse fast Fourier transform (IFFT), which maps the signal to orthogonal subcarrier frequencies. A cyclic prefix (CP) is added to the start of each OFDM symbol, i.e. a number of samples from the end of the symbol is appended to the start of the symbol<sup>§</sup>. The OFDM signals are then serialised using parallel-to-serial (P/S), followed by conversion to analogue signals using a digital-to-analogue converter (DAC) and filter. In order to convert the OFDM bipolar signal into a suitable unipolar signal for optical communication, a DC-bias is added to the signal. This technique is called DC-biased optical OFDM (DCO-OFDM). On the receiving side the process is almost the inverse of signal generation. The received signal is converted to a discrete time signal by filtering and an analogue-to-digital conversion (ADC) followed by CP removal and S/P conversion. A fast Fourier transform

---

<sup>§</sup>Although the CP introduces some redundancy, and reduces the overall data rate, it eliminates both inter-symbol interference and inter-carrier interference from the received signal.

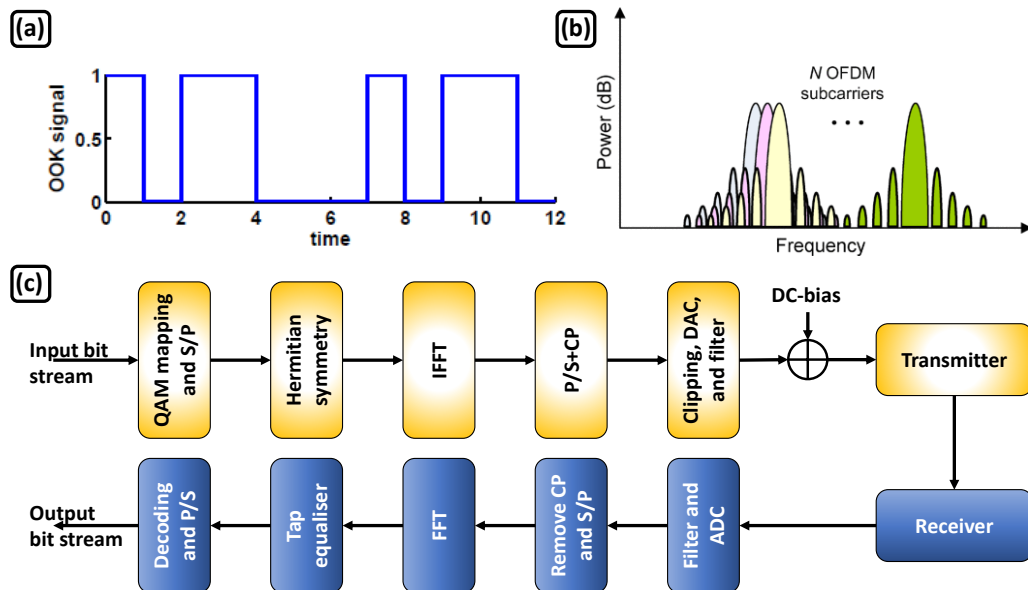


FIGURE 3.10: Time waveforms of a on-off keying signal; (b) orthogonal frequency division multiplexing (OFDM) subcarriers in the frequency domain [32]; (c) schematic block diagram of a DC-biased optical OFDM signal generation and demodulation (adapted from [2]).

(FFT) is applied to the signal followed by 1-tap frequency domain equalisation, P/S conversion and finally the symbol recovery [2, 32].

### 3.2.4.2 VLC experimental details

The capability of the blue-green and blue-violet micro-LED arrays to operate as two-colour WDM transmitters in two different experimental setups is explored in the following sections. In the first setup (referred to as WDM1 and shown in Fig. 3.11(a)), we placed one optical receiver to measure the communication performance of both channels by changing a bandpass filter (Laser 2000 FF01-392-23/25, FF01-445/20-25 and FF01-525-45/25, for violet, blue, and green, respectively). To ensure that the measured results were the same as in the case of simultaneous signal reception with the existence of crosstalk, we sent two different signal streams to different colour micro-LED channels. One stream was captured and demodulated, while the other one behaved as the interfering signal. Although this setup provided a capacity estimation for WDM (a “best case scenario”), simultaneous reception of both channels was not possible. To overcome this issue, dichroic mirrors were employed in a second experimental setup (referred to as WDM2), shown in Fig. 3.11(b). The light emitted from the dual-colour micro-LED array was directed onto the dichroic mirror (Thorlabs DMLP425 and DMLP490L, for blue-violet and blue-green micro-LED arrays, respectively) at 45 degrees which separated the beam into two individual components. The light transmitted through the dichroic

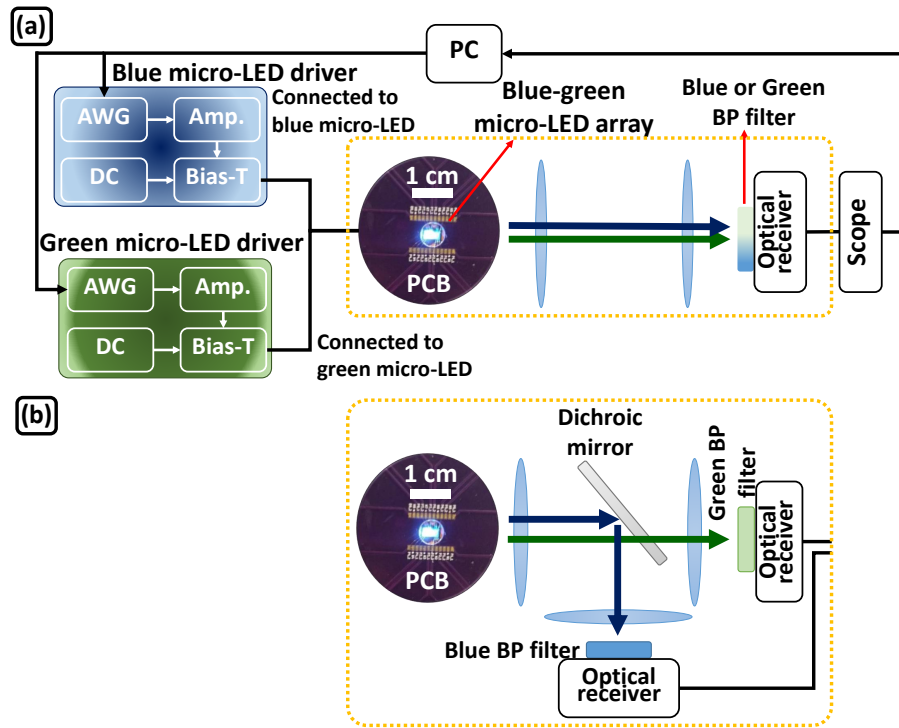


FIGURE 3.11: Schematic drawing of the experimental setups in wavelength division multiplexing data transmission experiments: (a) setup 1 (WDM1); (b) setup 2 (WDM2). The photograph inset in the schematics is the actual blue-green micro-LED array (wire bonded to a printed circuit board - PCB) being operated in WDM mode.

mirror was focused onto an optical receiver and the light reflected by the dichroic mirror was focused onto another optical receiver. Bandpass filters were also placed in front of the detectors in order to minimize crosstalk. This setup enabled simultaneous reception of both channels, although the use of the dichroic mirror leads to signal power losses. The distance between transmitter and detector was kept at 30 cm in both setups and throughout the measurements.

In both setups, two random bit streams, for the transmission via the two different colour emitting micro-LED channels, were generated and modulated with DC-biased optical orthogonal frequency division multiplexing by a PC using MATLAB™. The incoming bit stream was coded and mapped to M-ary quadrature amplitude modulation (M-QAM) symbols for each subcarrier at different frequencies. The time-domain OFDM symbols were generated after having the IFFT operation for the M-QAM symbols. A real-valued OFDM signal was obtained by using a Hermitian symmetry OFDM frame. The resulting time-domain OFDM signals were forwarded to an arbitrary waveform generator (AWG Keysight M8195A), which generated the corresponding analog signals. In order to make sure the input signals fully exploited the available linear dynamic range of the micro-LEDs, the output analogue signals were amplified by a power amplifier (Mini-Circuits ZHL-1A-S+), and a suitable operation current density was provided by a

power supply (Yokogawa GS610). The bipolar signals and the DC bias were combined using a bias-tee (Mini-Circuits ZFBT-4R2GW+), and the output of the bias-tees were connected to the micro-LED array to drive the two micro-LED pixels. On the receiver end, the light emitted by the dual-colour micro-LED array was focused onto a p-i-n photodetector (New Focus 1601AC) by using an aspheric condenser lens (ACL4532). The signal from the photodetector was captured by an oscilloscope (Keysight MSO7104B) and sent back to the PC for demodulation. In order to maximize the achievable data rate, a bit and energy loading algorithm [33] was applied. Therefore, the signal-to-noise ratio (SNR) on each subcarrier was estimated at the beginning of the communication performance measurement. Based on the estimated SNR and a bit-error-ratio (BER) target that is acceptable for the application of forward error correction (FEC) coding, modulation order and symbol energy on each subcarrier was calculated. Finally, the signals with bit and energy loading were transmitted and the achieved data rate and BER were measured.

### 3.2.4.3 Communication performance of the blue-green micro-LED array

The results of the blue-green micro-LED array operated in a WDM mode with different setups are summarized in Fig. 3.12. The blue and green micro-LEDs were operated at  $138 \text{ A/cm}^2$  and  $2.8 \text{ kA/cm}^2$ , respectively, whilst the modulation signal peak-to-peak voltage ( $V_{pp}$ ) was set to 1.5 V, after the amplifier. The sampling frequency was set as 16 GSa/s and number of samples per symbol was optimized for each link. The SNR and number of allocated bits, at the highest data rate below the FEC threshold of  $3.8 \times 10^{-3}$  BER, for the blue and green micro-LED are shown in Figs. 3.12(a) and 3.12(b), respectively. Figure 3.12(c) shows the blue and green micro-LEDs EL spectra overlaid with the DMLP490L dichroic mirror optical response (transmitted and reflected) and the blue and green bandpass filters.

The blue micro-LED channel exhibits a higher SNR than the green micro-LED channel due to the blue micro-LED higher optical power. Also, as shown in Fig. 3.12(a), there is no obvious difference in the SNR curves of the blue channel between the two different setups. On the other hand, compared with the WDM1 setup, the SNR curve of the green channel with the WDM2 setup presents a sharp drop when the frequency is over 150 MHz, shown in Fig. 3.12(b). This is mainly due to the optical power loss (roughly 25%) caused by the dichroic mirror used in WDM2 (Fig. 3.12(c)). This leads to a lower maximum achievable data rate in WDM2. The BER *vs* data transmission curves for the blue and green micro-LEDs, in both WDM setups, are presented in Fig. 3.12(d). The maximum data rates, below FEC threshold, achieved by the blue and green micro-LEDs in the WDM1 setup are 1261 and 667 Mbps, respectively. In the WDM2 setup the

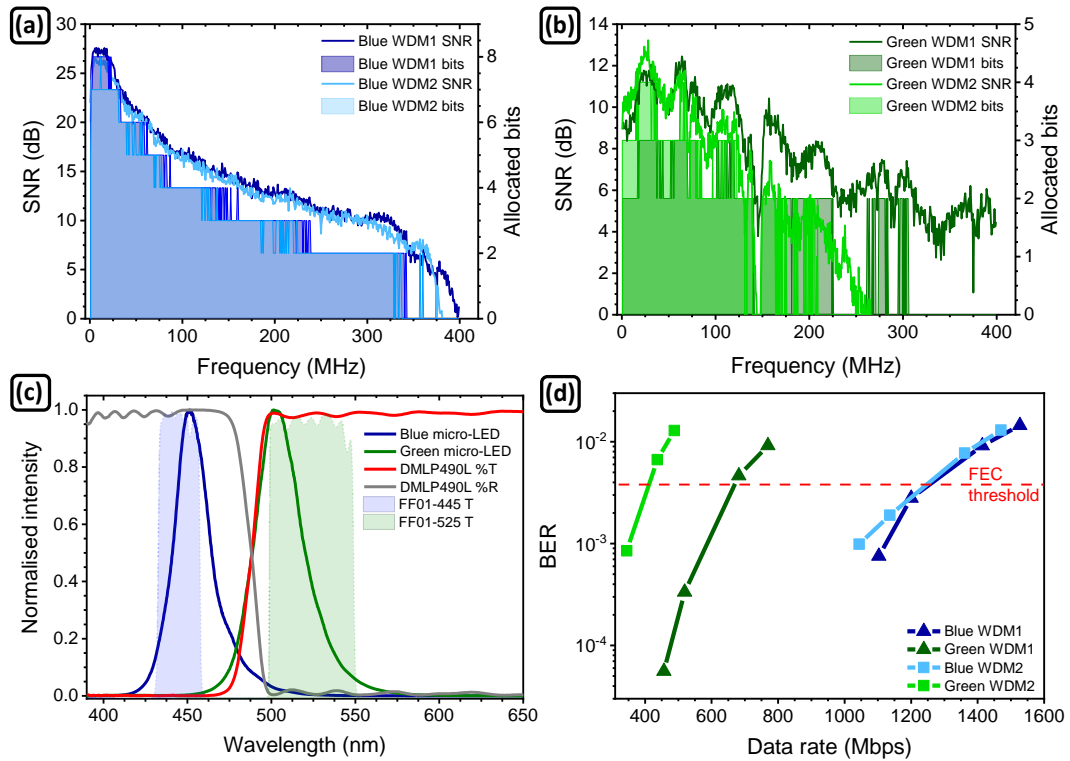


FIGURE 3.12: Signal-to-noise ratio and allocated bits (at maximum data rate below forward error correction threshold) in both WDM setups achieved by (a) the blue micro-LED and (b) the green micro-LED; (c) blue and green micro-LEDs EL spectra overlaid with the dichroic mirror and bandpass filters optical responses; (d) bit-error-ratio *vs* data rate for the blue and green micro-LEDs in both WDM setups.

maximum data rates, below FEC threshold, achieved by the blue and green micro-LEDs drop to 1245 and 410 Mbps, respectively.

Error-free data rates, calculated by applying the 7% FEC overhead reduction, for blue and green micro-LEDs and their aggregate in each WDM setup are shown in Table 3.2. In aggregate, 1.79 and 1.54 Gbps error-free data rates are achieved in the WDM1 and WDM2 setups, respectively.

TABLE 3.2: Error-free data rates for each channel and aggregated in WDM1 and WDM2 setups achieved by the blue-green micro-LED array.

Channel	WDM1		WDM2	
	Blue	Green	Blue	Green
Error-free data rate (Mbps)	1173	620	1158	381
	Aggregate		Aggregate	
	1793		1593	

### 3.2.4.4 Communication performance of the blue-violet micro-LED array

The blue-violet micro-LED array operation as a WDM transmitter followed the same approach as the blue-green one. The blue and violet micro-LEDs were operated at the same current density as the blue and green micro-LEDs, respectively. The SNR and number of allocated bits, at the highest rate below FEC threshold, in both WDM setups for the blue and violet micro-LEDs are shown in Figs. 3.13(a) and 3.13(b), respectively. Figure 3.13(c) shows the blue and violet micro-LEDs' EL spectra overlaid with the DMLP425 dichroic mirror optical response (transmitted and reflected) and the blue and violet bandpass filters.

The blue and violet micro-LED channels' maximum SNR is quite similar due their comparable optical power. Nonetheless, due to the violet micro-LED's higher E-O modulation bandwidth, the violet channel supports bit allocation up to 650 MHz. The introduction of the dichroic mirror, which has cut-off wavelength at 425 nm, results in a loss of optical power and, thus lower SNR for both channels, limiting the maximum achievable data rate in WDM2 (Fig. 3.13(c)). The violet (reflected) channel is more

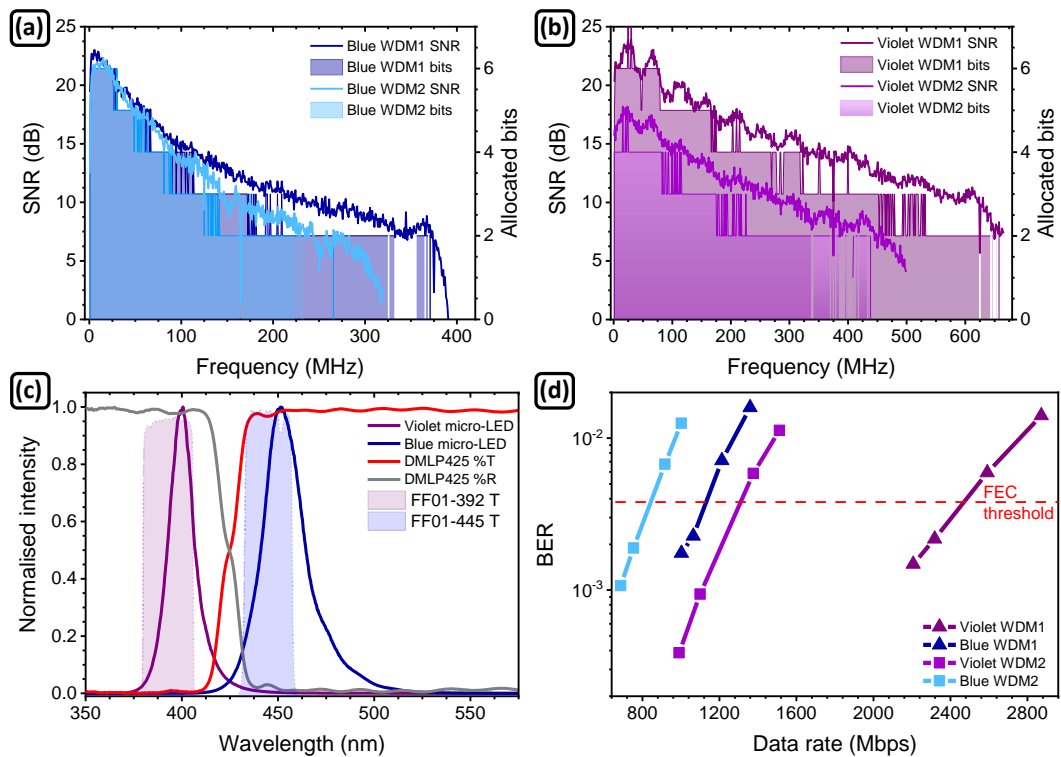


FIGURE 3.13: Signal-to-noise ratio and allocated bits (at maximum data rate below forward error correction) in both WDM setups achieved by (a) the blue micro-LED and (b) the violet micro-LED; (c) blue and violet micro-LEDs EL spectra overlaid with the dichroic mirror and bandpass filters optical responses; (d) bit-error-ratio *vs* data rate for blue and violet micro-LEDs in both WDM setups.



affected than the blue one due to the optical response of the dichroic mirror, with estimated optical power losses of 11%. The BER *vs* data transmission curve is presented in Fig. 3.13(d). The maximum data rates, below FEC threshold, achieved by the blue and violet micro-LEDs in the WDM1 setup are 1130 and 2472 Mbps, respectively. In the WDM2 setup the maximum data rates, below FEC threshold, achieved by the blue and violet micro-LEDs drop to 842 and 1309 Mbps, respectively.

The blue and violet channels and aggregate error-free data rates for WDM1 and WDM2 setups are shown in Table 3.3. In aggregate, the blue-green micro-LED array achieves error-free data rates of 3.35 and 2 Gbps, in the WDM1 and WDM2 setups, respectively.

TABLE 3.3: Error-free data rates for each channel and aggregated in WDM1 and WDM2 setups achieved by the blue-violet micro-LED array.

Channel	WDM1		WDM2	
	Blue	Violet	Blue	Violet
Error-free data rate (Mbps)	1051	2299	783	1217
	Aggregate		Aggregate	
	3350		2000	

### 3.2.5 Underwater Wireless Optical Communication

A schematic drawing of the UWOC demonstration experimental setup for the blue-green micro-LED array is shown in Fig. 3.14(a). A photograph of the 1.5 m long water tank is shown in Fig. 3.14(b). The UWOC setup is identical to the free-space WDM1 (shown in Fig. 3.11(a)) with a few exceptions.

In the UWOC demonstration, the data signal was generated using either a field-programmable gate array (FPGA, Opal Kelly XEM6310-LX45) or an AWG (Keysight M9502A). The FPGA is advantageous due to its small size and weight, which opens the possibility for easy integration into autonomous underwater vehicles (AUVs). However, the FPGA modulation signal peak-to-peak voltage is a fixed value, which does not allow an optimization of the micro-LED array’s modulation driving conditions. For this case, as we also wish to assess the upper modulation limits of these devices in water media, an AWG was also used to generate the data signal.

An OOK data signal, generated by either a FPGA or an AWG, combined with a DC bias (Yokogawa GS610) was used to modulate the micro-LED array through a bias-tee (ZFBT-4R2G+). When using the FPGA, RF attenuators were employed to adjust the  $V_{pp}$  to suitable values. When using the AWG, an external amplifier (Mini-Circuits ZHL-1A-S+) was used in order to explore the full dynamic range of the micro-LEDs. A

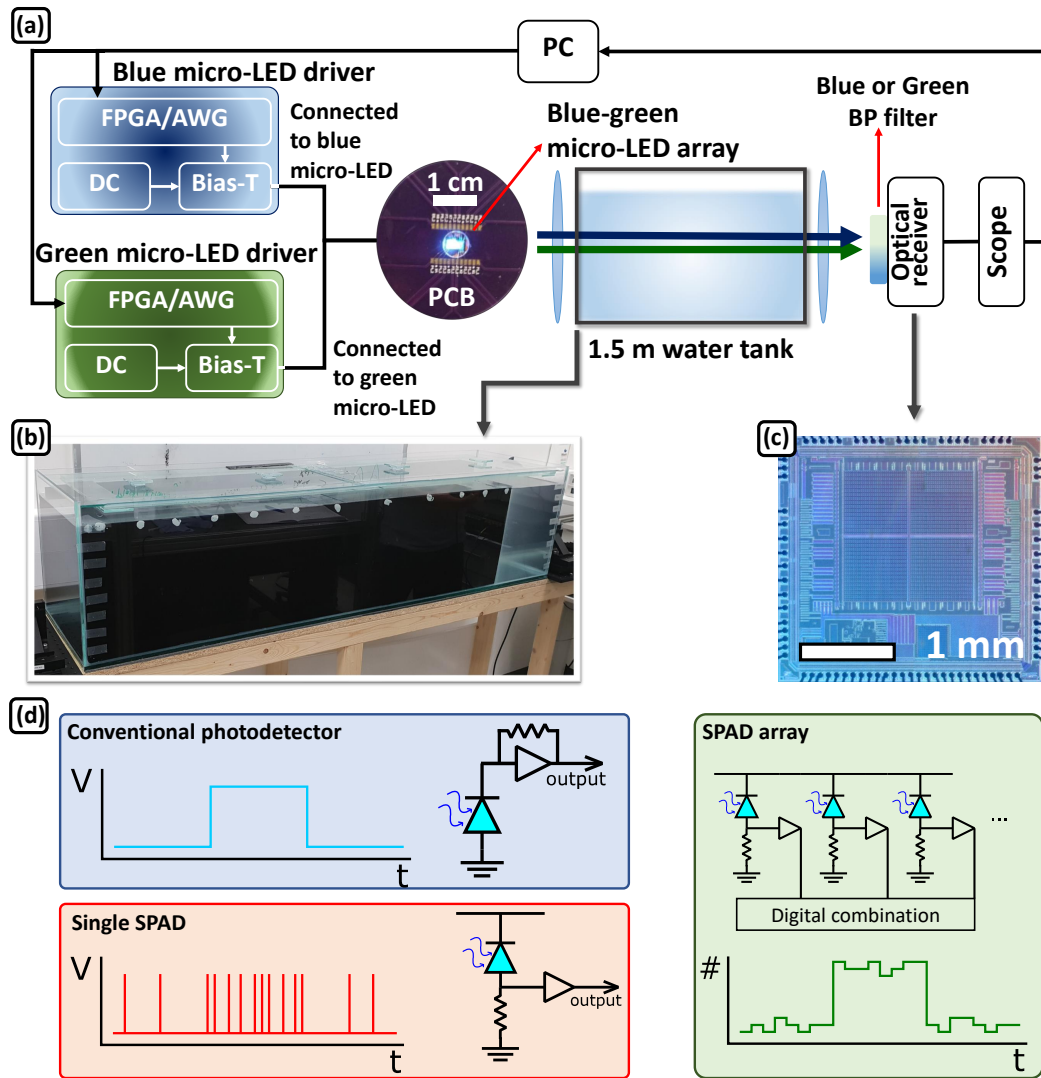


FIGURE 3.14: (a) Schematic drawing of the experimental setup used in the UWOC demonstration using either FPGA or AWG; (b) photograph of the 1.5 m water tank; (c) plan-view photograph of the 64x64 SPAD array used as detector; (d) schematic drawings of a conventional photodetector, a single SPAD, the SPAD array, and their respective electrical outputs.

sequence of length  $2^{15}$  was transmitted, consisting of a wide synchronisation pulse and a pseudo-random bit sequence. The blue-green (or blue-violet) micro-LEDs were operated simultaneously and each colour carried a different data stream. The dual-colour micro-LED array emission was collected and collimated by a condenser lens (Thorlabs, ACL50832U-A), propagated through a 1.5 m long water tank and then focused onto the receiver by a 4-inch diameter Fresnel lens (Edmund, #46-614). The measured channel was chosen by placing an appropriate bandpass filter in front of the receiver (Laser 2000 FF01-392-23/25, FF01-445/20-25 and FF01-525-45/25, for violet, blue, and green, respectively). The receiver, shown in detail in Fig. 3.14(c), consists of a 64 x 64 array of Si single photon avalanche diodes (SPADs), the working principles of a SPAD being

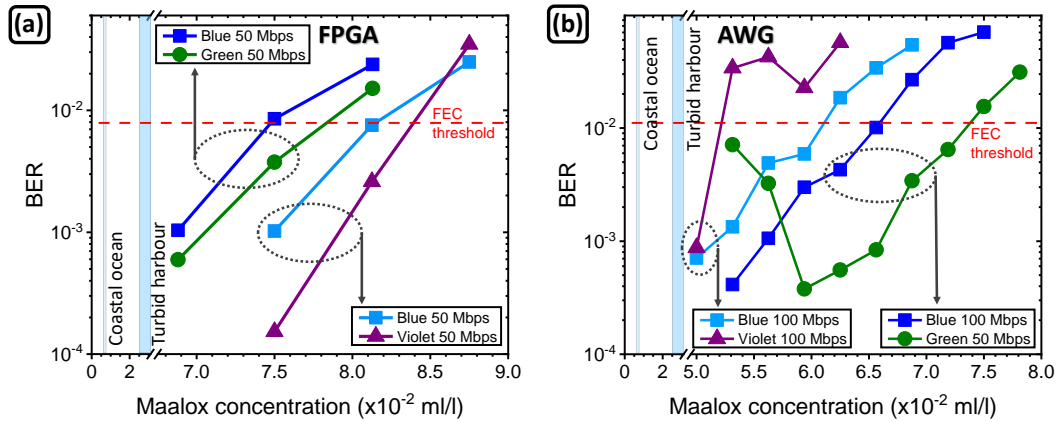


FIGURE 3.15: Bit-error-ratio vs Maalox concentration curves of the UWOC WDM demonstration using (a) a FPGA and (b) an AWG to generate the data signal.

described in Chapter 5, operating as a digital silicon photo-multiplier<sup>¶</sup>. Each receiver element contains a single p-well/deep-n-well SPAD biased at 15.2 V with a dead time of 12 ns (SPAD saturation 83 MHz) and a photon detection probability of 37% at 450 nm. A digital combination module combines the output of each SPAD array at a maximal rate of around 900 MHz limited only by wiring parasitics (not SPAD dead time). The SPAD array merges the single photon sensitivity achieved by SPADs with the speed of conventional photodetectors. The photon counts are summed over a time window of 5 ns and the count values outputted through a DAC. A schematic drawing of the SPAD array output is shown in Fig. 3.14(d), alongside with the outputs from a conventional photodetector and a single SPAD. The DAC signal was captured with an active oscilloscope probe and transferred to MATLAB<sup>™</sup> for offline processing to determine a BER. The turbidity of the water sample was varied by adding Maalox<sup>™</sup> antacid to tap water, a method widely used to mimic different natural water analogues in a laboratory setup [35].

Operation of the integrated blue-violet and blue-green micro-LED arrays as respective dual-wavelength WDM transmitters for underwater communication in high-turbidity conditions, using either a FPGA or an AWG, is shown in Figs. 3.15(a) and 3.15(b), respectively. Also identified in Figs. 3.15(a) and 3.15(b) are the Maalox<sup>™</sup> concentrations that correspond to coastal ocean ( $\sim 6 \times 10^{-3}$  ml/l) and turbid harbour ( $2.5 \times 10^{-2}$  -  $3.1 \times 10^{-2}$  ml/l) waters, which serve as turbidity reference points.

Using the FPGA, the blue-green micro-LED array (blue: DC=2.8 V and  $V_{pp}=1.5$  V, green: DC=7 V and  $V_{pp}=2.4$  V) achieves a 100 Mbps aggregate data rate, below the FEC threshold, at Maalox<sup>™</sup> concentrations of  $7.5 \times 10^{-2}$  ml/l. The blue-violet micro-LED array (blue: DC=2.6 V and  $V_{pp}=1.5$  V, violet: DC=3.3 V and  $V_{pp}=1.5$  V) achieves a

<sup>¶</sup>This SPAD array was developed by the University of Edinburgh and further details can be found in [34].

100 Mbps aggregate data rate, below the FEC threshold, at Maalox™ concentrations of  $8 \times 10^{-2}$  ml/l. The ability of the blue-violet micro-LED array to support error-free communication at higher Maalox™ concentrations than the blue-green, suggest that, in this case, the violet micro-LED higher optical power compensates the expected red-shift of water transparency window with turbidity [13].

Using an AWG, the blue-green micro-LED array (blue: DC=1.5 V and  $V_{pp}=4.3$  V, green: DC=0 V and  $V_{pp}=15$  V) achieves an aggregate data rate of 150 Mbps, below FEC, for Maalox™ concentrations up to  $6.5 \times 10^{-2}$  ml/l. In addition, the 50 Mbps green channel is capable of error-free communication up to  $\sim 7.4 \times 10^{-2}$  ml/l of Maalox™. The blue-violet micro-LED array (blue: DC=1.5 V and  $V_{pp}=4.3$  V, violet: DC=1 V and  $V_{pp}=5$  V) achieves an aggregate data rate of 200 Mbps, below FEC, for Maalox™ concentrations up to  $5.2 \times 10^{-2}$  ml/l. The blue channel supports a 100 Mbps error-free link up to  $6.1 \times 10^{-2}$  ml/l of Maalox™. The aggregate data rate achieved by the blue-green and blue-violet micro-LED arrays, using a FPGA or an AWG, are summarised in Table 3.4.

TABLE 3.4: Data rates for the blue-green and blue-violet micro-LED arrays using a FPGA or an AWG.

Device	FPGA		AWG	
	Blue-green	Blue-violet	Blue-green	Blue-violet
Aggregate data rate (Mbps)	100	100	150	200

### 3.3 In-series connected blue-green micro-LED array

#### 3.3.1 Device overview

The fabrication of the in-series connected blue-green micro-LED array follows the same process flow of the individually-addressable micro-LED arrays with a few notable exceptions. These will be discussed first for the green micro-LED and then for the suspended blue micro-LED platelets.

First, in order to increase the optical power, the green micro-LED pixel diameter was increased to  $30 \mu\text{m}$  (active area  $7.07 \times 10^{-6} \text{ cm}^2$ ). During the ICP mesa etch down to the PSS a common anode and cathode were defined. Fabrication of the green micro-LED was finalised after metallisation (Ti/Au thicknesses 100/200 nm) of the  $n$ -GaN layer and of the bonding pads. In this case, and contrary to the previous example, the green micro-LED device is not yet functional. Figure 3.16(a) shows a plan-view photograph of the green micro-LED device (mesa identified by a green square) before micro-TP of the blue micro-LED platelet.

The design of the blue micro-LED platelets was modified in order to facilitate the in-series electrical connecting scheme. For this purpose, instead of the L-shaped pixel, ICP was used to expose the underlying  $n$ -GaN layer defining a central square pixel ( $60 \times 60 \mu\text{m}^2$ ). Next, a square-shaped  $n$ -contact metal ring (Ti/Au thicknesses 100/200 nm) was deposited by metal sputtering. Suspension of the micro-LED platelets followed the same underetch process in hot KOH solution.

Heterogeneous integration of the blue micro-LED platelets onto the SU-8 coated PSS of the green micro-LED was enabled by micro-TP. After micro-TP, a  $4.5 \mu\text{m}$  thick Pa-C film was deposited as an electrical insulation layer for both green and blue micro-LEDs. Figure 3.16(b) shows a plan-view photograph after micro-TP and Pa-C vias definition (identified in red for both micro-LEDs). Next, a Ti/Au metallisation step defined tracks connecting the different colour micro-LEDs in-series (Fig. 3.16(c) - blue micro-LED platelet identified by a blue square). A plan-view photograph of the finalised device being driven at 2 mA is shown in Fig. 3.16(d). As the blue and green micro-LEDs are connected in series, each element is being driven at the same current. However, due to their different pixel size, a 2 mA current corresponds to current densities of  $56 \text{ A/cm}^2$  and  $283 \text{ A/cm}^2$  for the blue and green micro-LEDs, respectively. As such, in this section, for simplicity the results will be presented in current instead of current density.

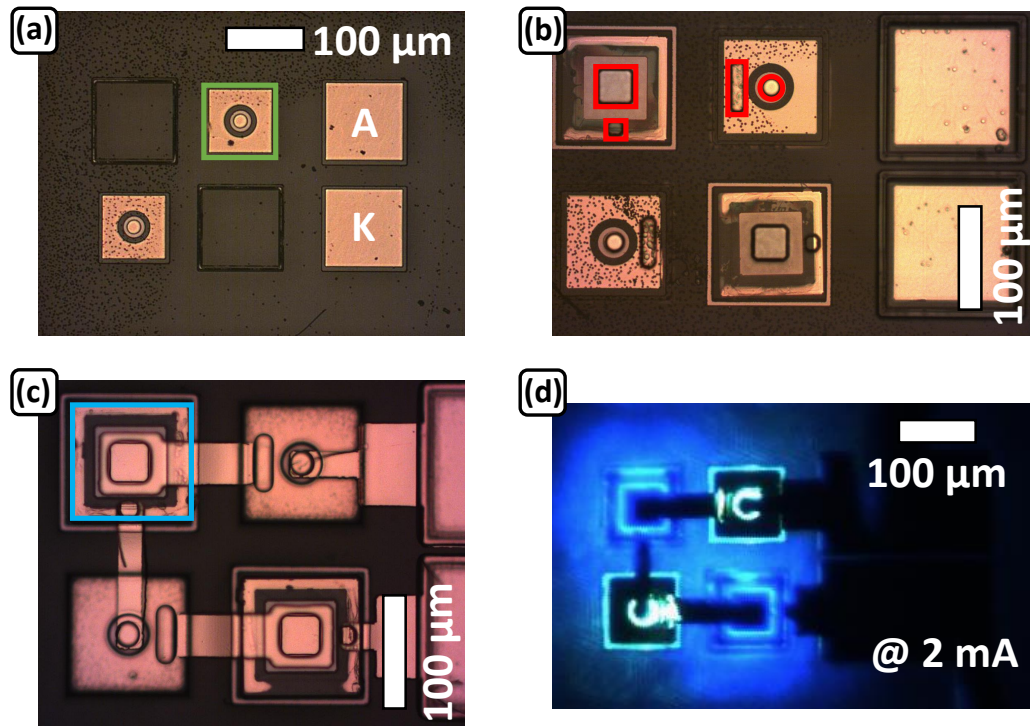


FIGURE 3.16: Plan-view optical photographs of (a) the green micro-LED device before micro-TP of a blue micro-LED platelet; (b) the blue-green micro-LED device after micro-TP after electrical vias definition; (c) the blue-green micro-LED device connected in series; (d) the in-series connected blue-green micro-LED array driven at 2 mA.

### 3.3.2 Electrical, optical and bandwidth performance of the in-series connected blue-green micro-LED array

The voltage *vs* current (IV) and optical power *vs* current (LI) performance of in-series connected blue-green micro-LED array is shown in Fig. 3.17(a). For comparison, the IV curve of a single blue micro-LED transfer printed onto on a glass substrate (plan-view photograph shown as an inset in Fig. 3.17(b)) is shown in Fig. 3.17(b). The IV characteristic was measured by a current source, through scanning each data point under DC conditions (Yokogawa GS610). The LI characteristic was measured using a calibrated Si photodiode detector (Thorlabs PM100D) in proximity to the backside of the micro-LED array. The in-series connected blue-green micro-LED array exhibits a turn-on voltage (at 1 mA) of 13.4 V. Taking into account that the turn-on voltage of a comparable single blue micro-LED is 3 V (Fig. 3.17(b)), one can deduce the turn-on voltage of a single green micro-LED to be  $\sim 3.7$  V. These values suggest a good ohmic contact between the metal contacts and the *p*-GaN. Setting the detection wavelength of

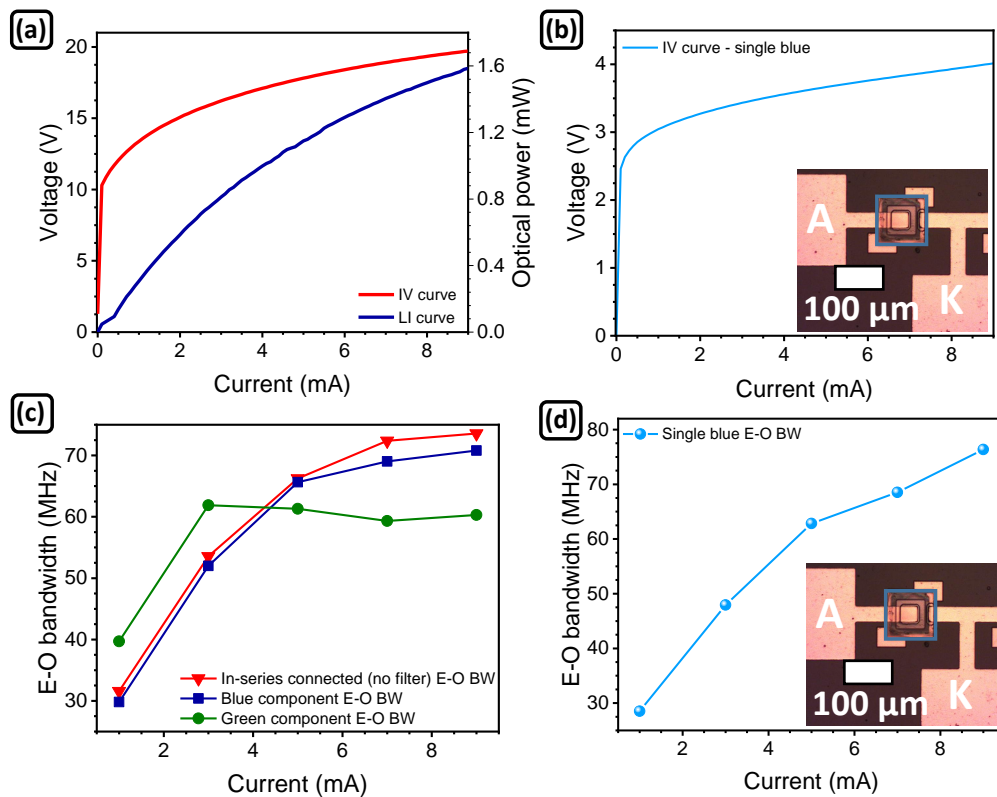


FIGURE 3.17: (a) Voltage *vs* current (IV) and optical power *vs* current (LI) curves of the in-series connected blue-green micro-LED array; (b) IV curve of a comparable single blue micro-LED printed onto glass - inset shows a plan-view photograph of the device; (c) E-O modulation bandwidth of the in-series connected micro-LED array *vs* current in aggregate, blue component, and green component; (d) E-O modulation bandwidth of a comparable single blue micro-LED printed onto glass.

the photodiode detector to 450 nm, the in-series connected blue-green micro-LED array achieves roughly 1.6 mW of optical power at 9 mA.

The E-O modulation bandwidth of the in-series connected blue-green micro-LED array was measured by applying a DC bias combined with a small-signal modulation from an HP8753ES network analyzer. The optical response was collected by a lens system and focused onto a fast photodiode (Femto HAS-X-S-1G4-SI bandwidth 1.4 GHz). In order to separate the contribution of the different colour micro-LEDs, bandpass filters (FF01-445/20-25 and FF01-525-45/25, for blue and green, respectively) were placed in front of the receiver. Figure 3.17(c) the modulation bandwidth *vs* current curves of the in-series connected blue-green micro-LED array measured with no filter (red curve), with the blue bandpass filter (blue curve), and with the green bandpass filter (green curve). With no filter, and at 9 mA, the in-series connected micro-LED array exhibits a modulation bandwidth of 73 MHz. The filtered blue component follows the same trend with current of the no filter curve, while the green component plateaus at  $\sim 60$  MHz for currents above 3 mA. This suggests that the bandwidth of the in-series connected blue-green micro-LED array is dominated by the blue micro-LED. This hypothesis is also supported by the modulation behaviour of the single blue micro-LED, shown in Fig. 3.17(d), which achieves 76 MHz at 9 mA.

According to literature, smaller active area micro-LEDs exhibit higher maximum modulation bandwidth than their larger area counterparts [36]. At the micron-size scale, the LED bandwidth is no longer limited by its  $RC$  time constant, but, instead, by its differential carrier lifetime ( $\tau_{diff}$ ). Following the  $ABC$  model, this differential carrier lifetime is a function of the carrier density ( $n$ ):

$$\tau_{diff}(n) = \frac{1}{A + 2Bn + 3Cn^2} \quad (3.1)$$

Where  $A$  and  $B$  are the Shockley-Read-Hall (SRH) non-radiative recombination and radiative recombination coefficients, respectively. The parameter  $C$  is a higher-order non-radiative recombination coefficient, usually associated to Auger recombination mechanisms [37]. Assuming that the carrier density is proportional to the current density, one can infer from Eq. 3.1 that as the current density increases,  $\tau_{diff}$  decreases and thus bandwidth increases. As smaller active area micro-LEDs support higher current density operation, they exhibit higher maximum modulation bandwidth.

However, comparing the L-shaped device with the  $60 \times 60 \mu\text{m}^2$  micro-LEDs, it was found that the larger active area and lower current density operation L-shaped pixel exhibits larger modulation bandwidth (Fig. 3.18(a)). This contradictory behaviour can be discussed using the  $ABC$  model. As the micro-LEDs were fabricated from the same wafer the epitaxial structure related coefficients  $B$  and  $C$  [2] should be similar. In



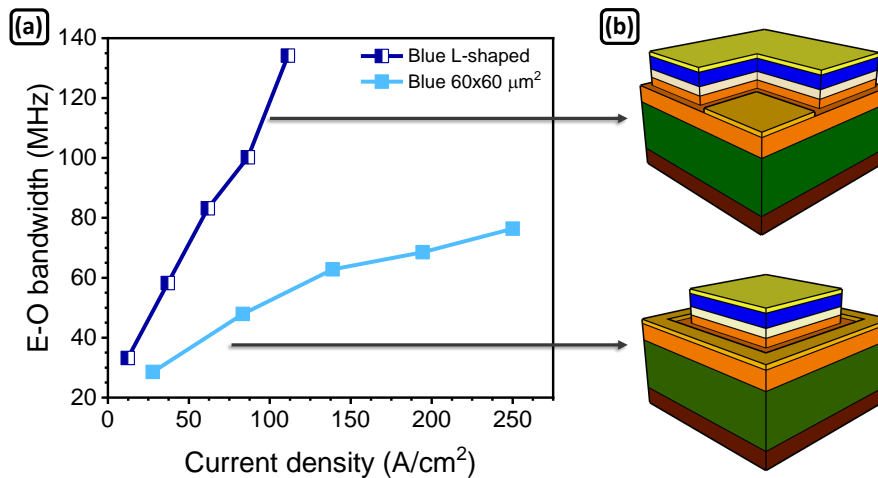


FIGURE 3.18: (a) Electrical to optical modulation bandwidth *vs* current density of the L-shaped and the 60x60  $\mu\text{m}^2$  blue micro-LEDs; (b) schematic drawings of the L-shaped and the 60x60  $\mu\text{m}^2$  micro-LEDs (not to scale).

addition, it has also been proposed that these two coefficients are independent of the LED size [38]. However, it should be taken into account that these LED structures are grown on 6 inch wafers that exhibit non-uniform peak emission. This can be attributed to different indium concentration in the quantum wells, or even local strain effects. It is then plausible to assume that micro-LEDs fabricated from different regions of the 6 inch wafer can exhibit similar but different  $B$  and  $C$  coefficients. On the other hand, the different geometry of the L-shaped and 60x60  $\mu\text{m}^2$  micro-LEDs (Fig. 3.18(b)) might explain why the L-shaped pixel presents a higher maximum modulation BW. The SRH non-radiative recombination coefficient  $A$  has been associated with sidewall defects. In the case of L-shaped pixel, the active area is only 5  $\mu\text{m}$  away from the mesa edge, while for the 60x60  $\mu\text{m}^2$  pixel this distance is 20  $\mu\text{m}$ . It is reasonable to assume that the L-shaped pixel sidewall suffers more damage during the mesa dry etching step, than the 60x60  $\mu\text{m}^2$  pixel. For example, in reference [39] the authors assumed that mesa etching would result in a 4  $\mu\text{m}$  wide damaged region. In addition, in the L-shaped design there is more sidewall and therefore the carriers are able to access more damaged material. This etch damage to the pixel sidewall creates defects where non-radiative recombination of carriers can occur, thus increasing the  $A$  coefficient. The difference in the  $B$  and  $C$  coefficients, associated to the non-uniform epitaxial structure, and expected difference in the  $A$  parameter, associated to the pixel design, might explain why the L-shaped pixel exhibits a higher maximum modulation bandwidth than the smaller 60x60  $\mu\text{m}^2$  pixel.



### 3.3.3 Colour properties of the in-series connected blue-green micro-LED array

Figure 3.19(a) shows the in-series connected blue-green micro-LED array EL spectra at different driving currents. The EL spectra were acquired by an optical fibre-coupled spectrometer (Avantes AvaSpec-2048L spectrometer). The EL spectrum (at 3 mA) consists of the superposition of a broad blue peak (centred at 452 nm) and a broad green peak (centred at 508 nm). With increasing current both peaks broaden due to band filling effects. The green peak slightly blue-shifts due to carrier screening of quantum confined Stark effect piezoelectric fields in the multi-quantum well active region. The

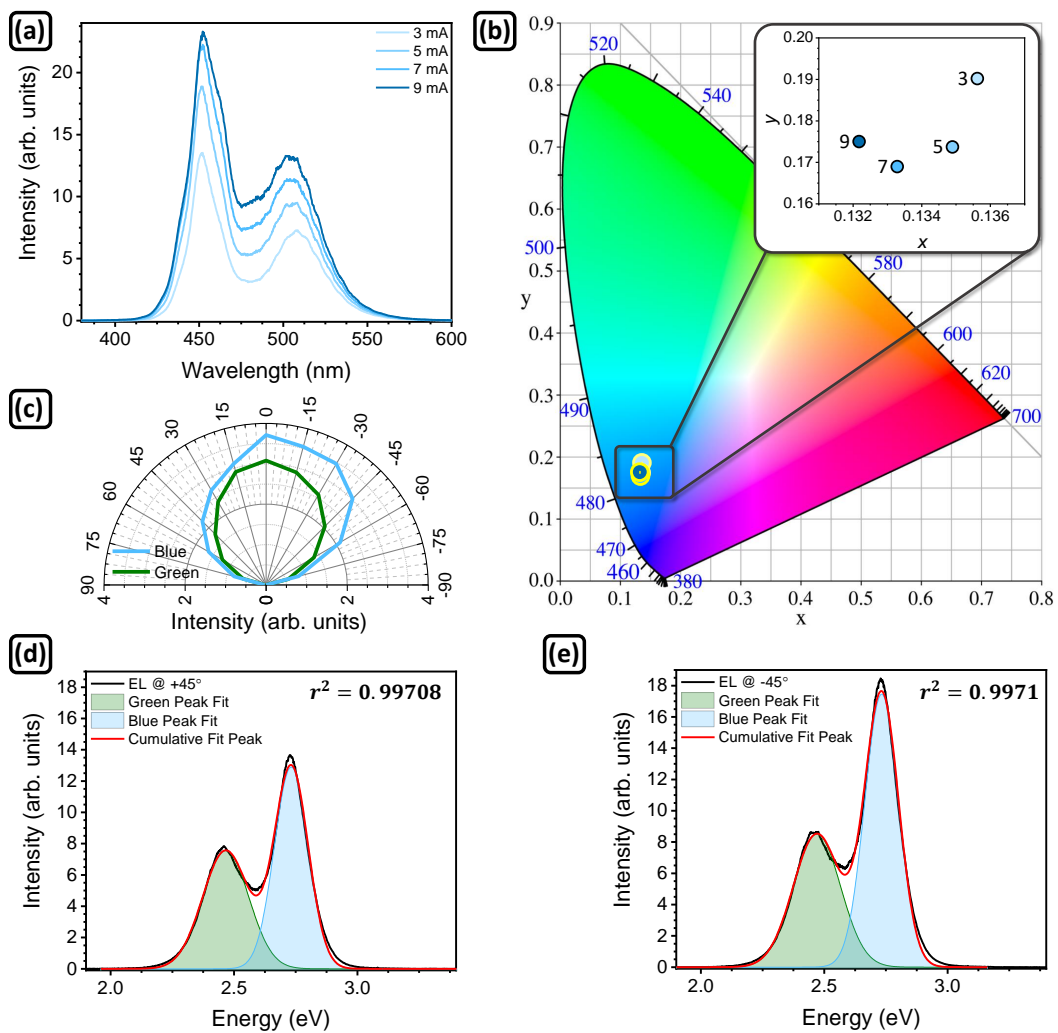


FIGURE 3.19: In-series connected blue-green micro-LED array (a) electroluminescence (EL) spectra and (b) CIE1931 colour coordinates at different driving currents; (c) angular distribution of the integrated area of the blue and green components of the EL spectrum at 9 mA; (d) and (e) EL spectra superimposed with gaussian fits at +45° and -45°, respectively.

CIE1931 colour coordinates of the in-series dual-colour device at different driving currents are shown in Fig. 3.19(b). Although, there is no individual control of the different colour micro-LEDs, fine-tuning of the perceived colour can be obtained by changing the driving current.

In addition, as the emitting footprint of the in-series connected array is roughly two times larger than the individually addressable array, the EL spectra angular distribution was investigated. For this purpose, the fibre-coupled spectrometer was mounted on a goniometer and the detection angle swept from  $-90^\circ$  to  $+90^\circ$  in  $15^\circ$  intervals. The EL integrated areas for the blue and green components *vs* detection angle are shown in Fig. 3.19(c).

Figures 3.19(d) and 3.19(e) present the EL spectra acquired at  $+45^\circ$  and at  $-45^\circ$ , respectively. Two gaussians were used to fit the data and extract the integrated area of the blue and green peaks. As shown in Figure 3.19(c) the green component follows a textbook Lambertian emission profile, expected for a planar LED [40]. On the other hand, the blue component exhibits a distorted Lambertian emission profile. This is also evident when comparing the intensity of the blue peak in Figs. 3.19(d) and 3.19(e). As the blue micro-LED is transfer printed onto the SU-8 layer, it is possible that this layer is preferentially guiding the light onto one of the edges of the diced chip, where it scatters. This effect is not as strong for the green micro-LED because its emission only goes through the transparent sapphire substrate, instead of SU-8/sapphire as the blue micro-LED.

### 3.3.4 VLC and UWOC application

Schematic drawings of the VLC and UWOC experimental setups are shown in Figs. 3.20(a) and 3.20(b), respectively. For the VLC demonstration, a random bit stream is encoded into an OFDM signal by MATLAB<sup>™</sup> and then generated by an AWG (Keysight M8195A). The analogue signal is amplified by a power amplifier (SHF S126A) and then combined with a DC bias (Yokogawa GS610) through a bias-tee (Tektronix PSPL5575A). The output of the bias-tee is connected to the micro-LED device. The link distance is set to 40 cm and aspheric condenser lenses (ACL4532A) have been used at both transmitter and receiver side. The optical signal is detected by a photoreceiver (Femto HSPR-X-I-1G4-SI). The output electrical signal is captured by an oscilloscope (Keysight DSA90804B) and then sent to the PC for processing using MATLAB<sup>™</sup>.

For the UWOC demonstration, an OOK data signal was generated by an AWG (Keysight M9502A). The analogue signal is amplified by a power amplifier (Mini-Circuits ZHL-1A-S+) and then combined with a DC bias (Yokogawa GS610). A sequence of

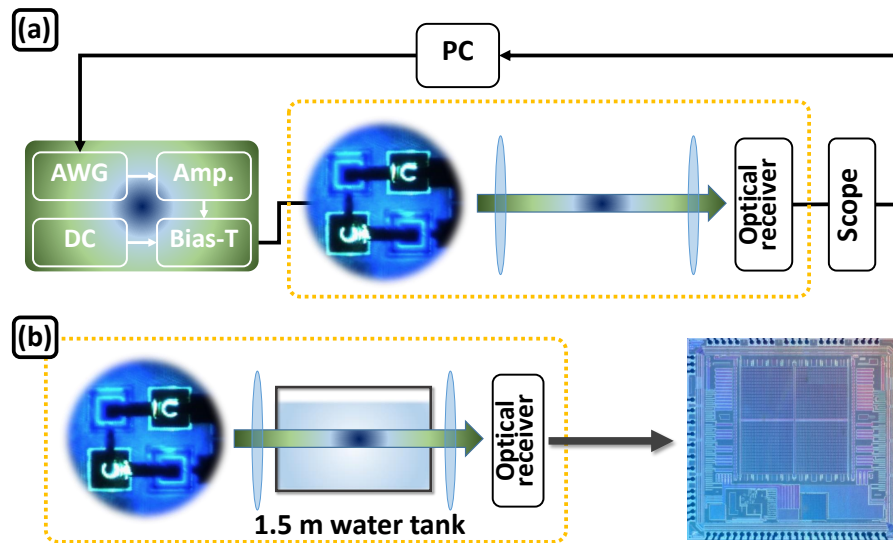


FIGURE 3.20: Schematic drawings of the experimental setups employed in the (a) VLC and (b) UWOC data transmission demonstrations.

length  $2^{15}$  was transmitted, consisting of a wide synchronisation pulse and a pseudo-random bit sequence. The in-series connected micro-LED array emission was collected and collimated by a condenser lens (Thorlabs, ACL50832U-A), propagated through a 1.5 m long water tank (with different Maalox<sup>TM</sup> concentrations) and was then focused onto the receiver by a 4-inch diameter Fresnel lens (Edmund, #46-614). The receiver, shown in detail in Fig. 3.20(b), is the same 64 x 64 array of Si SPADs used in the previous UWOC demonstration. The photon counts are summed over a time window of 5 ns and the count values outputted through a DAC. The DAC signal was captured with an active oscilloscope probe and transferred to MATLAB<sup>TM</sup> for offline processing to determine a BER. The turbidity of the water sample was varied, again, by adding Maalox<sup>TM</sup> antacid to tap water.

The VLC results of the in-series connected blue-green micro-LED array, at two different DC biases (9 and 23 mA), are summarised in Fig. 3.21. The modulation signal peak-to-peak voltage, for both DC bias and after the amplifier, was set to 7.05 V. The sampling frequency was set at 16 GSa/s and the number of samples per symbol was set at 5. The estimated SNR and number of allocated bits, at the highest data rate below the FEC threshold of  $3.8 \times 10^{-3}$  BER, for the in-series connected micro-LED array at a DC bias of 9 and 23 mA are shown in Fig. 3.21(a).

The in-series connected blue-green micro-LED array SNR decreases smoothly with frequency, supporting bit allocation up to 1600 MHz. Increasing the DC bias from 9 to 23 mA, results in an increase of the SNR and number of allocated bits throughout the full frequency range. These differences in SNR and bit allocation curves lead to the different BER *vs* data rate curves shown in Fig. 3.21(b). At 9 mA, the in-series

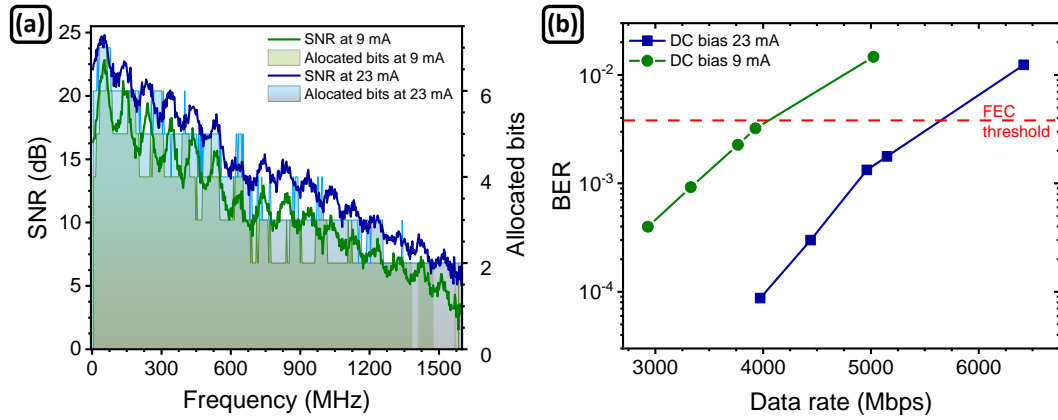


FIGURE 3.21: (a) Signal to noise ratio and number of allocated bits (at maximum data rate below forward error correction) at 9 and 23 mA of DC bias; (b) bit-error-ratio *vs* data rate curves for the different DC biases.

connected blue-green micro-LED array achieves a data rate, below FEC threshold, of 4054 Mbps. The increase in SNR at 23 mA, pushes the achievable data rate, below FEC, to 5649 Mbps. Applying the 7% FEC overhead reduction, error-free data rates of 3770 and 5254 Mbps are obtained, for the DC biases of 9 and 23 mA, respectively.

For the UWOC demonstration the in-series connected blue-green micro-LED array was DC-biased at 4.5 V and the modulation signal  $V_{pp}$  set to 20 V. Figure 3.22 shows the BER *vs* Maalox™ concentration in the water tank. A 50 Mbps link is established below FEC threshold up to Maalox™ concentrations of  $7.2 \times 10^{-2}$  ml/l.

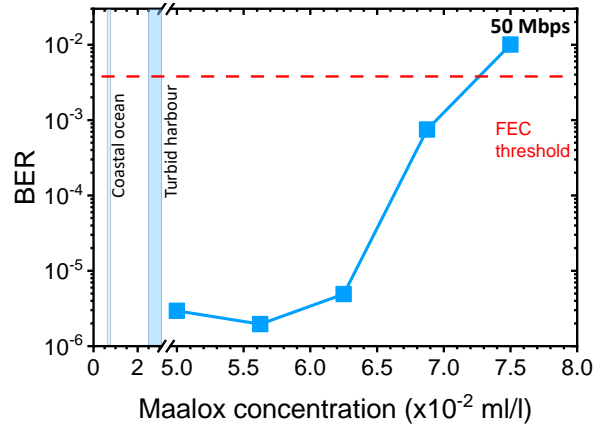


FIGURE 3.22: Bit-error-ratio *vs* Maalox concentration curve of the in-series connected blue-green micro-LED array in an UWOC demonstration.

### 3.4 Summary

This chapter presented the development of dual-colour micro-LED arrays in two different layouts (individually addressable and in-series connected). In both configurations

Gbps error-free VLC data rates are achieved. These results show the potential for multi-coloured pixelated clusters in micro-LED displays acting as VLC transmitters. In addition, due to water's transparency window in the visible spectrum, these devices have shown UWOC Mbps data rates in high-turbidity conditions. The results of the first section of this chapter were published in: J.F.C. Carreira *et al.*, *Optics Express* 27 (20), A1517-A1528 (2019).

## Bibliography

- [1] François Templier. GaN-based emissive microdisplays: A very promising technology for compact, ultra-high brightness display systems. *Journal of the Society for Information Display*, 24(11):669–675, 2016.
- [2] Sujan Rajbhandari, Jonathan J D McKendry, Johannes Herrnsdorf, Hyunchoe Chun, Grahame Faulkner, Harald Haas, Ian M Watson, Dominic O’Brien, and Martin D Dawson. A review of gallium nitride LEDs for multi-gigabit-per-second visible light data communications. *Semiconductor Science and Technology*, 32(2):023001, jan 2017.
- [3] H. Kaushal and G. Kaddoum. Underwater Optical Wireless Communication. *IEEE Access*, 4:1518–1547, 2016.
- [4] S. Zhang, Z. Gong, J. J. D. McKendry, S. Watson, A. Cogman, E. Xie, P. Tian, E. Gu, Z. Chen, G. Zhang, A. E. Kelly, R. K. Henderson, and M. D. Dawson. CMOS-Controlled Color-Tunable Smart Display. *IEEE Photonics Journal*, 4(5):1639–1646, Oct 2012.
- [5] Young Joon Hong, Chul-Ho Lee, Aram Yoon, Miyoung Kim, Han-Kyu Seong, Hun Jae Chung, Cheolsoo Sone, Yong Jo Park, and Gyu-Chul Yi. Visible-color-tunable light-emitting diodes. *Advanced Materials*, 23(29):3284–3288, 2011.
- [6] Kunook Chung, Jingyang Sui, Brandon Demory, Chu-Hsiang Teng, and Pei-Cheng Ku. Monolithic integration of individually addressable light-emitting diode color pixels. *Applied Physics Letters*, 110(11):111103, 2017.
- [7] Ronald S. Cok, Matthew Meitl, Robert Rotzoll, George Melnik, Alin Fecioru, Antonio Jose Trindade, Brook Raymond, Salvatore Bonafede, David Gomez, Tanya Moore, Carl Prevatte, Erich Radauscher, Scott Goodwin, Paul Hines, and Christopher A. Bower. Inorganic light-emitting diode displays using micro-transfer printing. *Journal of the Society for Information Display*, 25(10):589–609, 2017.
- [8] Yang Li, Jin Tao, Yongzhou Zhao, Jiaxian Wang, Jinguang Lv, Yuxin Qin, Jingqiu Liang, and Weibiao Wang. 48x48 pixelated addressable full-color micro display based on flip-chip micro LEDs. *Appl. Opt.*, 58(31):8383–8389, Nov 2019.
- [9] X. Li, L. Wu, Z. Liu, B. Hussain, W. C. Chong, K. M. Lau, and C. P. Yue. Design and characterization of active matrix led microdisplays with embedded visible light communication transmitter. *Journal of Lightwave Technology*, 34(14):3449–3457, July 2016.
- [10] H. Chun, S. Rajbhandari, G. Faulkner, D. Tsonev, E. Xie, J. J. D. McKendry, E. Gu, M. D. Dawson, D. C. O’Brien, and H. Haas. LED Based Wavelength Division Multiplexed 10 Gb/s Visible Light Communications. *Journal of Lightwave Technology*, 34(13):3047–3052, July 2016.
- [11] Technology development for ocean resources exploration. <https://www.jamstec.go.jp/sip/en/enforcement-2/index.html>, Accessed 2020-05-20.
- [12] Tsai-Chen Wu, Yu-Chieh Chi, Huai-Yung Wang, Cheng-Ting Tsai, and Gong-Ru Lin. Blue Laser Diode Enables Underwater Communication at 12.4Gbps. *Scientific Reports*, 7:40480, 2017.
- [13] Philip Lacovara. High-Bandwidth Underwater Communications. *Marine Technology Society Journal*, 42(1):93–102, 2008.

- [14] Z. Zeng, S. Fu, H. Zhang, Y. Dong, and J. Cheng. A survey of underwater optical wireless communications. *IEEE Communications Surveys Tutorials*, 19(1):204–238, Firstquarter 2017.
- [15] M. Doniec and D. Rus. BiDirectional optical communication with AquaOptical II. In *2010 IEEE International Conference on Communication Systems*, pages 390–394, Nov 2010.
- [16] G. N. Arvanitakis, R. Bian, J. J. D. McKendry, C. Cheng, E. Xie, X. He, G. Yang, M. S. Islim, A. A. Purwita, E. Gu, H. Haas, and M. D. Dawson. Gb/s Underwater Wireless Optical Communications Using Series-Connected GaN Micro-LED Arrays. *IEEE Photonics Journal*, 12(2):1–10, April 2020.
- [17] Yingjun Zhou, Xin Zhu, Fangchen Hu, Jianyang Shi, Fumin Wang, Peng Zou, Junlin Liu, Fengyi Jiang, and Nan Chi. Common-anode LED on a Si substrate for beyond 15 Gbit/s underwater visible light communication. *Photon. Res.*, 7(9):1019–1029, Sep 2019.
- [18] J. F. C. Carreira, G. N. Arvanitakis, A. D. Griffiths, J. J. D. McKendry, E. Xie, J. Kosman, R. K. Henderson, E. Gu, and M. D. Dawson. Underwater Wireless Optical Communications at 100 Mb/s using Integrated Dual-Color Micro-LEDs. In *2019 IEEE Photonics Conference (IPC)*, pages 1–2, Sep. 2019.
- [19] Absorption spectrum of liquid water. [https://commons.wikimedia.org/wiki/File:Absorption\\_spectrum\\_of\\_liquid\\_water.png](https://commons.wikimedia.org/wiki/File:Absorption_spectrum_of_liquid_water.png), Accessed 2020-05-20.
- [20] Mohamed Sufyan Islim, Ricardo X. Ferreira, Xiangyu He, Enyuan Xie, Stefan Videv, Shaun Viola, Scott Watson, Nikolaos Bamiedakis, Richard V. Penty, Ian H. White, Anthony E. Kelly, Erdan Gu, Harald Haas, and Martin D. Dawson. Towards 10 Gb/s orthogonal frequency division multiplexing-based visible light communication using a GaN violet micro-LED. *Photon. Res.*, 5(2):A35–A43, Apr 2017.
- [21] R. X. G. Ferreira, E. Xie, J. J. D. McKendry, S. Rajbhandari, H. Chun, G. Faulkner, S. Watson, A. E. Kelly, E. Gu, R. V. Penty, I. H. White, D. C. O’Brien, and M. D. Dawson. High Bandwidth GaN-Based Micro-LEDs for Multi-Gb/s Visible Light Communications. *IEEE Photonics Technology Letters*, 28(19):2023–2026, Oct 2016.
- [22] MicroChem. SU-8 2000 Permanent Epoxy Negative Photoresist, Processing guidelines for: SU-8 2000.5, SU-8 2002, SU-8 2005, SU-8 2007, SU-8 2010 and SU-8 2015. [http://www.micro-resist.de/daten/mcc/su\\_8\\_2000\\_5\\_2015.pdf](http://www.micro-resist.de/daten/mcc/su_8_2000_5_2015.pdf), Accessed 2020-01-15.
- [23] A del Campo and C Greiner. SU-8: a photoresist for high-aspect-ratio and 3D submicron lithography. *Journal of Micromechanics and Microengineering*, 17(6):R81–R95, May 2007.
- [24] Stephan Keller, Gabriela Blagoi, Michael Lillemose, Daniel Haefliger, and Anja Boisen. Processing of thin SU-8 films. *Journal of Micromechanics and Microengineering*, 18(12):125020, nov 2008.
- [25] Nan Chi. *Models of the Visible Light Channel*, pages 39–58. Springer Berlin Heidelberg, Berlin, Heidelberg, 2018.
- [26] J. Ryou, P. D. Yoder, J. Liu, Z. Lochner, H. Kim, S. Choi, H. J. Kim, and R. D. Dupuis. Control of Quantum-Confined Stark Effect in InGa<sub>N</sub>-Based Quantum Wells. *IEEE Journal of Selected Topics in Quantum Electronics*, 15(4):1080–1091, July 2009.
- [27] E. Fred Schubert. *Colorimetry*, page 292–305. Cambridge University Press, 2 edition, 2006.

- [28] J. F. C. Carreira, E. Xie, R. Bian, C. Chen, J. J. D. McKendry, B. Guilhabert, H. Haas, E. Gu, and M. D. Dawson. On-chip GaN-based dual-color micro-LED arrays and their application in visible light communication. *Opt. Express*, 27(20):A1517–A1528, Sep 2019.
- [29] M. Uysal and H. Nouri. Optical wireless communications — An emerging technology. In *2014 16th International Conference on Transparent Optical Networks (ICTON)*, pages 1–7, 2014.
- [30] H. Haas, L. Yin, Y. Wang, and C. Chen. What is LiFi? *Journal of Lightwave Technology*, 34(6):1533–1544, 2016.
- [31] Nan Chi. *The Modulation Technologies of Visible Light Communication*, pages 91–110. Springer Berlin Heidelberg, Berlin, Heidelberg, 2018.
- [32] J. Armstrong. OFDM for Optical Communications. *Journal of Lightwave Technology*, 27(3):189–204, 2009.
- [33] D. Tsonev, H. Chun, S. Rajbhandari, J. J. D. McKendry, S. Videv, E. Gu, M. Haji, S. Watson, A. E. Kelly, G. Faulkner, M. D. Dawson, H. Haas, and D. O’Brien. A 3-Gb/s Single-LED OFDM-Based Wireless VLC Link Using a Gallium Nitride  $\mu$ LED. *IEEE Photonics Technology Letters*, 26(7):637–640, April 2014.
- [34] J. Kosman, O. Almer, T. A. Abbas, N. Dutton, R. Walker, S. Videv, K. Moore, H. Haas, and R. Henderson. 29.7 A 500Mb/s -46.1dBm CMOS SPAD Receiver for Laser Diode Visible-Light Communications. In *2019 IEEE International Solid-State Circuits Conference - (ISSCC)*, pages 468–470, Feb 2019.
- [35] Brandon Cochenour, Linda Mullen, and John Muth. Effect of scattering albedo on attenuation and polarization of light underwater. *Opt. Lett.*, 35(12):2088–2090, Jun 2010.
- [36] Jonathan J. D. McKendry, David Massoubre, Shuailong Zhang, Bruce R. Rae, Richard P. Green, Erdan Gu, Robert K. Henderson, A. E. Kelly, and Martin D. Dawson. Visible-Light Communications Using a CMOS-Controlled Micro-Light-Emitting-Diode Array. *J. Lightwave Technol.*, 30(1):61–67, Jan 2012.
- [37] Richard P. Green, Jonathan J. D. McKendry, David Massoubre, Erdan Gu, Martin D. Dawson, and A. E. Kelly. Modulation bandwidth studies of recombination processes in blue and green InGaN quantum well micro-light-emitting diodes. *Applied Physics Letters*, 102(9):091103, 2013.
- [38] Francois Olivier, Anis Daami, Christophe Licitra, and Francois Templier. Shockley-Read-Hall and Auger non-radiative recombination in GaN based LEDs: A size effect study. *Applied Physics Letters*, 111(2):022104, 2017.
- [39] Jianquan Kou, Chih-Chiang Shen, Hua Shao, Jiamang Che, Xu Hou, Chunshuang Chu, Kangkai Tian, Yonghui Zhang, Zi-Hui Zhang, and Hao-Chung Kuo. Impact of the surface recombination on InGaN/GaN-based blue micro-light emitting diodes. *Opt. Express*, 27(12):A643–A653, Jun 2019.
- [40] E. Fred Schubert. *LED basics: Optical properties*, page 86–100. Cambridge University Press, 2 edition, 2006.



## Chapter 4

# Integration of AlGaInP red micro-LEDs by micro-TP onto unusual substrates for VLC and optogenetics applications

In this chapter, the integration of aluminium gallium indium phosphide (AlGaInP) red micro-LEDs by micro-transfer printing onto non-native substrates for visible light communication and optogenetics applications is presented. First, the integration of red micro-LEDs onto glass and diamond substrates and their application in Gbps free-space VLC is demonstrated. Second, the development of a dual colour-optrode for dual-excitation and/or excitation-inhibition of different neural populations is shown.

### 4.1 AlGaInP micro-LED platelets

AlGaInP red (630 nm) micro-LED platelets were acquired through a collaboration of Dr. Erdan Gu with a confidential company. The epitaxial structure of these red micro-LEDs follows that of conventional AlGaInP epistuctures grown on GaAs [1]. Figure 4.1(a) shows a schematic drawing of the epitaxial structure, where the grey, blue, green, magenta, and beige colours correspond to GaAs, GaInP (etch stopping layer - ESL),  $n$ -doped layer, active layer, and  $p$ -doped layer, respectively. Fabrication of the micro-LED platelets started by processing the topside of the AlGaInP/GaAs wafer following typical microfabrication procedures for mesa type LEDs. First, a  $6.96 \times 10^{-6} \text{ cm}^2$  active area pixel was defined by dry etching, exposing the  $n$  layer (Fig. 4.1(b)), followed

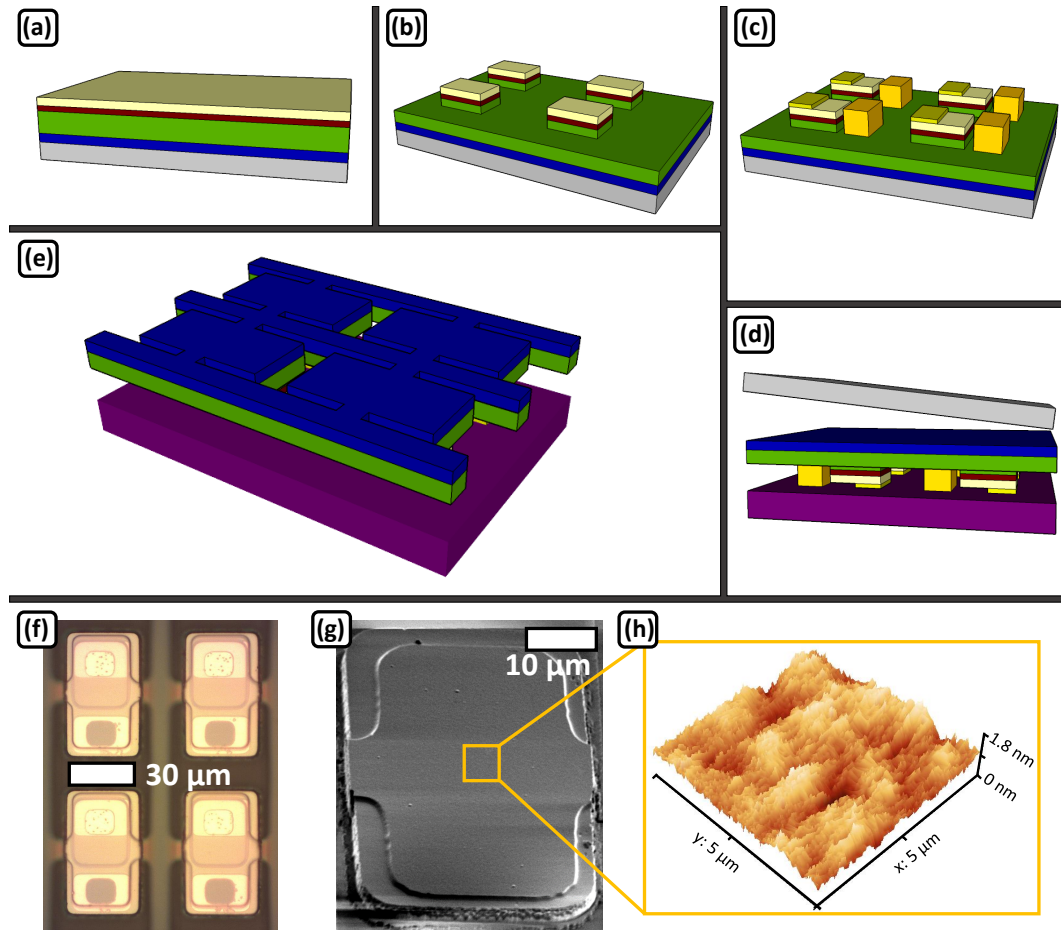


FIGURE 4.1: (a)-(e) Schematic drawings of the red micro-LED fabrication process (not to scale, see text for further details); (f) plan-view photograph of a 2x2 array of micro-LED platelets on the temporary sapphire carrier; (g) scanning electron microscopy micrograph of a micro-LED platelet backside; (h) representative  $5 \times 5 \mu\text{m}^2$  atomic force microscopy micrograph of a micro-LED platelet backside.

by deposition of AuGe/Au and Ti/Al/Ti/Au metal stacks on the  $n$  and  $p$  contacts, respectively (Fig. 4.1(c)). Next, the GaAs wafer was flip-chip bonded to a temporary sapphire carrier (identified in purple in Fig. 4.1(d)) and the GaAs bulk substrate removed by wet chemical etching [2]. Finally, the platelet was defined through the backside of the AlGaInP film by dry etching (Fig. 4.1(e)). Figure 4.1(f) shows a 2x2 array of the micro-LED platelets on the temporary sapphire wafer.

Figure 4.1(g) shows a scanning electron microscopy (SEM) micrograph of a red micro-LED platelet backside. Contrary to the GaN-based blue micro-LED platelets fabricated in this thesis, the red micro-LED platelets were found to be extremely flat (not curved). This can be attributed to the lattice matched and strain-free epitaxial growth of these LED structures on GaAs [3]. In addition, due to the high etching selectivity between the GaAs and the ESL, the backside of the micro-LED platelets is extremely smooth,

as shown by a representative  $5 \times 5 \mu\text{m}^2$  atomic force microscopy micrograph of a micro-LED platelet backside (Fig. 4.1(h)). The micro-LED platelets backside exhibit a root-mean-square roughness of 0.2 nm, approaching the instrument resolution. The flatness and smoothness of the micro-LED platelet backside are important factors for micro-TP applications, as they improve the adhesion between the platelet and the receiving substrate. Furthermore, the good contact between the micro-LED platelet and the receiving substrate ensures efficient heat transfer.

## 4.2 Gbps VLC based on AlGaInP red micro-LEDs micro-transfer printed onto diamond and glass

### 4.2.1 Introduction

Full-colour micro-LED displays have been realised by mass transfer techniques, such as micro-transfer printing (micro-TP or  $\mu\text{TP}$ ), of red-green-blue (RGB) singulated chiplets onto a common platform (Figs. 4.2(a) and 4.2(b)). Blue and green pixels are fabricated from highly-efficient indium gallium nitride alloys, while, the red emission is based on AlGaInP LED structures. In Chapter 3, the concept of smart displays acting both as a display and as a high-speed VLC transmitter was introduced and the suitability of blue-green and blue-violet clusters of micro-LEDs for wavelength dependent modulation schemes discussed. This study was motivated by the emergence of micro-LED displays, as well as by the proven capability of GaN-based micro-LEDs to achieve multi-Gbps VLC data rates. Although, there are several reports focused on AlGaInP-based LEDs in equivalent device geometries [7], with a strong emphasis in microdisplays (Fig. 4.2(c)) [6,

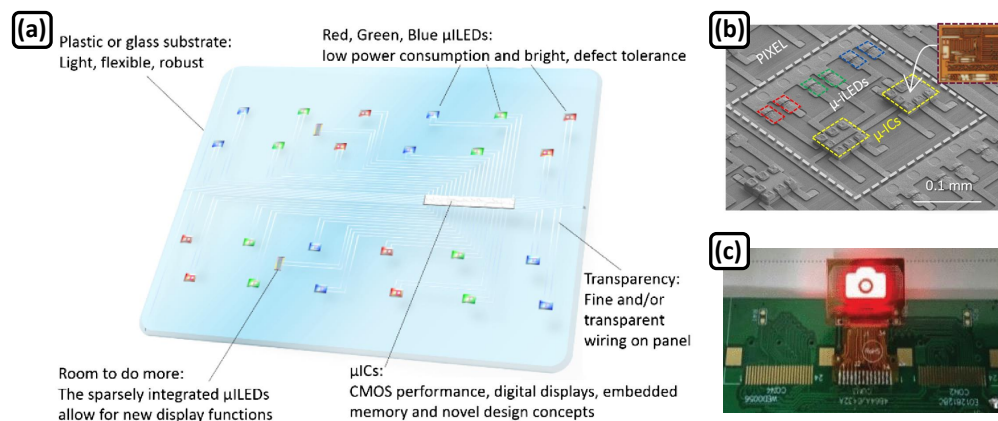


FIGURE 4.2: (a) Illustration of a conceptual micro-LED display [4]; (b) SEM micrograph of an RGB micro-LED IC-controlled pixel [5]; (c) AlGaInP-based micro-LED display [6].

8, 9], the data transmission capability of AlGaInP micro-LEDs has not been much studied. As such, there is a knowledge gap in the current state-of-the-art of AlGaInP micro-LEDs. In this chapter, AlGaInP micro-LEDs were micro-transfer printed onto a glass and diamond substrates and their modulation characteristics investigated.

#### 4.2.2 Device overview

A 2x2 array of micro-LEDs was sequentially printed directly, without any adhesion enhancement layer, onto glass and diamond substrates. The glass and single-crystal (synthetic) diamond substrates had the same dimensions, namely area  $4 \times 4 \text{ mm}^2$  and thickness  $500 \mu\text{m}$ . An elastomeric polydimethylsiloxane (PDMS) stamp array with pyramidal protrusions was used to pick-up the micro-LED platelets from the temporary sapphire carrier, thus flipping the platelets and exposing the  $p$  and  $n$  contacts (Fig. 4.3(a)). Next, a single elastomeric stamp was used to pick-up the platelets (with the electrical contacts upside) from the stamp array and print them onto both substrates (Fig. 4.3(b)). This two stage micro-TP was necessary in order to expose the micro-LED electrical contacts and to ensure a good contact between the platelets backside and the receiving substrates. After micro-TP, a Parylene-C (Pa-c) layer (thickness  $4 \mu\text{m}$ ) was deposited as insulation and encapsulation layer. Next, titanium/gold (Ti/Au thicknesses  $100/200 \text{ nm}$ ) metal

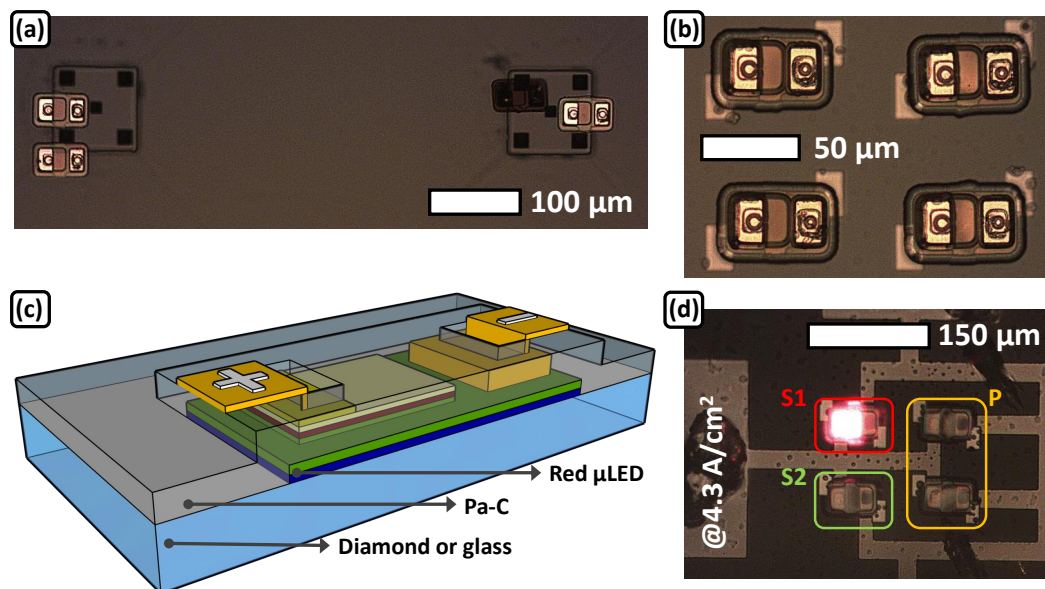


FIGURE 4.3: (a) Plan-view photograph of the red micro-LED platelets (with the electrical contacts facing up) on the stamp array; (b) plan-view photograph of a 2x2 micro-LED array micro-TP onto glass; (c) schematic drawing of a micro-TP red micro-LED after Pa-C encapsulation and metallisation; (d) plan-view photograph of a finalised 2x2 micro-LED array micro-TP onto glass with a single pixel (S1) driven at  $4.3 \text{ A/cm}^2$ .

tracks were lithographically defined, contacting the micro-LEDs through, previously reactive ion etching defined, localised apertures in the Pa-C layer. Figure 4.3(c) shows a schematic drawing of a micro-TP red micro-LED after Pa-C encapsulation and metallisation. The 2x2 array was arranged in order to have two individually addressable single micro-LEDs (identified in Fig. 4.3(d) as S1 and S2) and a 2x1 in-parallel micro-LED array (identified in Fig. 4.3(d) as P). Figure 4.3(d) shows the single micro-LED S1 driven at 4.3 A/cm<sup>2</sup>. It was found experimentally that the micro-LEDs S1 and S2 exhibit the same electrical and optical properties, on both substrates. Thus, for clarity sake, the device performance and application results are only shown for the micro-LED S1.

### 4.2.3 Device performance and application

#### 4.2.3.1 Micro-LED electrical, optical, and bandwidth characteristics

Figure 4.4(a) shows the voltage *vs* current density (JV) and optical power density *vs* current density (LJ) of the single micro-LED S1 on-diamond and on-glass. The JV characteristic was measured by a voltage source, through scanning each data point under direct current (DC) conditions. The LJ was measured using a calibrated Si photodiode detector (Thorlabs PM100D) placed in close proximity to the micro-LED backside. The forward diode voltage (at 32 A/cm<sup>2</sup>) of the single micro-LED on-diamond and on-glass was found to be 2.2 V and 2.1 V, respectively. The red micro-LED on-glass optical power density reaches a plateau of 16.6 W/cm<sup>2</sup> at 359 A/cm<sup>2</sup>. Due to diamond's superior thermal properties ( $k = 2200$  W/m.K) over glass ( $k = 1.42$  W/m.K) [10] the micro-LED on-diamond sustains current densities up to 790 A/cm<sup>2</sup> without any thermal roll-over. At the current density of 790 A/cm<sup>2</sup> the micro-LED on-diamond exhibits an optical power density of 39 W/cm<sup>2</sup> (more than twofold increase compared to the micro-LED on-glass).

The electrical to optical (E-O) modulation bandwidth of the single micro-LED S1 on different substrates was measured by applying a DC bias combined with a small-signal modulation from an HP8753ES network analyser. The optical response was lens-focused onto a silicon avalanche photodetector (Thorlabs — APD430A2/M bandwidth 400 MHz). Figure 4.4(b) shows the E-O bandwidth *vs* current density of the single micro-LED S1 on-diamond and on-glass. Devices on both glass and diamond exhibit similar performance for current densities below 100 A/cm<sup>2</sup>. Above this point, the micro-LED on-glass exhibits a lower modulation bandwidth until it reaches a plateau of 85 MHz at 431 A/cm<sup>2</sup>. On the other hand, the micro-LED on-diamond modulation bandwidth continues to increase up to 170 MHz at 1000 A/cm<sup>2</sup>.

Figures 4.5(a) and 4.5(b) show the electroluminescence (EL) spectra and CIE1931 colour coordinates of the single S1 micro-LED driven at  $359 \text{ A/cm}^2$  on both substrates, respectively. The EL spectra were acquired using an optical fiber-coupled spectrometer

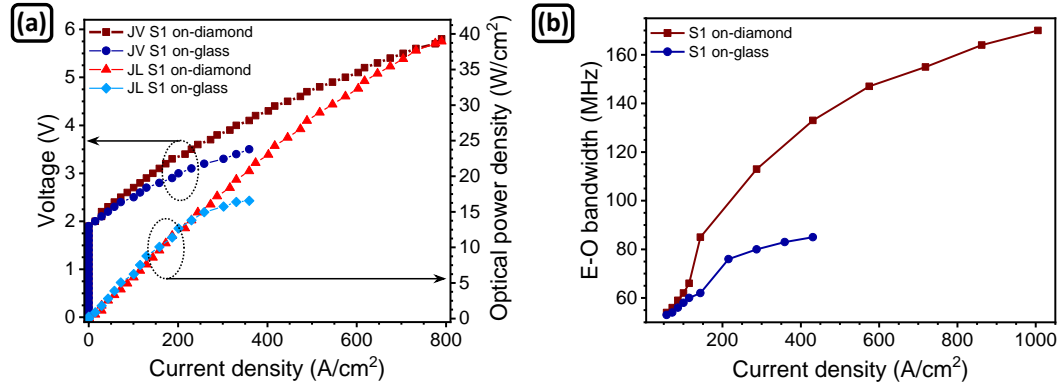


FIGURE 4.4: (a) Voltage vs current density (JV) and optical power density vs current density (LJ) curves of the micro-LED S1 on-diamond and on-glass; (b) electrical to optical modulation bandwidth vs current density of the single S1 micro-LED on both substrates.

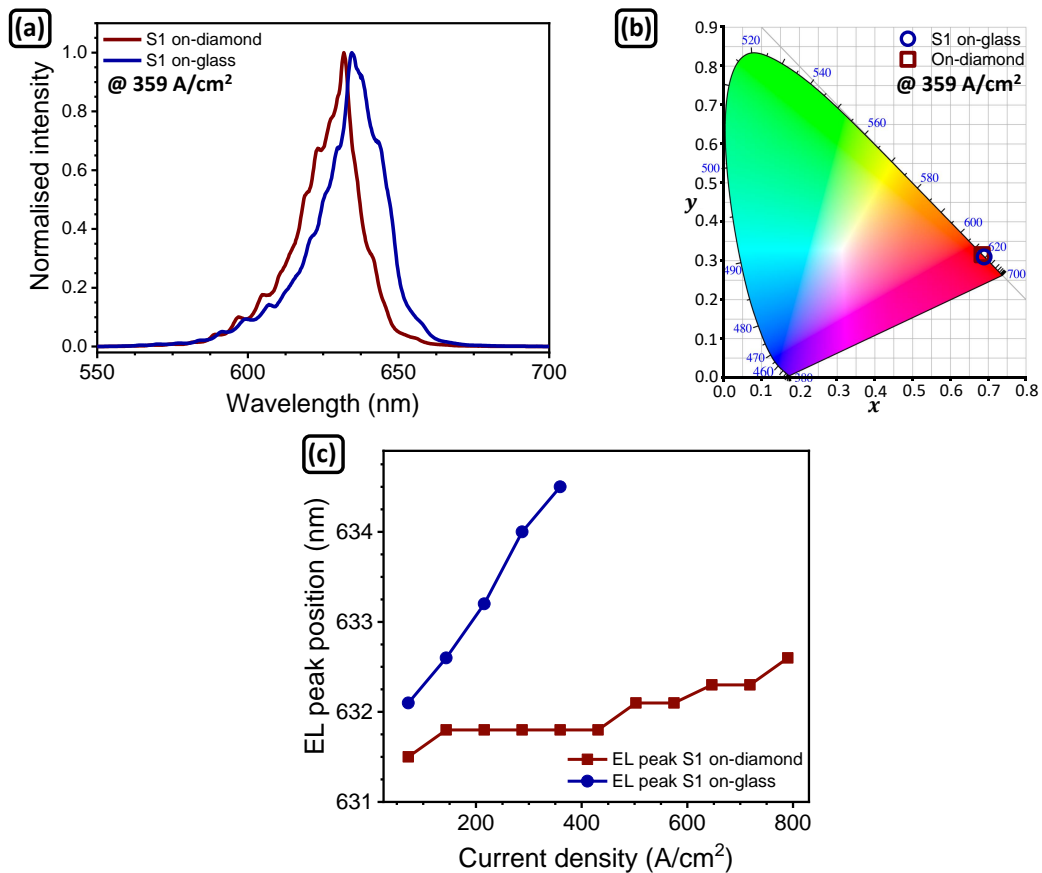


FIGURE 4.5: (a) Electroluminescence (EL) spectra and (b) CIE1931 colour coordinates of the single micro-LED S1 (at  $359 \text{ A/cm}^2$ ) on both substrates; (c) EL spectra peak position vs current density of the micro-LED S1 on both substrates.

(Avantes AvaSpec-2048L spectrometer). Both EL spectra show fringes due to the refractive index contrast between the LED epitaxial material ( $n=3.5$  [11]) and the receiving substrates (glass  $n=1.46$  [12], diamond  $n=2.41$  [13]). The micro-LED on-diamond exhibits an EL peak centred at 631.8 nm and a full width at full maximum (FWHM) of 19 nm. On the other hand, the micro-LED on glass EL peak is red-shifted (peak emission centred at 634.5 nm) and broadened (FWHM = 22 nm) due to bandgap shrinkage and band filling effects, respectively. Nevertheless, these variations have a marginal effect on the perceived colour, with the micro-LED on-diamond ( $x = 0.68, y = 0.32$ ) and on-glass ( $x = 0.69, y = 0.31$ ) showing similar  $(x, y)$  CIE1931 colour coordinates (Fig. 4.5(b)). This minimal variation of the colour coordinates shows that these red micro-LEDs are highly suitable for display applications. Figure 4.5(c) shows the EL peak position *vs* current density for the single micro-LED S1 printed on-diamond and on-glass. For the device on-glass, increasing the current density from 72 A/cm<sup>2</sup> to 359 A/cm<sup>2</sup> results in a steep red-shift of the peak position from 632.1 nm to 634.5 nm ( $\Delta\lambda = 2.4$  nm). On the other hand, for the device on-diamond, under the same current density interval, the peak only red-shifts by 0.3 nm. In fact, due to diamond's superior thermal properties varying the current density from 72 A/cm<sup>2</sup> to 790 A/cm<sup>2</sup> results in a red-shift from 631.5 nm to 632.6 nm ( $\Delta\lambda = 1.1$  nm).

#### 4.2.3.2 VLC application

Optical orthogonal frequency division multiplexing (O-OFDM) has proven to be spectrally efficient in VLC [14, 15]. In this work, an implementation of direct current biased optical OFDM (DCO-OFDM) is used for the wireless data transmission due to its simplicity and high spectral efficiency [16]. As intensity modulation and direct detection (IM/DD) is used in VLC, the transmitted signal should be both real and non-negative. Thus Hermitian symmetry is applied and a DC bias is added.

A schematic drawing of the VLC experimental set-up is shown in Fig. 4.6. A random bit stream is encoded into an OFDM signal by MATLAB<sup>TM</sup> and then generated by an

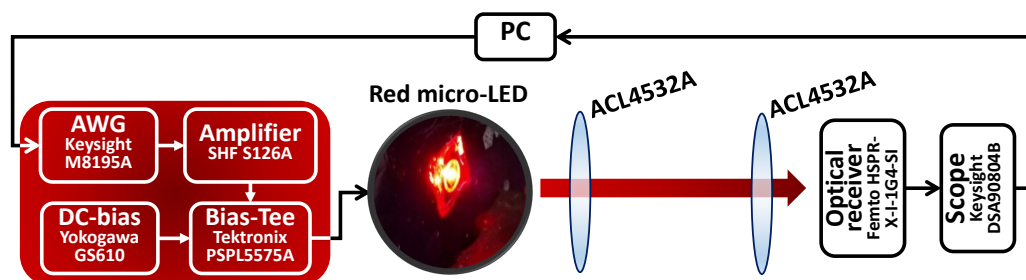


FIGURE 4.6: Schematic diagram of the visible light communication experimental setup. The photograph inset is the micro-LED on-diamond device (edge of the device is 1 cm).



arbitrary waveform generator (AWG, Keysight M8195A). The analogue signal is amplified by a power amplifier (SHF S126A) and then combined with a DC bias (Yokogawa GS610) through a bias-tee (Tektronix PSPL5575A). The output of the bias-tee is connected to the micro-LED device. The link distance is set to 40 cm, as in this case we wish to assess the upper modulation limits of the devices, and aspheric condenser lenses (ACL4532A) have been used at both transmitter and receiver side. The optical signal is detected by a photoreceiver (Femto HSPR-X-I-1G4-SI). The output electrical signal is captured by an oscilloscope (Keysight DSA90804B) and then sent to the PC for processing using MATLAB™.

Within each measurement, a channel estimation is first done to estimate the signal-to-noise ratio (SNR) at each subcarrier. Then the signal is generated using an adaptive bit and power loading algorithm based on the estimated SNR and a target bit error ratio (BER). Such signal is transmitted and the achieved data rate and BER are measured.

The VLC results of the red micro-LED devices on both substrates are summarised in Fig. 4.7. The DC bias and the modulation signal peak-to-peak voltage, after the amplifier, were set to 359 A/cm<sup>2</sup> (862 A/cm<sup>2</sup>) and 2.68 V (7.19 V), respectively, for the single S1 micro-LED on-glass (on-diamond). The sampling frequency was set at 16 GSa/s and the number of samples per symbol was optimized for each substrate. The estimated SNR and number of allocated bits, at the highest data rate below the FEC threshold of  $3.8 \times 10^{-3}$  BER, for the single micro-LED S1 on-glass (blue curve and blue bar plot) and on-diamond (red curve and red bar plot) are shown in Fig. 4.7(a). As the micro-LED on-glass exhibits lower optical power and bandwidth its SNR suffers a sharp drop with frequency, supporting bit loading only up to 656 MHz. On the other hand, the micro-LED on-diamond's higher optical power and bandwidth (due to its higher current

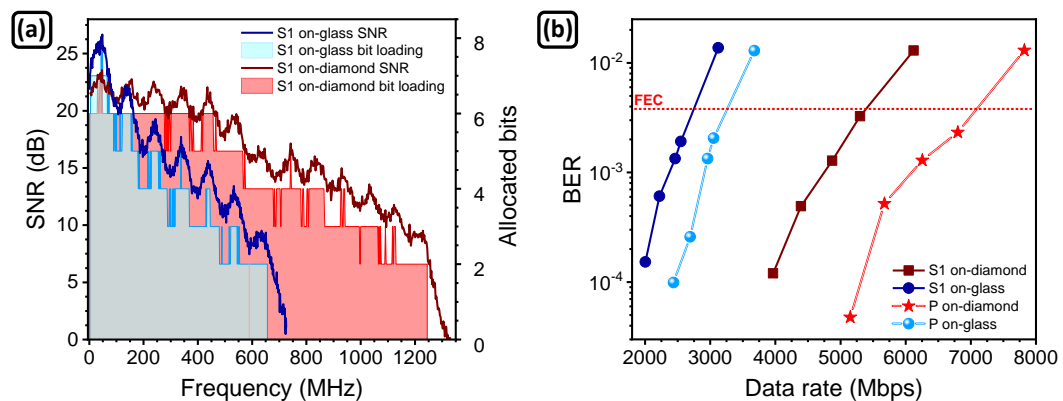


FIGURE 4.7: (a) Signal-to-noise ratio and number of allocated bits (at maximum data rate below forward error correction) of the single micro-LED S1 on both substrates (glass and diamond); (b) bit-error-ratio *vs* data rate of the single micro-LED S1 and in-parallel micro-LED array P on both substrates.



density operation) results in a smooth decrease of the SNR with frequency and bit loading up to 1245 MHz. These differences in SNR and bit loading lead to the difference in BER *vs* data rate curves shown in Fig. 4.7(b). At the BER of  $3.8 \times 10^{-3}$  a single micro-LED on-glass achieves a data rate of 2749 Mbps, with the device on-diamond achieving 5391 Mbps (roughly a twofold increase). These results show the importance of efficient thermal management in LED-based VLC transmitters. Applying the 7% FEC overhead reduction, error-free data rates of 2557 Mbps and 5014 Mbps are achieved for the single S1 micro-LED on-glass and on-diamond, respectively.

Also shown in Fig. 4.7(b) is the BER *vs* data rate performance of the 2x1 in-parallel (P) micro-LED array on both substrates. For this purpose, the DC bias and the modulation signal peak-to-peak voltage, after the amplifier, were set to 323 A/cm<sup>2</sup> (718 A/cm<sup>2</sup>) and 3.26 V (6.62 V), respectively, for the in-parallel micro-LED array on-glass (on-diamond). Although the current density is lower than a single micro-LED, the total optical power of the array is two times higher than of a single micro-LED. This translates into an increase in SNR and capacity to allocate more bits to the in-parallel micro-LED arrays. Thus, the in-parallel micro-LED array on-glass achieves 3262 Mbps below FEC threshold (a 1.2x increase compared to its single counterpart). For the device transfer printed on-diamond a data rate of 7093 Mbps, below FEC, is achieved (a 1.3x increase compared to a single device on-diamond). Again, applying the 7% FEC overhead reduction, error-free data rates of 3034 Mbps and 6596 Mbps are obtained for the in-parallel micro-LED array on-glass and on-diamond, respectively.

Table 4.1 compares the data rate, BER, and link distance achieved by the single micro-LED S1 and by the in-parallel micro-LED array P on-diamond, with other red LED-based VLC reports from our previous work. The data rates achieved in this work are higher than the ones obtained using commercially available LEDs [17] or resonant cavity LEDs [18] employing similar modulation schemes. Due to the micro-LEDs lower optical power the link distance is shorter than for commercial LEDs. However, it has been shown that the optical power can be increased, without any penalty in modulation bandwidth, by simply arranging several micro-LEDs in-parallel or in-series configurations [19].

TABLE 4.1: State-of-the-art of red LED-based VLC.

Transmitter	Data rate (Mbps)	BER	Link distance (m)	Ref.
Micro-LED	5391 (S1) 7093 (P)	$3.8 \times 10^{-3}$	0.4	This work
Commercial LED	4904	$2.5 \times 10^{-3}$	1.6	[17]
Resonant cavity LED	4000	$3.4 \times 10^{-3}$	1.5	[18]

## 4.3 Dual-colour optrodes for optogenetics application

### 4.3.1 Introduction

In optogenetics, neural cells are genetically modified to be susceptible to light stimulation, providing excitatory and/or inhibitory control of the neural circuitry with millisecond precision [20]. This can be used to map brain networks, gather knowledge about their working mechanisms and interrelations, and, as expected in the near future to treat brain disorders, such as dysfunctional Parkinsonian motor control [21] and depression [22]. A detailed overview of optogenetics is out of the scope of this thesis and can be found in [23–25]. Nevertheless, the following paragraph presents a brief introduction to the field.

Figure 4.8(a) shows the mechanism behind optogenetics. First, in order to make the neurons susceptible to light, opsins are introduced into the subject's brain, usually through a viral injection which causes the targeted neuron cells to be light sensitive\*. Opsins are single component light-sensing systems, which have a photoreceptive characteristic coupled to a biological function, can be excitatory or inhibitory and are susceptible to a wide range of wavelengths (400-630 nm) [23]. Consequently, the targeted neurons will express the introduced opsin and, when exposed to light, the photoreceptive proteins will promote a biological effect on those specific cells. One of the most common opsins, shown in Fig. 4.8(a), is the so-called channelrhodopsin-2 (ChR-2)<sup>†</sup>, which when exposed to blue light causes the neuronal ion channels to open resulting in neuron firing. The light is introduced into the brain by an optrode, which is a device capable of delivering light to neurons and electrically record them [20].

Figure 4.8(b) compares conventional electrical with optogenetics stimulation. Electrical stimulation approaches stimulate a large area of the brain without precise spatial control and cannot distinguish between different cell types. In addition, it is only excitatory (cannot silence neuron activity) and can also induce unwanted thermal heating of the surrounding tissue. On the other hand, optogenetics only affects opsin-expressing neurons and depending on the opsin and light wavelength is capable of excitatory (e.g. ChR-2 at 460 nm - blue light) and inhibitory control (halorhodopsin at 590 nm - yellow light).

One of the biggest challenges in optogenetics is delivering light into neural tissue with reliability and accuracy. As shown in Fig. 4.8(a) this is performed by an optrode, which

---

\*Cellular specificity can be obtained with viruses by specific promoters, by spatial targeting of virus injection, and by restriction of opsin activation to particular cells [26].

<sup>†</sup>ChR-2 is a microbial photosensitive protein derived from algae, which exhibits an irradiance stimulation threshold of 1 mW/mm<sup>2</sup> [20].

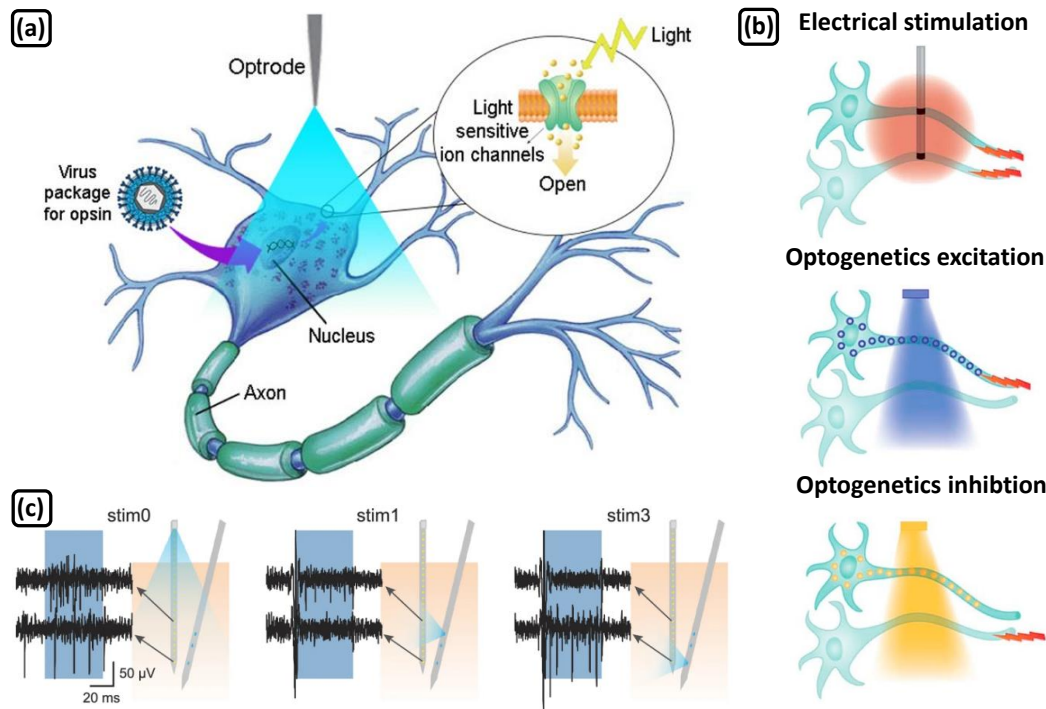


FIGURE 4.8: (a) Illustration of the optogenetic technique using blue light, which activates ChR2-expressing neuron cells by opening light sensitive channels [20]; (b) electrical stimulation *vs* optogenetics (excitation/inhibition) (adapted from [26]); (c) schematic of probe insertion and high-pass filtered signals from two separate recording channels showing the depth-dependent activation of neurons *in vivo* [27].

can be based on optical fibre or micro-LED shanks. Optical fibres optrodes are the most straightforward way of guiding light from an external light source (e.g. LEDs or laser diodes) into to the brain tissue. However, as it illuminates a large volume of the brain, spatial resolution is compromised. This is illustrated in Fig. 4.8(c) stim0. An optical fibre based optrode is used to illuminate a mouse's brain with blue light and the electrical response recorded from two different electrodes (separated by  $350 \mu\text{m}$ ). In the case of the optical fibre based optrode the signals from the different electrodes are very similar, showing poor spatial resolution. An alternative is to fabricate implantable micro-LED shank based optrodes. Stimulation based on such small emitters enables unique spatial resolution by delivering light at the cellular scale with millisecond precision. Fabricating arrays of these micro-LEDs on the optrode shank allows for depth-specific optogenetic control. This is shown in Fig. 4.8(c) stim1 and stim3. In this case, the same recording electrodes are used but the light is delivered by an array of micro-LEDs fabricated in an optrode shank. In this case, as the light sources are at different depths, minimal crosstalk between the two electrodes is observed [27]. In addition, when compared to conventional electrical probes, micro-LED based optrodes exhibit superior thermal properties, which translates into a minimal  $0.5 \text{ }^\circ\text{C}$  increase of temperature in the surrounding tissue [28].

Due to the abundance of opsins with different properties and wavelength susceptibility an optrode comprising dual-colour micro-LEDs and recording sites would be of great importance in the field of optogenetics. Such a device, would be capable of independent optical stimulation/inhibition of distinct neural populations and simultaneously recording with high spatial resolution. The following sections describe the fabrication of a blue-red micro-LED optrode by micro-TP of red micro-LED platelets onto a blue emitting micro-LED optrode. The contents shown in this thesis focus on the integration, by micro-TP, of red AlGaInP micro-LED platelets onto the optrodes and do not go into detail on the fabrication of the blue micro-LED optrode. Fabrication of the blue micro-LED optrode was in this case carried out by Mr. Ruaridh Winstanley from Prof. Keith Mathieson's research group within the Institute of Photonics at the University of Strathclyde.

### 4.3.2 Device overview

Optrodes were fabricated from commercial InGaN epistructures grown on a silicon (Si) 111-oriented substrate, following conventional microfabrication procedures [27]. This allows one to create monolithic GaN-based blue micro-LEDs for optical excitation and micro-electrodes ( $\mu$ -electrodes) for detection on a single shank. Figures 4.9(a) and 4.9(b) show a schematic drawing of the full optrode and of the tip of the shank, respectively. Figure 4.9(c) shows a plan-view photograph of the shank tip, before micro-TP, with 1 micro-LED and 4 micro-electrodes identified in blue and green, respectively. At this stage, the optrode is fully functional but still on its robust Si growth substrate. This simplifies handling and post-processing steps, which involve photolithography, after micro-TP of the red micro-LED platelets.

Figure 4.10(a) shows a schematic process flow of the micro-transfer printing of a red micro-LED platelet onto such an optrode<sup>‡</sup>. In order to aid in the release of the red micro-LED platelets the optrodes were covered in 800 nm of Pa-C prior to micro-TP. The red micro-LEDs were printed perpendicularly to the shank long axis, so as to further maximise the contact area between the micro-LED platelet backside and the optrode. After micro-TP, the Pa-C adhesion enhancement layer was removed in an oxygen plasma. Figure 4.10(b) shows an optrode after micro-TP of the red micro-LED platelets. The red micro-LEDs were transfer printed in between two micro-electrodes, which at the end of the encapsulation and metallisation process will not be exposed. Thus, in order to connect the micro-TP red micro-LED to the optrode bonding pads two sacrificial micro-electrodes (identified in green in Fig. 4.10(b)) are used.

---

<sup>‡</sup>In this case, a two stage flip-chip transfer printing process was employed, although, for simplicity sake, it is not shown in Fig. 4.10(a).

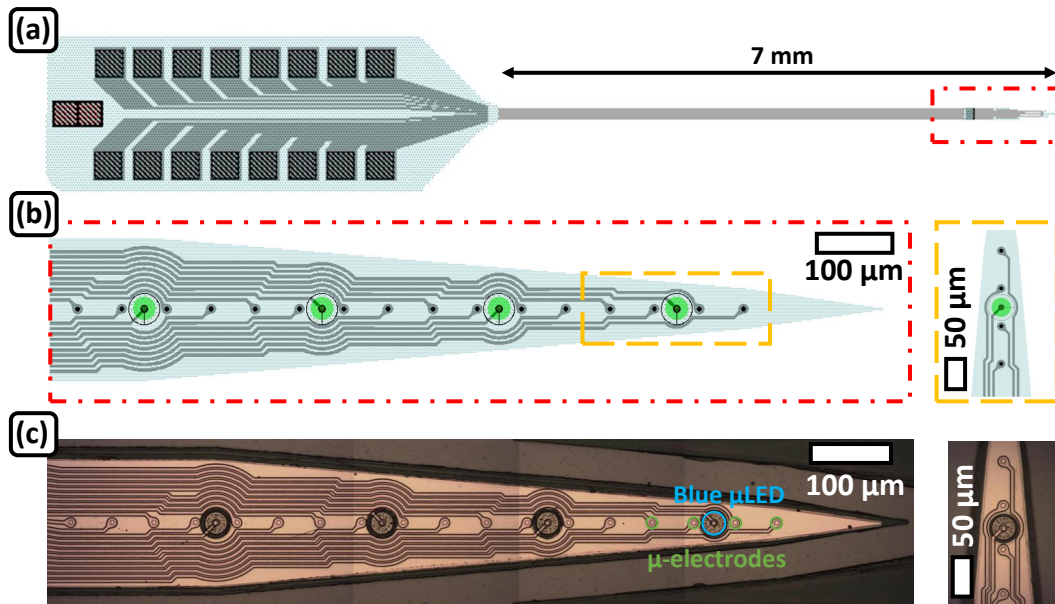


FIGURE 4.9: Schematic drawing of the (a) full optrode and (b) the tip of the shank with the micro-LEDs active area highlighted in green; (c) plan-view photograph of the shank tip with micro-LED ( $\mu$ LED) and  $\mu$ -electrodes identified in blue and green, respectively.

Following the micro-TP process and removal of the adhesion enhancement layer, a Pa-C film (thickness  $4 \mu\text{m}$ ) was deposited as insulation and encapsulation layer. This layer was patterned as a circle around the red micro-LED platelet, with vias on top of the  $p$  and  $n$  contacts. Next, Ti/Au (thicknesses 100/200 nm) metal tracks were lithographically defined, connecting the red-micro-LED  $p$  and  $n$  contacts to sacrificial micro-electrodes. Figures 4.11(a) and 4.11(b) show a  $45^\circ$  tilted SEM micrograph of the shank tip and of a pair of red and blue micro-LEDs after Pa-C encapsulation and metallisation, respectively.

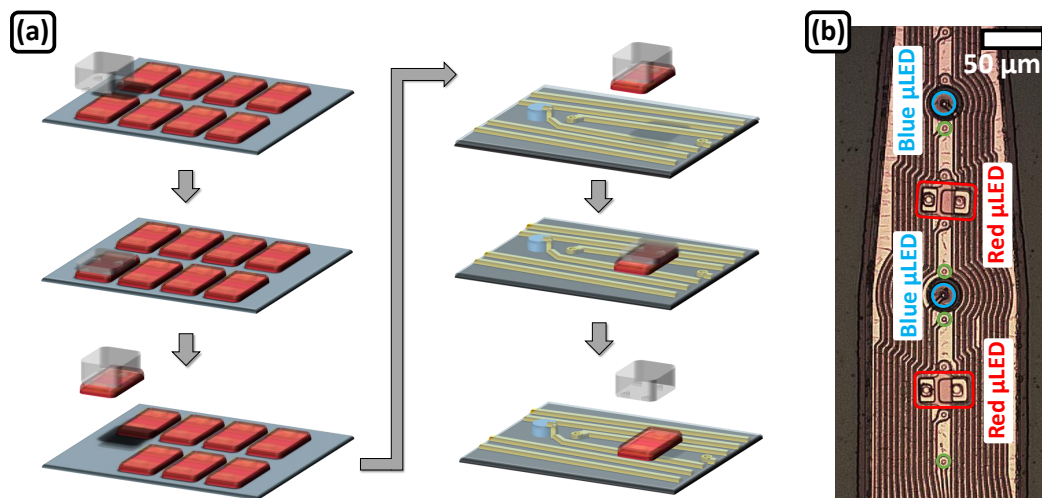


FIGURE 4.10: (a) Schematic process flow of the micro-transfer printing of a red micro-LED platelet onto an optrode (courtesy of Mr. Ruaridh Winstanley); (b) plan-view photograph of an optrode after micro-TP of the red micro-LED platelets.

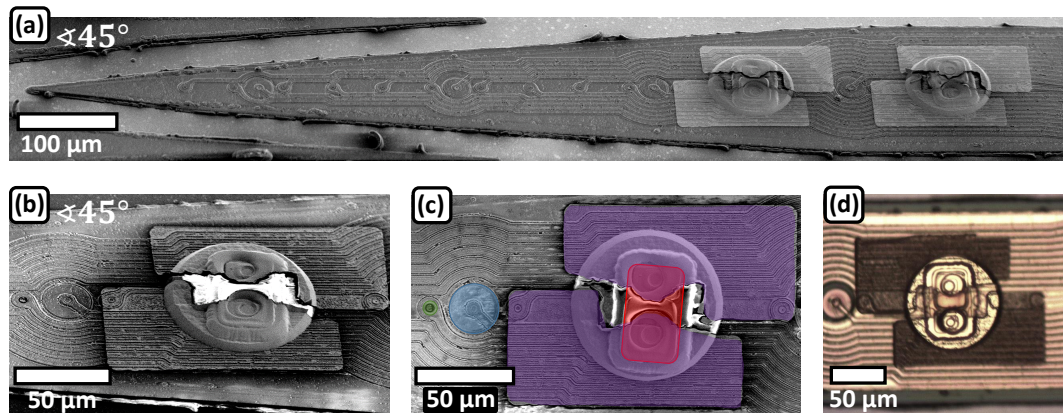


FIGURE 4.11: 45° tilted scanning electron microscopy (SEM) micrograph, after Pa-C encapsulation and metallisation, of (a) the shank tip and of (b) a red and a blue micro-LED ; (c) colourised SEM micrograph (the colours green, blue, purple and red correspond to the micro-electrode, the blue micro-LED, the metal tracks and the red micro-LED, respectively) - courtesy of Mr. Ruaridh Winstanley; (d) plan-view photograph of the red micro-LED after Pa-C encapsulation and metallisation.

For clarity's sake, Fig. 4.11(c) shows a colourised SEM micrograph of the dual-colour micro-LEDs. The red micro-LED, identified in red, is electrically connected by metal tracks, in purple, to the sacrificial micro-electrodes. The blue micro-LED, identified in blue, is also shown along with a micro-electrode, in green. Finally, Fig. 4.11(d) shows a plan-view photograph of the dual-colour micro-LED pair after Pa-C encapsulation and metallisation.

At this point, the red micro-LEDs are fully functional (as shown in the following section), while the shank is still on its growth substrate. The path towards fully free-standing optrodes involves a 50  $\mu\text{m}$  deep etching into the Si substrate, followed by thinning down of the Si substrate by mechanical polishing. However, those steps are out of the scope of this thesis and will not be described.

### 4.3.3 Electrical and optical characterisation

Figures 4.12(a) and 4.12(b) show the JV and LJ curves of the monolithic blue micro-LED and of the printed red micro-LED, respectively, alongside with a plan-view photograph of the shank tip with both micro-LEDs being driven simultaneously at 100  $\mu\text{A}$ . The measurements were performed by probing the dual-colour optrode on its Si substrate. The J-V characteristic was measured by a voltage source, through scanning each data point under direct current (DC) conditions (Yokogawa GS610). The LJ was measured using a calibrated Si photodiode detector (9 mm diameter active area, Thorlabs PM100D) placed in close proximity to the micro-LEDs topside. A Lambertian emission profile was assumed to convert the collected optical power into values quoted for the full forward



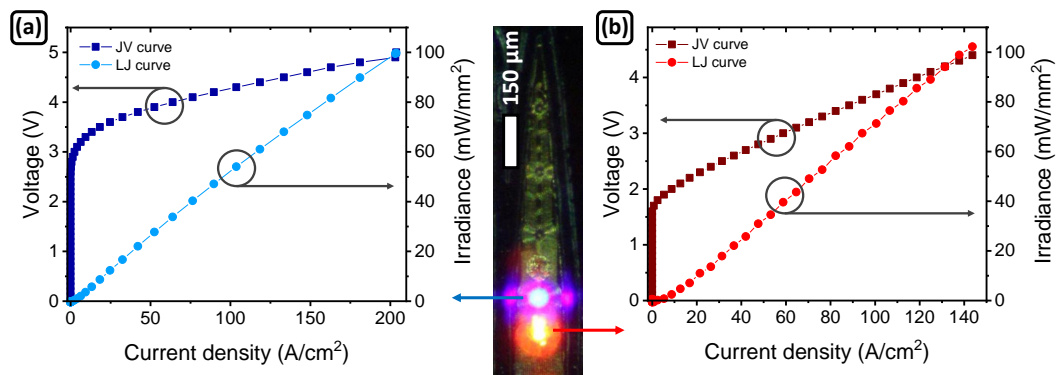


FIGURE 4.12: Voltage *vs* current density and irradiance *vs* current density curves of (a) the monolithic blue micro-LED and of (b) the transfer printed red micro-LED, respectively, alongside with a plan-view photograph of the shank tip with both micro-LEDs being driven simultaneously at 100  $\mu$ A.

hemisphere. The forward diode voltages (at 32 A/cm<sup>2</sup>) of the blue and the red micro-LEDs are 3.7 V and 2.5 V, respectively. These low forward diode voltages enable the integration of these optrodes with low-power consumption electronics, which is a crucial step towards miniaturization of these devices. In terms of optical power, both blue and red micro-LEDs achieve 100 mW/mm<sup>2</sup>, which, for the blue micro-LED, translates into an excitable volume up to  $2.5 \times 10^{-3}$  mm<sup>3</sup> (250 neurons) [27].

The monolithic blue and the micro-TP red micro-LED individual EL spectra, acquired using an optical fibre-coupled spectrometer (Avantes AvaSpec-2048L spectrometer), are shown in Fig. 4.13. The absorption spectra of the opsins ChR-2, Chrimson, and Jaws are also shown [29, 30]. These opsins were chosen as they illustrate the multifunctionality of the dual-colour optrode reported in this work. ChR-2 and Chrimson are excitatory opsins, centred at 465 and 590 nm, respectively [29]. While, Jaws is an inhibitory red-shifted opsin centred at 590 nm [30]. The blue micro-LED EL spectrum consists a broad peak centred at 450 nm, exhibiting a strong (minimal) overlap with the ChR-2 (Chrimson and Jaws) opsin absorption band. The red micro-LED EL spectrum consists of a broad peak centred at 630 nm, showing strong (marginal) overlap with the Chrimson and Jaws (ChR-2) opsin absorption band. Considering the ChR-2 and Chrimson opsins case, this means that the dual-colour optrode is capable of independent optical excitation of distinct neural populations. On the other hand and considering the case of ChR-2 and Jaws opsins, it also means that the dual-colour optrode is capable of optical excitation and inhibition of different neural populations. This is an extremely versatile optogenetics tool that can be used in cases of dual-excitation or excitation-inhibition behaviours.

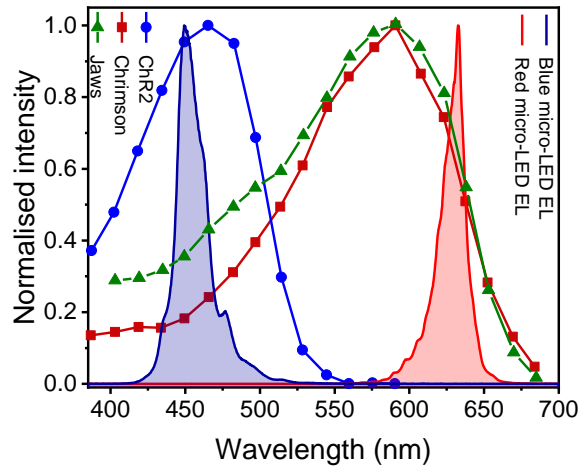


FIGURE 4.13: Monolithic blue and micro-TP red micro-LEDs individual EL spectra superimposed with ChR-2, Chrimson and Jaws opsins absorption spectra (adapted from [29, 30]).

## 4.4 Summary

In this chapter Gbps VLC based on AlGaInP micro-LEDs printed onto glass and diamond substrates was demonstrated. These devices show the highest reported VLC data rate based on red LED based illumination. In addition, a dual-colour optrode was developed by micro-TP of red AlGaInP micro-LEDs onto a GaN-based shank optrode. This dual-colour optrode has the potential to excite and/or inhibit different neural populations. The results in the first section of this chapter were published in: J.F.C. Carreira *et al.*, Optics Express 28 (8), 12149-12156 (2020).



## Bibliography

- [1] R. Horng, H. Chien, K. Chen, W. Tseng, Y. Tsai, and F. Tarntair. Development and Fabrication of AlGaInP-Based Flip-Chip Micro-LEDs. *IEEE Journal of the Electron Devices Society*, 6(1):475–479, 2018.
- [2] Ming-Chun Tseng, Chi-Lu Chen, Nan-Kai Lai, Shih-I Chen, Tzu-Chieh Hsu, Yu-Ren Peng, and Ray-Hua Horng. P-side-up thin-film AlGaInP-based light emitting diodes with direct ohmic contact of an ITO layer with a GaP window layer. *Opt. Express*, 22(S7):A1862–A1867, Dec 2014.
- [3] Th. Gessmann and E. F. Schubert. High-efficiency AlGaInP light-emitting diodes for solid-state lighting applications. *Journal of Applied Physics*, 95(5):2203–2216, 2004.
- [4] Christopher A. Bower, Matthew A. Meitl, Brook Raymond, Erich Radauscher, Ronald Cok, Salvatore Bonafede, David Gomez, Tanya Moore, Carl Prevatte, Brent Fisher, Robert Rotzoll, George A. Melnik, Alin Fecioru, and António José Trindade. Emissive displays with transfer-printed assemblies of  $8\ \mu\text{m} \times 15\ \mu\text{m}$  inorganic light-emitting diodes. *Photon. Res.*, 5(2):A23–A29, Apr 2017.
- [5] Ronald S. Cok, Matthew Meitl, Robert Rotzoll, George Melnik, Alin Fecioru, Antonio Jose Trindade, Brook Raymond, Salvatore Bonafede, David Gomez, Tanya Moore, Carl Prevatte, Erich Radauscher, Scott Goodwin, Paul Hines, and Christopher A. Bower. Inorganic light-emitting diode displays using micro-transfer printing. *Journal of the Society for Information Display*, 25(10):589–609, 2017.
- [6] R. Horng, H. Chien, F. Tarntair, and D. Wu. Fabrication and Study on Red Light Micro-LED Displays. *IEEE Journal of the Electron Devices Society*, 6:1064–1069, 2018.
- [7] Jeong-Tak Oh, Sang-Youl Lee, Yong-Tae Moon, Ji Hyung Moon, Sunwoo Park, Ki Yong Hong, Ki Young Song, Chanhyoung Oh, Jong-In Shim, Hwan-Hee Jeong, June-O Song, Hiroshi Amano, and Tae-Yeon Seong. Light output performance of red AlGaInP-based light emitting diodes with different chip geometries and structures. *Opt. Express*, 26(9):11194–11200, Apr 2018.
- [8] R. Horng, H. Chien, K. Chen, W. Tseng, Y. Tsai, and F. Tarntair. Development and Fabrication of AlGaInP-Based Flip-Chip Micro-LEDs. *IEEE Journal of the Electron Devices Society*, 6:475–479, 2018.
- [9] Sang-Il Park, Yujie Xiong, Rak-Hwan Kim, Paulius Elvikis, Matthew Meitl, Dae-Hyeong Kim, Jian Wu, Jongseung Yoon, Chang-Jae Yu, Zhuangjian Liu, Yonggang Huang, Keh-chih Hwang, Placid Ferreira, Xiuling Li, Kent Choquette, and John A. Rogers. Printed Assemblies of Inorganic Light-Emitting Diodes for Deformable and Semitransparent Displays. *Science*, 325(5943):977–981, 2009.
- [10] A. J. Trindade, B. Guilhabert, E. Y. Xie, R. Ferreira, J. J. D. McKendry, D. Zhu, N. Laurand, E. Gu, D. J. Wallis, I. M. Watson, C. J. Humphreys, and M. D. Dawson. Heterogeneous integration of gallium nitride light-emitting diodes on diamond and silica by transfer printing. *Opt. Express*, 23(7):9329–9338, Apr 2015.
- [11] Xiaoyu Lin, Duo Liu, Guanjun Lin, Qian Zhang, Naikun Gao, Dongfang Zhao, Ran Jia, Zhiyuan Zuo, and Xiangang Xu. Periodic indentation patterns fabricated on AlGaInP light emitting diodes and their effects on light extraction. *RSC Adv.*, 4:63143–63146, 2014.

- [12] Sami Franssila. *Introduction to Microfabrication*. John Wiley & Sons, Ltd, 2010.
- [13] Rich P. Mildren. *Intrinsic Optical Properties of Diamond*, chapter 1, pages 1–34. John Wiley & Sons, Ltd, 2013.
- [14] M. Z. Afgani, H. Haas, H. Elgala, and D. Knipp. Visible light communication using OFDM. In *2nd International Conference on Testbeds and Research Infrastructures for the Development of Networks and Communities, 2006. TRIDENTCOM 2006.*, pages 6 pp.–134, March 2006.
- [15] J. Armstrong and A. J. Lowery. Power efficient optical OFDM. *Electronics Letters*, 42(6):370–372, March 2006.
- [16] H. Haas, L. Yin, Y. Wang, and C. Chen. What is LiFi? *Journal of Lightwave Technology*, 34(6):1533–1544, March 2016.
- [17] R. Bian, I. Tavakkolnia, and H. Haas. 15.73 Gb/s Visible Light Communication With Off-the-Shelf LEDs. *Journal of Lightwave Technology*, 37(10):2418–2424, May 2019.
- [18] H. Chun, S. Rajbhandari, G. Faulkner, D. Tsonev, E. Xie, J. J. D. McKendry, E. Gu, M. D. Dawson, D. C. O’Brien, and H. Haas. LED Based Wavelength Division Multiplexed 10 Gb/s Visible Light Communications. *Journal of Lightwave Technology*, 34(13):3047–3052, July 2016.
- [19] E. Xie, X. He, M. S. Islim, A. A. Purwita, J. J. D. McKendry, E. Gu, H. Haas, and M. D. Dawson. High-Speed Visible Light Communication Based on a III-Nitride Series-Biased Micro-LED Array. *Journal of Lightwave Technology*, 37(4):1180–1186, Feb 2019.
- [20] S B Goncalves, J F Ribeiro, A F Silva, R M Costa, and J H Correia. Design and manufacturing challenges of optogenetic neural interfaces: a review. *Journal of Neural Engineering*, 14(4):041001, may 2017.
- [21] Alexxai V. Kravitz, Benjamin S. Freeze, Philip R. L. Parker, Kenneth Kay, Myo T. Thwin, Karl Deisseroth, and Anatol C. Kreitzer. Regulation of parkinsonian motor behaviours by optogenetic control of basal ganglia circuitry. *Nature Neuroscience*, 466:622–626, 2010.
- [22] Elizabeth E Steinberg, Daniel J Christoffel, Karl Deisseroth, and Robert C Malenka. Illuminating circuitry relevant to psychiatric disorders with optogenetics. *Current Opinion in Neurobiology*, 30:9 – 16, 2015. SI: Neuropsychiatry.
- [23] Lief Fenno, Ofer Yizhar, and Karl Deisseroth. The Development and Application of Optogenetics. *Annual Review of Neuroscience*, 34(1):389–412, 2011. PMID: 21692661.
- [24] Christina K. Kim, Avishek Adhikari, and Karl Deisseroth. Integration of optogenetics with complementary methodologies in systems neuroscience. *Nature Reviews Neuroscience*, 18:222–235, 2017.
- [25] Karl Deisseroth. Optogenetics: 10 years of microbial opsins in neuroscience. *Nature Neuroscience*, 18:1213–1225, 2015.
- [26] Karl Deisseroth. Optogenetics. *Scientific Reports*, 8:26–29, 2011.
- [27] Robert Scharf, Tomomi Tsunematsu, Niall McAlinden, Martin D. Dawson, Shuzo Sakata, and Keith Mathieson. Depth-specific optogenetic control in vivo with a scalable, high-density  $\mu$ LED neural probe. *Scientific Reports*, 6:28381, 2016.

- [28] Niall McAlinden, David Massoubre, Elliot Richardson, Erdan Gu, Shuzo Sakata, Martin D. Dawson, and Keith Mathieson. Thermal and optical characterization of micro-LED probes for in vivo optogenetic neural stimulation. *Opt. Lett.*, 38(6):992–994, Mar 2013.
- [29] Nathan C Klapoetke, Yasunobu Murata, Sung Soo Kim, Stefan R Pulver, Amanda Birdsey-Benson, Yong Ku Cho, Tania K Morimoto, Amy S Chuong, Eric J Carpenter, Zhijian Tian, Jun Wang, Yinlong Xie, Zhixiang Yan, Yong Zhang, Brian Y Chow, Barbara Surek, Michael Melkonian, Vivek Jayaraman, Martha Constantine-Paton, Gane Ka-Shu Wong, and Edward S Boyden. Independent optical excitation of distinct neural populations. *Nature Methods*, 11:338–346, 2014.
- [30] Amy S Chuong, Mitra L Miri, Volker Busskamp, Gillian A C Matthews, Leah C Acker, Andreas T Sørensen, Andrew Young, Nathan C Klapoetke, Mike A Henninger, Suhasa B Kodandaramaiah, Masaaki Ogawa, Shreshtha B Ramanlal, Rachel C Bandler, Brian D Allen, Craig R Forest, Brian Y Chow, Xue Han, Yingxi Lin, Kay M Tye, Botond Roska, Jessica A Cardin, and Edward S Boyden. Noninvasive optical inhibition with a red-shifted microbial rhodopsin. *Nature Neuroscience*, 17:1123–1129, 2014.

## Chapter 5

# Direct integration of micro-LEDs onto CMOS circuitry by micro-transfer printing

This chapter presents the direct integration of micro-LEDs onto complementary metal oxide semiconductor (CMOS) circuitry by micro-transfer printing. An 8x8 micro-LED array was realised with high brightness and bandwidth uniformity. Application of this device in an optical camera communication (OCC) link, and in on-chip data communication and time-of-flight ranging applications is presented.

### 5.1 Introduction

The integration of micro-LEDs with CMOS circuitry allows active-matrix addressing of individual micro-LEDs, dynamic video graphic imaging, and short pulse generation, just to name a few. These characteristics have led to the application of CMOS-driven micro-LED arrays in several fields, such as microdisplays (Fig 5.1(a)), VLC (Fig 5.1(b)), spatial navigation (Fig 5.1(c)), UV maskless photolithography (Fig 5.1(d)), and optoelectronic tweezing (Fig 5.1(e)). At the core of these applications is the CMOS technology, which will be described in the next section.

#### 5.1.1 Complementary metal-oxide-semiconductor background

Complementary metal oxide semiconductor (CMOS) technology employs both  $n$  and  $p$  metal oxide semiconductor field-effect transistors (MOSFET), commonly referred to

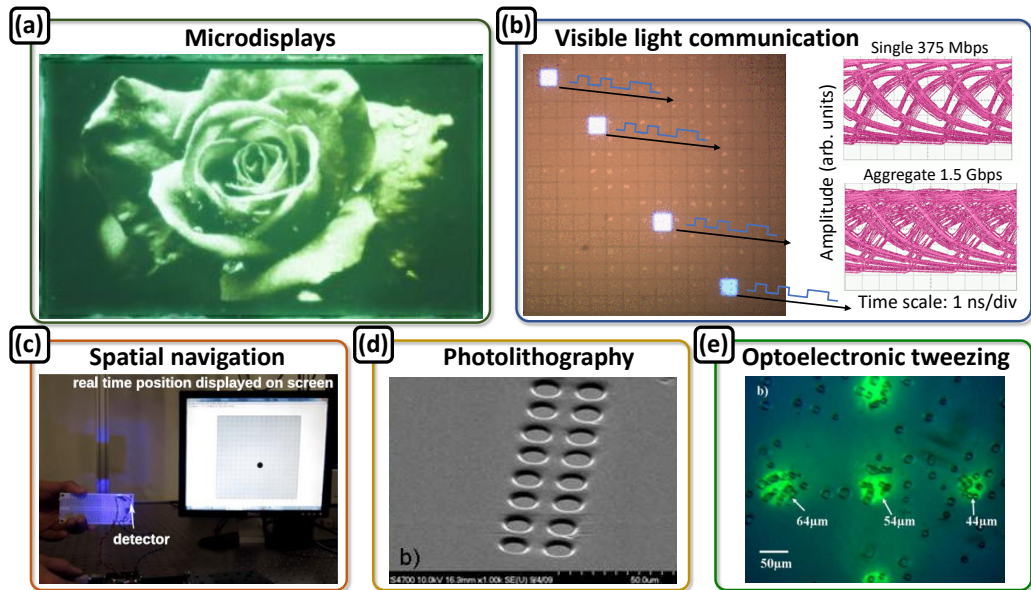


FIGURE 5.1: CMOS-driven micro-LED arrays in several applications: (a) microdisplays [1]; (b) visible light communication [2]; (c) spatial navigation [3]; (d) maskless photolithography [4]; and (e) optoelectronic tweezing [5].

as NMOS and PMOS, respectively, to form logic elements. A schematic cross-section drawing of the NMOS and PMOS are shown in Figs. 5.2(a) and 5.2(b), respectively. The NMOS is a four terminal device consisting of a  $p$ -substrate with two heavily doped  $n$ -type regions, indicated as the source and drain regions. A thin layer of  $\text{SiO}_2$ , typically 1 to 10 nm thick, is grown on top of the substrate, covering the area between the source and drain regions. Metal is deposited on top of the oxide layer, forming the gate electrode of the device. Metal contacts to the source, drain, and body are also deposited. The PMOS is similar to the NMOS, consisting instead of a  $n$ -type substrate with two heavily doped  $p$ -regions [6, 7].

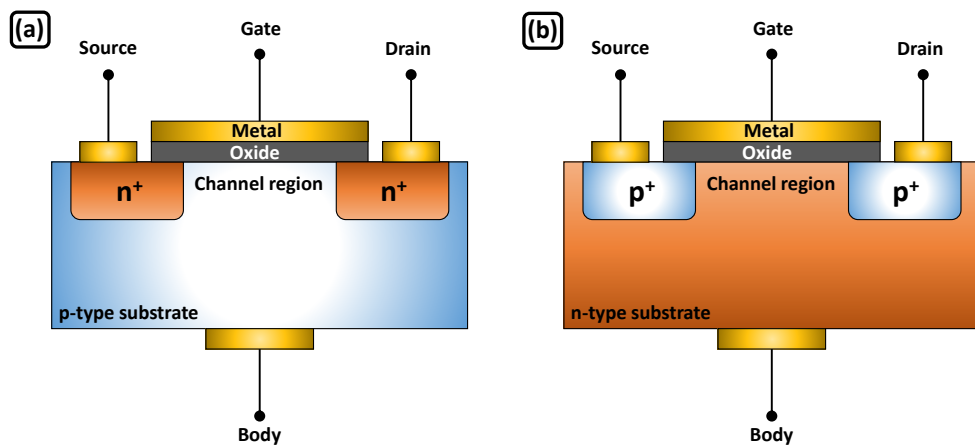


FIGURE 5.2: Schematic cross-section drawing of (a) NMOS and (b) PMOS (adapted from [6]).

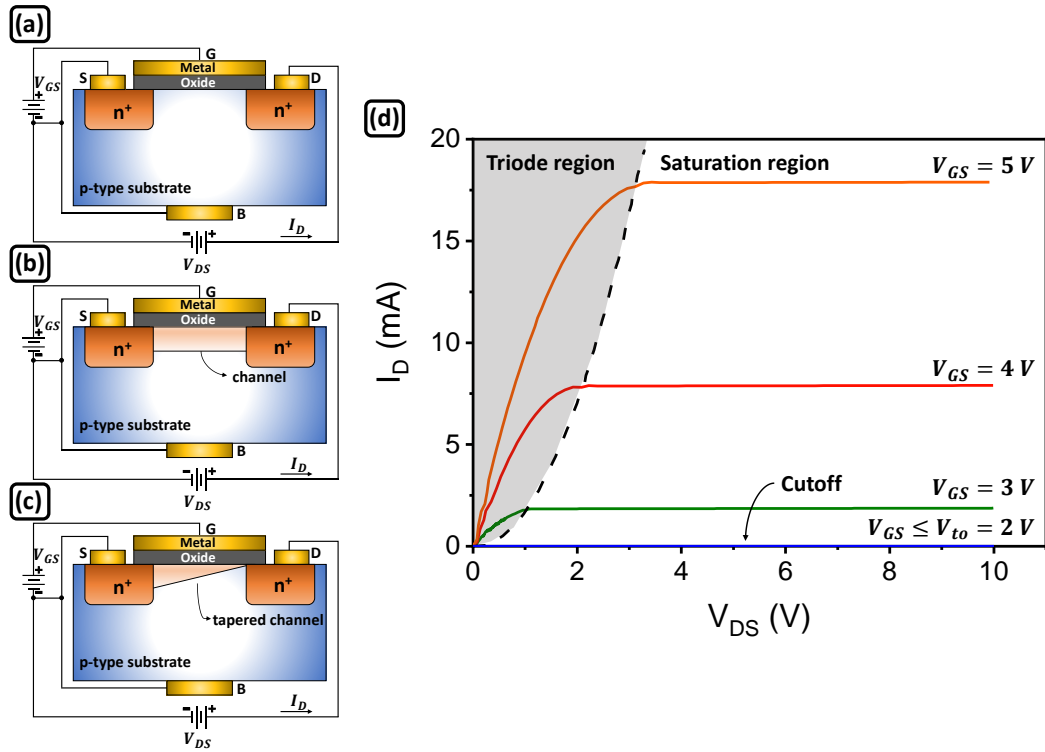


FIGURE 5.3: (a)-(c) Schematic cross-section drawing of an NMOS during cutoff, triode, and saturation regions, respectively; (d) characteristic curves for an NMOS (adapted from [8]).

Operation of a MOSFET can be divided into: cutoff, triode, and saturation regions. Figure 5.3 summarises the operation of an NMOS in these three regimes. In the cutoff case, the voltage applied to the gate is zero ( $V_{GS}=0$ ). Applying a positive voltage  $V_{DS}$  to the drain relative to the source results in a reverse biased  $pn$  junction at the drain and body interface (Fig. 5.3(a)). Thus, and while the gate voltage is lower than a particular value called threshold voltage ( $V_{to}$ ) no current flows ( $i_D=0$ ). In the triode region,  $V_{GS} > V_{to}$  and the voltage applied to drain is smaller than gate voltage minus the threshold voltage ( $V_{DS} < V_{GS} - V_{to}$ ). The electric field resulting from the applied gate voltage repels holes from the  $p$ -doped region under the gate, leaving behind a carrier-depletion region. Concurrently, also attracts free electrons from the heavily doped source and drain regions, thus creating an  $n$ -type channel between the drain and the source (Fig. 5.3(b)). As  $V_{DS}$  increases, electrons from the source flow through the created channel and into to the drain (by convention current flows from the drain to the source). As  $V_{DS}$  increases, electrons in the channel are pulled into the drain region leading to tapering of the channel thickness. For  $V_{DS} > V_{GS} - V_{to}$ , the channel depth at the drain end reduces to zero, giving rise to the term channel pinch-off (Fig. 5.3(c)). Increasing  $V_{DS}$  above this point has no effect on the channel shape and charge, and the current through the channel remains constant. The NMOS is then said to be in the saturation region. Figure 5.3(d) shows the characteristic IV curves of an NMOS at different values of  $V_{GS}$  [7, 8].

In a PMOS device the semiconductor regions are reversed in polarity to those of an NMOS. Thus the characteristics of a PMOS are very similar to those of an NMOS, except that the voltage polarities are inverted. In this case, applying a negative voltage to the PMOS gate, creates a  $p$  channel between the source and the drain. Applying a negative voltage to the drain attracts holes from the source, which flow through the channel into to the drain (current flows from source to drain). In similar fashion to the NMOS, increasing  $V_{DS}$  leads to channel pinch-off and the PMOS is said to be saturated. PMOS technology emerged before NMOS, due to difficulties in fabricating NMOS transistors, and dominated the early integrated circuit manufacturing industry. As NMOS fabrication processes evolved, this technology eventually supplanted PMOS, due to its greater gains and speeds of operation than PMOS devices. CMOS technology employs both NMOS and PMOS on the same chip, which allows for much more powerful circuit configurations and logic operations [7, 8].

### 5.1.2 CMOS logic-gate circuits

CMOS digital circuits use NMOS and PMOS transistors operating as on/off switches. This is achieved by controlling the gate voltage to operate the transistor in the triode region (*on*) or in the cutoff region (*off*). An NMOS transistor behaves as a closed switch when its gate voltage is *high*, usually at the power-supply level  $V_{DD}$ , which represents a logic 1. When the gate voltage is *low*, the transistor is cut off, acting as an open switch, which represents a logic 0. The PMOS transistor operates in a complementary fashion. The transistor is on when the gate voltage is low (logic 0), and off when the gate voltage is raised to  $V_{DD}$  (logic 1) [7]. Three of the most basic and important building blocks of digital systems are the NOT (inverter), NAND, and NOR gates, which are constructed using CMOS technology.

A logic inverter (NOT gate) inverts the logic value of its input signal, thus for a logic 0 input, the output will be a logic 1, and vice versa (Fig. 5.4(a)). It consists of an NMOS and a PMOS transistor, with the gate terminals (input terminal) and the drain terminals (output terminal) connected together (Fig. 5.4(b)). When the input voltage is high ( $V_{in}=V_{DD}$ ), that is  $X=1$ , the NMOS transistor is on, thus a conducting channel is induced between the drain and source of the NMOS transistor (closed switch). However, the PMOS transistor is off, behaving like an open switch, thus the output voltage will be zero and  $Y=0$  (Fig. 5.4(c)). When  $X=0$  ( $V_{in}=0$ ), the NMOS transistor is off and the PMOS transistor behaves as a closed circuit, connecting the output terminal to  $V_{DD}$ . Thus the output voltage is equal to  $V_{DD}$  and  $Y=1$  [7, 8].

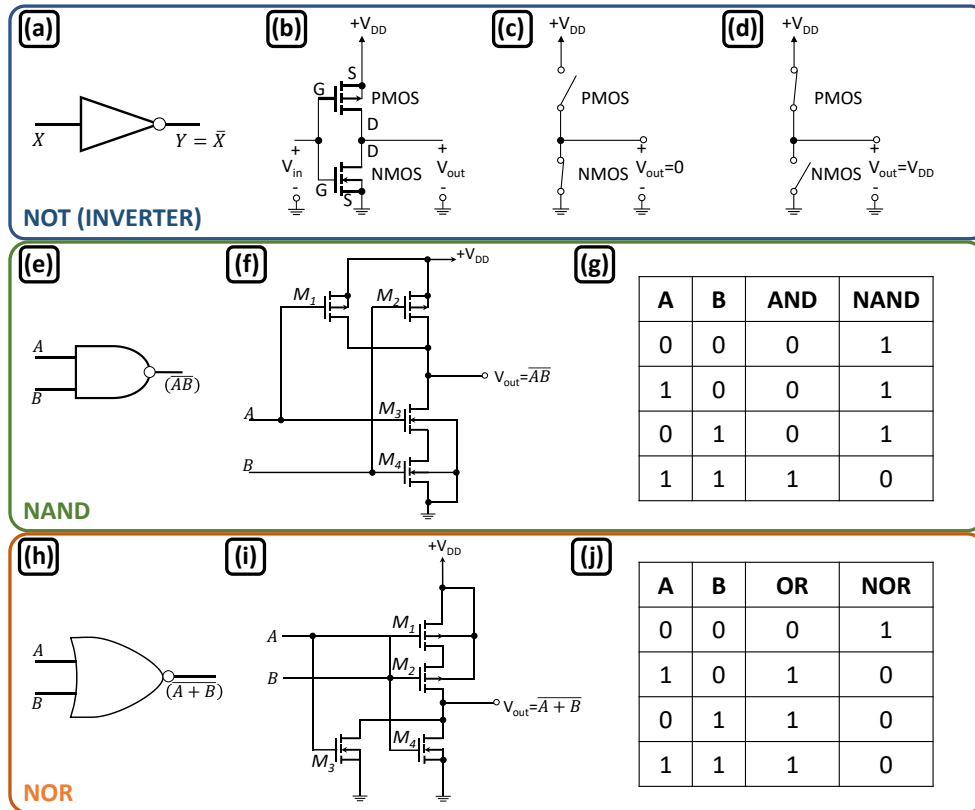


FIGURE 5.4: (a)-(d) NOT gate block representation, circuit diagram, and operation when the logic input is a logic 1 and a 0, respectively; (e)-(g) NAND gate block representation, circuit diagram, and truth table, respectively; (h)-(j) NOR gate block representation, circuit diagram, and truth table, respectively (adapted from [8]).

The two input NAND function is described by the Boolean expression  $Y = \overline{AB}$ \* (Fig. 5.4(e)). The NAND gate is constructed by adding transistors to the inverter circuit, in this case there are two PMOS transistors in parallel and two NMOS transistors in series (Fig. 5.4(f)). When the gates are high, the NMOS (PMOS) devices are on (off), and when their gates are low, the NMOS (PMOS) devices are off (on). Figure 5.4(g) shows the truth table of the NAND function, which summarises the possible outputs depending on A and B, being low (0) or being high (1) [7, 8].

The two input NOR function is described by the Boolean expression  $Y = \overline{A+B}$ † (Fig. 5.4(h)). In this case, there are two PMOS transistors in series and two NMOS transistors in parallel (Fig. 5.4(i)). Similarly to the NAND gate, when the gates are high, the NMOS (PMOS) devices are on (off), and when their gates are low, the NMOS (PMOS) devices are off (on). The truth table (Fig. 5.4(j)) shows that  $V_{out} = V_{DD}$  ( $Y = 1$ ) only when all the gates are low (NMOS transistors behave as an open switch and PMOS as a closed switch) [7, 8].

\*It can be interpreted as an AND function followed by a NOT function.

†It can be interpreted as an OR function followed by a NOT function.



These three logic circuits are the basics of integrated circuits, and as such, also the basic building blocks of the CMOS chip used in this work.

## 5.2 Device overview

### 5.2.1 Blue micro-LEDs fabrication

In this chapter, blue (450 nm) top-emitting through the *p*-GaN micro-LED platelets were fabricated from commercial InGaN LED epistuctures, grown on a silicon (Si) 111-oriented substrate, following the same processes described in Chapter 3. The only difference is that, in order to yield top-emitting micro-LED platelets, a nickel/gold (Ni/Au thicknesses 10/20 nm) bilayer was electron beam deposited, lithographically patterned, and annealed in an air environment at 510 °C defining a semitransparent *p*-GaN metal contact.

### 5.2.2 CMOS chip

The CMOS chip was developed by Prof. Robert Henderson’s CMOS Sensor and Systems group at the University of Edinburgh and implemented in a standard 0.35  $\mu\text{m}$ , 3.3 V CMOS technology by Austria Microsystems. It consists of a 16x16 array of individually-controllable 100x100  $\mu\text{m}^2$  *p*-MOS driver cells on a centre-to-centre pitch of 100  $\mu\text{m}$  [9]. The driver follows a four-metal-layer design in which the bottom two layers are used to route the CMOS transistor signals, the third layer acts as protective layer to the bottom layers towards the LED voltages, and the top layer is patterned into bonding pads to interface with the micro-LED array. Table 5.1 summarises the CMOS specifications.

The CMOS backplane driver circuit is shown in Fig. 5.5. The inputs *ROW* and *COL* are used to select the active pixels by addressing rows and columns, respectively.

TABLE 5.1: CMOS chip specifications.

Chip dimensions (mm <sup>2</sup> )	3.55x3.55
Array size	16x16
Individual driver size ( $\mu\text{m}^2$ )	100x100
Driver centre-to-centre pitch ( $\mu\text{m}$ )	100
Max. output voltage (V)	~9
Max. output current per driver (mA)	~230
Min/max electrical pulse duration (ns)	0.3/48

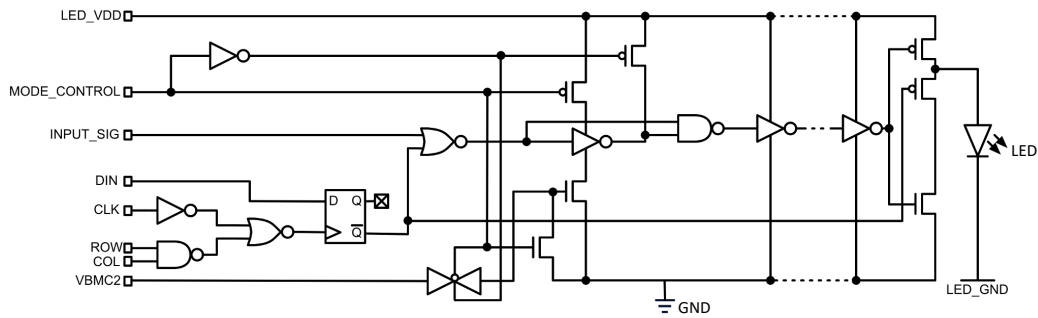


FIGURE 5.5: CMOS backplane driver circuit (reproduced from [9]).

When a certain driver is selected, the inputs *ROW* and *COL* are set high, and the output of the *D*-type flip-flop matches the driver input (*DIN*) state on the rising edge of clock signal (*CLK*). *DIN* controls if a driver is active or not, and the *D*-type flip-flop maintains its state. The output of *D*-type flip-flop is then sent to the addressed CMOS driver by setting the driver input signal (*INPUT\_SIG*) high. *INPUT\_SIG* can be sourced by a DC signal from the motherboard, an on-chip voltage-controlled oscillator (*VCO*) or an external signal. In this work, *INPUT\_SIG* was always an external signal. The state of *MODE\_CONTROL* (high or low) determines whether the output follows *INPUT\_SIG* directly (*MODE\_CONTROL* high), as previously described, or in pulsed mode (*MODE\_CONTROL* low). In the pulsed mode, *INPUT\_SIG* is sent through an inverter to introduce a time delay, which is controlled by an external voltage *VBCM2*. As also shown in Fig. 5.5 the ground terminal of the main CMOS logic circuit (*GND*) is physically separated from the LED ground (*LED\_GND*). This allows one to increase the value of *LED\_VDD* above 3.3 V without damaging the CMOS electronics by negative biasing *LED\_GND* with respect to *GND*.

### 5.2.2.1 Heterogeneous integration by flip-chip bonding

This chip was custom designed to be integrated with on-sapphire 16x16 micro-LED arrays by conventional gold bump flip-chip bonding. A schematic drawing of the flip-chip bonding process is shown in Figs. 5.6(a)-5.6(c). Gold bumps are deposited onto the CMOS chip. Next, the micro-LED array is held above the CMOS chip and aligned with the CMOS array. Finally, thermo-sonic bonding is used to partially melt the Au bumps and make physical and electrical connection between the CMOS and the micro-LEDs. However, flip-chip integration can result in issues with uniformity in the emission from large arrays due to the bump bonding process (Fig. 5.6(d) [10]), and multiple reflection paths within the thick sapphire substrate can lead to cross-talk between pixels (Figs. 5.6(e) and 5.6(f)). Furthermore, flip-chip bonding is not suitable in cases where the device emission, or detection, wavelength is absorbed by the flipped substrate.

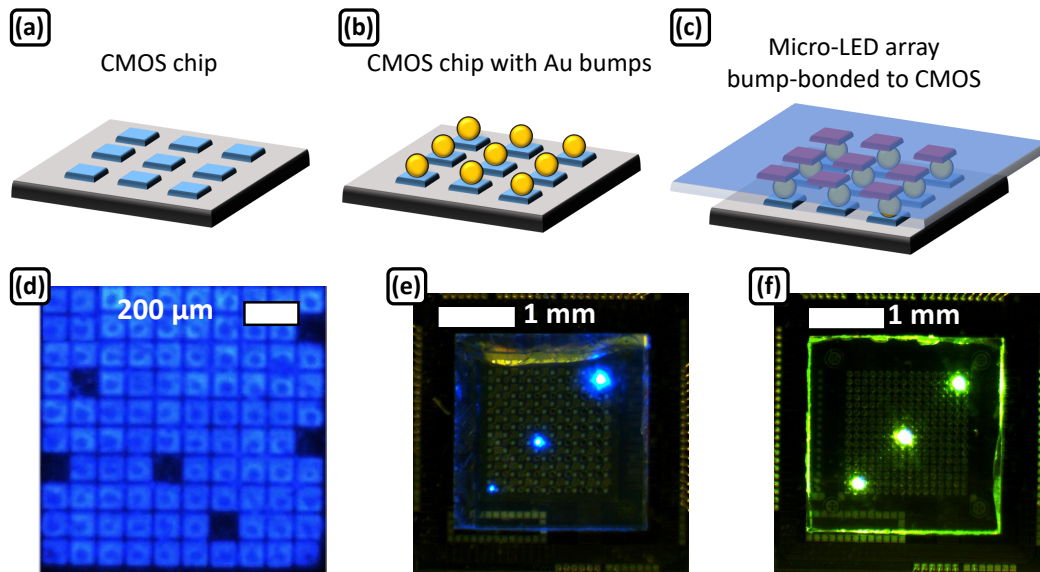


FIGURE 5.6: (a)-(c) Schematic drawing of the flip-chip bonding process; (d) micro-LED array flip-chip bump-bonded to a CMOS showing a few defects (reproduced from [10]); (e) blue and (f) green micro-LED arrays flip-chip bump-bonded to a CMOS showing light waveguiding in the sapphire substrate.

### 5.2.3 Heterogeneous integration by micro-transfer printing

An alternative integration technique is micro-transfer printing (micro-TP or  $\mu$ TP). This technique allows the population of the host substrate with devices only where required, removing issues associated with a flip-chipped substrate. A preliminary 1x8 array micro-LED device was realised following the methods described in Chapter 3, however, it was found that during the Parylene-C (Pa-C) etching process the CMOS chip electrical properties deteriorate, rendering it nonfunctional. This led to a detailed investigation of the CMOS chip properties before and after etching and the development of a microfabrication process to etch Pa-C without damaging the CMOS drivers and bonding pads.

#### 5.2.3.1 Pre-processing of the CMOS chip

Optical photographs of the CMOS bare chip and drivers, before any processing, are shown in Figs. 5.7(a)-5.7(c). Figure 5.7(d) shows the voltage *vs* current curves of the *LED\_VDD* to *LED\_VDD* (green curve) and *BU\_MOD\_CONT* to *BU\_COL\_SEL* (red curve) bonding pads of the CMOS chip (see Fig. 5.7(a)). The IV curves were acquired by direct micro-probing of the bonding pads using a probe station Wentworth 280X. *LED\_VDD* and *BU\_MOD* were chosen due their characteristic IV curves, which allow for a non-destructive inspection of the CMOS chip electrical properties at different stages of the process.

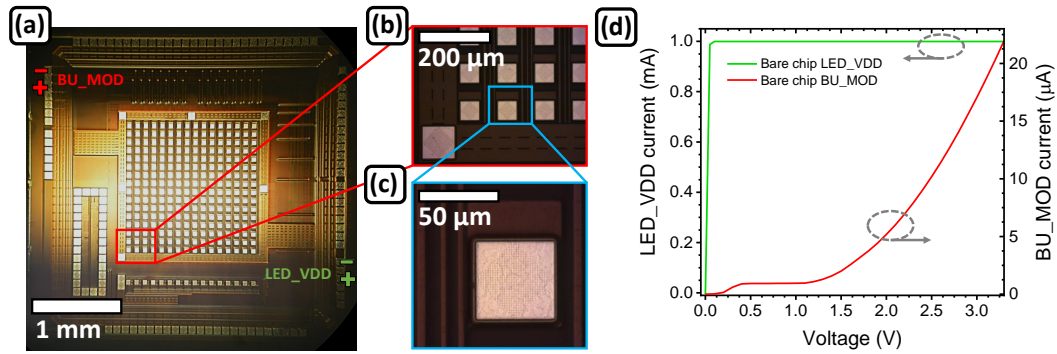


FIGURE 5.7: (a)-(c) Optical photographs of the CMOS bare chip and drivers, before any processing, at different magnifications; (d) voltage *vs* current curves of the *LED\_VDD* to *LED\_VDD* (green curve) and *BU\_MOD-CONT* to *BU\_COL\_SEL* (red curve) bonding pads before any process.

Figures 5.8(a) and 5.8(b) show optical photographs of the CMOS chip after oxygen etching of the Pa-C insulation layer. The different colour of the bonding pads might suggest that the Pa-C was not fully etched. However, a 17% overetch was applied to guarantee that the polymer was completely etched. In addition, a transfer printed micro-LED could be driven by directly probing the micro-LED through the Pa-C vias, as small as  $15 \times 15 \mu\text{m}^2$  (Fig 5.8(c)), which further suggests that the Pa-C layer was efficiently removed in the oxygen plasma. Inspection of the electrical properties of the CMOS bonding pads reveal that no current flows up to 3.3 V (Fig. 5.8(d)). This explains why the micro-LEDs could be electrical driven by external probes but not by the CMOS.

Analysis by energy-dispersive X-ray spectroscopy<sup>‡</sup> (EDS or EDXS) of the CMOS bonding pads and drivers (SEM micrograph shown in Fig. 5.8(e)) revealed that the top metallisation layer consists mainly of aluminium<sup>§</sup> (Fig. 5.8(f)). Aluminium is well-known to be etched in chlorine-based plasma chemistries [12]. Taking into account that the Pa-C molecule consists of benzene rings with a chlorine atom and that its etching mechanism is not fully understood, it is plausible to suggest that Pa-C etching byproducts might attack the aluminium layer, deteriorating the CMOS drivers and bonding pads electrical properties.

<sup>‡</sup>EDS acquired using the same tungsten low-vacuum JEOL JSM-IT100 InTouchScope SEM system.

<sup>§</sup>Aluminium alloys are commonly used as a metallisation layers on CMOS foundries due to their high conductivity and good ohmic contact with polysilicon [11].

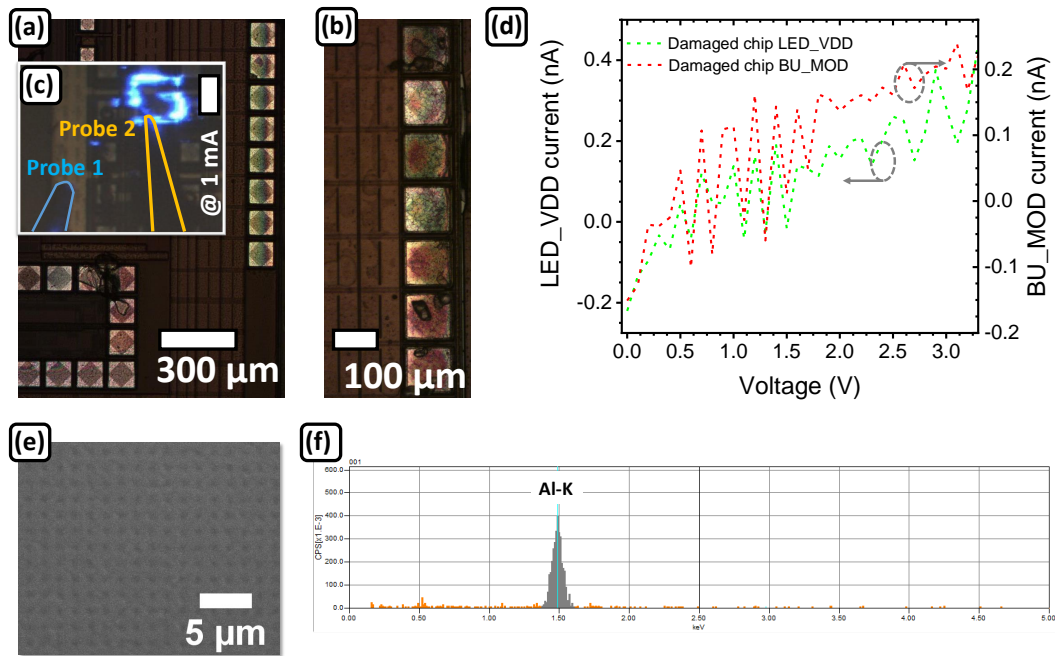


FIGURE 5.8: (a) and (b) optical images of the CMOS chip bonding pads after oxygen etching of the Pa-C layer; (c) optical image of a transfer printed micro-LED, after Pa-C etching, being electrical driven by external probes - scale bar corresponds to 100 μm; (d) current *vs* voltage curves of the *LED\_VDD* to *LED\_VDD* (green curve) and *BU\_MOD\_CONT* to *BU\_COL\_SEL* (red curve) bonding pads after Pa-C etching; (e) scanning electron microscopy micrograph of a CMOS driver and (f) correspondent energy-dispersive X-ray spectroscopy spectrum.

In order to prevent exposure of the aluminium CMOS top layers to the Pa-C etching byproducts a Ti/Au bilayer (100/200 nm thicknesses) was patterned on top of the CMOS drivers and bonding pads. Figure 5.9(a) shows a plan-view photograph of the CMOS chip after patterning of the Ti/Au bilayer on top of the bonding pads and *n*- and *p*-drivers (identified in yellow) before transfer printing and Pa-C etching. Figure 5.9(b) shows a plan-view photograph of the CMOS chip after transfer printing of the micro-LEDs and Pa-C etching. It can be observed that the etching of vias on the Pa-C layer to access the *p*-drivers stops at the Ti/Au protective layer. In this case, no change in colour after the etching process is observed. Figure 5.9(c) shows the *LED\_VDD* and *BU\_MOD\_CONT* IV curves of the bare chip and after Pa-C etching of the Ti/Au protected drivers. Protecting the CMOS drivers and bonding pads allows to retain the same electrical characteristics of the CMOS chip. This pre-processing of the CMOS proved to be crucial for the development of the micro-TP enabled micro-LED CMOS device shown in this chapter.

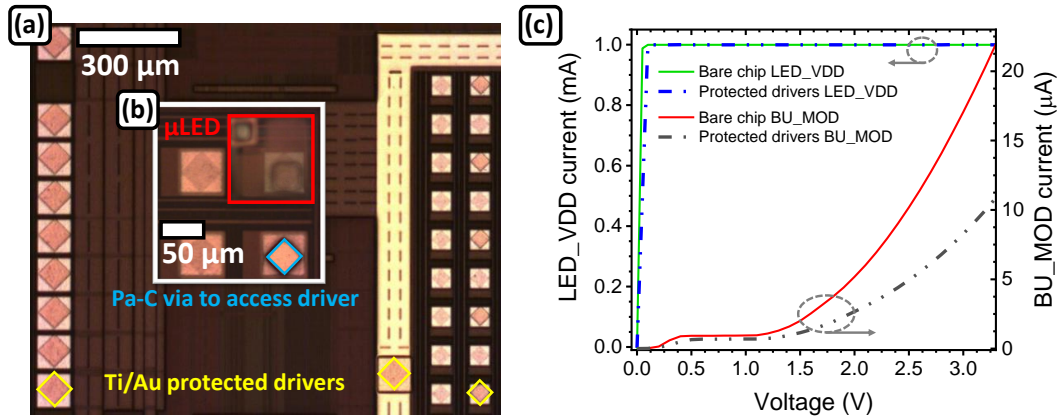


FIGURE 5.9: (a) Plan-view photograph of the CMOS bonding pads and drivers after the Ti/Au patterning step and before the Pa-C etching; (b) plan-view photograph of the CMOS driver after Pa-C etching; (c)  $LED\_VDD$  and  $BU\_MOD\_CONT$  IV curves of the bare chip (in solid) and after Pa-C etching the CMOS chip with protected drivers (in dash).

### 5.2.3.2 Micro-TP of an 8x8 micro-LED array onto a pre-processed CMOS chip

After protecting the CMOS drivers and bonding pads, an 8x8 array of micro-LEDs was sequentially transfer printed directly, without any adhesion enhancement layer, onto the CMOS drivers. An elastomeric polydimethylsiloxane (PDMS) stamp, with pyramidal protrusions, was used to pick-up the suspended micro-LED platelets from their Si substrate (Fig. 5.10(a)) and print them onto every other CMOS drivers (Fig. 5.10(b)) [13]. Since the micro-LED mesa is the same size as the CMOS driver and the micro-LED backside is non-conductive, the adjacent CMOS driver was used to address each respective micro-LED. For this purpose, after micro-TP of the micro-LEDs, a Pa-c layer (thickness 4.5 μm) was deposited and apertures on the micro-LED contacts and CMOS drivers were lithographically defined. Next, Ti/Au (thicknesses 100/200 nm) metal tracks were lithographically defined, connecting the p-MOS driver to the micro-LED  $p$ -contact and the micro-LED  $n$ -contact to the common LED ground.

Figure 5.10(c) shows a schematic cross-section view of the micro-LED directly printed onto the CMOS. Figure 5.10(d) shows an optical image of the finalised device. In addition to the 16x16 main array of driver pixels, the CMOS chip also contains a single free running single photon avalanche diode (SPAD). As described earlier, the SPAD is an avalanche photodiode operating in Geiger mode, providing digital pulses on the detection of a single photon [14]. The potential is therefore available for a single chip, with suitable optical bonded devices, to act as both an optical transmitter and receiver. Figure 5.10(e) shows in further detail the monolithic SPAD, while Figs. 5.10(f) and



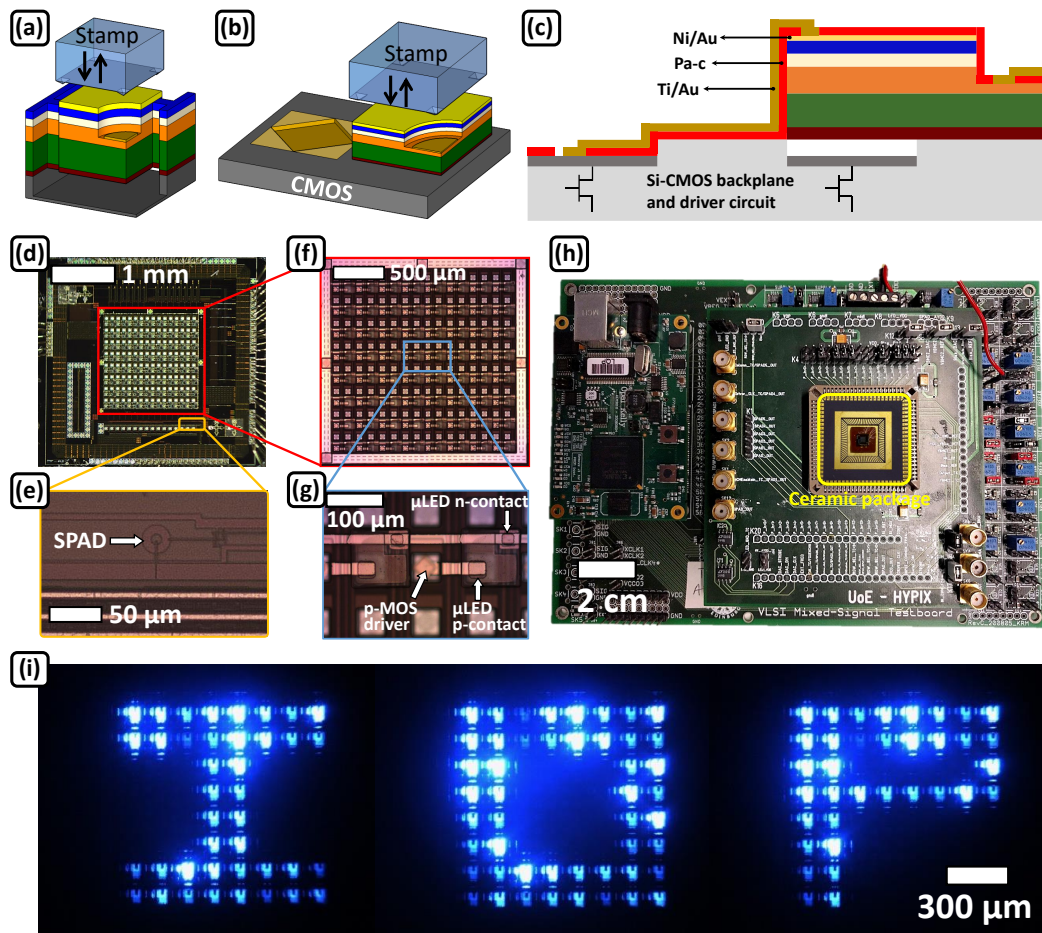


FIGURE 5.10: Schematic drawing of the micro-transfer printing process during (a) pick-up and (b) printing of the micro-LED platelet; (c) schematic cross-section drawing of the finalised device; (d) optical image of the CMOS chip with the CMOS drivers array and SPAD identified in red and yellow, respectively; (e) magnification showing in further detail the SPAD active area; (f) magnification of the CMOS chip showing the 8x8 array of transfer printed micro-LEDs; (g) shows, in further detail, the micro-LED *p*-GaN electrical connection through the adjacent *p*-MOS driver; (h) plan-view photograph of the motherboard used to interface with the CMOS chip; (i) plan-view photograph of the CMOS driven micro-LED array displaying the Institute of Photonics (IOP) logo.

5.10(g) show the full micro-LED array and the micro-LED electrical connecting scheme through the adjacent *p*-MOS driver, respectively.

The CMOS chip was then wire-bonded to a ceramic package (CCJ08428) and integrated with a custom designed motherboard controlled by a field programmable gate array (FPGA - Opal Kelly XEM3010), as shown in Fig. 5.10(h). The FPGA establishes a connection between the motherboard and a PC, providing not only power, but also controlling the logic signals through a graphical user interface (GUI) or Matlab™. The logic signals are transferred to the CMOS device by a daughtercard, which houses an SMA connector for the *INPUT\_SIG*. Figure 5.10(i) shows a plan-view photograph of the

CMOS-driven micro-LED array displaying the Institute of Photonics (IOP) logo<sup>¶</sup>.

### 5.3 Single micro-LED and full array performance

#### 5.3.1 Single micro-LED electrical, optical, and bandwidth performance

Figure 5.11 shows the voltage *vs* current density, JV, and optical power density *vs* current density, LJ, characteristics of a representative micro-LED in the 8x8 CMOS-driven array. The inset in Fig. 5.11 presents the electroluminescence (EL) spectrum acquired at 22.2 A/cm<sup>2</sup>. The JV characteristic was measured by a voltage source, through scanning each data point under direct current (DC) conditions (Yokogawa GS610). The LJ was measured using a calibrated Si photodiode detector (9 mm diameter active area, Thorlabs PM100D) placed in close proximity (5 mm) to the micro-LED topside. A Lambertian emission profile was assumed to convert the collected optical power into values quoted for the full forward hemisphere. The EL spectrum was acquired using an optical fibre-coupled spectrometer (Avantes AvaSpec-2048L spectrometer). The forward diode voltage of commercial LED's (250x250  $\mu\text{m}^2$  size) is usually defined at 20 mA, corresponding to a current density of 32 A/cm<sup>2</sup> [15]. At this current density the CMOS-driven micro-LED, reported in this work, exhibits a forward voltage of 3.65 V. The micro-LED presents an optical power density of 11 W/cm<sup>2</sup>, at 161 A/cm<sup>2</sup>, which translates into a brightness of 7.79x10<sup>5</sup> cd/m<sup>2</sup>. The EL spectrum is composed of one major peak centred

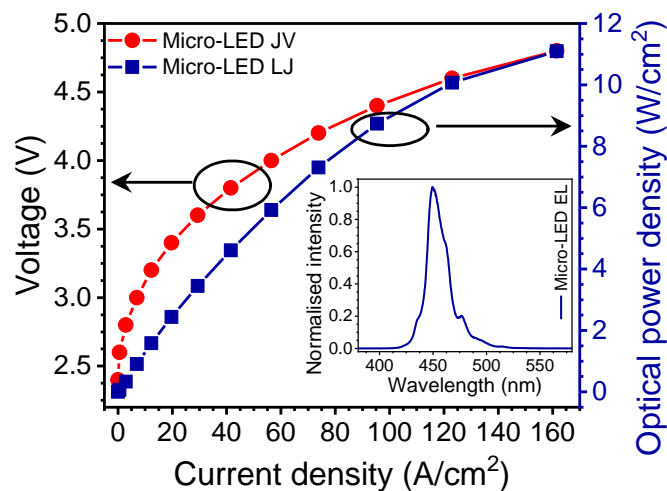


FIGURE 5.11: CMOS-driven micro-LED voltage *vs* current density (JV) curve, optical power density *vs* current density (LJ) curve, and electroluminescence spectrum (EL).

<sup>¶</sup>It must be noted that the non-uniformity seen is due to the imaging conditions.



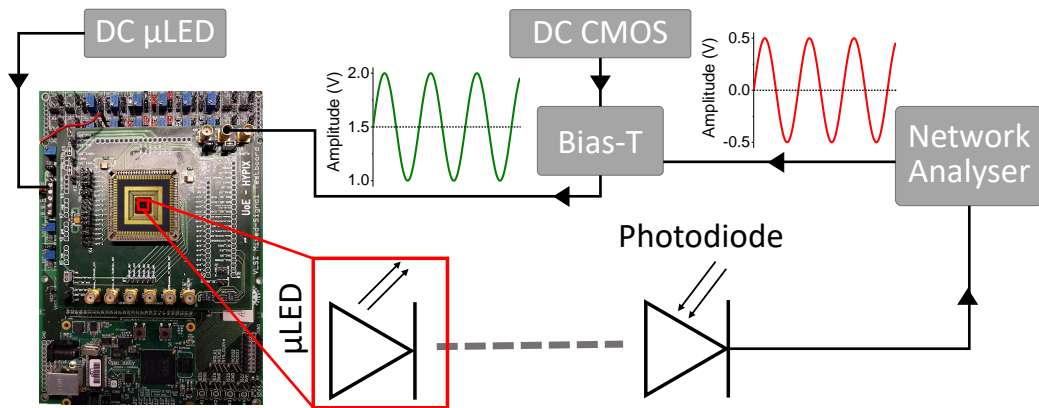


FIGURE 5.12: Schematic drawing of the experimental setup of electrical-to-optical modulation bandwidth measurement.

at 450 nm and broadened by Fabry-Perot interference occurring due to high refractive index contrast between the GaN epilayers and air [16].

The electrical-to-optical (E-O) modulation bandwidth of the CMOS-driven micro-LED was measured using a network analyser (HP8753ES) and a Si avalanche photodetector (Thorlabs — APD430A2/M bandwidth 400 MHz). A schematic drawing of the experimental setup is shown in Fig. 5.12. As the CMOS driver is a digital device, 1 V peak-to-peak output from the network analyser was combined with a DC offset (1.5 V) to reach the logic threshold of the electronics and then sent to the CMOS driver board through an SMA connector to modulate the corresponding micro-LED. This results in a square wave driving signal for the micro-LED, modulating between 0 V and an adjustable micro-LED bias voltage. The optical output of the micro-LED was then lens-focused onto the detector and the electrical output of the detector was fed back to the network analyser.

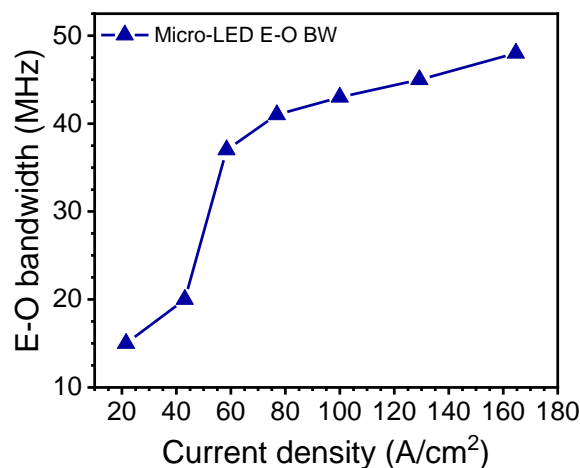


FIGURE 5.13: CMOS-driven micro-LED electrical-to-optical (E-O) modulation bandwidth vs current density.

The modulation bandwidth of the CMOS-driven micro-LED, at different current densities, is shown in Fig. 5.13. The CMOS-driven micro-LED exhibits a modulation bandwidth of 48 MHz at  $165 \text{ A/cm}^2$ , which is lower than the E-O bandwidth of the L-shaped pixel micro-LED shown in Chapter 3. This is attributed to the high modulation depth of the CMOS driver output [2].

### 5.3.2 Micro-LED array performance

The micro-LED yield and uniformity of electrical/optical characteristics across the full array are important factors for applications. The micro-transfer printing enabled hybridization process exhibits a 100% yield, with 64 out of 64 operational micro-LEDs. No electrical crosstalk has been observed showing a suitable insulation and electrical contact scheme. In addition, as each micro-LED is a singulated device, no optical crosstalk between neighbouring micro-LEDs has been observed.

Figures 5.14(a) and 5.14(b) show a “heat map” distribution of the forward voltage (defined at  $32 \text{ A/cm}^2$ ) and optical power density at  $60 \text{ A/cm}^2$  across the full array, respectively. The mean and standard deviation values for the forward voltage and power density are  $3.9 \pm 0.3 \text{ V}$  and  $6 \pm 1 \text{ W/cm}^2$ , respectively. The most erratic values originate from column 1 row 6 and column 1 row 7, which exhibit some electrical leakage behaviour. Similar electrical leakage behaviour has also been observed on micro-LEDs printed onto a glass substrate [17]. It has been suggested that this is due to damage to the device sidewalls occurring when the Si substrate is removed, leaving a rough surface and increasing opportunities for tunneling. This can be further investigated by

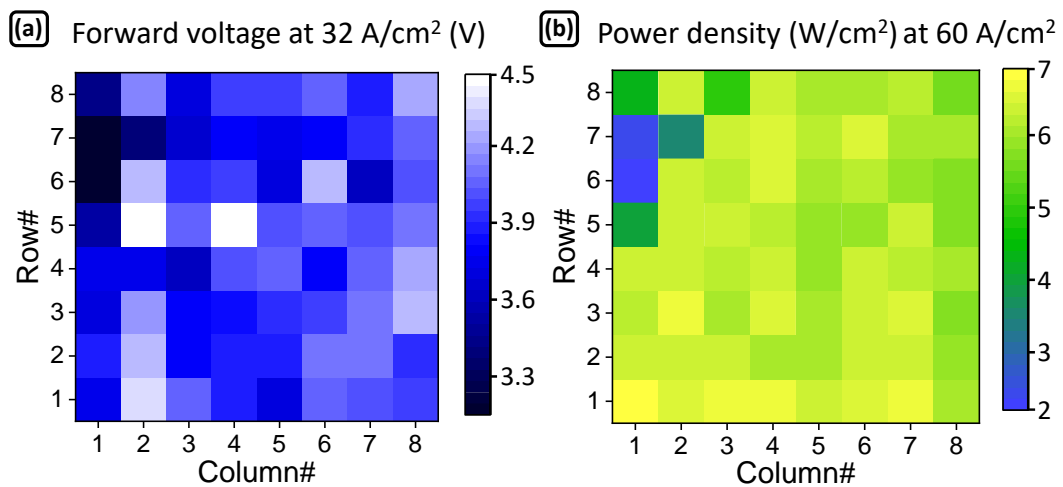


FIGURE 5.14: “Heat map” distribution of (a) forward voltage and (b) optical power density at  $60 \text{ A/cm}^2$  across the full array.

topographic and conductive atomic force microscopy and scanning Kelvin probe microscopy [18]. Nevertheless, these pixels are fully operational and can be used in practical applications as detailed in the following results. In addition, the bandwidth of 5 randomly selected CMOS-driven micro-LEDs at 4.6 V forward bias was found to be of high uniformity:  $44.8 \pm 0.5$  MHz.

## 5.4 OCC application

Optical camera communication (OCC) is a particular thread of VLC, in which image sensors (e.g. smartphone cameras, automotive cameras) are used as receivers [19, 20]. The development of high-speed and high-resolution CMOS cameras and their implementation in smartphones has opened the doors towards ubiquitous user-friendly pocket-sized OCC receivers. Unlike conventional photodetectors, as cameras are capable of spatial resolution, the data rates can be readily increased by employing spatial modulation schemes, such as multiple-input-multiple-output (MIMO). MIMO camera communication is based on a LED array ( $M \times N$ ) or a display board for the transmission of data and a camera image sensor for the reception of data (Fig. 5.15). Each light emitter of the array/display can be seen as an independent VLC transmitter. The emitted light is detected by individual pixels across the image sensor. Each activated pixel generates a voltage proportional to the number of photons that impinge on it. At the same time, each pixel is connected to an external circuit, which converts the pixel voltage into binary data [21].

In this work, an OCC link using spatio-temporal modulation of the full CMOS-driven micro-LED array and an ultrafast camera receiver<sup>‡</sup> (Photron Fastcam UX100 [22]) is demonstrated. This has previously been demonstrated with a flip-chip bonded array and a smartphone camera receiver in reference [23], however uniformity issues and

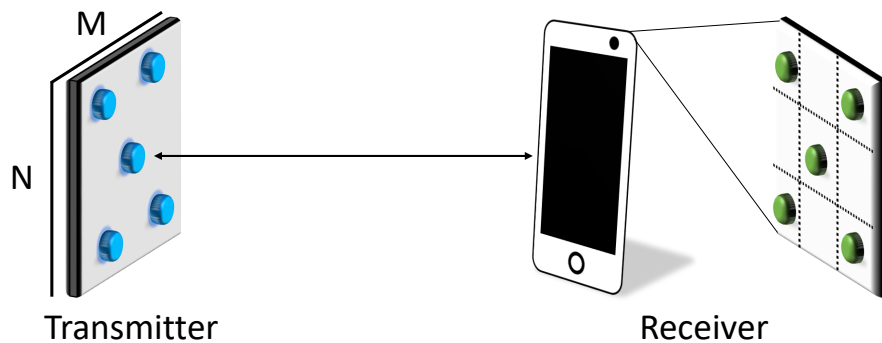


FIGURE 5.15: Multiple-input-multiple-output (MIMO) optical camera communication link (adapted from [19]).

<sup>‡</sup>As we wish to assess the upper modulation limits of the CMOS-driven micro-LED device.

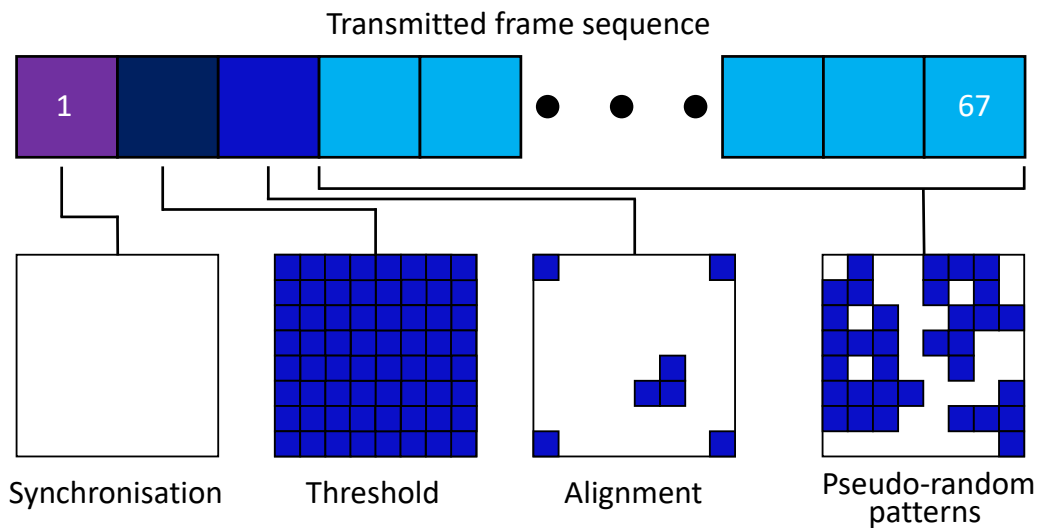


FIGURE 5.16: The block of frames transmitted for synchronisation, threshold, alignment, and data transmission.

faulty pixels in the array were a significant cause of errors in transmission in that case. In addition, the smartphone camera maximum frame rate acquisition of 960 fps limited the achievable data rate. With the transfer printed device, yield and uniformity are significantly improved. Furthermore, as the ultrafast camera receiver has a much higher maximum frame rate than the smartphone camera better results are expected.

For the OCC demonstration the CMOS-driven micro-LED array was DC biased at 4.6 V (average total current of 12.5 mA) producing an average total optical power of 2.77 mW. The patterns were updated at a rate of 2 kHz, being only limited by the full-array refresh rate of the CMOS electronics [3]. Thus each micro-LED pixel is transmitting independent binary data at 2 kHz, resulting in a net data rate of  $2000 \times 8 \times 8 = 128$  kbps. 4 blocks of 67 frames (a total of 268 frames) are transmitted with an overhead of 4.48% (3 frames in every 67) for synchronisation, and determining thresholds and alignment (Fig. 5.16). This overhead can be reduced, depending on the number of data frames per transmitted block. A pseudorandom sequence of  $2^{14}$  useful bits were transmitted in order to measure a bit-error-ratio (BER). The emitted light was lens-focused (Nikon Plan Fluor 4x/0.13) onto the ultrafast camera. The camera acquisition parameters were set at 8000 frames per second (fps), resolution of 1280x616, and a total acquisition time of 302 ms. Figure 5.17(a) shows the BER as a function of the received power by the camera. The received power was changed by placing different neutral density filters at the receiver. The BER floor of  $6.10 \times 10^{-5}$  ( $1/2^{14}$ ) occurs as  $2^{14}$  total bits were transmitted, so a lower BER cannot be measured.

For optical power values lower than  $0.02 \mu\text{W}$  the BER is larger than the  $3.8 \times 10^{-3}$  limit for forward error correction (FEC) coding [24]. Example image frames for the full

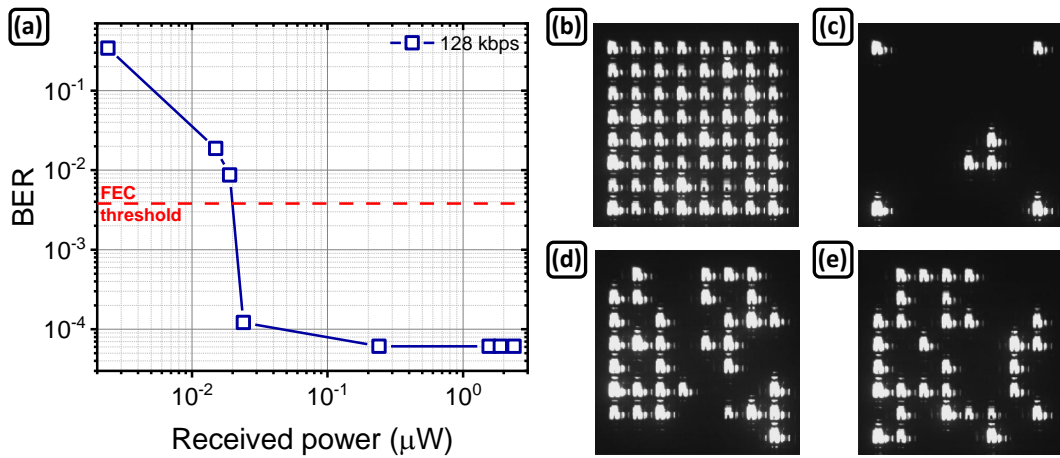


FIGURE 5.17: (a) Bit-error-ratio (BER) measured as a function of received power by the ultrafast camera; (b)-(e) show the captured frames from the 8000 fps video for all active micro-LEDs, alignment conditions, and two different pseudo-random patterns, respectively.

array, alignment frame and two example data frames are shown in Figs. 5.17(b)-5.17(e), respectively.

## 5.5 On-chip single micro-LED/SPAD operation

The multifunctional capability of the CMOS-driven integrated emitter and receiver has been demonstrated by its application as an optical communication transceiver and time-of-flight (ToF) ranging device. A single DC biased micro-LED pixel was used for both experiments. It was experimentally verified that the on-chip crosstalk between the micro-LED and SPAD is insignificant, and therefore it is impossible to establish a direct detection link without additional optics. Thus, the micro-LED (identified in red - Fig. 5.18(a)) light was lens-collected, back reflected, and focused onto the SPAD (identified in yellow)

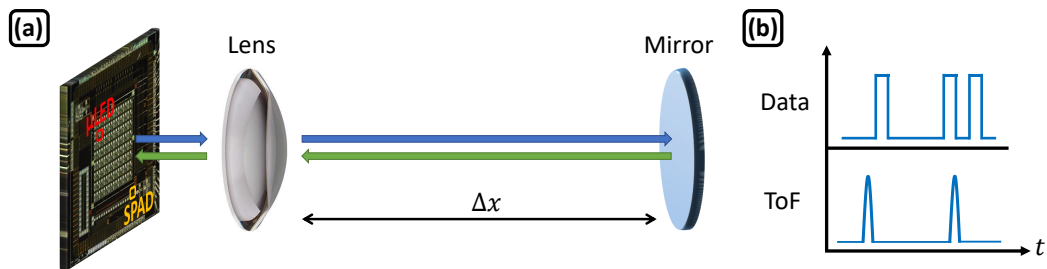


FIGURE 5.18: (a) Schematic drawing of the experimental setup used in VLC ( $\Delta x \sim 2$  cm) and ToF ranging ( $\Delta x = 0:0.2:1.2$  m) demonstrations; (b) schematic drawing of the input electrical signal for the VLC and ToF experiments.

- Fig. 5.18(a)). This setup provides an estimation of the device performance as an integrated transceiver. Figure 5.18(b) shows a schematic drawing of the input electrical signal for the VLC and ToF ranging experiments.

### 5.5.1 SPAD working principles

SPADs are  $pn$  junctions reverse biased at a voltage ( $V_A$ ) above the diode breakdown voltage ( $V_b$ ), the so-called Geiger mode. This mode of operation enables detection of single photons, when the diode is equipped with the means to detect and regenerate the current associated with photon detection. At  $V_A$ , the electric field is so high ( $>3 \times 10^5$  V/cm) that a photo-generated carrier in the depletion region can trigger a diverging avalanche multiplication of carriers by impact ionisation (Fig. 5.19(a)). This effect generates several hundreds of thousands of secondary electron-hole pairs, thus causing the diode's depletion capacitance to be rapidly discharged. As a result, a sharp current pulse is generated\*\*. Current continues to flow until the avalanche is quenched, by lowering the bias voltage down to or below  $V_b$ . Once the avalanche has been quenched, the SPAD needs to be recharged to the bias voltage so it can detect subsequent photons. The time required to quench the avalanche and recharge the diode up to 90% of its nominal excess bias is defined as the dead time. The probability of detecting a photon hitting the SPAD's surface, known as the photon detection probability (PDP), depends on the quantum efficiency and the probability of an electron or hole to trigger an avalanche [14, 25, 26]. Table 5.2 summarises the SPAD specifications.

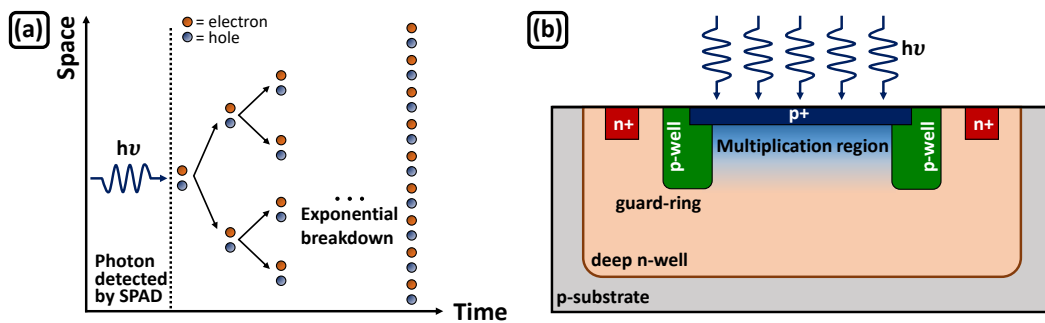


FIGURE 5.19: (a) Illustration of avalanche breakdown and (b) schematic cross-section of a single-photon avalanche diode (adapted from [14, 25]).

A schematic cross-section drawing of the SPAD is shown in Fig. 5.19(b). It consists of a circular  $p^+$ -anode/deep  $n$ -well/ $p$ -substrate dual junction structure. The  $p^+$ -anode/deep  $n$ -well junction forms the avalanche multiplication region where the Geiger

\*\*It must be noted that the signal amplitude does not provide intensity information since all the current pulses have the same amplitude. Instead intensity information can be obtained by counting the pulses during a certain period of time or by measuring the mean time interval between successive pulses [14].

breakdown occurs. The deep  $n$ -well/ $p$ -substrate junction allows to bias the  $p^+$ -anode independently from the  $p$ -substrate, while also preventing electrical crosstalk due to minority carriers diffusing in the substrate. The  $p$ -well guard-ring, surrounding the  $p^+$ -anode, prevents premature breakdown of the diode [14].

TABLE 5.2: Single photon avalanche diode specifications.

SPAD dead time (ns)	40
SPAD saturation (MHz)	25
SPAD active area ( $\mu\text{m}^2$ )	$\sim 28$
SPAD photon detection probability at 450 nm (%)	$\sim 2$

### 5.5.2 VLC transceiver

In the first demonstration a free-space VLC link is implemented. For this, the micro-LED was modulated with an on-off signal provided by an FPGA module (Opal Kelly XEM6310-LX45) and applied to the CMOS control electronics. An aspheric lens (Thorlabs ACL25416U-A) was used to approximately collimate the emission. The light was reflected by a mirror at a distance of approximately 2 cm, and transmitted back through the lens. The angle of the mirror was adjusted to focus the light back on to the SPAD, which is laterally  $\sim 2$  mm away from the emitting micro-LED. The output signal from a SPAD is a series of digital pulses indicating the detection of a photon, including noise and dark counts. Therefore, to produce a meaningful data signal, counts must be summed over a time interval. Photon counts per data period can then be compared to a threshold value to decode a data signal. The output of the SPAD was captured by an oscilloscope and processed offline in MATLAB<sup>TM</sup>. A pseudorandom bit sequence of length  $2^{12}$  bits

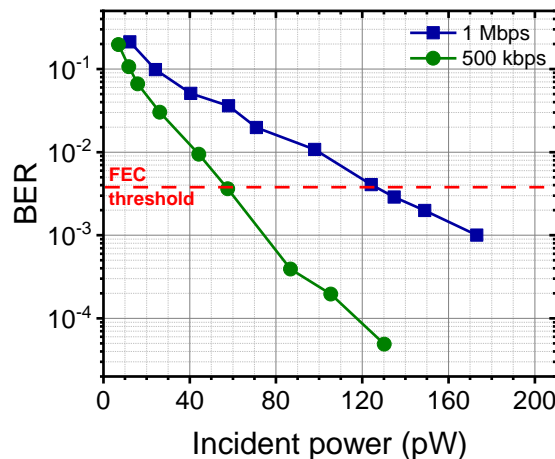


FIGURE 5.20: Bit-error-ratio (BER) measured as a function of the incident power on the SPAD.

was transmitted, and repeated to transmit a total of over  $4 \times 10^4$  bits, sufficient to justify a BER of less than  $1 \times 10^{-4}$ .

Figure 5.20 shows the BER as a function of incident power on the SPAD. VLC links of 500 kbps and 1 Mbps, below the FEC threshold, are demonstrated. For the 500 kbps link, communication, below FEC, is possible down to 58 pW of incident power. By increasing the data rate to 1 Mbps the minimum incident power for communication below the FEC limit is 135 pW.

### 5.5.3 Time-of-flight ranging

Time-of-flight (ToF) incorporates several different range measurement techniques, such as sonar, radar and lidar. All of these are based on measuring the turn-around time of a propagating wave with a known propagation velocity ( $v_p$ ), and calculating the distance between the measuring system and a target [27]:

$$d = \frac{1}{2} \cdot v_p \cdot \Delta t \tag{5.1}$$

Pulsed optical ToF is considered one of the most straightforward ToF techniques, as the turn-around time is measured directly. Figure 5.21 illustrates the working principle of pulsed optical ToF. A very short light pulse (shown in blue) is emitted by the transmitter, propagates into free-space, until it is scattered (shown in green) by the target, and then detected by the receiver [28]. Knowing the time interval between emission and detection and the speed of light ( $c$ ), the distance between the measuring system and the target can be calculated by Eq. 5.1.

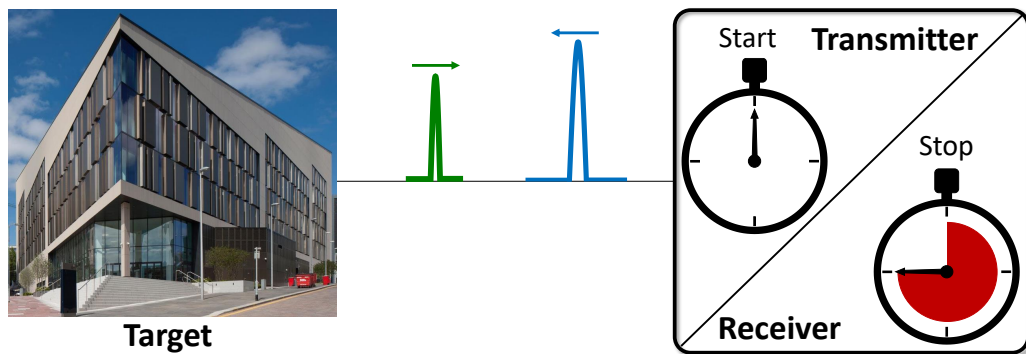


FIGURE 5.21: Pulsed optical time-of-flight working principle (adapted from [27]). The target is a photograph of the Technology and Innovation Centre building in Glasgow, UK (retrieved from [29]).

The main disadvantage of this method is the requirement for a sufficiently large return signal from the object to permit an accurate distance measurement. This can be



problematic when the imaged object is distant and/or non-scattering. This can be easily addressed by employing high-power laser systems, however, depending on the application, this solution might fail to meet eye-safety requirements. An alternative is to use a sensitive photon-counting technique, such as time-correlated single-photon counting (TCSPC) to monitor the return signal. TCSPC is a statistical averaging technique that has single photon detection sensitivity and picosecond timing accuracy. The object is illuminated with a high repetition rate train of short pulses, and each short pulse triggers a counting event. The scattered return signal is routed onto a photon-counting detector, which stops the counting event on arrival of the first photon. After many photon-timing events ( $10^4$  to  $10^6$ ) a histogram, that represents the probability distribution of arrival times of returning photons, is generated (Fig. 5.22(a)). When a high-repetition rate ( $>100$  kHz) source is used, it is more efficient to use reverse TCSPC. In this case, the photon-counting detector starts the counting event and the stop is given by the excitation pulses shifted by a delay. In reverse mode, photon events with longer turn-around time will have a shorter arrival time, which means that the histogram is temporally reversed (Fig. 5.22(b)) [28, 30, 31].

To demonstrate the ranging capability of the CMOS-driven micro-LED device, a single micro-LED was operated in a pulsed manner. The FPGA module was used to generate 20 ns wide electrical pulses at a repetition rate of 3.13 MHz. This rate was

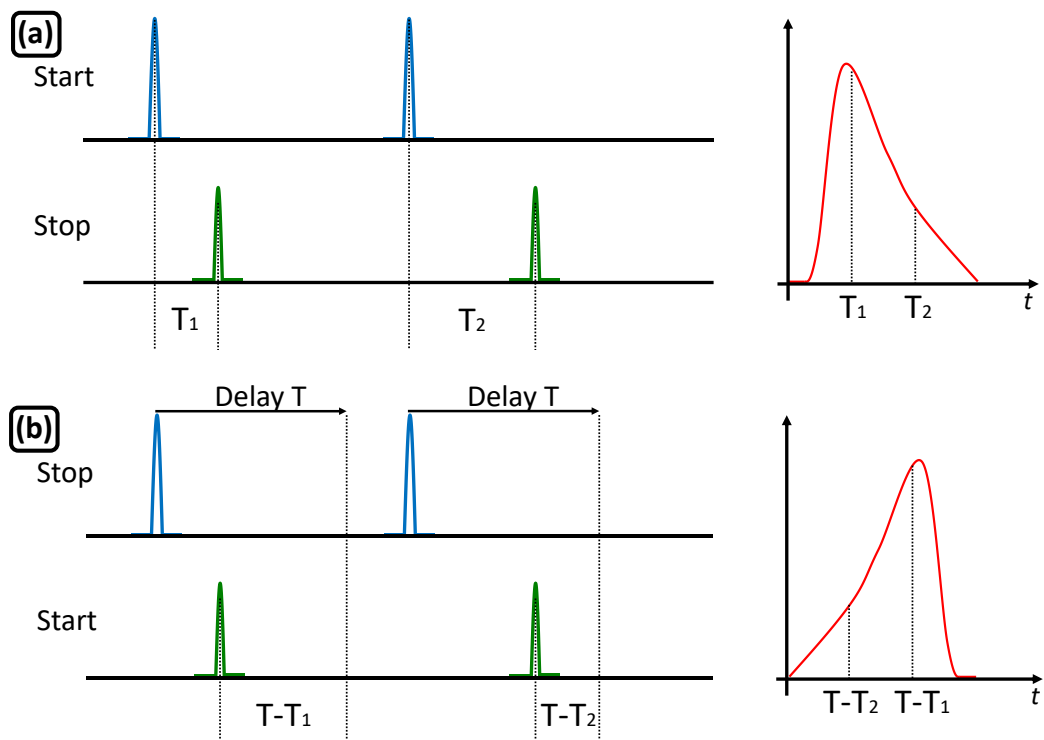


FIGURE 5.22: (a) Forward and (b) reverse time-correlated single-photon counting operation modes.

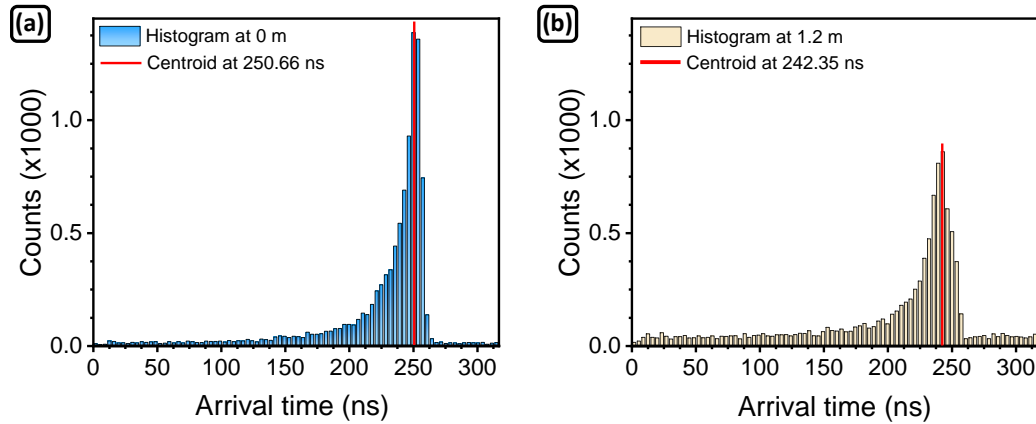


FIGURE 5.23: Photons arrival time histogram acquired at (a) 0 m and at (b) 1.2 m.

chosen as a compromise between rapid acquisition of ranging data and the ability to fully resolve individual pulses. As the CMOS and the micro-LED bandwidth limit the rise and fall times, applying this signal to the CMOS driver generates optical pulses from the micro-LED with a full width at half maximum of 19 ns. An aspheric lens (Thorlabs ACL50832U-A) was used to collimate the micro-LED output. A large mirror (COMAR 250 MC 160) was used to reflect the light back to the chip and refocus on to the SPAD. The distance from the CMOS chip to the mirror was changed from 0 to 1.2 m in 0.2 m intervals. The SPAD output was used as the start signal to trigger a time-to-digital converter (Texas Instruments TDC7200), with a stop signal provided by the FPGA module. Thus, time of flight for single photons is recorded using reverse TCSPC methods. By repeating the single photon arrival time measurements and building up a histogram, the optical pulse shape is recovered, and time of flight can be measured by finding the centroid of the received peak [32]. For these experiments,  $10^4$  arrival times were measured in dark laboratory conditions. Using a repetition rate of 3.13 MHz ( $Rep$ ) and  $10^4$  samples ( $N$ ) gives an acquisition time ( $T$ ) of  $\sim 3$  ms ( $T = N/Rep$ ), which provides an adequate capture for simple time of flight ranging. In addition, at this repetition rate, an effective accessible range (i.e. spatial pulse separation divided by two) of 48 m is achieved. Figures 5.23(a) and 5.23(b) show the histogram acquired at 0 and at 1.2 m. Increasing the distance from 0 to 1.2 results in a decrease of the maximum counts peak and increase of the floor level due to power losses. More important, the centroid shifts from 250.66 to 242.35 ns, which, applying Eq. 5.1, corresponds to a distance of 1.24 m. The resulting distance measurements are shown in Fig. 5.24. While the precision is limited by the width of the optical pulses, this proof-of-concept demonstration shows cm-scale distance measurements over a 1.2 m distance with a root-minimum-square deviation of 8.14 cm.

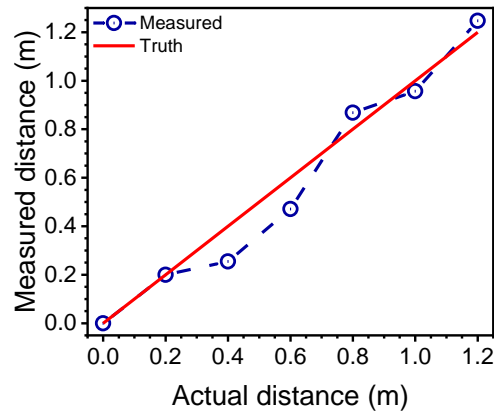


FIGURE 5.24: Measured distance plotted as a function of the actual distance in a ranging setup.

## 5.6 Summary

In this chapter, the direct integration of micro-LEDs onto CMOS circuitry by micro-transfer printing is demonstrated. An 8x8 micro-LED array was thus realised with high brightness and modulation bandwidth uniformity across the full array. This led to a 128 kbps optical camera communication link demonstration using an ultrafast camera. Taking advantage of the monolithic SPAD on the CMOS chip operation as a VLC transceiver and ranging device was also demonstrated. The results in this chapter were published in: J.F.C. Carreira *et al.*, *Optics Express* 28 (5), 6909-6917 (2020).

## Bibliography

- [1] François Templier, Ludovic Dupré, Bertrand Dupont, Anis Daami, Bernard Aventurier, Franck Henry, Denis Sarrasin, Sébastien Renet, Frédéric Berger, François Olivier, and Lydie Mathieu. High-resolution active-matrix 10  $\mu\text{m}$  pixel-pitch GaN LED microdisplays for augmented reality applications. In Liang-Chy Chien, Tae-Hoon Yoon, and Qiong-Hua Wang, editors, *Advances in Display Technologies VIII*, volume 10556, pages 100 – 105. International Society for Optics and Photonics, SPIE, 2018.
- [2] S. Zhang, S. Watson, J. J. D. McKendry, D. Massoubre, A. Cogman, E. Gu, R. K. Henderson, A. E. Kelly, and M. D. Dawson. 1.5 Gbit/s Multi-Channel Visible Light Communications Using CMOS-Controlled GaN-Based LEDs. *Journal of Lightwave Technology*, 31(8):1211–1216, April 2013.
- [3] J. Herrnsdorf, M. J. Strain, E. Gu, R. K. Henderson, and M. D. Dawson. Positioning and Space-Division Multiple Access Enabled by Structured Illumination With Light-Emitting Diodes. *Journal of Lightwave Technology*, 35(12):2339–2345, June 2017.
- [4] D. Elfström, B. Guilhabert, J. McKendry, S. Poland, Z. Gong, D. Massoubre, E. Richardson, B. R. Rae, G. Valentine, G. Blanco-Gomez, E. Gu, J.M. Cooper, R.K. Henderson, and M.D. Dawson. Mask-less ultraviolet photolithography based on CMOS-driven micro-pixel light emitting diodes. *Opt. Express*, 17(26):23522–23529, Dec 2009.
- [5] Alicja Zarowna-Dabrowska, Steven L. Neale, David Massoubre, Jonathan McKendry, Bruce R. Rae, Robert K. Henderson, Mervyn J. Rose, Huabing Yin, Jonathan M. Cooper, Erdan Gu, and Martin D. Dawson. Miniaturized optoelectronic tweezers controlled by GaN micro-pixel light emitting diode arrays. *Opt. Express*, 19(3):2720–2728, Jan 2011.
- [6] S. M. Sze and Kwok K. Ng. *Physics of Semiconductor Devices: Third Edition*. John Wiley & Sons, Inc., 2006.
- [7] Abel S. Sedra Kenneth C. Smith Tony Chan Carusone Vincent Gaudet. *Microelectronic Circuits - 8<sup>th</sup> edition*. Oxford University Press, 2020.
- [8] Allan R. Hambley. *Electrical Engineering - Principles and Applications (7<sup>th</sup> Edition)*. Pearson Education Limited, 2019.
- [9] B. R. Rae, J. Yang, J. McKendry, Z. Gong, D. Renshaw, J. M. Girkin, E. Gu, M. D. Dawson, and R. K. Henderson. A Vertically Integrated CMOS Microsystem for Time-Resolved Fluorescence Analysis. *IEEE Transactions on Biomedical Circuits and Systems*, 4(6):437–444, Dec 2010.
- [10] J. Herrnsdorf, J. J. D. McKendry, S. Zhang, E. Xie, R. Ferreira, D. Massoubre, A. M. Zuhdi, R. K. Henderson, I. Underwood, S. Watson, A. E. Kelly, E. Gu, and M. D. Dawson. Active-Matrix GaN Micro Light-Emitting Diode Display With Unprecedented Brightness. *IEEE Transactions on Electron Devices*, 62(6):1918–1925, June 2015.
- [11] Sami Franssila. *Introduction to Microfabrication*. Wiley, 2010.
- [12] D. A. Danner and D. W. Hess. Reaction of atomic and molecular chlorine with aluminum. *Journal of Applied Physics*, 59(3):940–947, 1986.

- [13] J. F. C. Carreira, A. D. Griffiths, E. Xie, B. J. E. Guilhabert, J. Herrnsdorf, R. K. Henderson, E. Gu, M. J. Strain, and M. D. Dawson. Direct integration of micro-LEDs and a SPAD detector on a silicon CMOS chip for data communications and time-of-flight ranging. *Opt. Express*, 28(5):6909–6917, Mar 2020.
- [14] C. Niclass, M. Sergio, and E. Charbon. A Single Photon Avalanche Diode Array Fabricated in Deep-Submicron CMOS Technology. *Proceedings of the Design Automation Test in Europe Conference*, 1:1–6, March 2006.
- [15] E. Fred Schubert. *Light-Emitting Diodes*. Cambridge University Press, 2006.
- [16] A. J. Trindade, B. Guilhabert, D. Massoubre, D. Zhu, N. Laurand, E. Gu, I. M. Watson, C. J. Humphreys, and M. D. Dawson. Nanoscale-accuracy transfer printing of ultra-thin AlInGaN light-emitting diodes onto mechanically flexible substrates. *Applied Physics Letters*, 103(25):253302, Dec 2013.
- [17] K. Rae, P. P. Manousiadis, M. S. Islim, L. Yin, J. Carreira, J. J. D. McKendry, B. Guilhabert, I. D. W. Samuel, G. A. Turnbull, N. Laurand, H. Haas, and M. D. Dawson. Transfer-printed micro-LED and polymer-based transceiver for visible light communications. *Opt. Express*, 26(24):31474–31483, Nov 2018.
- [18] X.A Cao, J.A Teetsov, F Shahedipour-Sandvik, and S.D Arthur. Microstructural origin of leakage current in GaN/InGaN light-emitting diodes. *Journal of Crystal Growth*, 264(1):172 – 177, 2004.
- [19] Nam Tuan Le, Mohammad Arif Hossain, and Yeong Min Jang. A survey of design and implementation for optical camera communication. *Signal Processing: Image Communication*, 53:95 – 109, 2017.
- [20] T. Nguyen, A. Islam, T. Hossain, and Y. M. Jang. Current Status and Performance Analysis of Optical Camera Communication Technologies for 5G Networks. *IEEE Access*, 5:4574–4594, 2017.
- [21] N. Saha, M. S. Iftekhar, N. T. Le, and Y. M. Jang. Survey on optical camera communications: challenges and opportunities. *IET Optoelectronics*, 9(5):172–183, 2015.
- [22] Photron. Fastcam Mini UX Model UX50/UX100 Datasheet. <https://photron.com/wp-content/uploads/2019/12/Mini-UX19.12.17-compressed.pdf>, Accessed 2020-03-04.
- [23] Alexander D. Griffiths, Johannes Herrnsdorf, Michael J. Strain, and Martin D. Dawson. Scalable visible light communications with a micro-LED array projector and high-speed smartphone camera. *Opt. Express*, 27(11):15585–15594, May 2019.
- [24] International Telecommunication Union. Forward error correction for high bit-rate DWDM submarine systems. *ITU, Geneva, Switzerland, Tech. Rep. ITU-T G.975.1*, Nov 2013.
- [25] B R Rae, C Griffin, J McKendry, J M Girkin, H X Zhang, E Gu, D Renshaw, E Charbon, M D Dawson, and R K Henderson. CMOS driven micro-pixel LEDs integrated with single photon avalanche diodes for time resolved fluorescence measurements. *Journal of Physics D: Applied Physics*, 41(9):094011, apr 2008.
- [26] F. Zappa, S. Tisa, A. Tosi, and S. Cova. Principles and features of single-photon avalanche diode arrays. *Sensors and Actuators A: Physical*, 140(1):103 – 112, 2007.

- 
- [27] R. Lange, S. Böhmer, and B. Buxbaum. *11 - CMOS-based optical time-of-flight 3D imaging and ranging*, pages 319 – 375. Woodhead Publishing Series in Electronic and Optical Materials. Woodhead Publishing, second edition edition, 2020.
- [28] J. S. Massa, A. M. Wallace, G. S. Buller, S. J. Fancey, and A. C. Walker. Laser depth measurement based on time-correlated single-photon counting. *Opt. Lett.*, 22(8):543–545, Apr 1997.
- [29] John Curry. Technology and Innovation Centre, University of Strathclyde - BDP.com. <https://www.pinterest.co.uk/pin/363243526193280327/>, Accessed 2020-03-05.
- [30] John S. Massa, Gerald S. Buller, Andrew C. Walker, Sergio Cova, Manikam Umasuthan, and Andrew M. Wallace. Time-of-flight optical ranging system based on time-correlated single-photon counting. *Appl. Opt.*, 37(31):7298–7304, Nov 1998.
- [31] Wolfgang Becker. *Advanced Time-Correlated Single Photon Counting Techniques*. Springer Series in Chemical Physics, 2005.
- [32] Alexander D. Griffiths, Haochang Chen, David Day-Uei Li, Robert K. Henderson, Johannes Hermsdorf, Martin D. Dawson, and Michael J. Strain. Multispectral time-of-flight imaging using light-emitting diodes. *Opt. Express*, 27(24):35485–35498, Nov 2019.

## Chapter 6

# Outlook and future work

The work presented in this thesis is focused on the integration of GaN-based and AlGaInP-based micro-LEDs onto capability enhancing substrates by micro-transfer printing. The main body of the work can be divided into two threads: (1) development of dual-colour micro-LED arrays for optical communications and optogenetics applications, and (2) integration of optical devices with control electronics for optical communications and time of flight ranging applications. These were enabled by the development of high-yield advanced transfer printing methods (e.g. flip-chip TP without adhesive layers) and efficient insulation/encapsulation strategies.

Chapter 1 gives a general introduction and overview of LEDs, in particular based on III-nitrides and III-phosphides. The physics of semiconductors and the *pn* junction operating principles were described. The role of double heterostructures and quantum wells in increasing LED's quantum efficiency was revised. Due to the relevance to this work, III-nitride LEDs and AlGaInP-based LEDs growth and doping conditions and their importance in realising highly efficient solid state emitters were discussed. Mechanisms behind III-nitrides astonishing performance, despite their high dislocation density and polarisation effects, were also presented. The efficiency droop phenomena, which strongly affects III-nitride LEDs at moderate current density levels, and possible mechanisms behind it were described. Micro-LEDs and their application in optical communications were briefly discussed. In the end, micro-transfer printing was introduced as a highly-versatile technique which has enabled tremendous advancements in the field of heterogeneous integration, in particular for flexible optoelectronic applications.

In Chapter 2, the tools and techniques required in the fabrication of suspended GaN-based micro-LED platelets are described in detail. Most of the techniques are common to commercial LEDs, with the main exception being the underetch step, which releases

the platelets from their silicon growth substrate. The physical concepts behind elastomeric transfer printing, in particular the kinetically controlled reversible adhesion of microstructured stamps are discussed. The stamp fabrication process and the adapted for micro-TP nanolithography system are presented. In the end, two different strategies for insulation/encapsulation of micro-LEDs are compared in terms of the devices' optical and electrical performance.

Chapter 3 presents the development of on-chip dual-colour micro-LED arrays and their application in free-space and underwater optical communications. Devices were fabricated in two different configurations: (1) individually addressable blue-violet and blue-green; and (2) 2x2 in-series connected blue-green micro-LED array. The individually addressable arrays exhibit high modulation bandwidths and allow for fine tuning of the perceived colour by adjusting the current density. In the optical communication context, in WDM scheme these arrays are capable of achieving Gbps data rates in free-space and up to 200 Mbps in highly-turbid water media. This work paves the way towards clusters of multi-colour micro-LEDs acting as fast VLC transmitters in the emerging micro-LED displays. The 2x2 in-series connected blue-green micro-LED array, with only one anode and one cathode, benefits from a simpler electric addressing scheme, in which the current flowing through the different size and different colour micro-LEDs is the same. In free-space VLC, the in-series connected array is capable of achieving several Gbps. In underwater optical communication, the limited bandwidth of the array combined with the simplicity of the modulation scheme limited the achievable data rate to 50 Mbps.

Chapter 4 presents the integration of pre-fabricated AlGaInP-based red micro-LEDs onto unusual substrates for optical communication and optogenetics applications. In optical communication context, a 2x2 array of red micro-LEDs was transfer printed onto diamond and glasses substrates. The versatility of the micro-TP technique was demonstrated by executing a two stages flip-chip transfer of the platelets onto the receiving substrates, without the use of adhesive layer. The device on-diamond exhibited higher current density operation and thus higher optical power and bandwidth. In free-space VLC, both devices exhibited Gbps data rates, with the 2x1 in-parallel array on-diamond achieving up to 6.6 Gbps. To the best of our knowledge, this is the fastest VLC link based on AlGaInP red micro-LEDs. The integration of the AlGaInP-based micro-LEDs onto non-native substrates is also interesting for optogenetics applications. In this case, AlGaInP-based micro-LEDs were integrated onto a monolithic GaN-based optrode consisting of blue micro-LEDs and recording electrodes. The integration process is described in detail and a fully functional blue-red micro-LED optrode is shown at the end of the chapter.



Chapter 5 presents the direct integration of micro-LEDs onto CMOS circuitry. Firstly, complementary-metal-oxide-semiconductor technology and how CMOS circuitry can be used to realise logic-circuits are described. Micro-transfer printing is presented as an alternative technique to common flip-chip integration of micro-LEDs with CMOS. An 8x8 micro-LED array was realised with high brightness and modulation bandwidth uniformity. The full array was spatio-temporal modulated at 2 kHz and an optical camera communication 128 kbps link was established at optical power values higher than  $0.02 \mu\text{W}$ . In addition to the main micro-LED driving area the CMOS also contained a single photon avalanche diode, which opens the possibility for excitation and detection on a single chip. Following on that, the capability of this device to act as VLC transmitter was demonstrated with data rates of up to 1 Mbps being achieved. Furthermore, operation as a time-of-flight ranging device was also presented, with ranging up to 1.2 m being demonstrated.

## 6.1 Future work

Based on the work developed in this thesis, three future research topics are suggested: (1) wavelength division multiplexing (WDM) multiple-input-multiple-output (MIMO), (2) red-green-blue (RGB) micro-LED arrays, and (3) integration of vertical cavity surface emitting lasers (VCSELs) onto CMOS circuitry.

### WDM MIMO

In Chapter 3.2, the capability of blue-green and blue-violet micro-LED arrays to operate as Gbps WDM VLC transmitters was demonstrated. In this case, the blue-green (blue-violet) array consisted of one monolithic green (violet) micro-LED and one transfer printed blue micro-LED. This concept was further expanded into a 2x4 array of blue-green and blue-violet micro-LEDs, with 8 monolithic and 8 transfer printed micro-LEDs on a centre-to-centre pitch of 1 mm (Fig. 6.1(a)). The blue, green, and violet 2x4 micro-LED arrays exhibit good electrical and optical uniformity, as shown in Figs. 6.1(b)-6.1(d), respectively.

For optical communication purposes, such on-chip 2x4 dual-colour micro-LED arrays can be operated in WDM ganging or in WDM multiple-input-multiple-output modes. Taking into consideration the 2x4 blue-green micro-LED array. In WDM ganging mode, the blue and green micro-LEDs are modulated with different signal streams, however, the signal streams are the same for each LED of the same colour. The light of the 16 micro-LEDs is focused onto one optical receiver and the performance of the blue and

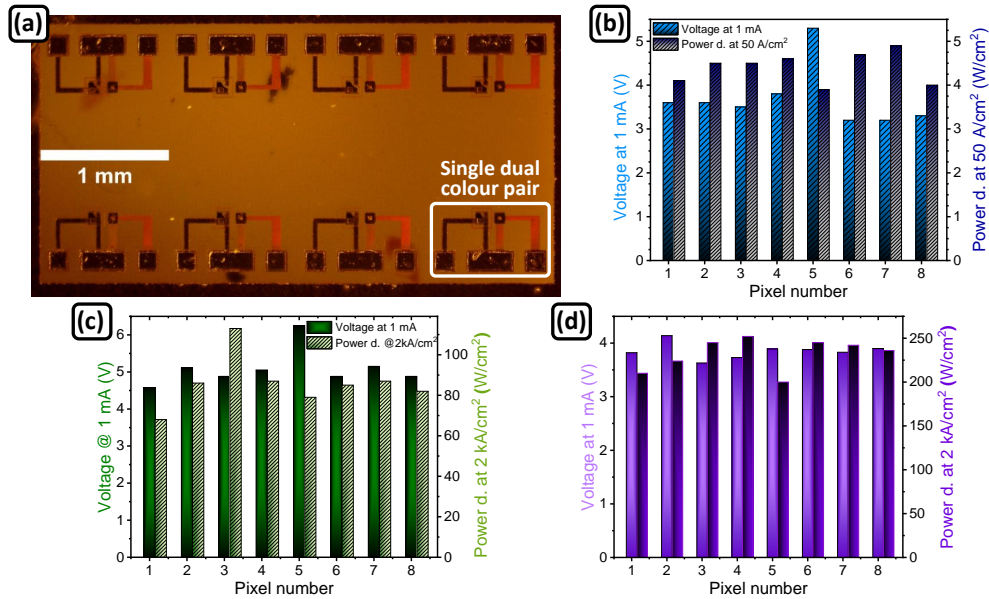


FIGURE 6.1: (a) Plan-view photograph of the 2x4 array of dual-colour micro-LEDs (either blue-violet or blue-green); (b)-(d) voltage and optical power density distribution of blue, green, and violet micro-LED arrays, respectively.

green channel measured by changing a bandpass filter. The expected increase in optical power (each different colour channel is now composed by 8 micro-LEDs), leads to an increase of the channel SNR and thus increase in data rate.

The spatial multiplexing MIMO technique relies on a certain number of transmitters each carrying an independent data stream to enhance spectral efficiency. The channel capacity is proportional to the minimum of transmitters  $M$  and receivers  $N$  [1]. The suitability of micro-LED arrays for high-speed imaging MIMO systems has been demonstrated in [2], with aggregate data rates of up to 7 Gbps being achieved. WDM MIMO has been employed in RGB LED systems in order to increase the maximum data rate per wavelength, with data rates of 6.36 Gbps being reported [3]. In WDM MIMO, each blue and each green micro-LED of the 2x4 array carry a different data stream (Fig. 6.2). In this case each blue-green micro-LED pair behaves as an individual MIMO transmitter, thus in this configuration  $M = 8$ . On the detection side, an array of photodetectors ( $N = 8$ ) is placed. Using imaging optics, the light emitted by each blue-green pair is focused onto a different photodetector. By changing a bandpass filter in front of the photodetector array, the performance of the different colour 2x4 arrays can be measured. This approach combines a 2x4 (8 transmitters) MIMO spatial modulation scheme with a two channel WDM modulation, resulting in 16 independent channels for data transmission. Taking into account that in Chapter 3.2 a single blue-green pair achieved an error-free data rate of 1793 Mbps, such WDM MIMO approach has the potential to achieve up to 14.3 Gbps.

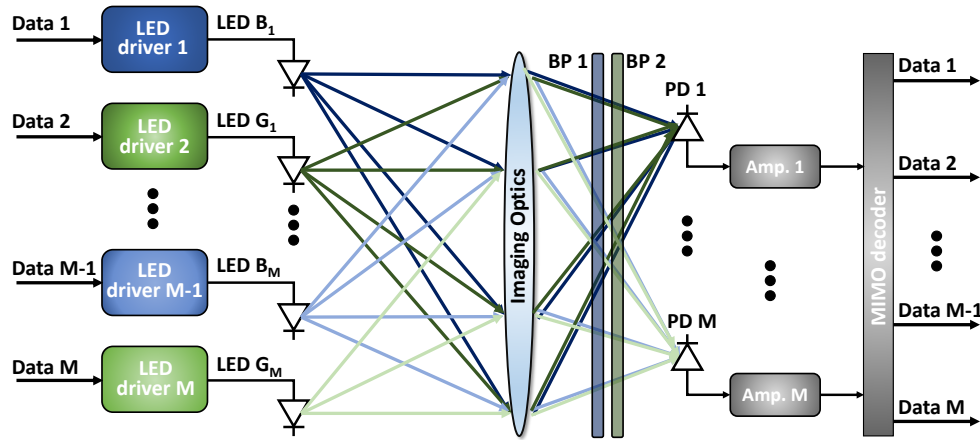


FIGURE 6.2: Block diagram of wavelength division multiplexing multiple-input-multiple-output modulation scheme.

### RGB micro-LED array

Chapters 3 and 4 presented the development of on-chip blue-green micro-LED arrays and the integration of red micro-LEDs onto non-native substrates, respectively. The techniques shown in these two chapters can be applied to develop on-chip RGB micro-LED arrays, and thus achieve white light emission (Fig. 6.3). Such array can be fabricated by simply transfer printing the GaN-based blue platelets and the AlGaInP-based red platelets onto the substrate of a pre-fabricated green micro-LED (similarly to Chapter 3). A different approach would be to transfer print the three different colour materials onto a common platform, such as a CMOS chip. In this case, the green micro-LED grown on sapphire could be suspended following similar techniques to the ones described for the blue platelet, replacing the chemical wet etch by a laser lift-off step\* [4].

RGB micro-LED arrays have already been reported in the context of micro-LED displays, however, their application in optical communications has not yet been reported. Similarly to the work presented in Chapter 3, RGB micro-LED clusters can behave as

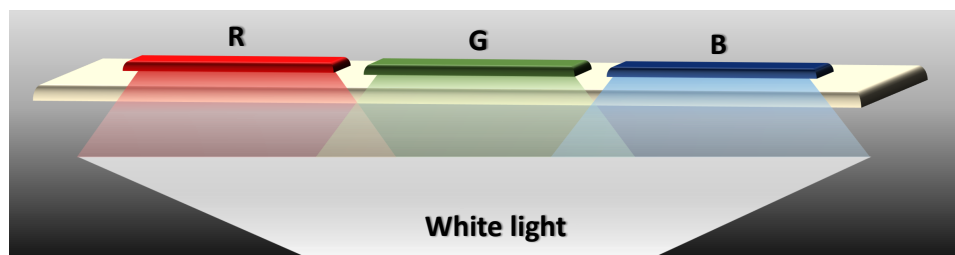


FIGURE 6.3: Schematic drawing of a red-green-blue (RGB) micro-LED array enabled by micro-transfer printing.

\*The GaN thin-film/sapphire interface is heated using a KrF pulsed-excimer laser (248 nm), resulting in the decomposition of the interfacial GaN into Ga metal. Separation of GaN thin-film from the sapphire substrate is then completed by melting the thin Ga-rich interfacial layer [4].

a fast VLC transmitter in microdisplays. In addition, as white light can be achieved by efficient color mixing of the three RGB components, such array would also meet the basic requirements of a VLC transmitter (white light + high modulation bandwidth). Furthermore, this RGB micro-LED array could have important implications in the field of underwater optical communications, where water's transparency windows shifts towards longer wavelengths with increasing turbidity. Again, in free-space and underwater, WDM modulation schemes could be employed to increase the aggregate data rate.

## Integration of VCSELs onto CMOS

Chapter 5 presented the direct integration of micro-LEDs onto CMOS circuitry by micro-TP. The strategies demonstrated in this chapter can be extended to a myriad of optical devices. GaAs-based VCSELs are particularly interesting due to their low threshold current, high quantum efficiency and high-speed modulation bandwidth at low current. These characteristics have led to their dissemination in various fields, with strong emphasis in data communication and sensing (e.g. face recognition). A VCSEL consists of an active region within an optical cavity with two highly reflective semiconductor distributed Bragg reflectors (DBRs) to form a vertical resonator (Fig. 6.4(a)) [5]. The total thickness of the grown layers is usually 5-10  $\mu\text{m}$  and the active area of the device is typically 10  $\mu\text{m}$  in dimension while the chip size is typically 250-300  $\mu\text{m}$  [6].

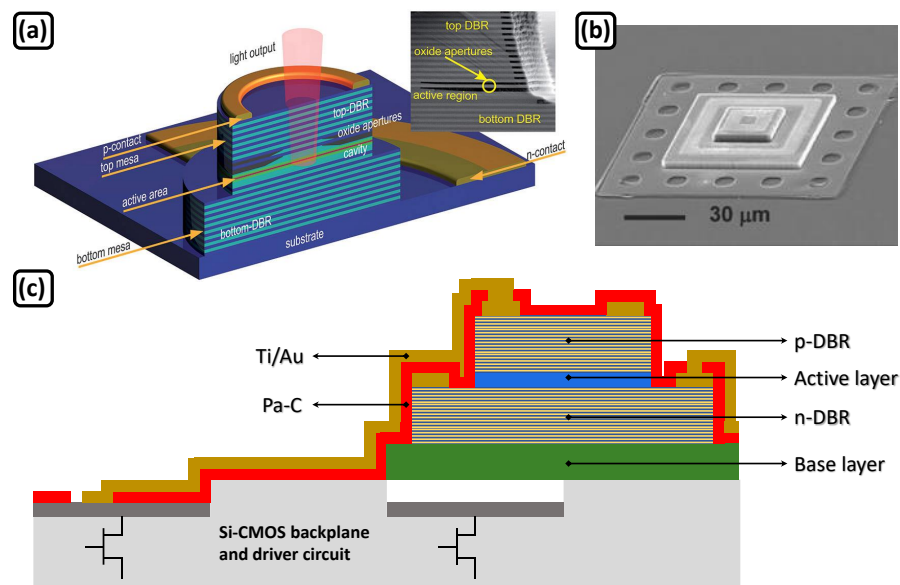


FIGURE 6.4: (a) Schematic of a top-emitting VCSEL (inset shows a cross-sectional electron microscopy micrograph) [7]; (b) scanning electron microscopy micrograph of a single micro-VCSEL printed on glass [8]; (c) schematic cross-section of a micro-VCSEL printed on a CMOS.

By epitaxially growing VCSEL structures with sacrificial release layers, micro-VCSELs can be separated from their growth substrate and transferred onto non-native substrates (Fig. 6.4(b)) [8]. Thus, there is a great opportunity to integrate VCSELs with the electronic drive and receive circuits to form compact transceivers [6]. Micro-VCSELs can easily be integrated with CMOS electronics (Fig. 6.4(c)) by following the strategies shown in Chapter 5, which can be of importance in the growing field of 3D sensing.

## Bibliography

- [1] Sujan Rajbhandari, Jonathan J D McKendry, Johannes Herrnsdorf, Hyunchae Chun, Grahame Faulkner, Harald Haas, Ian M Watson, Dominic O'Brien, and Martin D Dawson. A review of gallium nitride LEDs for multi-gigabit-per-second visible light data communications. *Semiconductor Science and Technology*, 32(2):023001, jan 2017.
- [2] S. Rajbhandari, A. V. N. Jalajakumari, H. Chun, G. Faulkner, K. Cameron, R. Henderson, D. Tsonev, H. Haas, E. Xie, J. J. D. McKendry, J. Herrnsdorf, R. Ferreira, E. Gu, M. D. Dawson, and D. O'Brien. A Multigigabit per Second Integrated Multiple-Input Multiple-Output VLC Demonstrator. *Journal of Lightwave Technology*, 35(20):4358–4365, Oct 2017.
- [3] I. Lu, C. Lai, C. Yeh, and J. Chen. 6.36 Gbit/s RGB LED-based WDM MIMO visible light communication system employing OFDM modulation. In *2017 Optical Fiber Communications Conference and Exhibition (OFC)*, pages 1–3, 2017.
- [4] W. S. Wong, T. Sands, N. W. Cheung, M. Kneissl, D. P. Bour, P. Mei, L. T. Romano, and N. M. Johnson. Fabrication of thin-film InGaN light-emitting diode membranes by laser lift-off. *Applied Physics Letters*, 75(10):1360–1362, 1999.
- [5] Anjin Liu, Philip Wolf, James A. Lott, and Dieter Bimberg. Vertical-cavity surface-emitting lasers for data communication and sensing. *Photon. Res.*, 7(2):121–136, Feb 2019.
- [6] Brian Corbett, Ruggero Loi, Weidong Zhou, Dong Liu, and Zhenqiang Ma. Transfer print techniques for heterogeneous integration of photonic components. *Progress in Quantum Electronics*, 52:1 – 17, 2017.
- [7] Hui Li, Philip Wolf, Philip Moser, Gunter Larisch, James A. Lott, and Dieter Bimberg. Vertical-cavity surface-emitting lasers for optical interconnects. *SPIE Newsroom*, 2014.
- [8] Dongseok Kang, Sung-Min Lee, Zhengwei Li, Ashkan Seyedi, John O'Brien, Jianliang Xiao, and Jongseung Yoon. Compliant, Heterogeneously Integrated GaAs Micro-VCSELs towards Wearable and Implantable Integrated Optoelectronics Platforms. *Advanced Optical Materials*, 2(4):373–381, 2014.

# List of publications

## Journals

- [1] K. Rae, P. P. Manousiadis, M. S. Islim, L. Yin, J. Carreira, J. J. D. McKendry, B. Guilhabert, I. D. W. Samuel, G. A. Turnbull, N. Laurand, H. Haas, and M. D. Dawson, *Transfer-printed micro-LED and polymer-based transceiver for visible light communications*, Optics Express **26** (24), 31474-31483 (2018)
- [2] J.F.C. Carreira, E. Xie, R. Bian, C. Chen, J.J.D. McKendry, B. Guilhabert, H. Haas, E. Gu and M.D. Dawson, *On-chip GaN-based dual-color micro-LED arrays and their application in visible light communication*, Optics Express **27** (20), A1517-A1528 (2019)
- [3] J.F.C. Carreira, A.D. Griffiths, E. Xie, B.J.E. Guilhabert, J. Herrnsdorf, R.K. Henderson, E. Gu, M.J. Strain and M.D. Dawson, *Direct integration of micro-LEDs and a SPAD detector on a silicon CMOS chip for data communications and time-of-flight ranging*, Optics Express **28** (5), 6909-6917 (2020)
- [4] J.F.C. Carreira, E. Xie, R. Bian, J. Herrnsdorf, H. Haas, E. Gu, M.J. Strain and M.D. Dawson, *Gigabit per second visible light communication based on AlGaInP red micro-LED micro-transfer printed onto diamond and glass*, Optics Express **28** (8), 12149-12156 (2020)

## Conference Proceedings

- [5] J.F.C. Carreira, E. Xie, R. Bian, J.J.D. McKendry, B. Guilhabert, I.M. Watson, H. Haas, E. Gu and M.D. Dawson, *Dual-Color Micro-LED Transmitter for Visible Light Communication*, 2018 IEEE Photonics Conference (IPC), 1-2 (2018)
- [6] J.F.C. Carreira, B.J.E. Guilhabert, J.J.D. McKendry, E. Xie, K. Mathieson, R.K. Henderson, I.M. Watson, E. Gu and M.D. Dawson, *Integration of Micro-LED Array on CMOS by Transfer Printing*, 2018 IEEE Photonics Conference (IPC), 1-2 (2018)
- [7] José F.C. Carreira, Georgios N. Arvanitakis, Alexander D. Griffiths, Jonathan J.D. McKendry, Enyuan Xie, John Kosman, Robert K. Henderson, Erdan Gu and Martin D. Dawson, *Underwater Wireless Optical Communications at 100 Mb/s using Integrated Dual-Color Micro-LEDs*, 2019 IEEE Photonics Conference (IPC), 1-2 (2019)

## Conferences

(Presenter highlighted by bold letters)

- [8] **José F.C. Carreira**, Enyuan Xie, Jonathan J. D. McKendry, Benoit Guilhabert, Erdan Gu, Ian M. Watson and Martin D. Dawson, *Design, fabrication and characterisation of dual-colour micro-LED arrays for Visible Light Communication* (poster), UK Nitrides Consortium, 2018, United Kingdom
- [9] **J.F.C. Carreira**, E. Xie, R. Bian, J. J. D. McKendry, B. Guilhabert, I. Watson, H. Hass, E. Gu and M.D. Dawson, *Micro-Light Emitting Diodes: Beyond Displays* (oral), IONSScandinavia, 2018, Denmark
- [10] **J.F.C. Carreira**, B. J. E. Guilhabert, J. J. D. McKendry, E. Xie, K. Mathieson, R. K. Henderson, I. M. Watson, E. Gu and M. D. Dawson, *Integration of Micro-LED Array on CMOS by Transfer Printing* (oral), IEEE Photonics Conference (IPC), 2018, United States
- [11] **J.F.C. Carreira**, E. Xie, R. Bian, J. J. D. McKendry, B. J. E. Guilhabert, H. Haas, I. M. Watson, E. Gu, M. D. Dawson, *Dual-Color Micro-LED Transmitter for Visible Light Communication* (oral), IEEE Photonics Conference (IPC), 2018, United States
- [12] **José F.C. Carreira**, Enyuan Xie, R. Bian, Jonathan J. D. McKendry, Benoit Guilhabert, Harald Haas, Michael J. Strain, Erdan Gu, Ian M. Watson and Martin D. Dawson, *Blue-violet and blue-green GaN-based micro-LED arrays for Visible Light Communication* (poster), UK Nitrides Consortium, 2019, United Kingdom
- [13] **José F.C. Carreira**, Georgios N. Arvanitakis, Alexander D. Griffiths, Jonathan J. D. McKendry, Enyuan Xie, John Kosman, Robert K. Henderson, Erdan Gu and Martin D. Dawson, *Transfer-printed dual-colour micro-LEDs for underwater wireless optical communication* (oral), UK Semiconductors, 2019, United Kingdom
- [14] **José F.C. Carreira**, **Georgios N. Arvanitakis**, Alexander D. Griffiths, Jonathan J. D. McKendry, Enyuan Xie, John Kosman, Robert K. Henderson, Erdan Gu and Martin D. Dawson, *Underwater Wireless Optical Communications at 100 Mb/s using Integrated Dual-Color Micro-LEDs* (oral), IEEE Photonics Conference (IPC), 2019, United States
- [15] **R. Winstanley**, S. Stoyanov, **J.C. Carreira**, R. Scharf, E. Gu, M. D. Dawson, and K. Mathieson, *A Wireless Optogenetics System paired with  $\mu$ LED probe* (poster), Optogen2019, 2019, Italy
- [16] **José F.C. Carreira**, Alexander D. Griffiths, Enyuan Xie, Benoit J. E. Guilhabert, Johannes Hermsdorf, Robert K. Henderson, Erdan Gu, Michael J. Strain, and Martin D. Dawson, *Transfer printing integration of GaN micro-LEDs on CMOS* (oral), UK Nitrides Consortium, 2020, United Kingdom



# Dual-color micro-LED transmitter for Visible Light Communication

J. F. C. Carreira, E. Xie, J. J. D. McKendry, B. J. E. Guilhabert, I. M. Watson, E. Gu, M. D. Dawson  
Institute of Photonics, Department of Physics  
University of Strathclyde  
Glasgow, G1 1RD, United Kingdom  
e-mail address: jose.correia-carreira@strath.ac.uk

R. Bian, H. Haas  
Institute for Digital Communications, Li-Fi R&D Centre  
University of Edinburgh  
Edinburgh EH9 3JL, UK

**Abstract**— We report the integration of blue micro-LED onto the substrate of green micro-LED, by transfer printing. This dual-color device fabrication and performance as a visible light communication transmitter is demonstrated.

**Keywords**—micro-LED; transfer printing; VLC;

## I. INTRODUCTION

Gallium nitride-based light emitting diodes (LEDs) have shown great potential in Visible Light Communications (VLC), with over Mbit/s data transmission rates achieved by a single broad area LED. Further increase of transmission rates is limited by the low optical modulation bandwidth (BW) of these broad area LEDs, around the tens of MHz [1]. In the past years, we have shown that simply by reducing the size of the LED down to the micro scale (micro-LEDs) a tenfold increase in bandwidth is observed. This has led to a whole new field of VLC transmitters, with several reports of multi-Gbit/s data rates achieved by micro-LED devices [1], [2]. In this work we report a dual-color micro-LED array VLC transmitter that combines green and blue emitting micro-LED on the same substrate. By a pick-and-place technique, we have successfully transfer printed a blue-emitting micro-LED platelet from its silicon growth substrate onto the sapphire substrate of the green-emitting micro-LED. The electro-optical characteristics of this device are assessed and its performance as a VLC transmitter is evaluated by BW and data rate measurements.

## II. EXPERIMENTAL DETAILS

The dual-color micro-LED device reported in this work results from the integration of a blue micro-LED onto the substrate of a fully operational green micro-LED (Fig.1 a)). The fabrication processes of the green and blue micro-LEDs are, until the dual-color integration step, independent of each other. As such, they will be described separately.

The green micro-LED is fabricated from green emitting (505 nm) commercial InGaN epistuctures grown on c-plane sapphire. A 20  $\mu\text{m}$  diameter flip-chip micro-LED is defined by conventional photolithography techniques, as described elsewhere [3]. An important additional step is the deep etching of the mesa structure (90x90  $\mu\text{m}^2$ ) down to the patterned sapphire substrate (PSS). This allows reduction of the green

micro-LED capacitance [2] as well as compensation for height differences between the green and blue micro-LED in further processes [4].

Blue micro-LED platelets (100x100  $\mu\text{m}^2$ ) are fabricated from commercially available blue emitting (450 nm) InGaN epistuctures grown on (111)-oriented silicon (Si). The process is similar to the conventional GaN-based LED fabrication, with 3 main differences: 1) during mesa etching, supporting “anchors” are defined and etched down to the silicon substrate; 2) next, an extra etching step is introduced, exposing the Si(110) planes; 3) followed by a hot (80  $^\circ\text{C}$ ) 30% potassium hydroxide bath used to underetch the Si(110) planes. Upon completion of the underetching, the micro-LED platelets (2  $\mu\text{m}$  thin) are held suspended, above an air gap, by the two diagonally opposed sacrificial anchors [5].

The dual-color micro-LED fabrication is enabled by transfer printing (TP). In this technique, an elastomer stamp is used to pick-up one of the suspended blue micro-LED platelets and print it on the PSS of the green micro-LED (Fig.1 b)). It is worth mentioning that, due to the textured nature of the PSS a thick adhesion enhancement layer of SU-8 (4.5  $\mu\text{m}$ ) is spin coated prior to the printing. The gap between these two micro-LEDs is set to 50  $\mu\text{m}$ , however our TP system is capable of nanoscale placement accuracy [5]. After printing, a highly conformal film of parylene-C (4  $\mu\text{m}$  thick) is deposited, electrically insulating the sidewalls of the blue micro-LED. Localized apertures on the parylene-C layer, above the *n* and *p* contacts of the micro-LED, are lithographically defined and electrically addressed by Ti/Au (50/250 nm) metal tracks.

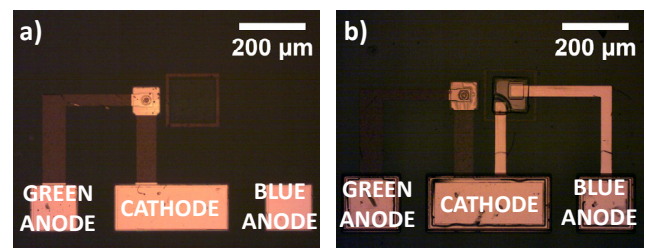


Fig. 1 – Optical photographs of the green micro-LED before transfer printing; b) of the dual-color device after transfer printing the blue micro-LED.

### III. RESULTS AND DISCUSSION

#### A. Electro-optical performance

The electro-optical response of the dual-color micro-LED array is shown in Fig. 2. The green micro-LED is able to sustain much higher current density than the blue micro-LED, due to their difference in size. Despite this size difference the maximum optical power of the two micro-LEDs is quite similar, 0.45 mW (at 3.8 kA/cm<sup>2</sup>) and 0.6 mW (at 120 A/cm<sup>2</sup>), for the green and blue micro-LED, respectively.

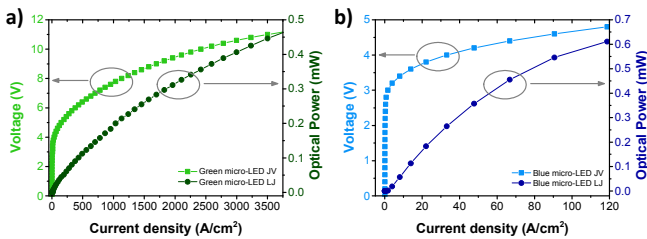


Fig. 2 – Current density-voltage (JV) and current density – optical power (LJ) of a) the green micro-LED and b) the blue micro-LED.

#### B. VLC Application

The capability of the dual-color micro-LED array on VLC has been evaluated in terms of the LEDs electrical-to-optical modulation BW, data transmission rate, and electroluminescence (EL).

Both micro-LEDs exhibit BW values above 100 MHz (Fig. 3a)). These extremely high values have been attributed to the ability of micro-LEDs to sustain high current density as well as to their low capacitance [3]. Data transmission experiments have been performed by driving the micro-LEDs with a direct current bias from a power supply combined, by a bias-tee, with a modulated signal from a signal generator. The modulated signal is based on an orthogonal frequency-division multiplexing (OFDM) data encoding scheme. The bit-error-ratio (BER) as a function of the data rate is shown in Fig. 3b). The blue micro-LED (blue-squares), operating at 10 mA driving current, can achieve 800 Mbit/s before reaching the  $3.8 \times 10^{-3}$  forward-error-correction (FEC) threshold. The influence of the green micro-LED, operating at 11 mA, and a bandpass filter centered at 470 nm on the blue micro-LED data rate is also shown (light blue circles). In this case, the maximum achieved by the blue micro-LED data rate is around 500 Mbit/s. The corresponding EL spectra (Fig. 3c) – Blue/Green curve) shows that the bandpass filter effectively blocks the light from the green micro-LED, and as such, the lower values for data rate are likely due to the blue micro-LED optical power losses at the filter. The same measurements have been performed for the green micro-LED. A maximum data rate of 613 Mbit/s and 480 Mbit/s is achieved, for single green micro-LED (green triangles) and green micro-LED with a 480 nm longpass filter and blue micro-LED (light green stars). When in ganging mode (both LEDs transmitting the same input signal) the maximum achieved data rate below the FEC threshold is 430 Mbit/s (Fig. 3b)).

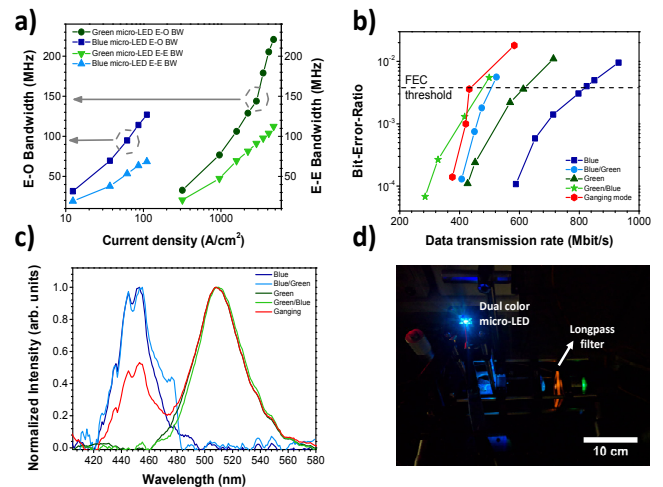


Fig. 3 – a) BW as a function of current density; b) BER as a function of data rate; c) EL spectra of single micro-LED and dual-color pair; d) picture of the micro-LEDs driven at the same time with a 480 nm longpass filter before the spectrometer.

### IV. CONCLUSION

We have successfully transfer printed a blue emitting micro-LED onto the growth substrate of a green emitting micro-LED, creating an individually driven dual-color array. The potential of this device as a VLC transmitter has been demonstrated with data rates of 800 Mbit/s and 600 Mbit/s for the blue and green micro-LED, respectively.

#### ACKNOWLEDGMENT

This work is funded under the EPSRC UP-VLC grant (EP/K00042X/1) and EPSRC CDT in Medical Devices & Health Technologies grant (EP/L015595/1). Plessey Semiconductors is acknowledged for providing GaN-on-Si wafer. Data available at <http://dx.doi.org/10.15129/979dbf5d-b42a-4052-88b4-56a3dcd099>.

#### REFERENCES

- [1] S. Rajbhandari *et al.*, “A review of gallium nitride LEDs for multi-gigabit-per-second visible light data communications,” *Semicond. Sci. Technol.*, vol. 32, no. 2, p. 23001, Feb. 2017.
- [2] R. X. G. Ferreira *et al.*, “High Bandwidth GaN-Based Micro-LEDs for Multi-Gb/s Visible Light Communications,” *IEEE Photonics Technol. Lett.*, vol. 28, no. 19, pp. 2023–2026, Oct. 2016.
- [3] J. J. D. McKendry *et al.*, “Visible-Light Communications Using a CMOS-Controlled Micro-Light-Emitting-Diode Array,” *J. Light. Technol.*, vol. 30, no. 1, pp. 61–67, Jan. 2012.
- [4] K. Rae *et al.*, “Integrated dual-color InGaN light-emitting diode array through transfer printing,” in *2015 IEEE Photonics Conference (IPC)*, 2015, pp. 390–391.
- [5] A. J. Trindade *et al.*, “Nanoscale-accuracy transfer printing of ultra-thin AlInGaN light-emitting diodes onto mechanically flexible substrates,” *Appl. Phys. Lett.*, vol. 103, no. 25, p. 253302, Dec. 2013.

# Integration of micro-LED array on CMOS by transfer printing

J. F. C. Carreira, B. J. E. Guilhabert, J. J. D. McKendry, E. Xie, K. Mathieson, I. M. Watson, E. Gu, M. D. Dawson

Institute of Photonics, Department of Physics  
University of Strathclyde, Glasgow, UK  
e-mail address: jose.correia-carreira@strath.ac.uk

R. K. Henderson

Joint Research Institute for Integrated Systems  
University of Edinburgh, Edinburgh, UK

**Abstract**— Transfer printing of 450 nm-emitting micro-LED 8x8 arrays onto CMOS platform is reported. The pixels' average optical power density was measured at 4.4 W/cm<sup>2</sup> (50 A/cm<sup>2</sup>). Sub-nanosecond pulses as well as MHz bandwidth modulation are other modes of operation of the hybrid device.

**Keywords**—micro-LED; transfer printing; CMOS

## I. INTRODUCTION

Integration of GaN-based micro light emitting diodes (micro-LEDs) arrays with complementary metal oxide semiconductor (CMOS) control electronics is sought after for applications such as micro-displays [1], [2], light engines [2] and smart optical sources for lighting and communications [3], [4]. The existing integration approaches involve either 1) bump flip-chip of a pre-processed micro-LED array onto a CMOS chip, 2) monolithic GaN comprising LED and electronics, and 3) directly bonding GaN epilayers onto CMOS, with further processing into micro-LEDs [2]. In this work, we report the integration of fully fabricated micro-LEDs onto an off-the-shelf CMOS chip by transfer printing (TP). This prototype showcases the capability of integrating within current silicon foundries photonic components such as, CMOS drivers, by a deterministic, high accuracy pick-and-place technique [5]. This process can be further optimized to allow parallel and high-throughput assembly of multi-wavelength micro-LEDs with sub-micron pitch. In addition, the process does not require extra adhesion-promoting layers such as SU-8 or benzocyclobutene (BCB) and is fully carried out at low temperature (~ 100 °C) which allows the integration with other photonic materials and devices such as organic semiconductors, photodetectors and waveguides.

## II. FABRICATION AND CHARACTERIZATION OF THE TRANSFER PRINTED MICRO-LEDs

Blue micro-LED platelets (100x100 μm<sup>2</sup>) were fabricated from commercially available InGaN epistructures grown on silicon (111)-oriented substrate. The process to fabricate suspended micro-LED platelets, capable of being transfer printed, followed the typical GaN-based LED manufacture procedure. The suspended platelets were held on the growth wafer by sacrificial “anchors” – defined during the micro-LEDs mesa etching step (Fig. 1a) – to avoid their unintentional separation from the growth substrate. A hot 30%

potassium hydroxide (KOH) bath etched the Si(110) crystal directions underneath each platelet; Fig. 1.b) shows an interrupted process where the arrows indicate the etch direction. Arrays of suspended 2 μm-thin micro-LED platelets were obtained. The integration of these micro-LED platelets with other substrates was realized by a pick-and-place technique, known as transfer printing (TP). In order to pick up and manipulate these micro-LED platelets a PDMS micro-stamp was mounted onto a modified nanolithography system. The TP technique relies on the principle of reversible adhesion [6], where the stamp retrieves micro-LEDs from their growth substrate by maximizing the contact area between the platelets and the micro-stamp (Fig. 1c) and prints them onto different substrates by a competitive adhesion of the platelet with the receiving surface and the stamp. Fig. 1d) shows a micro-LED transfer printed onto a SU-8 coated patterned sapphire substrate (PSS). The interference fringes observed through the transparent GaN are associated with the air gap between the receiving substrate and the micro-LED backside, due to the inherent bowing of the suspended micro-LED resulting from the strained nature of InGaN epilayers grown on Si. An estimated 14% contact area was measured previously [7]. The TP process is nonetheless scalable and allows the sequential or parallel printing of micro-LEDs onto various receiving surfaces

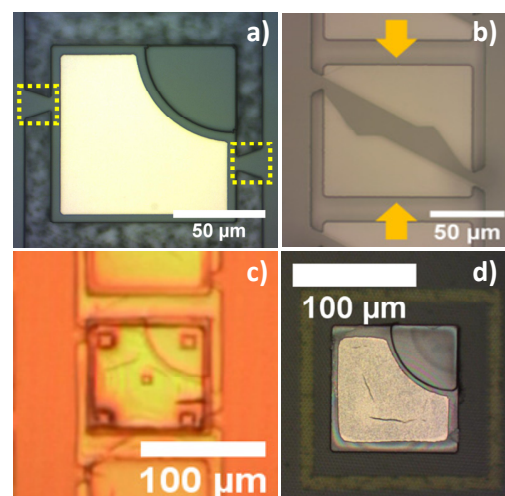


Fig. 1 – Optical photographs of a) 100x100 μm<sup>2</sup> micro-LED platelet; b) KOH underetch of a GaN platelet; c) micro-LED being pick-up from its growth substrate; d) micro-LED printed on SU-8 coated PSS.



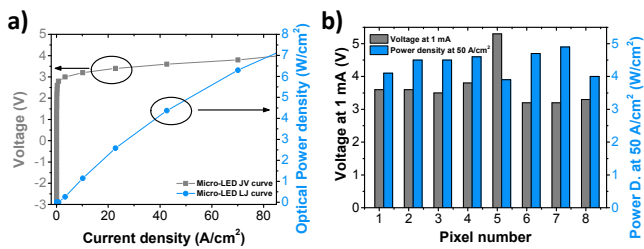


Fig. 2 – a) Current density-voltage-optical power curves of a TP micro-LED; b) voltage and optical power distribution of a 2x4 TP micro-LED array onto SU-8 coated PSS.

The electrical current vs forward bias performance and the optical output power density of a representative micro-LED printed on SU-8 coated PSS is shown in Fig. 2a). Fig. 2b) shows the voltage and optical power density distribution of a 2x4 micro-LED array on SU-8 coated PSS. The array forward bias at 1 mA presents an 18% variation around a mean value of 3.7 V, while the power distribution at 50 A/cm<sup>2</sup> shows an 8% variation around a mean value of 4.4 W/cm<sup>2</sup>. The good electrical and optical uniformity of this array suggest that the micro-LED fabrication and TP integration process are suitable to employ for integration with CMOS technologies.

### III. INTEGRATION WITH CMOS

An array of 8x8 micro-LEDs was transfer printed onto a CMOS chip (3.1 x 3.1 mm<sup>2</sup>) as shown in Fig. 3a). This chip active area consists of 16x16 *p*-drivers and a shared *n*-contact outer squared ring, as it was originally designed to receive a gold-bumped 16x16 flip-chip micro-LED array. In this work, the micro-LEDs were directly transfer printed onto the CMOS *p*-drivers' as shown in Fig. 3b), without intermediate bonding layer such SU-8 or BCB as it is commonly. Nonetheless, the micro-LEDs were strongly bonded to the CMOS drivers owing to the high quality of the backside of the micro-LEDs [7]. No displacement of the micro-LEDs was observed during subsequent processing. The electrical insulation and encapsulation of the micro-LEDs was made by a highly conformal coating of Parylene-C (4 μm thick), then vias were lithographically defined, exposing the micro-LEDs *n* and *p* contacts. Since the micro-LED backside is non-conductive (silicon nitride and Al(Ga)N graded buffer layer), the micro-LEDs were electrically addressed using neighboring CMOS *p*-driver and the micro-LED *n*-contact to the outer ring by Ti/Au (50/200 nm) metal tracks (Fig. 3 c) and d)).

### IV. CONCLUSION

In this work, we propose a novel approach of integrating photonic devices/materials, non-compatible with silicon foundries, with CMOS. By a pick-and-place technique, we have successfully transfer printed an 8x8 array of 100x100 μm<sup>2</sup> blue emitting micro-LEDs onto the CMOS active area.

### ACKNOWLEDGMENT

This work is supported by EPSRC UP-VLC grant (EP/K00042X/1) and EPSRC CDT in Medical Devices &

Health Technologies grant (EP/L015595/1). Plessey Semiconductors is acknowledged for providing GaN wafer. Data available at <http://dx.doi.org/10.15129/54622fe7-d798-4377-ac31-d38abed61f9e>.

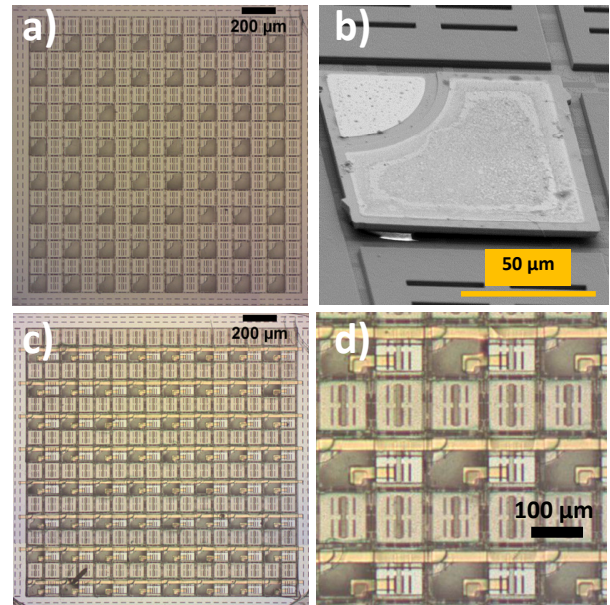


Fig. 3 – a) Photograph of the CMOS active area after transfer printing the 8x8 micro-LED array; b) Scanning electron microscope image of a TP micro-LED; c) Photograph of the CMOS active area after Ti/Au tracking; d) close-up view of c).

### REFERENCES

- [1] C. A. Bower *et al.*, "Emissive displays with transfer-printed assemblies of 8 μm × 15 μm inorganic light-emitting diodes," *Photonics Res.*, vol. 5, no. 2, p. A23, Apr. 2017.
- [2] F. Templier, "GaN-based emissive microdisplays: A very promising technology for compact, ultra-high brightness display systems," *J. Soc. Inf. Disp.*, vol. 24, no. 11, pp. 669–675, Nov. 2016.
- [3] J. McKendry *et al.*, "Individually Addressable AlInGaN Micro-LED Arrays With CMOS Control and Subnanosecond Output Pulses," *IEEE Photonics Technol. Lett.*, vol. 21, no. 12, pp. 811–813, Jun. 2009.
- [4] J. J. D. McKendry *et al.*, "Visible-Light Communications Using a CMOS-Controlled Micro-Light-Emitting-Diode Array," *J. Light. Technol.*, vol. 30, no. 1, pp. 61–67, Jan. 2012.
- [5] A. J. Trindade *et al.*, "Nanoscale-accuracy transfer printing of ultra-thin AlInGaN light-emitting diodes onto mechanically flexible substrates," *Appl. Phys. Lett.*, vol. 103, no. 25, p. 253302, Dec. 2013.
- [6] S. Kim *et al.*, "Microstructured elastomeric surfaces with reversible adhesion and examples of their use in deterministic assembly by transfer printing," *Proc. Natl. Acad. Sci. U. S. A.*, vol. 107, no. 40, pp. 17095–100, Oct. 2010.
- [7] A. J. Trindade *et al.*, "Heterogeneous integration of gallium nitride light-emitting diodes on diamond and silica by transfer printing," *vol. 23, no. 7, pp. 9329–9338, 2015.*



# Transfer-printed micro-LED and polymer-based transceiver for visible light communications

K. RAE,<sup>1,\*</sup> P. P. MANOUSIADIS,<sup>2</sup> M. S. ISLIM,<sup>3</sup> L. YIN,<sup>3</sup>  
J. CARREIRA,<sup>1</sup> J. J. D. MCKENDRY,<sup>1</sup> B. GUILHABERT,<sup>1</sup>  
I. D. W. SAMUEL,<sup>2</sup> G. A. TURNBULL,<sup>2</sup> N. LAURAND,<sup>1</sup> H. HAAS,<sup>3</sup>  
AND M. D. DAWSON<sup>1</sup>

<sup>1</sup>*Institute of Photonics, Department of Physics, SUPA, University of Strathclyde, Glasgow, UK*

<sup>2</sup>*Organic Semiconductor Centre, School of Physics and Astronomy, SUPA, University of St Andrews, UK*

<sup>3</sup>*LiFi R&D Centre, Institute for Digital Communications, University of Edinburgh, UK*

\**katherine.rae@glasgow.ac.uk*

**Abstract:** Visible light communications (VLC) is an emerging technology that uses LEDs, such as found in lighting fixtures and displays, to transmit data wirelessly. Research has so far focused on LED transmitters and on photoreceivers as separate, discrete components. Combining both types of devices into a single transceiver format will enable bi-directional VLC and offer flexibility for the development of future advanced VLC systems. Here, a proof of concept for an integrated optical transceiver is demonstrated by transfer printing a microsize LED, the transmitter, directly onto a fluorescent optical concentrator edge-coupled to a photodiode, the receiver. This integrated device can simultaneously receive (downlink) and transmit (uplink) data at rates of 416 Mbps and 165 Mbps, respectively. Its capability to operate in optical relay mode at 337 Mbps is experimentally demonstrated.

Published by The Optical Society under the terms of the [Creative Commons Attribution 4.0 License](https://creativecommons.org/licenses/by/4.0/). Further distribution of this work must maintain attribution to the author(s) and the published article's title, journal citation, and DOI.

## 1. Introduction

InGaN-based visible light emitting diodes (LEDs) are widely used in solid-state lighting and display technologies [1, 2]. Because of their high modulation bandwidth, ranging from 20 MHz for large-area LEDs [3, 4] up to several hundreds of megaHertz for microsize LEDs ( $\mu$ LEDs) [5, 6], they can also double as wireless transmitters in visible light communications (VLC) applications [7]. In particular,  $\mu$ LEDs have been demonstrated in VLC links with data transmission rates approaching 8 Gbps [6]. In a VLC system, LED transmitters are intensity modulated at high speeds and photoreceivers convert the optical signals into the electric domain. Research has so far mainly considered LED transmitters and photoreceivers as discrete devices. VLC demonstrations have also been principally unidirectional, the downlink using VLC and the uplink another technology like Wi Fi (wireless fidelity) or infrared communications. Here, in order to enable bi-directional VLC, we devise an integrated transceiver with a  $\mu$ LED as the transmitter. The signal-to-noise ratio (SNR) at the receiver and the overall bandwidth are key factors that affect the performance of VLC. Advanced modulation schemes, e.g. orthogonal frequency division multiplexing (OFDM), are often implemented in order to maximize utilization of the available bandwidth [6]. The size of the photoreceiver can be increased to enhance the SNR but this is at the detriment of the bandwidth as photoreceivers with large active areas tend to be slow [8]. One solution is to keep the active area of the receiver small and increase the amount of light arriving onto it with an optical element known as a fluorescent concentrator [9, 10], the downshifted light is waveguided to the edge of the concentrator where a small area receiver is positioned. Unlike lenses, these fluorescent concentrators make use of fluorescence (and an accompanying Stokes shift) and not exclusively reflection and refraction and can therefore be used to circumvent the étendue limit. This enables the collection of an incident signal over a wide

area and its concentration onto the detector whilst maintaining high bandwidth and excellent field of view of the receiver. In the following we report an integrated optical transceiver that combines a 450 nm transfer printed (TP)  $\mu$ LED (the transmitter) with such a fluorescent optical concentrator (the receiver). Transfer printing is a heterogeneous integration technique where micro- and nano-sized optoelectronic devices are "printed" onto non-native, capability enhancing, substrates [11–19]. The advantage of a TP  $\mu$ LED is for integration of the transmitter with the concentrator receiver in a small form factor. Using a full  $\mu$ LED-on-sapphire device, rather than a TP  $\mu$ LED, would lead to a device with at least twice the thickness and furthermore raise the issue of cross-talk at the receiver side. The performance of GaN-on-sapphire  $\mu$ LEDs for VLC is typically better than GaN-on-Si devices [20] in terms of bandwidth and optical power. An alternative would be to transfer print  $\mu$ LEDs fabricated on sapphire and then released from their substrate by laser lift off [11]. On the other hand, the utilization of Si offers cost effectiveness, potential for scalability and a wide choice of substrate removal approaches. We note that TP  $\mu$ LEDs used in this demonstration have been shown to have modulation bandwidths of 100s of MHz, and data transmission rates of 120 Mbps on flexible and silica substrates [21, 22].

We describe the design and fabrication of an optical transceiver device and assess its operation using OFDM as the VLC modulation scheme. The device can simultaneously receive and transmit VLC signals, i.e. it can implement both the VLC downlink and uplink. It benefits from the wide-angle detection capability of the optical concentrator and can also operate as an optical relay, thereby providing a solution to the line-of-sight limitations of indoor communications [9].

## 2. Design and fabrication

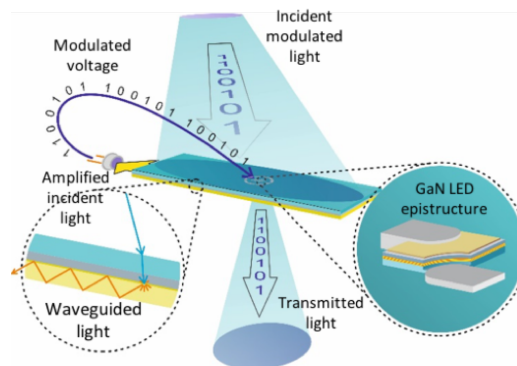


Fig. 1. Illustration of the optical transceiver concept. External modulated light is collected and concentrated by the optical antenna (fluorescent concentrator). This concentrated light is detected by an avalanche photodiode (APD) on the edge of the transceiver. For operation as a repeater, this signal is then demodulated, before being re-modulated and used to drive the transfer printed  $\mu$ LED transmitter.

The schematic in Fig. 1 shows the concept of the integrated optical transceiver device with the  $\mu$ LED on the top surface of the optical concentrator. Fabrication first entails TP the blue-emitting  $\mu$ LED onto a 1 mm-thick 25 mm  $\times$  75 mm glass substrate (microscope slide). TP makes use of the reversible adhesion of an elastomeric stamp to pick-up, transfer and print objects (here the  $\mu$ LED) onto a non-native substrate. Previously used in the fabrication of mechanically-flexible inorganic semiconductor devices [17, 18], we have demonstrated the technique for printing InGaN  $\mu$ LEDs with  $< 200$  nm resolution onto optically inactive substrates [21, 23] and onto multi-color devices for VLC applications [22, 24]. Prior to TP, the 100  $\mu$ m  $\times$  100  $\mu$ m  $\mu$ LED is fabricated in a suspended format from a GaN-on-Si LED epistructure. The Si substrate is

underetched with potassium hydroxide (KOH) to leave ultra-thin  $\mu$ LED platelets, suspended by 10  $\mu$ m-wide anchors that can be easily removed from their growth wafer with an elastomeric stamp. Figure 2(a) shows a schematic of the TP process. After TP, the  $\mu$ LED contacts are defined by photolithography [21]. Figures 3(a)–3(c) show microscope images of the  $\mu$ LED TP on the glass slide (seen on the bottom right of the three images) with metal tracks added. The metal track design gives scope to print a  $6 \times 6$  array of  $\mu$ LEDs, but this is beyond this first device demonstration. Figure 3(d) gives the current-voltage characteristic for such a TP  $\mu$ LED, these start to emit light around 3.5 V. It is important to note that these  $\mu$ LEDs can have some leakage current, and so we only see light-emission after around 1 mA of drive current. This is possibly due to damage to the device sidewalls occurring when the Si substrate is removed, leaving a rough surface and increasing opportunities for tunneling. The current-optical power characteristic for these TP  $\mu$ LEDs is given in Fig. 3(e) and the emission spectrum when printed on the glass slide can be seen in Fig. 3(f). These TP  $\mu$ LEDs emit at 460 nm, and achieve over 50  $\mu$ W of optical power at 3.5 mA.

Before removal from their Si substrate, these  $\mu$ LEDs have a lower turn on voltage and begin to emit light at around 2.8 V as reported in [21]. The optical power of 100  $\mu$ m x 100  $\mu$ m InGaN-on-Si  $\mu$ LEDs, fabricated in the same way but without any underetching of the Si substrate, is difficult to measure though, as the flip-chip configuration of these  $\mu$ LEDs means light is not significantly transmitted until the Si substrate is removed. Top-emitting, broad-area,  $\mu$ LEDs processed on the same wafer as the TP  $\mu$ LEDs used in this work show a spectral emission around 450 nm. We attribute the 10 nm redshift between the spectral emission on Si and the TP  $\mu$ LEDs (see Fig. 3(f)) to strain effects induced when the  $\mu$ LED is removed from its growth substrate.

The glass substrate integrated with the TP  $\mu$ LED forms the top cladding of the transceiver. The other part of the transceiver is fabricated by blade coating a 70 nm-thick fluorescent film on a second microscope slide – this glass slide is the bottom cladding of the fluorescent concentrator, see Fig. 2(b). The fluorescent material is a conjugated poly (p-phenylene vinylene) copolymer, commonly known as “super yellow” (SY), acquired from Merck KGaA (PDY 132). The absorption and typical emission of SY respectively peak at 450 nm and 560 nm [25]. While we focus here on demonstrating a device concept and a stability study was not conducted, we did not observe any degradation of the fluorescence during experiments. We note that SY is a relatively stable copolymer, in widespread use in OLEDs, and given the device geometry, it is encapsulated by glass, which is beneficial for stability. Initially a 4 mg/ml solution of SY in chlorobenzene was prepared. An automatic film applicator (ZAA 2300, Zehntner GmbH) was used to blade coat the solution onto the glass. The temperature was set to 40°C, the speed to 30 mm/s and the height of the blade (ZUA 2000.80) was 100  $\mu$ m above the microscope slide. A circular area (diameter 3 mm) of the SY film directly under the targeted position of the TP LED was mechanically removed. This is to prevent absorption of  $\mu$ LED light emitted from the TP  $\mu$ LED, which falls within the absorption band of SY, by the optical concentrator as this would otherwise cause interference, at the receiver end, when the device simultaneously transmits and receives. Furthermore, the  $\mu$ LED transmits through the glass cladding as shown in Fig. 1 and any absorption would diminish the optical power of the transmitter. To finalize the transceiver, the microscope slide with the SY film was coated with the optical epoxy NOA 13685 (Norland Inc.), placed in contact with the backside of the glass cladding on which the  $\mu$ LED was printed, and UV cured (365 nm, 7 J/cm<sup>2</sup>). For the experiments described in section 3, the edge of the optical concentrator was coupled to a Hamamatsu (S8664-50K) avalanche photodiode (APD). This APD has a peak sensitivity at 600 nm (spectral response range 320–1000 nm), a quantum efficiency of 70 % (at 420 nm) [8], and a 3-dB bandwidth of 60 MHz but the overall bandwidth of the system is set by the pulse-shaping filter (see section 3 for details).



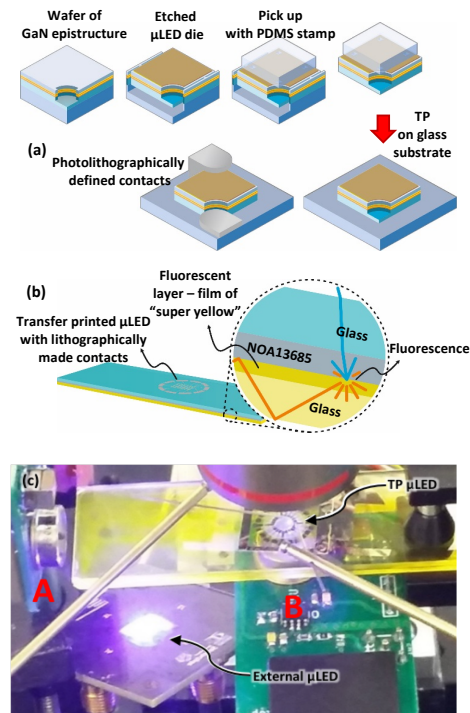


Fig. 2. (a) Illustration of the transfer printing process. (b) Schematic representation of the structure of the device. The inset shows the different layers of the fluorescent concentrator (Glass/Epoxy/Fluorescent medium/Glass). (c) Photograph of the setup used to characterize the optical transceiver device.

### 3. VLC demonstration and discussion

Two separate experiments were performed to demonstrate the capability of the transceiver device for VLC. The first consisted of operating the device to simultaneously transmit and receive independent data (transceiver mode). In the second experiment the device was operated to receive and re-transmit data (optical relay mode). In both these experiments, an external  $\mu$ LED source (respectively blue, 450 nm, and 3 violet, 405 nm,  $\mu$ LEDs in series) and a second APD are used to respectively send a signal to and receive a signal from the transceiver. The typical electrical-to-optical modulation bandwidth of these external LEDs is above 100 MHz. The maximum optical power is approximately 9 mW at 175 mA and 9.5 mW at 45 mA for the blue and 3 series violet emitting LEDs, respectively. Information on the design, fabrication, and characteristics of the blue  $\mu$ LED used as an external source in this demonstration can be found in [26]. The power versus injection current for the 3 violet  $\mu$ LEDs is plotted in Fig. 4.

The setup used for the experiments is shown in Fig. 2(c). The TP LED and the external LED source are driven with a direct current (DC) bias from a power supply combined by a bias-tee with a modulated alternating current (AC) signal from a signal generator. The modulated signal is based on an OFDM data encoding scheme. To generate this OFDM signal, an incoming stream of bits was modulated into  $M$ -ary quadrature amplitude modulated ( $M$ -QAM) symbols where  $M$  is the constellation size. Hermitian symmetry and fast Fourier transformation (FFT) operation are then applied to NFFT  $M$ -QAM symbols. 1024 subcarriers are equally spaced over the system bandwidth. The resulting OFDM stream drives the  $\mu$ LEDs through an arbitrary waveform



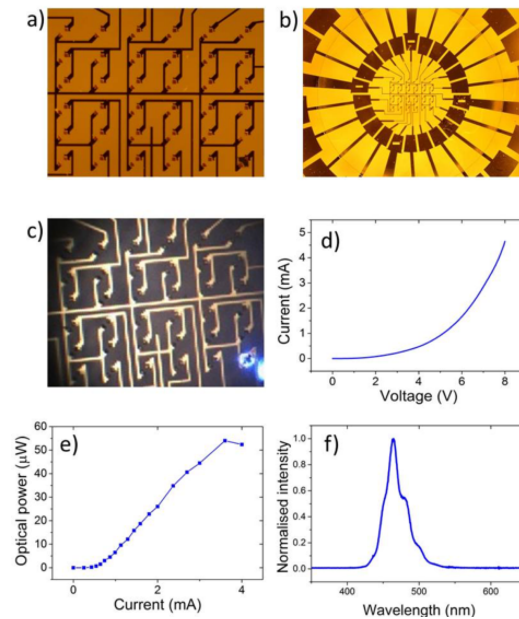


Fig. 3. (a) and (b) photographs of the TP  $\mu$ LED and metal tracks on the fluorescent concentrator. (c) Photograph of TP  $\mu$ LED illuminating. (d) Current-voltage curve, (e) power-current curve, and (f) spectral characteristics of the TP  $\mu$ LED on the microscope slide.

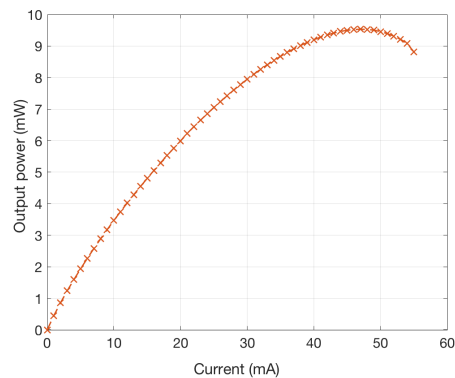


Fig. 4. Optical power – current characteristic of the 3 violet  $\mu$ LED pixels in series used in the optical repeater demonstration.

generator (AWG) Agilent®81180A with a sampling frequency of 720 MS/sec (transceiver mode experiment) or 1200 MS/sec (optical relay mode experiment). A root raised cosine (RRC) pulse shaping filter is used with an oversampling factor of 8, which results in a single side modulation bandwidth of 45 MHz for the transceiver mode experiment and 75 MHz for the optical relay mode experiment. This is because of the higher SNR in the optical relay experiment, which we believe is related to the addition of a small lens directly under the TP  $\mu$ LED (see below). Light from the external  $\mu$ LED source is collected by the optical concentrator and waveguided to the edge facet of the structure to the APD at the position labeled A in Fig. 2(c). This optical

link is referred to hereafter as link A, a spectrum of the light collected here is shown in Fig. 5. This shows a major peak at 563 nm from the color-converted SY light and a smaller peak at 460 nm from unconverted blue light from the incident  $\mu$ LED. Light from the TP  $\mu$ LED (460 nm) is emitted down and straight through the glass and epoxy layers to the external APD at the position labeled B in Fig. 2(c). This optical link is referred to in the following as link B. The data rates given in the following are for a bit error rate (BER) target of  $3.8 \times 10^{-3}$  [27]. The drive conditions in this first experiment are 6.1 V and 3 mA for the TP  $\mu$ LED and the 4.1 V and 24 mA for the external  $\mu$ LED. The optical power of these  $\mu$ LEDs is approximately  $44.5 \mu$ W for the TP  $\mu$ LED and 2 mW for the external  $\mu$ LED at these drive currents. The typical electrical-to-optical modulation bandwidth for the TP  $\mu$ LEDs on glass is around 50 MHz [23].

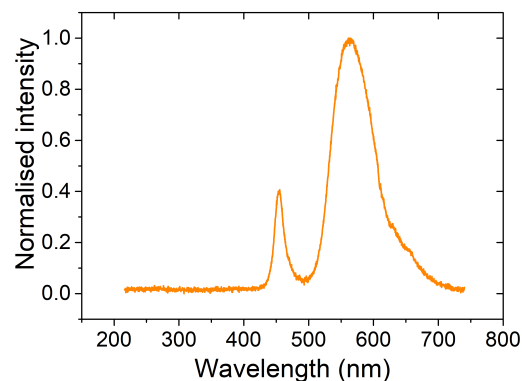


Fig. 5. Optical spectrum of the light at the receiver (position B). The spectrum of the light transmitted by the device (at position A) can be seen in Fig. 3f).

The SNR for both links is shown in Fig. 6(a). The higher SNR for link A is due to the higher optical power of the external  $\mu$ LED. Figure 6(b) shows the data rates for both link A and link B. The link B with the TP  $\mu$ LED transmitter reaches a data rate of 165 Mbps. The link between the external  $\mu$ LED and the transceiver (link A) has a data transmission rate of 416 Mbps. These performance values are consistent with the SNR of both links. The sharp drop in the SNR as the modulation bandwidth is increased past 40 MHz is attributed to the pulse shaping filter.

The second experiment demonstrates the integrated transceiver operating as an optical relay in decode and forward regime. The experimental setup is similar, but the external source is an array of 3 violet LEDs (405 nm) in place of the blue LED. The violet LEDs are used in this case to boost the received optical power at APD A. It also shows the wavelength flexibility at detection of the device while still demonstrating a viable VLC system, with violet LEDs an emerging enabling technology for white light solid state lighting as well as for communications [6, 28, 29]. The three violet  $\mu$ LEDs were driven in series, with a combined current of 30 mA (at 12V), the optical power of the three violet  $\mu$ LEDs was 7 mW. A lens (focal length 2.5 mm, diameter 2.5 mm) is also added onto the underside of the device, directly under the TP  $\mu$ LED, to increase the light collected by APD B. The emitted light of the external LEDs is collected by the fluorescent concentrator and detected at APD A. This detected signal is sent to an oscilloscope (MSO7104B) and demodulated offline in MATLAB, where all the signal processing operations are performed as described in [30]. The demodulated -QAM symbols are then remodulated and fed to the TP  $\mu$ LED. The TP  $\mu$ LED was driven at 1 mA (at 5.7V). The three violet  $\mu$ LEDs have a modulation bandwidth of 350 MHz, while the TP  $\mu$ LEDs typically have electrical-to-optical modulation bandwidths of just over 20 MHz at 1 mA [23]. The light from the TP  $\mu$ LED is emitted through the glass structure and is in turn detected at APD B. Below forward error correction (FEC) level of  $3.8 \times 10^{-3}$ , the data rate is 375 Mbps for link A and 337 Mbps for link B, as shown in Fig.

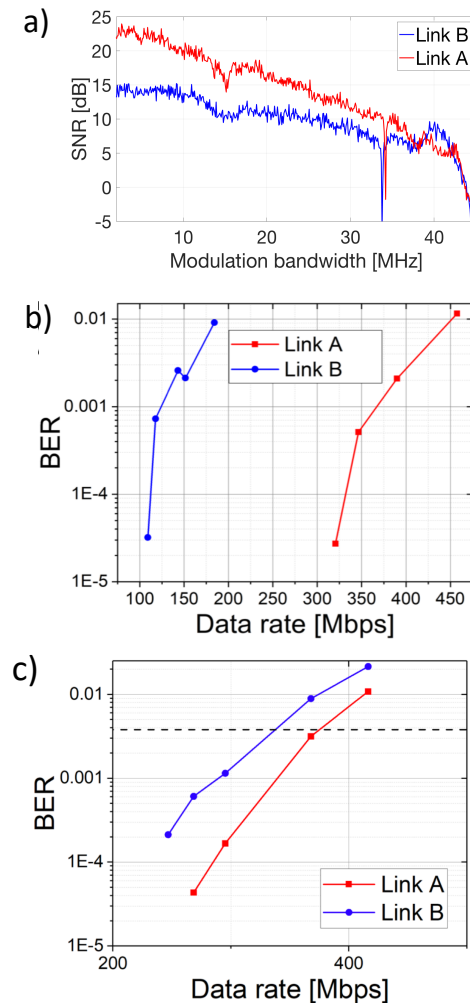


Fig. 6. Transceiver mode operation; (a) The SNR of external  $\mu$ LED (Link A) and TP  $\mu$ LED (Link B). (b) BER vs data transmission rates for link A and link B. (c) The BER results for link A and link B when the device is working as an optical relay. The dip in the SNR of both links seen in (a) around 35 MHz is an artefact from the measurement equipment used in this demonstration, and is not caused by the devices.

6(c). The optical relay functions at up to 337 Mbps, as it is limited by the speed of the slowest component – in this case the TP  $\mu$ LED. The improvement in data transmission rate from the TP  $\mu$ LED (link B) between the first experiment (165 Mbps) and the second experiment (337 Mbps) is attributed to the integration of a lens to more effectively transmit light from the TP  $\mu$ LED to the APD.

This is a first concept device demonstration, and tests are done at short-range in order to define the ultimate performance. For longer range VLC demonstrations, it can be noted that  $\mu$ LEDs have been demonstrated in free-space VLC at data transmission rates in excess of 1 Gb/s over distances of up to several meters. Hence we believe this concept device could potentially be extended to communicate over comparable distances in the future [31, 32]. Transfer printing

arrays of  $\mu$ LEDs, rather than a single  $\mu$ LED as in this demonstration, will increase the light output power and therefore the range of the device. Additionally, increasing the light output power will increase the SNR, and consequently the data transmission rate. As seen in Fig. 3(e), these  $\mu$ LEDs typically rollover at 4–6 mA, and so can't be driven to high currents - limiting their power. Printing an array of  $\mu$ LEDs would also go some way to negating this issue.

One of the main visions of VLC is that conventional room lighting can be used to transmit data through free space. We therefore chose here GaN-on-sapphire  $\mu$ LEDs as the external sources (rather than the same  $\mu$ LEDs used for TP but before removal from their Si substrate), as they are the conventional materials for solid-state lighting fixtures.

In any real-life VLC system, it would be important to minimize the required power of this device to integrate with other electronic components; one way to reduce this would be as in [33].

While this demonstration has focused on the VLC applications of this device, it could just as easily be applied to biomedical applications, such as optogenetics and biosensing, as demonstrated in [34–37], to wirelessly transmit signals to analysis equipment.

#### 4. Conclusion

In conclusion, we have demonstrated, for the first time to our knowledge an integrated optical transceiver and repeater for visible light communications. The device is based on a transfer printed  $\mu$ LED as the transmitter, and a fluorescent concentrator as the receiver. It was experimentally demonstrated that the optical transceiver can achieve beyond 100 Mbps data rates for reception and transmission. We believe that this new VLC device will be very suitable for implementing smart devices and enable IoT applications.

Supporting data can be found at DOI: 10.15129/7c4e99c7-94c5-4e69-b1b5-1d9e962cf164.

#### Funding

Engineering and Physical Sciences Research Council (EPSRC) (EP/K00042X/1).

#### Acknowledgments

The authors would like to acknowledge Erdan Gu, Xiangyu Wu, and Enyuan Xie for the fabrication of the external  $\mu$ LED devices. IDWS is a Royal Society Wolfson research merit award holder.

#### References

1. S. Nakamura and M. R. Krames, "History of gallium-nitride-based light-emitting diodes for illumination," *Proceedings of the IEEE* **101**(10), 2211–2220 (2013).
2. Y. Zhao, H. Fu, G. T. Wang, and S. Nakamura, "Toward ultimate efficiency: progress and prospects on planar and 3D nanostructured nonpolar and semipolar InGaN light-emitting diodes," *Adv. Opt. Photon.* **10**(1), 246–308 (2018).
3. H. Haas, L. Yin, Y. Wang, and C. Chen, "What is LiFi?" *J. Light. Technol.* **34**(6), 1533–1544 (2015)
4. S. Rajbhandari, J. J. D. McKendry, J. Herrnsdorf, H. Chun, G. Faulkner, H. Haas, I. M. Watson, D. O'Brien, and M. D. Dawson, "A review of Gallium Nitride LEDs for multi-gigabit-per-second visible light data communications," *Semicond. Sci. Technol.* **32**(2), 1–44 (2016).
5. J. J. D. McKendry, R. P. Green, A. E. Kelly, Z. Gong, B. Guilhabert, D. Massoubre, E. Gu, and M. D. Dawson, "High-speed visible light communications using individual pixels in a micro light-emitting diode array," *IEEE Photon. Technol. Lett.* **22**(18), 1346–1348 (2010).
6. M. S. Islim, R. X. Ferreira, X. He, E. Xie, S. Videv, S. Viola, S. Watson, N. Bamiedakis, P. V. Plenty, I. H. White, A. E. Kelly, E. Gu, H. Haas, and M. D. Dawson, "Towards 10 Gb/s OFDM-based visible light communication using a GaN violet micro-LED," *Photon. Res.* **5**(2), A35–A43 (2017).
7. H. Kopetz, "Real-time systems: design principles for distributed embedded applications," Springer (1997).
8. "Hamamatsu Photonics: Si APD," [Online] <http://hamamatsu.com/jp/en/product/category/3100/4003/4110/index.html>. [Accessed: 27 Jan 2017].
9. P. P. Manousiadis, S. Rajbhandari, R. Mulyawan, D. A. Vithanage, H. Chun, G. Faulkner, D. O'Brien, G. A. Turnbull, S. Collins, and I. D. W. Samuels, "Wide field-of-view fluorescent antenna for visible light communications beyond the étendue limit," *Optica* **3**(7), 702–706 (2016).
10. T. Peyronel, K. J. Quirk, S. C. Wang, and T. G. Tietze, "Luminescent detector for free-space optical communication," *Optica* **3**(7), 787–792 (2016).







11. T.-I. Kim, Y. H. Jung, J. Song, D. Kim, Y. Li, H.-S. Kim, I.-S. Song, J. J. Wierer, H. A. Pao, Y. Huang, and J. A. Rogers "High-efficiency, microscale GaN light-emitting diodes and their thermal properties on unusual substrates," *Small* **8**(11), 1643–1649 (2012).
12. R.-H. Kim, S. Kim, Y. M. Song, H. Jeong, T. Kim, J. Lee, X. Li, K. D. Choquette, and J. A. Rogers "Flexible vertical light emitting diodes," *Small* **8**(20), 3123–3128 (2012).
13. S.-I. Park, Y. Xiong, R.-H. Kim, P. Elvikis, M. Meitl, D.-H. Kim, J. Wu, J. Yoon, C.-J. Yu, Z. Liu, Y. Huang, K.-C. Hwang, P. Ferreira, X. Li, K. Choquette, and J. A. Rogers "Printed assemblies of inorganic light-emitting diodes for deformable and semitransparent displays," *Science* **325**(5943), 977–981 (2009).
14. A. De Groot, P. Cardile, A. Z. Subramanian, A. M. Fecioru, C. Bower, D. Delbecke, R. Baets, and G. Roelkens, "Transfer-printing-based integration of single-mode waveguide-coupled III-V-on-silicon broadband light emitters," *Opt. Express* **24**(13), 13754–13762 (2016).
15. B. Guilhabert, A. Hurtado, D. Jevtics, Q. Gao, H. H. Tan, C. Jagadish, and M. D. Dawson, "Transfer printing of semiconductor nanowires with lasing emission for controllable nanophotonic device fabrication," *ACS Nano* **10**(4), 3951–3958 (2016).
16. D. Kang, B. Gai, B. Thompson, S. M. Lee, N. Malmstadt, and J. Yoon, "Flexible opto-fluidic fluorescence sensors based on heterogeneously integrated micro-VCSELs and silicon photodiodes," *ACS Photonics* **3**(6), 912–918 (2016).
17. D.-H. Kim, R. Ghaffari, N. Lu, and J. A. Rogers, "Flexible and stretchable electronics for biointegrated devices," *Annu. Rev. Biomed. Eng.* **14**, 113–128 (2012).
18. S. Chary, J. Tamiel, and K. Turner, "A microfabricated gecko-inspired controllable and reusable dry adhesive," *Smart Mater. Struct.* **22**(2), 25013 (2013).
19. C.-H. Cheng, T.-W. Huang, C.-L. Wu, M. K. Chen, C. H. Chu, Y.-R. Wu, M.-H. Shih, C.-K. Lee, H.-C. Kuo, D. P. Tsai, and G.-R. Lin, "Transferring the bendable substrateless GaN LED grown on a thin C-rich SiC buffer layer to flexible dielectric and metallic plates," *J. Mater. Chem. C* **5**(3), 607–617 (2016).
20. P. Tian, J. J. D. McKendry, Z. Gong, S. Zhang, S. Watson, D. Zhu, I. M. Watson, E. Gu, A. E. Kelly, C. J. Humphreys, and M. D. Dawson, "Characteristics and applications of micro-pixelated GaN-based light emitting diodes on Si substrates," *J. Appl. Phys.* **115**, 033112 (2014).
21. A. J. Trindade, B. Guilhabert, D. Massoubre, D. Zhu, N. Laurant, E. Gu, I. M. Watson, C. J. Humphreys, and M. D. Dawson, "Nanoscale-accuracy transfer printing of ultra-thin AlInGaN light-emitting diodes onto mechanically flexible substrates," *Appl. Phys. Lett.* **103**(25), 253302 (2013).
22. K. Rae, C. Foucher, B. Guilhabert, M. S. Islam, L. Yin, D. Zhu, R. A. Oliver, D. J. Wallis, H. Haas, N. Laurant, and M. D. Dawson "InGaN micro-LEDs integrated onto an ultra-thin, colloidal quantum dot functionalized glass platform," *Opt. Express* **25**(16) 19179–19184 (2017).
23. A. J. Trindade, B. Guilhabert, E. Xie, R. Ferreira, J. J. D. McKendry, D. Zhu, N. Laurant, E. Gu, D. J. Wallis, I. M. Watson, C. J. Humphreys, and M. D. Dawson "Heterogeneous integration of gallium nitride light-emitting diodes on diamond and silica by transfer printing," *Opt. Express* **23**(7), 9329–9338 (2015).
24. K. Rae, E. Y. Xie, A. J. Trindade, B. Guilhabert, R. X. Ferreira, J. J. D. McKendry, D. Zhu, N. Laurant, E. Gu, I. M. Watson, C. J. Humphreys, D. J. Wallis, and M. D. Dawson "Integrated dual-color InGaN light-emitting diode array through transfer printing," in the proceedings of IEEE conference on Photonics (IPC, 2015), pp. 390–391.
25. Sigma-Aldrich Super Yellow datasheet: [www.sigmaaldrich.com/catalog/product/aldrich/900438?lang=en&region=GB](http://www.sigmaaldrich.com/catalog/product/aldrich/900438?lang=en&region=GB) (visited August 2018).
26. J. M. M. Santos, S. Rajbhandari, D. Tsonev, H. Chun, B. Guilhabert, A. B. Krysa, A. E. Kelly, H. Haas, D. C. O'Brien, N. Laurant, and M. D. Dawson, "Visible light communication using InGaN optical sources with AlInGaP nanomembrane downconverters," *Opt. Express* **24**(9), 10020–10029 (2016).
27. F. Chang and V. S. Corp, "Forward error correction for 100 G transport networks," *IEEE Commun. Mag.* **48**(3), 48–55 (2010).
28. P. F. Smet, A. B. Parmentier, and D. Poelman, "Selecting conversion phosphors for white light-emitting diodes," *J. Electrochem. Soc.* **158**(6), R37–R54 (2011).
29. Soraa, blue-free lighting: [www.soraa.com/learn/science/blue-free-light-what-you-need-know](http://www.soraa.com/learn/science/blue-free-light-what-you-need-know) (visited August 2018).
30. D. Tsonev, H. Chun, S. Rajbhandari, J. J. D. McKendry, S. Videv, E. Gu, M. Haji, S. Watson, A. E. Kelly, G. Faulkner, M. D. Dawson, H. Haas, and D. O'Brien, "A 3-Gb/s single-LED OFDM-based wireless VLC link using a Gallium Nitride micro-LED," *IEEE Photon. Technol. Lett.* **26**(7), 637–640 (2014).
31. S. Rajbhandari, A. V. N. Jalajakumari, H. Chun, G. Faulkner, K. Cameron, R. Henderson, D. Tsonev, H. Haas, E. Xie, J. J. D. McKendry, J. Herrnsdorf, R. Ferreira, E. Gu, M. D. Dawson, and D. O'Brien, "A multigigabit per second integrated multiple-input multiple-output VLC demonstrator," *J. Light. Technol.* **35**(20), 4358–4365 (2017).
32. Z. Lu, P. Tian, H. Chen, I. Baranowski, H. Fu, X. Huang, J. Montes, Y. Fan, H. Wang, X. Liu, R. Liu, and Y. Zhao "Active tracking system for visible light communication using a GaN-based micro-LED and NRZ-OOK," *Opt. Express* **25**(15), 17971–17981 (2017).
33. C. K. Jeong, K.-I. Park, J. H. Son, G.-T. Hwang, S. H. Lee, D. Y. Park, H. E. Lee, H. K. Lee, M. Byuna, and K. J. Lee "Self-powered fully-flexible light-emitting system enabled by flexible energy harvester," *Energy Environ. Sci.* **7**(12), 4035–4043 (2014).
34. H. E. Lee, J. Choi, S. H. Lee, M. Jeong, J. H. Shin, D. J. Joe, D. Kim, C. W. Kim, J. H. Park, J. H. Lee, D. Kim, C. S. Shin, and K. J. Lee, "Monolithic flexible vertical GaN light-emitting diodes for a transparent wireless brain optical stimulator," *Adv. Mater.* **30**, 1800649 (2018).

35. S. H. Lee, K.-I. Park, C. Huh, M. Koo, H. G. Yoo, S. Kim, C. S. Ah, G. Y. Sung, and K. J. Lee “Water-resistant flexible GaN LED on a liquid crystal polymer substrate for implantable biomedical applications,” *Nano Energy* **1**, 145–152 (2012).
36. S. H. Lee, J. Kim, J. H. Shin, H. E. Lee, I.-S. Kang, K. Gwak, D.-S. Kim, D. Kim, and K. J. Lee “Optogenetic control of body movements via flexible vertical light-emitting diodes on brain surface,” *Nano Energy* **44**, 447–455 (2018).
37. H. E. Lee, S. H. Lee, M. Jeong, J. H. Shin, Y. Ahn, D. Kim, S. H. Oh, S. H. Yun, and K. J. Lee, “Trichogenic photostimulation using monolithic flexible vertical AlGaInP light-emitting diodes,” *ACS Nano* **12**(12), 9587–9595 (2018).





# On-chip GaN-based dual-color micro-LED arrays and their application in visible light communication

J. F. C. CARREIRA,<sup>1,3,4</sup>  E. XIE,<sup>1,3,5</sup>  R. BIAN,<sup>2,3</sup> C. CHEN,<sup>2</sup> J. J. D. MCKENDRY,<sup>1</sup>  B. GUILHABERT,<sup>1</sup>  H. HAAS,<sup>2</sup>  E. GU,<sup>1</sup> AND M. D. DAWSON<sup>1</sup> 

<sup>1</sup>*Institute of Photonics, Department of Physics, University of Strathclyde, Glasgow G1 1RD, UK*

<sup>2</sup>*Institute for Digital Communications, Li-Fi R&D Centre, University of Edinburgh, Edinburgh EH9 3JL, UK*

<sup>3</sup>*These authors contributed equally to this work*

<sup>4</sup>*jose.correia-carreira@strath.ac.uk*

<sup>5</sup>*enyuan.xie@strath.ac.uk*

**Abstract:** Integrated multi-color micron-sized light emitting diode (micro-LED) arrays have been demonstrated in recent years for display applications; however, their potential as visible light communication (VLC) transmitters is yet to be fully explored. In this work, we report on the fabrication and characterization of on-chip dual-color micro-LED arrays and their application in VLC. For this purpose, blue-green and blue-violet micro-LED arrays were fabricated by transfer printing blue-emitting micro-LEDs onto the substrate of green and violet micro-LEDs, respectively. The potential of these dual-color micro-LED arrays as VLC transmitters is demonstrated with respective error-free data rates of 1.79 and 3.35 Gbps, achieved by the blue-green and blue-violet devices in a dual wavelength multiplexing scheme.

Published by The Optical Society under the terms of the [Creative Commons Attribution 4.0 License](https://creativecommons.org/licenses/by/4.0/). Further distribution of this work must maintain attribution to the author(s) and the published article's title, journal citation, and DOI.

## 1. Introduction

The interest in gallium nitride (GaN)-based micron-sized light emitting diodes (micro-LEDs), of lateral dimension smaller than 100  $\mu\text{m}$ , has increased dramatically in recent years [1]. GaN-based micro-LEDs offer exceptional brightness, contrast, fast response time, long operation lifetime, and low power consumption, which have facilitated their application in several fields, such as microdisplays [2–4], visible light communication (VLC) [5,6], fluorescence sensing [7], and optoelectronic tweezing [8]. Despite the huge success of monochromatic GaN-based micro LED with different configurations for the aforementioned applications, a general thread common to many applications is the desire for different color micro-emitters on a single chip platform. Multi-color emission can be achieved by using color converters to downshift the GaN-based micro-LED blue emission to longer wavelengths. However, due to the color converters' lower efficiency, slow response time, and short lifespan, this solution is unsuitable for many applications [3]. Although possible [9–11], the growth of highly efficient inorganic red, green, and blue emitting materials on a single wafer is still in its early stages and is extremely challenging. As, currently, highly efficient blue and green emitting LED structures are GaN-based, while efficient red emitters are aluminum gallium indium phosphide-based [12]. An alternative is to fabricate blue, green, and red emitting micro-LEDs on their respective growth wafers and then transfer the three different color emitting micro-LEDs onto a common substrate. Conventional assembly techniques, relying on robotic systems for placement of materials mechanically diced from a source wafer onto a common platform, are incapable of handling ultrasmall micro-LEDs

[13]. This has pushed research into strategies of suspending releasable ultrathin micro-LED platelets (still tethered to their growth substrate) and subsequent assembly by transfer printing (TP) techniques [13,14]. Following this approach, several reports of TP-enabled multi-color inorganic micro-LED arrays, targeting microdisplay applications, have emerged [15–17].

To the best of our knowledge, however, the potential of on-chip multi-color inorganic micro-LED arrays as VLC transmitters has not yet been fully explored. Monochromatic GaN-based micro-LEDs have been successfully demonstrated as multi-Gbps VLC transmitters [18–20]. Their success has been attributed to their hundreds of MHz -6 dB electrical modulation bandwidth combined with spectrally efficient modulation schemes, such as orthogonal frequency division multiplexing (OFDM) [19]. Furthermore, the communication capacity can be increased by using different color emitting micro-LEDs and wavelength division multiplexing (WDM) techniques. This concept has been successfully implemented in a multi-Gbps VLC link using separate micro-LED chips of different colors [21]. But where the micro-LED transmitters were spatially separated by 10's of cm and optics were required for efficient color mixing.

In this work, we report the fabrication, characterization, and VLC application of transfer printing-enabled on-chip GaN-based blue-green and blue-violet micro-LED arrays. In section 2, we present the micro-LED fabrication process on their growth substrates and subsequent integration of the blue emitting micro-LEDs, onto the green or violet micro-LED substrate by transfer printing. In section 3, firstly the electrical, optical, and bandwidth performance of individual violet, green, and blue micro-LEDs are shown; secondly the color mixing properties of the blue-green and blue-violet micro-LED arrays are presented in terms of their color coordinates; finally the capability of the blue-green and blue-violet micro-LED arrays as VLC transmitters in two different WDM experimental set-ups (with and without a dichroic mirror) is demonstrated with Gbps error free data rates achieved by respective pairs of micro-LEDs. These results show the potential for micro-LED arrays that act both as a display and as a high-speed VLC transmitter.

## 2. Device fabrication

### 2.1. Violet and green micro-LEDs based on GaN-on-sapphire epitaxy

Violet and green emitting (405 nm and 520 nm, respectively) micro-LEDs in flip-chip configuration were fabricated from commercial InGaN epistuctures, grown on c-plane patterned sapphire substrate (PSS), following previously reported microfabrication procedures [20]. The violet LED epitaxial structure consisted of a 4.5  $\mu\text{m}$  GaN buffer layer, a 1.8  $\mu\text{m}$  thick n-doped GaN, an 116 nm thick active layer, a 85 nm magnesium-doped aluminum gallium nitride (AlGaIn:Mg) cladding layer, and finally a 25 nm thick p-doped GaN layer. The green LED epitaxial structure consisted of a 3  $\mu\text{m}$  undoped GaN buffer layer, 4  $\mu\text{m}$  of n-doped GaN, a 130 nm thick active layer, and was topped with a 300 nm thick p-doped GaN layer. In the first fabrication step, a p-GaN metal contact (Palladium (Pd), thickness 100 nm) was electron-beam deposited, lithographically patterned, and annealed in a nitrogen environment at 300 °C. Inductively coupled plasma (ICP) etching was used to expose the underlying n-GaN layer defining a 20  $\mu\text{m}$  diameter pixel ( $3.15 \times 10^{-6}$  cm<sup>2</sup> active area). Another ICP etch step created a 90  $\mu\text{m}$  side square mesa down to the PSS, thus further reducing the micro-LEDs capacitance [19]. Then, a metal sputter deposition (Titanium (Ti)/Gold (Au), thicknesses 50/200 nm) defined the n-GaN metal contact layer. Next, a 300 nm silicon dioxide (SiO<sub>2</sub>) passivation layer was deposited by plasma-enhanced chemical vapor deposition (PE-CVD) and a SiO<sub>2</sub> aperture on top of the p-GaN was defined by reactive ion etching (RIE). Finally, a second Ti/Au metallization step defined the metal track.

### 2.2. Blue micro-LED platelets from a GaN-on-silicon wafer

Blue emitting (450 nm) micro-LED platelets with flip-chip configuration were fabricated from commercial InGaN epistuctures, grown on a silicon (Si) 111-oriented substrate. The blue LED



epitaxial structure consisted of a 200 nm thick aluminum nitride (AlN) layer, followed by a 650 nm Al-graded GaN buffer layer, a 300 nm non-intentionally doped GaN layer, an 800 nm thick n-doped GaN, an 100 nm thick active layer, and an 140 nm thick p-doped GaN layer. An L-shaped pixel (active area of  $6.5 \times 10^{-5} \text{ cm}^2$ ) and a 100  $\mu\text{m}$  squared mesa were defined by the same processes as for the violet and green micro-LEDs. The blue TP micro-LED pixel size was chosen to be larger than the violet and green micro-LEDs in order to compensate for its lower optical power density. Additionally, in order to yield transferable micro-LED platelets, the following steps were undertaken. First, supporting “anchors”, that tether the micro-LED platelet to the growth substrate, were defined during the ICP mesa etching. Second, an additional etching step was used to expose the chemically preferentially etched Si(110) planes. Third, by wet etching (30% potassium hydroxide (KOH) solution at 80 °C) the Si(110) planes underneath the micro-LED platelets were removed. Upon completion of the underetch step, the blue micro-LED platelets are held suspended, above an air gap (2  $\mu\text{m}$ ), by the two diagonally opposed sacrificial anchors [22].

### 2.3. Dual-color micro-LED arrays integrated by transfer printing

Heterogeneous integration of the blue micro-LED platelets onto the sapphire substrate of respective violet and green micro-LEDs was enabled by transfer printing [22]. In this process, an elastomeric polydimethylsiloxane (PDMS) stamp, fabricated by a micromolding technique, was used to pick-up the blue micro-LED platelets from their Si substrate and print them onto the pre-prepared green and violet sapphire substrate micro-LED chips. When printing, the adhesion force between the receiving substrate (in this case, PSS) and the micro-LED platelet backside must be larger than the adhesion force between the micro-LED platelet and the stamp. In order to assist the release of the micro-LED platelet, the PSS of violet/green micro-LED was coated with an adhesion-enhancing layer (SU-8 photoresist, 4.5  $\mu\text{m}$  thick). The effect of this SU-8 layer on the PSS surface topography was investigated by atomic force microscopy. Figure 1(a) shows the PSS surface topography before SU-8 coating. The periodic patterned surface exhibits a root-mean-square (RMS) roughness of 342 nm with a maximum height feature of 1.9  $\mu\text{m}$ . The PSS roughness combined with the micro-LED platelet concave curvature (due to strain effects on release from the growth substrate [23]), greatly reduce the effective contact area of the micro-LED platelet backside with the receiving substrate, rendering the release of the micro-LED platelet from the stamp quite challenging. After SU-8 coating, as shown in Fig. 1(b), the RMS roughness and the maximum height feature of the periodic patterned surface is down to 16.9 nm and 118 nm, respectively, which enabled a successful and repeatable release of the micro-LED platelet from the PDMS stamp. In this work, the blue micro-LED was placed 50  $\mu\text{m}$  apart from the violet or green micro-LED mesa. Next, a 4.5  $\mu\text{m}$  thick Parylene-C film was deposited as the insulation layer. Parylene-C was chosen due to its excellent chemical stability, electrical insulation properties, and exceptional conformity [24] that allow one to efficiently insulate the KOH roughed sidewalls of the transfer printed micro-LED [25]. Afterward, 40  $\mu\text{m}$  wide metal tracks (Ti/Au, 50/200 nm thick) were lithographically defined, contacting the micro-LED platelet through, previously RIE defined, localized apertures in the Parylene-C. Figures 1(c) and 1(d) show plan-view optical micrographs of the blue-green micro-LED array before and after transfer printing of the blue micro-LED platelet, respectively. The micro-LEDs in this array are individually anode-addressable sharing a common cathode (K). The blue-violet micro-LED array has the same layout. Plan view optical micrographs of the individually driven violet (at 318 A/cm<sup>2</sup>), blue (at 15 A/cm<sup>2</sup>), and green (at 318 A/cm<sup>2</sup>) micro-LEDs are shown in Figs. 1(e)–1(g), respectively.

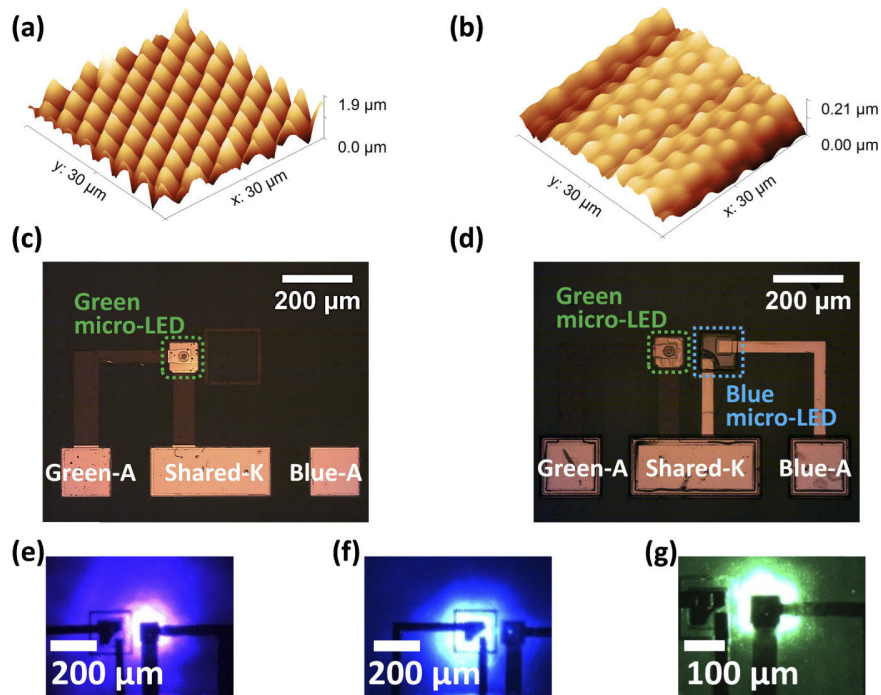


**Fig. 1.** Atomic force microscopy image of the PSS (a) before and (b) after SU-8 coating; plan-view optical micrograph of the blue-green micro-LED array (c) before and (d) after transfer printing of the blue micro-LED platelet. A and K are the respective anode and common cathode contact pads. Plan-view optical micrograph of the (e) violet, (f) blue, and (g) green micro-LEDs individually driven at the current density of 318 A/cm<sup>2</sup>, 15 A/cm<sup>2</sup>, and 318 A/cm<sup>2</sup>, respectively.

### 3. Device performance and application

#### 3.1. Electrical, optical and bandwidth performance of single-color micro-LEDs

The room-temperature (RT) current density – voltage (J-V) and optical power – current density (L-J) performance of the violet, green, and blue micro-LEDs fabricated in this work are shown in Figs. 2(a)–2(c), respectively. In addition, the electroluminescence (EL) spectra of each single-color micro-LED, acquired at value of current density of 318 A/cm<sup>2</sup> for the violet and green micro-LEDs and 15 A/cm<sup>2</sup> for the blue micro-LED, are also presented. The J-V characteristic was measured by a current source, through scanning each data point under direct current (DC) conditions (Yokogawa GS610). While, the L-J was measured using a calibrated Si photodiode detector (Thorlabs PM100D) in proximity to the backside of the micro-LEDs. The EL spectra were acquired by an optical fiber-coupled spectrometer (Avantes AvaSpec-2048L spectrometer). The violet and green micro-LEDs present a respective turn-on voltage (at 318 A/cm<sup>2</sup>) of 3.5 V and 5.4 V and, at 2.8 kA/cm<sup>2</sup>, their optical powers are 0.85 mW and 0.34 mW, respectively. At the current density of 318 A/cm<sup>2</sup>, the violet and green micro-LED EL spectra exhibit a broad peak centred at 400 and 512 nm, respectively. The blue micro-LED exhibits a turn-on voltage (at 15 A/cm<sup>2</sup>) and optical power (at 138 A/cm<sup>2</sup>) of 3 V and 1.04 mW, respectively. The lower current density operation of the TP micro-LED is a direct consequence of its larger pixel size. At 15 A/cm<sup>2</sup>, the blue micro-LED EL spectrum exhibits a broad peak centred at 453 nm. The TP micro-LED exhibits a reverse leakage current, under dark conditions, of 350 nA at -3 V. This

value is lower than the one achieved by a similar device employing SU-8 as insulation layer, which demonstrates the superior capability of parylene-C as an electrical insulation layer for these TP micro-LEDs. In addition, the low reverse leakage current is also a good indicator of the excellent JV performance shown by the TP micro-LED.

The RT -6 dB electrical modulation bandwidths of the micro-LEDs with different colors were measured by applying a DC bias combined with a small-signal modulation from an HP8753ES network analyzer. The optical response was collected by a lens system and focused onto a fast photodiode (Femto HAS-X-S-1G4-SI bandwidth 1.4 GHz). The -6 dB electrical modulation bandwidths of each micro-LED, at different current densities, are shown in Fig. 2(d). The violet and green micro-LEDs exhibit the -6 dB electrical bandwidth up to 427 MHz and 144 MHz, respectively. The lower bandwidth and optical power of the green micro-LED, when compared to the violet micro-LED, can be attributed to its higher In content in the active region, and thus stronger quantum confined stark effect [26]. Furthermore, the transfer printed blue micro-LED shows a -6 dB electrical bandwidth up to 134 MHz. The lower value achieved by this micro-LED is related to its larger size and, thus, lower current density operation.

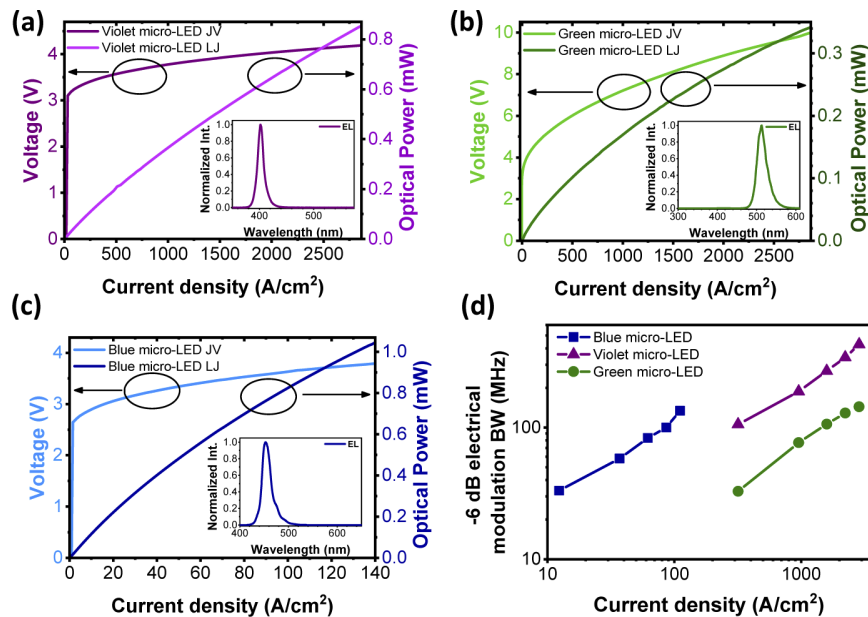


**Fig. 2.** (a), (b), and (c) Violet, green, and blue micro-LEDs current density-voltage curve, current density-optical power curve, and electroluminescence spectra, respectively; (d) Violet, green, and blue micro-LEDs -6 dB electrical modulation bandwidth as a function of the current density.

### 3.2. Color properties of dual-color micro-LED arrays

CIE1931 color coordinates of the blue-green and blue-violet micro-LED array on the color space chromaticity diagram are shown in Figs. 3(a) and 3(b), respectively. For the blue-green array, by increasing the current density of the blue micro-LED from 0 to 15 A/cm<sup>2</sup> and simultaneously decreasing the current density of the green micro-LED from 318 to 0 A/cm<sup>2</sup>, it is possible to tune the *xy* color coordinates from (0.15, 0.04), for only the blue micro-LED, to (0.11, 0.71), for only the green micro-LED. The optical photographs in Fig. 3(a) show that the blue-green array is capable of efficient color mixing (without any additional optic elements) under different bias

conditions. The slightly violet appearance of the blue micro-LED, at  $15 \text{ A/cm}^2$ , is a digital artifact due to the photographic camera detector. On the other hand, for the blue-violet array, varying the driving current of both micro-LEDs results in a small change of the CIE color coordinates. The enlarged inset shows, in further detail, how indistinguishable the CIE color coordinates of blue-violet array at different biases are. This is due to the poorer human eye response in the violet-blue region, when compared to blue-green spectral region [27]. The typical blue-green and blue-violet array EL spectra, at different integrated area ratios of blue-green and blue-violet, respectively, correspond to the superposition of the individual spectra of each light source, as shown in Fig. 3(c).

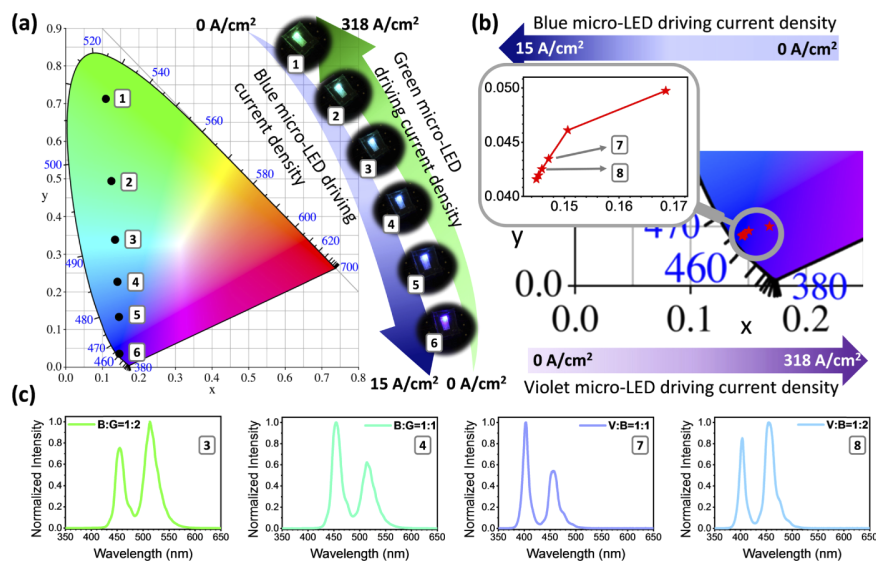


**Fig. 3.** (a) Blue-green micro-LED array CIE1931 coordinates on the CIE1931 color space chromaticity diagram and photographs of the device at different biases; (b) blue-violet micro-LED array CIE1931 color coordinates at different biases; (c) electroluminescence spectra from the blue-green and blue-violet array at different integrated area ratios of blue-green and blue-violet, respectively.

### 3.3. VLC application of dual-color micro-LED arrays in WDM mode

The capability of the blue-green and blue-violet micro-LED arrays to operate as two-color WDM transmitters in two different experimental set-ups are explored in the following sections. In the first set-up (referring as WDM1 and shown in Fig. 4(a)), we placed one optical receiver to measure the communication performance of both channels by changing a bandpass filter (Laser 2000 FF01-392-23/25, FF01-445/20-25 and FF01-525-45/25, for violet, blue, and green, respectively). To ensure that the measured results were the same as in the case of simultaneous signal reception with the existence of crosstalk, we sent two different signal streams to different color micro-LED channels. One stream was captured and demodulated, while the other one behaved as the interfering signal. Although this set-up provided a capacity estimation for WDM (a “best case scenario”), simultaneous reception of both channels was not possible. To overcome this issue, dichroic mirrors were employed in a second experimental set-up (referring as WDM2), shown in Fig. 4(b). The light emitted from the dual-color micro-LED array was directed onto the dichroic mirror (Thorlabs DMLP425 and DMLP490L, for blue-violet and blue-green micro-LED arrays, respectively) at 45 degrees which separated the beam into two individual components.

The light transmitted through the dichroic mirror was focused onto an optical receiver and the light reflected by the dichroic mirror was focused onto another optical receiver. Bandpass filters were also placed in front of the detectors in order to minimize crosstalk. This set-up enabled simultaneous reception of both channels, though the use of the dichroic mirror leads to signal power losses. The distance between transmitter and detector was kept at 30 cm, in both set-ups and throughout the measurements.

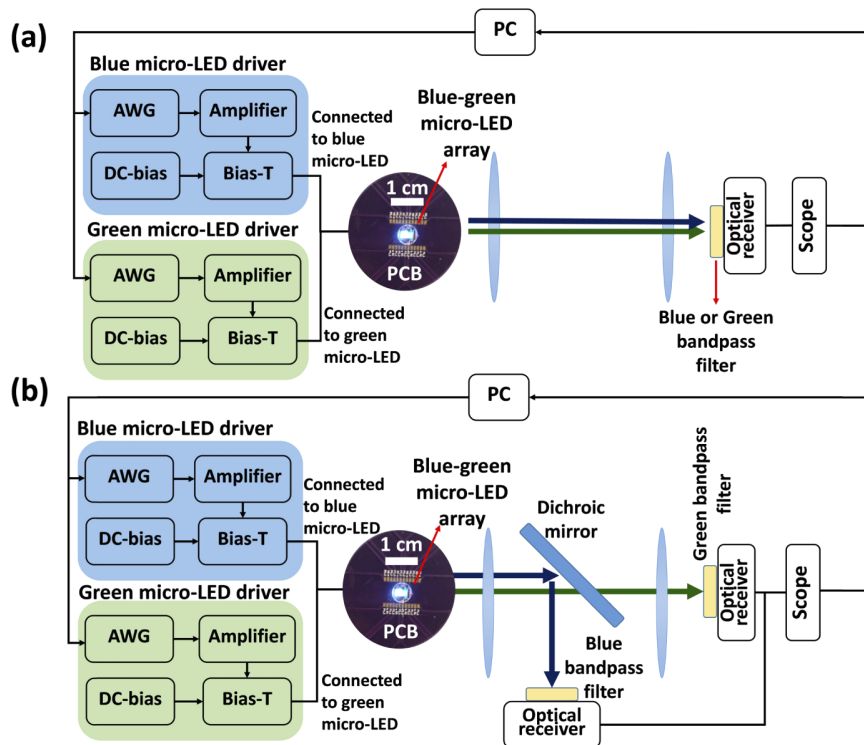


**Fig. 4.** Schematic drawing of the experimental set-ups in wavelength division multiplexing data transmission experiments: (a) set-up 1 (WDM1); (b) set-up 2 (WDM2). The photograph inset in the schematics is the actual blue-green micro-LED array (wire bonded to a printed circuit board - PCB) being operated in WDM mode.

In both set-ups, two random bit streams, for the transmission via the two different color emitting micro-LED channels, were generated and modulated with DC-biased optical OFDM (DCO-OFDM) by a PC using MATLAB. The incoming bit stream was coded and mapped to M-ary quadrature amplitude modulation (M-QAM) symbols for each subcarrier at different frequencies. The time-domain OFDM symbols were generated after having the inverse fast Fourier transform (IFFT) operation for the M-QAM symbols. A real-valued OFDM signal was obtained by using a Hermitian symmetry OFDM frame. The resulting time-domain OFDM signals were forwarded to an arbitrary waveform generator (AWG Keysight M8195A), which generated the corresponding analog signals. In order to make sure the input signals fully exploited the available linear dynamic range of the micro-LEDs, the output analog signals were amplified by a power amplifier (Mini-Circuits ZHL-1A-S+), and a suitable operation current density was provided by a power supply (Yokogawa GS610). The bipolar signals and the DC bias were combined using a bias-tee (Mini-Circuits ZFBT-4R2GW+), and the output of the bias-tees were connected to the micro-LED array to drive the two micro-LED pixels. On the receiver end,



the light emitted by the dual-color micro-LED array was focused onto a p-i-n photodetector (New Focus 1601AC) by using an aspheric condenser lens (ACL4532). The signal from the photodetector was captured by an oscilloscope (Keysight MSO7104B) and sent back to the PC for demodulation. In order to maximize the achievable data rate, a bit and energy loading algorithm [18] was applied. Therefore, the signal-to-noise ratio (SNR) on each subcarrier was estimated at the beginning of the communication performance measurement. Based on the estimated SNR and a bit-error-ratio (BER) target that is acceptable for the application of forward error correction (FEC) coding, modulation order and symbol energy on each subcarrier was calculated. Finally, the signals with bit and energy loading were transmitted and the achieved data rate and BER were measured.

### 3.4. Communication performance of the blue-green micro-LED array

The results of the blue-green micro-LED array operated in a WDM mode with different set-ups are summarized in Fig. 5. The blue and green micro-LEDs were operated at  $138 \text{ A/cm}^2$  and  $2.8 \text{ kA/cm}^2$ , respectively, whilst the modulation signal peak-to-peak voltage was set to 1.5 V, after the amplifier. The sampling frequency was set as 16 GSa/s and number of samples per symbol was optimized for each link. The SNR and number of allocated bits, at the highest data rate below the FEC threshold of  $3.8 \times 10^{-3}$  BER, for the blue and green micro-LED are shown in Figs. 5(a) and 5(b), respectively.

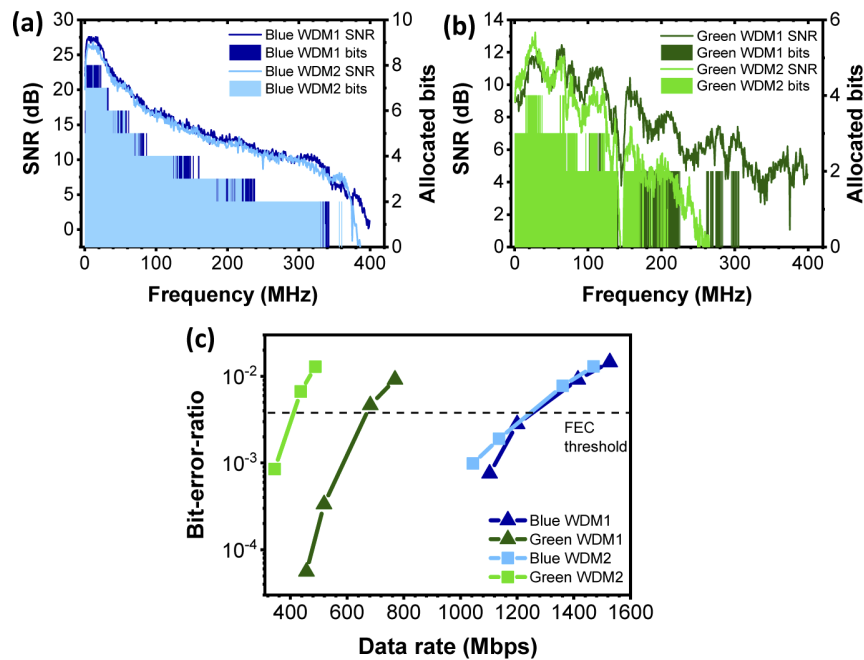


**Fig. 5.** Signal-to-noise ratio and allocated bits (at maximum data rate below forward error correction threshold) in both WDM set-ups achieved by (a) the blue micro-LED and (b) the green micro-LED; (c) BER vs data rate for the blue and green micro-LEDs in both WDM set-ups.

The blue micro-LED channel exhibits a higher SNR than the green micro-LED channel due to the blue micro-LED higher optical power. Also, as shown in Fig. 5(a), there is no obvious difference on the SNR curves of the blue channel between the two different set-ups. On the other hand, compared with the WDM1 set-up, the SNR curve of the green channel with the WDM2

set-up presents a sharp drop when the frequency is over 150 MHz, shown in Fig. 5(b). This is mainly due to the optical power loss (roughly 25%) caused by the dichroic mirror used in WDM2. This leads to a lower maximum achievable data rate in WDM2. The BER vs data transmission curves for the blue and green micro-LEDs, in both WDM set-ups, are presented in Fig. 5(c). The maximum data rates, below FEC threshold, achieved by the blue and green micro-LEDs in the WDM1 set-up are 1261 and 667 Mbps, respectively. In the WDM2 set-up the maximum data rates, below FEC threshold, achieved by the blue and green micro-LEDs drop to 1245 and 410 Mbps, respectively.

Error-free data rates, calculated by applying the 7% FEC overhead reduction, for blue and green micro-LEDs and their aggregate in each WDM set-up are shown in Table 1. In aggregate, 1.79 and 1.54 Gbps error-free data rates are achieved in the WDM1 and WDM2 set-ups, respectively.

**Table 1. Error-free data rates for each channel and aggregated in WDM1 and WDM2 set-ups achieved by the blue-green micro-LEDs array.**

Channel	WDM1		WDM2	
	Blue	Green	Blue	Green
<b>Error-free data rate (Mbps)</b>	1173	620	1158	381
	Aggregate		Aggregate	
	1793		1539	

### 3.5. Communication performance of the blue-violet micro-LED array

The blue-violet micro-LED array operation as a WDM transmitter followed the same approach as the blue-green one. In this case, the blue and violet micro-LEDs were operated at the same current density as the blue and green micro-LEDs, respectively. The SNR and number of allocated bits, at the highest rate below FEC threshold, in both WDM set-ups for the blue and violet micro-LEDs are shown in Figs. 6(a) and 6(b), respectively.

The blue and violet micro-LED channels maximum SNR is quite similar due their comparable optical power. Nonetheless, due to the violet micro-LED higher -6 dB electrical modulation bandwidth, the violet channel supports bit allocation up until 650 MHz. The introduction of the dichroic mirror, which has cut-off wavelength at 425 nm, results in a loss of optical power and, thus lower SNR for both channels, limiting the maximum achievable data rate in WDM2. The violet (reflected) channel is more affected than the blue one due to the optical response of the dichroic mirror, with estimated optical power losses of 11%. The BER vs data transmission curve is presented in Fig. 6(c). The maximum data rates, below FEC threshold, achieved by the blue and violet micro-LEDs in the WDM1 set-up are 1130 and 2472 Mbps, respectively. In the WDM2 set-up the maximum data rates, below FEC threshold, achieved by the blue and violet micro-LEDs drop to 842 and 1309 Mbps, respectively.

The blue and violet channels and aggregate error-free data rates for WDM1 and WDM2 set-ups are shown in Table 2. In aggregate, the blue-violet micro-LED array achieves error-free data rates of 3.35 and 2 Gbps, in the WDM1 and WDM2 set-ups, respectively.

**Table 2. Error-free data rates for each channel and aggregated in WDM1 and WDM2 set-ups achieved by the blue-violet micro-LED array.**

Channel	WDM1		WDM2	
	Blue	Violet	Blue	Violet
<b>Error-free data rate (Mbps)</b>	1051	2299	783	1217
	Aggregate		Aggregate	
	3350		2000	

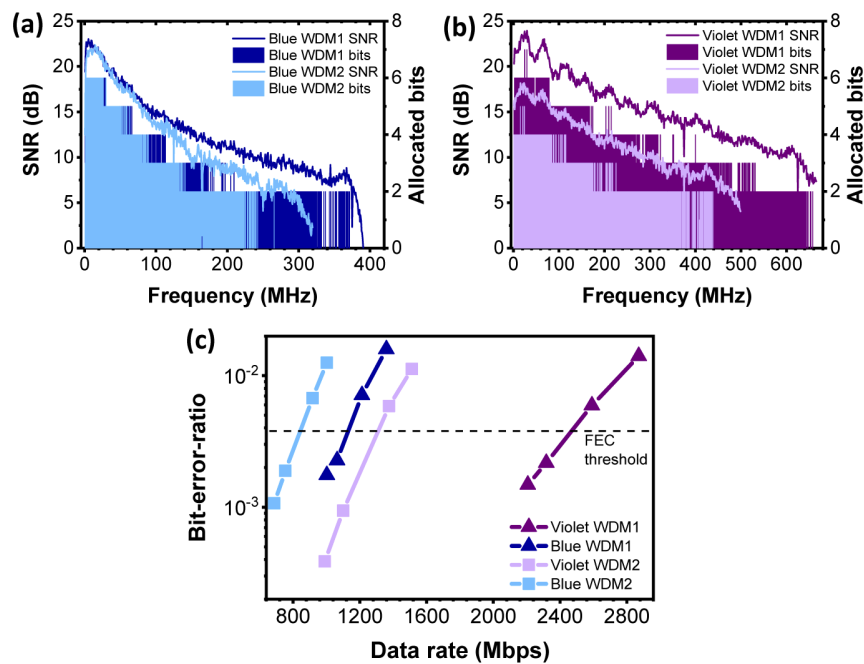


**Fig. 6.** Signal-to-noise ratio and allocated bits (at maximum data rate below forward error correction) in both WDM set-ups achieved by (a) the blue micro-LED and (b) the violet micro-LED; (c) BER vs data rate for blue and violet micro-LEDs in both WDM set-ups.

#### 4. Conclusions

In conclusion, we have demonstrated the fabrication, characterization and VLC application of on-chip dual-color micro-LED arrays. Blue-green and blue-violet micro-LED arrays were fabricated by transfer printing a blue emitting micro-LED onto the substrate of the green and violet micro-LEDs, respectively. The violet, green, and blue individual micro-LEDs exhibit an optical power of 0.85, 0.34, and 1.04 mW, at the current densities of 2.8 kA/cm<sup>2</sup>, 2.8 kA/cm<sup>2</sup>, and 138 A/cm<sup>2</sup>, respectively. The violet, green, and blue present -6 dB electrical modulation bandwidths up to 427, 144, and 134 MHz, respectively. Operation of the blue-green micro-LED array at different biases allows one to fine tune the perceived color from blue ( $x$  0.15;  $y$  0.04) to green ( $x$  0.11;  $y$  0.71) on the CIE1931 color diagram. Due to the human eye's poorer optical response in the blue-violet spectral region, operation of the blue-violet micro-LED array at different biases results in a very small variation of its color coordinates. In the two free space WDM VLC set-ups investigated in this work, the blue-green micro-LED array achieves an aggregated error-free data rate of 1.79 and 1.54 Gbps and the blue-violet micro-LED array 3.35 and 2 Gbps.

The two on-chip dual-color micro-LED arrays reported in this work can potentially be integrated into the same package to give a 3-color output. Furthermore, these on-chip dual color micro-LED arrays should be suitable for underwater and plastic optical fiber VLC, as the micro-LED EL spectra match both mediums transparency windows. This work opens the way to multi-colored pixelated clusters in micro-LED displays acting as WDM visible light communications links.

Supporting data can be found at <https://doi.org/10.15129/82b872f9-a0b3-4ec8-94c2-9dcdcc95fe2b>.



## Funding

Engineering and Physical Sciences Research Council (EP/L015595/1, EP/M01326X/1).

## Acknowledgments

The authors would like to thank P. Hill and J. Smith for the atomic force microscopy measurements. Plessey Semiconductors is acknowledged for providing the GaN-on-Si material.

## References

1. H. X. Jiang and J. Y. Lin, "Nitride micro-LEDs and beyond - a decade progress review," *Opt. Express* **21**(S3), A475 (2013).
2. J. Herrnsdorf, J. J. D. McKendry, S. Zhang, E. Xie, R. Ferreira, D. Massoubre, A. M. Zuhdi, R. K. Henderson, I. Underwood, S. Watson, A. E. Kelly, E. Gu, and M. D. Dawson, "Active-Matrix GaN Micro Light-Emitting Diode Display With Unprecedented Brightness," *IEEE Trans. Electron Devices* **62**(6), 1918–1925 (2015).
3. S. Zhang, Z. Gong, J. J. D. McKendry, S. Watson, A. Cogman, E. Xie, P. Tian, E. Gu, Z. Chen, G. Zhang, A. E. Kelly, R. K. Henderson, and M. D. Dawson, "CMOS-Controlled Color-Tunable Smart Display," *IEEE Photonics J.* **4**(5), 1639–1646 (2012).
4. F. Templier, "GaN-based emissive microdisplays: A very promising technology for compact, ultra-high brightness display systems," *J. Soc. Inf. Disp.* **24**(11), 669–675 (2016).
5. S. Rajbhandari, J. J. D. McKendry, J. Herrnsdorf, H. Chun, G. Faulkner, H. Haas, I. M. Watson, D. O'Brien, and M. D. Dawson, "A review of gallium nitride LEDs for multi-gigabit-per-second visible light data communications," *Semicond. Sci. Technol.* **32**(2), 023001 (2017).
6. X. Li, L. Wu, Z. Liu, B. Hussain, W. C. Chong, K. M. Lau, and C. P. Yue, "Design and Characterization of Active Matrix LED Microdisplays With Embedded Visible Light Communication Transmitter," *J. Lightwave Technol.* **34**(14), 3449–3457 (2016).
7. Y. Wang, B. R. Rae, R. K. Henderson, Z. Gong, J. McKendry, E. Gu, M. D. Dawson, G. A. Turnbull, and I. D. W. Samuel, "Ultra-portable explosives sensor based on a CMOS fluorescence lifetime analysis micro-system," *APL Adv.* **1**(3), 032115 (2011).
8. A. Zarowna-Dabrowska, S. L. Neale, D. Massoubre, J. McKendry, B. R. Rae, R. K. Henderson, M. J. Rose, H. Yin, J. M. Cooper, E. Gu, and M. D. Dawson, "Miniaturized optoelectronic tweezers controlled by GaN micro-pixel light emitting diode arrays," *Opt. Express* **19**(3), 2720 (2011).
9. K. Chung, J. Sui, B. Demory, C.-H. Teng, and P.-C. Ku, "Monolithic integration of individually addressable light-emitting diode color pixels," *Appl. Phys. Lett.* **110**(11), 111103 (2017).
10. Y.-H. Ra, R. Wang, S. Y. Woo, M. D. Javid, S. M. Sadaf, J. Lee, G. A. Botton, and Z. Mi, "Full-Color Single Nanowire Pixels for Projection Displays," *Nano Lett.* **16**(7), 4608–4615 (2016).
11. Y. J. Hong, C.-H. Lee, A. Yoon, M. Kim, H.-K. Seong, H. J. Chung, C. Sone, Y. J. Park, and G.-C. Yi, "Visible-Color-Tunable Light-Emitting Diodes," *Adv. Mater.* **23**(29), 3284–3288 (2011).
12. C.-M. Kang, J.-Y. Lee, D.-J. Kong, J.-P. Shim, S. Kim, S.-H. Mun, S.-Y. Choi, M.-D. Park, J. Kim, and D.-S. Lee, "Hybrid Full-Color Inorganic Light-Emitting Diodes Integrated on a Single Wafer Using Selective Area Growth and Adhesive Bonding," *ACS Photonics* **5**(11), 4413–4422 (2018).
13. H. Zhang and J. A. Rogers, "Recent Advances in Flexible Inorganic Light Emitting Diodes: From Materials Design to Integrated Optoelectronic Platforms," *Adv. Opt. Mater.* **7**(2), 1800936 (2019).
14. H. Kim, E. Brueckner, J. Song, Y. Li, S. Kim, C. Lu, J. Sulkin, K. Choquette, Y. Huang, R. G. Nuzzo, and J. A. Rogers, "Unusual strategies for using indium gallium nitride grown on silicon (111) for solid-state lighting," *Proc. Natl. Acad. Sci. U. S. A.* **108**(25), 10072–10077 (2011).
15. M. Choi, B. Jang, W. Lee, S. Lee, T. W. Kim, H.-J. Lee, J.-H. Kim, and J.-H. Ahn, "Stretchable Active Matrix Inorganic Light-Emitting Diode Display Enabled by Overlay-Aligned Roll-Transfer Printing," *Adv. Funct. Mater.* **27**(11), 1606005 (2017).
16. M. K. Choi, J. Yang, K. Kang, D. C. Kim, C. Choi, C. Park, S. J. Kim, S. I. Chae, T.-H. Kim, J. H. Kim, T. Hyeon, and D.-H. Kim, "Wearable red–green–blue quantum dot light-emitting diode array using high-resolution intaglio transfer printing," *Nat. Commun.* **6**(1), 7149 (2015).
17. C. A. Bower, M. A. Meitl, B. Raymond, E. Radauscher, R. Cok, S. Bonafede, D. Gomez, T. Moore, C. Prevatte, B. Fisher, R. Rotzoll, G. A. Melnik, A. Fecioru, and A. J. Trindade, "Emissive displays with transfer-printed assemblies of  $8\ \mu\text{m} \times 15\ \mu\text{m}$  inorganic light-emitting diodes," *Photonics Res.* **5**(2), A23 (2017).
18. D. Tsonev, H. Chun, S. Rajbhandari, J. J. D. McKendry, S. Videv, E. Gu, M. Haji, S. Watson, A. E. Kelly, G. Faulkner, M. D. Dawson, H. Haas, and D. O'Brien, "A 3-Gb/s Single-LED OFDM-Based Wireless VLC Link Using a Gallium Nitride  $\mu$ LED," *IEEE Photonics Technol. Lett.* **26**(7), 637–640 (2014).
19. R. X. G. Ferreira, E. Xie, J. J. D. McKendry, S. Rajbhandari, H. Chun, G. Faulkner, S. Watson, A. E. Kelly, E. Gu, R. V. Penty, I. H. White, D. C. O'Brien, and M. D. Dawson, "High Bandwidth GaN-Based Micro-LEDs for Multi-Gb/s Visible Light Communications," *IEEE Photonics Technol. Lett.* **28**(19), 2023–2026 (2016).

20. M. S. Islam, R. X. Ferreira, X. He, E. Xie, S. Videv, S. Viola, S. Watson, N. Bamiedakis, R. V. Penty, I. H. White, A. E. Kelly, E. Gu, H. Haas, and M. D. Dawson, "Towards 10 Gb/s orthogonal frequency division multiplexing-based visible light communication using a GaN violet micro-LED," *Photonics Res.* **5**(2), A35 (2017).
21. H. Chun, S. Rajbhandari, G. Faulkner, D. Tsonev, E. Xie, J. J. D. McKendry, E. Gu, M. D. Dawson, D. C. O'Brien, and H. Haas, "LED Based Wavelength Division Multiplexed 10 Gb/s Visible Light Communications," *J. Lightwave Technol.* **34**(13), 3047–3052 (2016).
22. A. J. Trindade, B. Guilhabert, D. Massoubre, D. Zhu, N. Laurand, E. Gu, I. M. Watson, C. J. Humphreys, and M. D. Dawson, "Nanoscale-accuracy transfer printing of ultra-thin AlInGaN light-emitting diodes onto mechanically flexible substrates," *Appl. Phys. Lett.* **103**(25), 253302 (2013).
23. A. J. Trindade, B. Guilhabert, E. Y. Xie, R. Ferreira, J. J. D. McKendry, D. Zhu, N. Laurand, E. Gu, D. J. Wallis, I. M. Watson, C. J. Humphreys, and M. D. Dawson, "Heterogeneous integration of gallium nitride light-emitting diodes on diamond and silica by transfer printing," *Opt. Express* **23**(7), 9329 (2015).
24. D. Kang, A. Standley, J. H.-C. Chang, Y. Liu, and Y.-C. Tai, "Effects of deposition temperature on Parylene-C properties," in *2013 IEEE 26th International Conference on Micro Electro Mechanical Systems (MEMS)* (IEEE, 2013), pp. 389–390.
25. H. M. Ng, N. G. Weimann, and A. Chowdhury, "GaN nanotip pyramids formed by anisotropic etching," *J. Appl. Phys.* **94**(1), 650–653 (2003).
26. J.-H. Ryou, P. D. Yoder, J. Liu, Z. Lochner, H. Kim, S. Choi, H. J. Kim, and R. D. Dupuis, "Control of Quantum-Confined Stark Effect in InGaN-Based Quantum Wells," *IEEE J. Sel. Top. Quantum Electron.* **15**(4), 1080–1091 (2009).
27. E. F. Schubert, "Human eye sensitivity and photometric qualities," in *Light-Emitting Diodes* (Cambridge University Press, 2006), pp. 275–291.

# Underwater Wireless Optical Communications at 100 Mb/s Using Integrated Dual-Color Micro-LEDs

José F. C. Carreira<sup>1\*</sup>, Georgios N. Arvanitakis<sup>1\*</sup>, Alexander D. Griffiths<sup>1</sup>, Jonathan J. D. McKendry<sup>1</sup>, Enyuan Xie<sup>1</sup>, John Kosman<sup>2</sup>, Robert K. Henderson<sup>2</sup>, Erdan Gu<sup>1</sup>, Martin D. Dawson<sup>1</sup>

<sup>1</sup>*Institute of Photonics, Department of Physics, University of Strathclyde, Glasgow, United Kingdom*

<sup>2</sup>*Joint Research Institute for Integrated Systems, University of Edinburgh, Edinburgh, United Kingdom*

jose.correia-carreira@strath.ac.uk; georgios.arvanitakis@strath.ac.uk

\* These two authors contributed equally to this work

**Abstract** — Integrated blue-violet and blue-green micro-LED arrays, fabricated via a transfer printing method, were employed to demonstrate wavelength division multiplexing underwater data transmission at 100 Mb/s over up to 9 attenuation lengths in a 1.5 m long water tank.

**Keywords** — micro-LED, transfer printing, WDM, VLC, UWOC, turbid

## I. INTRODUCTION

The development of high-speed underwater wireless communication channels is of paramount importance for industrial, scientific, and military underwater activities [1], as tethered links can be impractical due to the challenging underwater environment. Underwater acoustics offer long range (tens of km), but suffer from high latency and limited data rates (tens of kb/s). Radio frequency communication are attenuated by seawater's conductivity resulting in data rates up to Mb/s for sub-meter ranges [2]. Optical devices operating at visible wavelengths, where water's lowest overall attenuation is exhibited, can enable high-speed transmission over tens of meters. For instance, Donic *et al.* using an array of 18 light-emitting diodes (LEDs) demonstrated 25 Mb/s in 50 m of clear water [3]. Tian *et al.*, presented 800 Mb/s over 0.6 m of clear tap water using a single micro-LED [4]. It is worth noting, however, that as water becomes more turbid the optical window of lowest loss tends to redshift [2], thus a wavelength-adaptable transmitter is greatly desirable.

We report here the deployment of micro-transfer printing (TP) enabled hybrid blue-violet and blue-green micro-LED arrays for underwater wireless optical communications (UWOC) using a single-photon avalanche diode (SPAD) array receiver. By having two different wavelengths integrated in the same transmitter chip, the option of tuning the optimum color depending on the water conditions is enabled. Furthermore, the two chips can potentially be integrated into the same package to give 3-color output. Data transmission rates of 50 Mb/s for each single color of micro-LED over 1.5 m of highly turbid water are demonstrated. When operating in a wavelength division multiplexing (WDM) mode, with the respective pairs of colors, a 100 Mb/s link is established in each case over up to 9 attenuation lengths.

## II. DUAL COLOR MICRO-LED ARRAYS FABRICATION

Blue-violet and blue-green micro-LED arrays were fabricated by TP a blue-micro-LED platelet onto the substrate of the violet and green micro-LED, respectively. The blue-violet array follows the same fabrication process as the blue-green array which is discussed in detail in [5].

Briefly, violet (405 nm) and green (510 nm) 20  $\mu\text{m}$  diameter active area flip-chip micro-LEDs were fabricated

from commercially available InGaN epistuctures grown on c-plane sapphire by conventional photolithography techniques. Suspended flip-chip micro-LED platelets ( $6.5 \times 10^{-5} \text{ cm}^2$  active area) were then fabricated from commercially available blue emitting (450 nm) InGaN epistuctures grown on (111)-oriented silicon (Si). An elastomeric stamp was used to pick-up the blue micro-LED platelets from their Si substrate and print them onto the pre-prepared green and violet sapphire substrate micro-LED chips. The blue micro-LED platelet was then electrically insulated by parylene-C and addressed by Ti/Au (50/200 nm) metal tracks, following the process described in [5]. Fig. 1a) shows a plan view optical photograph of the resulting integrated blue-green micro-LED array (the blue-violet array shares the same layout). The micro-LEDs are individually anode-addressable sharing a common cathode. Fig. 1b) shows, by way of illustration, the blue-green device being simultaneously driven.

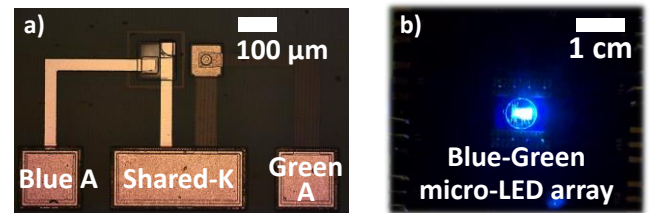


Fig. 1 – Plan view optical photographs of the blue-green micro-LED array a) magnified view; b) with both emitters simultaneously driven. Scale bars are shown inset.

## III. CHARACTERIZATION AND APPLICATION

### A. Micro-LEDs performance

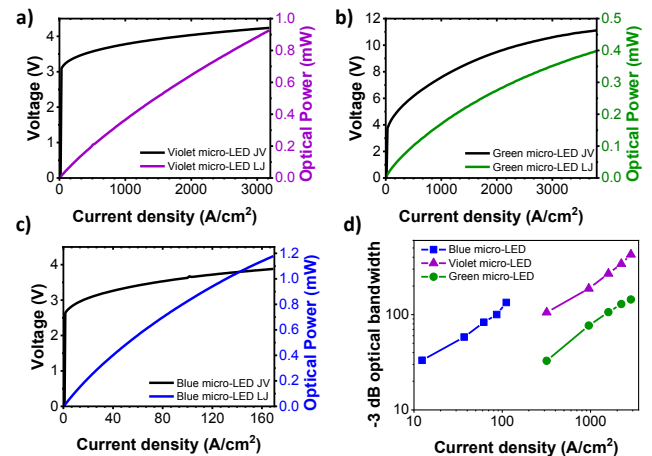


Fig. 2 – a), b) and c) current density-voltage (JV) and current density – optical power (LJ) curves of the violet, green, and blue micro-LED, respectively; d) micro-LEDs -3 dB optical bandwidth vs current density.

The individual electrical and optical performance of the chip-integrated violet, green, and blue micro-LEDs are shown

in Fig. 2 a), b), and c) respectively. The through-sapphire directed optical power output shown in Fig. 2 was measured using a calibrated Si photodiode detector butt-coupled to the device. In these conditions, the maximum optical power achieved by the violet, green, and blue micro-LED are 0.9, 0.4 and 1.2 mW, respectively. All micro-LEDs exhibit a -3dB optical bandwidth above 100 MHz (Fig. 2 d)), which renders them highly suitable for data transmission.

### B. UWOC Application

For the UWOC demonstration, an on-off keying (OOK) data signal was generated using a field-programmable gate array (FPGA, Opal Kelly XEM6310-LX45), modulating the micro-LED through a bias-tee. A sequence of length  $2^{15}$  was transmitted, consisting of a wide synchronisation pulse and a pseudo-random bit sequence. The micro-LED emission was collected and collimated by a condenser lens (Thorlabs, ACL50832U-A), propagated through a 1.5 m long water tank and then focused onto the receiver by a 4-inch diameter Fresnel lens (Edmund, #46-614). The receiver is a 64 x 64 array of Si SPADs developed by the University of Edinburgh (details found in [6]) which operates as a digital silicon photo-multiplier. The photon counts are summed over a time window of 5 ns and the count values outputted through a digital-to-analog converter (DAC). The DAC signal was captured with an active oscilloscope probe and transferred to MATLAB® for offline processing to determine a bit-error ratio (BER). The turbidity of the water sample was varied by adding Maalox® antacid to tap water, a method widely used [7] to mimic different natural water analogs in a laboratory set-up. A block diagram of the experimental setup is shown in Fig. 3.

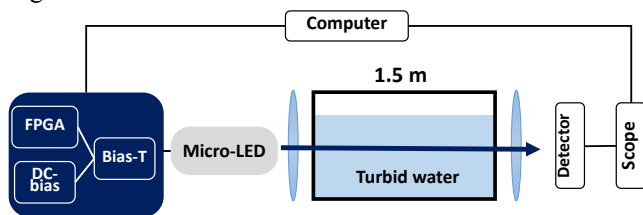


Fig. 3 – Block diagram of the experimental system.

The effect of increasing turbidity levels on the BER for individually driven micro-LEDs at the three wavelengths is shown in Fig. 4a). A 50 Mb/s communication channel, below the  $3.8 \times 10^{-3}$  forward error correction (FEC) threshold, is achieved for all the micro-LEDs for Maalox® concentration of 0.075 mL/L. For the blue and green micro-LEDs this concentration of Maalox® corresponds to a number of attenuation lengths (calculated following [8]) of 7.2 and 8.3, respectively. The operation of the integrated blue-violet and blue-green micro-LED arrays as respective dual wavelength WDM transmitters for underwater communication is shown in Fig. 4b). The blue and green micro-LED were operated simultaneously (as shown in Fig. 1b)) and each color carried a different data stream. In order to select which micro-LED was being detected bandpass filters (Laser 2000: blue FF01-445/20-25, green FF01-525-45/25) were placed in front of the detector. This results in a 100 Mb/s aggregate data rate link, below FEC, at a Maalox® concentration of 0.069 mL/L for the blue-green micro-LED array. The same measurements were repeated for the blue-violet micro-LED array, but with the use of a Laser 2000 FF01-392-23/25 bandpass filter for the

violet micro-LED. In this case, a 100 Mb/s link, below FEC, at a Maalox® of 0.075 mL/L is achieved by the blue-violet micro-LED array. It should be noticed, that used data rates are limited by the driving method, and future work could reach an aggregate data rate of several hundred Mb/s with OOK.

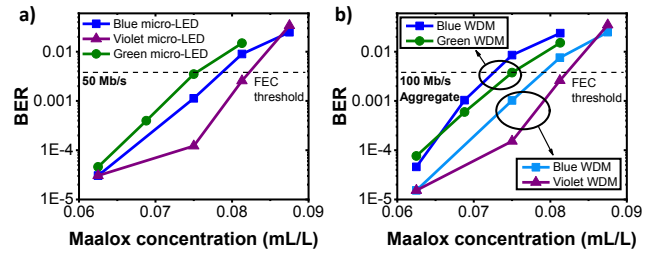


Fig. 4 – Bit-error-ratio vs Maalox® concentration a) for individually driven blue, violet and green micro-LEDs; b) Blue-green and blue-violet micro-LED arrays operated in wavelength division multiplexing mode.

### IV. CONCLUSION

By micro-TP we have fabricated on-chip dual-color (respectively blue-violet and blue-green) micro-LED arrays. The potential of these devices as a UWOC transmitter in highly turbid underwater environments has been demonstrated with 100 Mb/s data rates achieved over multiple attenuation lengths using WDM and a SPAD-based receiver.

### ACKNOWLEDGMENT

This work is funded under the EPSRC Quantic (EP/M01326X/1) and EPSRC CDT in Medical Devices & Health Technologies grant (EP/L015595/1). Plessey Semiconductors is acknowledged for providing the GaN-on-Si wafer.

### REFERENCES

- [1] H. Kaushal and G. Kaddoum, "Underwater Optical Wireless Communication," *IEEE Access*, vol. 4, pp. 1518–1547, 2016.
- [2] P. Lacovara, "High-Bandwidth Underwater Communications," *Mar. Technol. Soc. J.*, vol. 42, no. 1, pp. 93–102, Mar. 2008.
- [3] M. Doniec and D. Rus, "BiDirectional optical communication with AquaOptical II," in *2010 IEEE International Conference on Communication Systems*, 2010, pp. 390–394.
- [4] P. Tian *et al.*, "High-speed underwater optical wireless communication using a blue GaN-based micro-LED," *Opt. Express*, vol. 25, no. 2, p. 1193, 2017.
- [5] J. F. C. Carreira *et al.*, "Dual-Color Micro-LED Transmitter for Visible Light Communication," in *2018 IEEE Photonics Conference (IPC)*, 2018, pp. 1–2.
- [6] J. Kosman *et al.*, "29.7 A 500Mb/s -46.1dBm CMOS SPAD Receiver for Laser Diode Visible-Light Communications," in *2019 IEEE International Solid-State Circuits Conference - (ISSCC)*, 2019, pp. 468–470.
- [7] B. Cochenour, L. Mullen, and J. Muth, "Effect of scattering albedo on attenuation and polarization of light underwater," *Opt. Lett.*, vol. 35, no. 12, pp. 2088–2090, 2010.
- [8] W. Cox and J. Muth, "Simulating channel losses in an underwater optical communication system," *J. Opt. Soc. Am. A*, vol. 31, no. 5, p. 920, 2014.





# Direct integration of micro-LEDs and a SPAD detector on a silicon CMOS chip for data communications and time-of-flight ranging

J. F. C. CARREIRA,<sup>1,\*</sup>  A. D. GRIFFITHS,<sup>1</sup>  E. XIE,<sup>1</sup>  B. J. E. GUILHABERT,<sup>1</sup>  J. HERRNSDORF,<sup>1</sup> R. K. HENDERSON,<sup>2</sup>  E. GU,<sup>1</sup> M. J. STRAIN,<sup>1</sup>  AND M. D. DAWSON<sup>1</sup> 

<sup>1</sup>*Institute of Photonics, Department of Physics, University of Strathclyde, Glasgow G1 1RD, UK*

<sup>2</sup>*Institute for Integrated Micro and Nano Systems, School of Engineering, University of Edinburgh, Edinburgh EH9 3FF, UK*

\**jose.correia-carreira@strath.ac.uk*

**Abstract:** We present integration of singulated micron-sized light emitting diodes (micro-LEDs) directly onto a silicon CMOS drive chip using a transfer printing method. An 8x8 micro-LED device array with individual control over each pixel is demonstrated with modulation bandwidths up to 50 MHz, limited by the large modulation depth of the driver chip. The 2 kHz frame rate CMOS driver also incorporates a Single Photon Avalanche Diode device thus allowing detection and transmission functionality on a single integrated chip. Visible light communications at data rates up to 1 Mbps, and time-of-flight ranging with cm-scale resolution are demonstrated using this hybrid integrated system.

Published by The Optical Society under the terms of the [Creative Commons Attribution 4.0 License](https://creativecommons.org/licenses/by/4.0/). Further distribution of this work must maintain attribution to the author(s) and the published article's title, journal citation, and DOI.

## 1. Introduction

Arrays of micron-sized light emitting diodes (micro-LEDs or  $\mu$ LEDs) on sapphire substrates can be directly integrated with their electronic drive chips using standard flip-chip bonding processes [1,2], producing individually addressable, high-speed sources for visible light communications (VLC) [3] and spatial navigation [4] in compact, chip-scale systems. The transparency of sapphire at typical III-N emission wavelengths allows for vertical emission of individual pixels through the substrate. Patterning of lenses [5] and surface features [6] allows for enhanced emission out of the substrate bulk. However, flip-chip integration can result in issues with uniformity in the emission from large arrays due to the bump bonding process, and multiple reflection paths within the substrate can lead to cross-talk between pixels. Furthermore, flip-chip bonding is not suitable in cases where the device emission, or detection, wavelength is absorbed by the flipped substrate. An alternative integration technique is micro-transfer printing ( $\mu$ TP), where individual thin film devices are removed from their growth substrate and transferred onto a host chip, using an accurate form of pick and place [7]. This technique allows the population of the host substrate with devices only where required, removing issues associated with a flip-chipped substrate. This method has been shown to be able to handle micro-LED chips as small as  $8 \times 15 \mu\text{m}^2$ , with extremely high-yield [8], and has been used to realise, for example, micro-displays on flexible substrates [9] or optical gain on silicon photonics [10]. In addition to the printing of optically active devices, direct integration of optical and electronic layers has been demonstrated on flexible substrates [11]. Nevertheless, the majority of transfer printed systems use electronic tracks and wire-bonds to connect the optical devices to their respective drive electronics, limiting the potential for dense integration and compact system geometries.

In this work, we present the integration of nitride micro-LED devices directly onto silicon (Si)-CMOS drive chips. Micro-LED platelets are fabricated on their native Si substrate and then transfer printed onto pixels of a CMOS chip for individual control over each pixel. An 8x8 array of devices is realised with operation bandwidths in the 10's of MHz range, with excellent uniformity both in brightness and modulation performance across the pixel array. High-speed optical camera communications (OCC) are demonstrated using spatio-temporal modulation of the array. The silicon driver chip also includes a Single Photon Avalanche Diode (SPAD) device that allows the single chip to act as a transceiver. Demonstration of data communications and time-of-flight (ToF) ranging operation, using the SPAD as a receiver, is presented.

## 2. Micro-LED fabrication and integration onto CMOS by $\mu$ TP

Blue (450 nm) top-emitting through the *p*-GaN micro-LED platelets were fabricated from commercial InGaN LED epistuctures, grown on a Si 111-oriented substrate, following conventional microfabrication procedures [12]. The LED epitaxial structure comprises a 200 nm thick aluminum nitride (AlN) layer, followed by a 950 nm Al-graded GaN buffer layer, an 800 nm thick *n*-doped GaN, a 100 nm thick multi-quantum well (MQW) layer, and a 140 nm thick *p*-doped GaN layer (Fig. 1(a1)). In the first fabrication step, a nickel/gold (Ni/Au thicknesses 10/20 nm) bilayer was electron beam deposited, lithographically patterned, and annealed in an air environment at 510 °C defining a semitransparent *p*-GaN metal contact (Fig. 1(a2)). Inductively coupled plasma (ICP) etching was used to expose the underlying *n*-GaN layer, thus defining a  $6.5 \times 10^{-5}$  cm<sup>2</sup> active area pixel (Fig. 1(a3)). Another ICP etch step down to the Si(111) substrate created a 100x100  $\mu$ m<sup>2</sup> mesa and exposed the chemically preferentially etched Si(110) planes (Fig. 1(a4)). In order to fabricate suspended transferable micro-LED platelets, supporting "anchors", which tether the micro-LED platelet to the Si substrate, were also defined during the ICP mesa etching. The Si (110) planes, underneath the micro-LED platelets, were anisotropically etched away in a 30% potassium hydroxide solution at 80 °C (Fig. 1(a5)). Upon completion of this etching step, the micro-LED platelets are held suspended above an air gap (2  $\mu$ m), by two sacrificial supporting "anchors" [13].

The CMOS chip was implemented in standard 0.35  $\mu$ m CMOS technology and consists of a 16x16 array of individually-controllable 100x100  $\mu$ m<sup>2</sup> p-MOS driver cells on a center-to-center pitch of 100  $\mu$ m (backplane driver circuit shown in [14]). This chip was custom designed to be integrated with on-sapphire 16x16 micro-LED arrays by conventional gold bump flip-chip bonding. Integrated devices using this driver chip have been demonstrated for VLC [3], spatial navigation [4], and OCC [15]. In addition to the 16x16 main array of driver pixels, the CMOS chip also contains a single free running SPAD. The SPAD, which has a dead time of 40 ns (saturation of 25 MHz) and active area diameter of 6  $\mu$ m (further details and pixel circuit in [16]) is an avalanche photodiode operating in Geiger mode, providing digital pulses on the detection of a single photon. The potential is therefore available for a single chip, with suitable optical bonded devices, to act as both an optical transmitter and receiver.

An 8x8 array of micro-LEDs was sequentially transfer printed directly, without any adhesion enhancement layer, onto the CMOS drivers. An elastomeric polydimethylsiloxane (PDMS) stamp, with pyramidal protrusions, was used to pick-up the suspended micro-LED platelets from their Si substrate (Fig. 1(b)) and print them onto every other CMOS drivers (Fig. 1(c)) [13]. Since the micro-LED mesa is the same size as the CMOS driver and the micro-LED backside is non-conductive, the adjacent CMOS driver was used to address each respective micro-LED. For this purpose, after  $\mu$ TP of the micro-LEDs, a parylene-C (Pa-c) layer (thickness 4.5  $\mu$ m) was deposited and apertures on the micro-LED contacts and CMOS drivers were lithographically defined. Next, titanium/gold (Ti/Au thicknesses 100/200 nm) metal tracks were lithographically defined, connecting the p-MOS driver to the micro-LED *p*-contact and the micro-LED *n*-contact to the common ground. Figure 1(d) shows a schematic cross-section view of the micro-LED

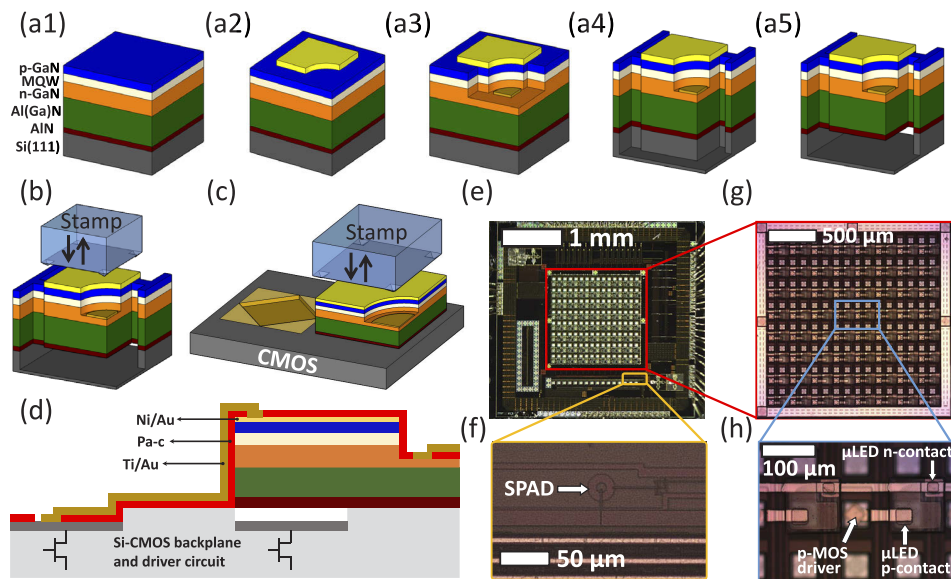


**Fig. 1.** (a) Schematic drawings of the micro-LED platelets fabrication process (not to scale, see text for further details); (b) and (c) schematic drawing of the transfer printing process during pick-up and printing of the micro-LED platelet, respectively; (d) schematic cross-section drawing of the finalised device; (e) optical image of the CMOS chip with the micro-LED active area and SPAD identified in red and yellow, respectively; (f) magnification showing in further detail the SPAD active area; (g) magnification of the CMOS chip showing the 8x8 array of transfer printed micro-LEDs; (h) shows, in further detail, the micro-LED *p*-GaN electrical connection through the adjacent *p*-MOS driver.

directly printed onto the CMOS. Figure 1(e) shows an optical image of the finalised device. Figure 1(f) shows in further detail the monolithic SPAD, while Figs. 1(g) and 1(h) show the full micro-LED array and the micro-LED electrical connecting scheme through the adjacent *p*-MOS driver, respectively.

### 3. Single micro-LED and full array performance

#### 3.1. Single micro-LED electrical, optical, and bandwidth performance

Figure 2(a) shows the current density *vs* voltage, J-V, and optical power density *vs* current density, L-J, characteristics of a representative micro-LED in the 8x8 CMOS-driven array. The inset of Fig. 2(a) presents the electroluminescence (EL) spectrum acquired at 22.2 A/cm<sup>2</sup>. The J-V characteristic was measured by a voltage source, through scanning each data point under direct current (DC) conditions (Yokogawa GS610). The L-J was measured using a calibrated Si photodiode detector (9 mm diameter active area, Thorlabs PM100D) placed in close proximity (5 mm) to the micro-LED topside. A Lambertian emission profile was assumed to convert the collected optical power into values quoted for the full forward hemisphere. The EL spectrum was acquired using an optical fiber-coupled spectrometer (Avantes AvaSpec-2048L spectrometer). The forward diode voltage of commercial LED's (250x250 μm<sup>2</sup> size) is usually defined at 20 mA, corresponding to a current density of 32 A/cm<sup>2</sup> [17]. At this current density the CMOS-driven micro-LED, reported in this work, exhibits a forward voltage of 3.65 V. The micro-LED presents an optical power density of 11 W/cm<sup>2</sup>, at 161 A/cm<sup>2</sup>, which translates into a brightness of 7.79x10<sup>5</sup> cd/m<sup>2</sup>. The EL spectrum is composed of one major peak centred at 450 nm and

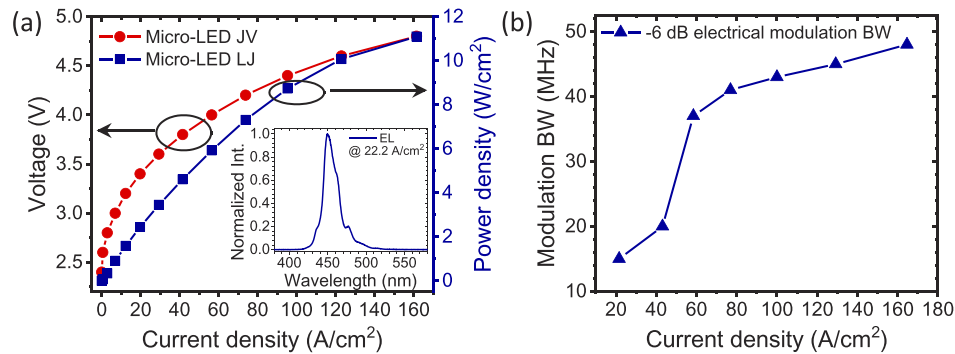


**Fig. 2.** (a) CMOS-driven micro-LED current density vs voltage (JV) curve, current density vs optical power density (LJ) curve, and electroluminescence spectra (EL); (b) CMOS-driven micro-LED -6 dB electrical modulation bandwidth vs current density.

broadened by Fabry-Perot interference occurring due to high refractive index contrast between the GaN epilayers and air [13].

The -6 dB electrical modulation bandwidth of the CMOS-driven micro-LED was measured using a network analyzer (HP8753ES) and a Si avalanche photodetector (Thorlabs — APD430A2/M bandwidth 400 MHz). As the CMOS driver is a digital device, 1 V peak-to-peak output from the network analyzer was combined with a DC offset (1.5 V) to reach the logic threshold of the electronics and then sent to the CMOS driver board through an SMA connector to modulate the corresponding micro-LED. This results in a square wave driving signal for the micro-LED, modulating between 0 V and an adjustable micro-LED bias voltage. The optical output of the micro-LED was then lens-focused onto the detector and the electrical output of the detector was fed back to the network analyzer. The modulation bandwidth of the CMOS-driven micro-LED, at different current densities, is shown in Fig. 2(b). The CMOS-driven micro-LED exhibits a modulation bandwidth of 48 MHz at 165 A/cm<sup>2</sup>, which is lower than a comparable transfer printed micro-LED packaged on a printed circuit board (PCB) [18]. This is attributed to the high modulation depth of the CMOS driver output [3].

### 3.2. Micro-LED array performance

The micro-LED yield and uniformity of electrical/optical characteristics across the full array are important factors for applications. The reported  $\mu$ TP-enabled hybridization process exhibits a 100% yield, with 64 out of 64 operational micro-LEDs. No electrical crosstalk has been observed showing a suitable insulation and electrical contact scheme. In addition, as each micro-LED is a singulated device, no optical crosstalk between neighbouring micro-LEDs has been observed.

Figures 3(a) and 3(b) show a “heat map” distribution of the forward voltage (defined at 32 A/cm<sup>2</sup>) and optical power density at 60 A/cm<sup>2</sup> across the full array, respectively. The mean and standard deviation values for the forward voltage and power density are  $3.9 \pm 0.3$  V and  $6 \pm 1$  W/cm<sup>2</sup>, respectively. The most erratic values originate from column 1 row 6 and column 1 row 7, which exhibit some electrical leakage behavior. Similar electrical leakage behavior has also been observed on micro-LEDs  $\mu$ TP onto a glass substrate [19]. It has been suggested that this is due to damage to the device sidewalls occurring when the Si substrate is removed, leaving a rough surface and increasing opportunities for tunneling. This can be further investigated by topographic and conductive atomic force microscopy and scanning Kelvin probe microscopy [20]. Nevertheless, these pixels are fully operational and can be used in practical applications as detailed in the following results. In addition, the bandwidth of 5 randomly selected CMOS-driven micro-LEDs at 4.6 V forward bias was found to be of high uniformity:  $44.8 \pm 0.5$  MHz.



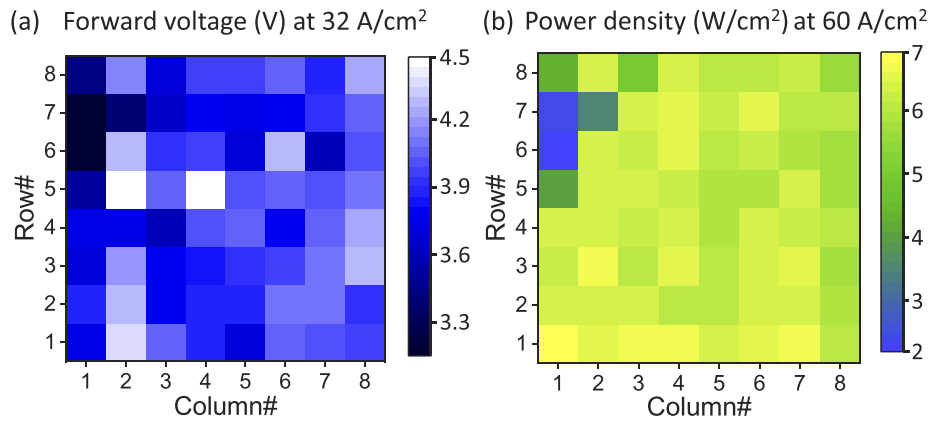


**Fig. 3.** “Heat map” distribution of (a) forward voltage and (b) optical power density at 60 A/cm<sup>2</sup> across the full array.

In order to demonstrate that the  $\mu$ TP-enabled hybridization process does not physically damage the CMOS, operation of the CMOS-driven micro-LED array as a transmitter in an OCC link is demonstrated. This has previously been demonstrated with a flip-chip bonded array in Ref. [15], however uniformity issues and faulty pixels in the array were a significant cause of errors in transmission. With the  $\mu$ TP device, yield and uniformity are significantly improved, so better results are expected. For this the CMOS-driven micro-LED array was DC biased at 4.6 V (average total current of 12.5 mA) producing an average total optical power of 2.77 mW. The patterns were updated at a rate of 2 kHz, being only limited by the full-array refresh rate of the CMOS electronics [4]. Thus each micro-LED pixel is transmitting independent binary data at 2 kHz, resulting in a net data rate of  $2000 \times 8 \times 8 = 128$  kbps. 4 blocks of 67 frames (a total of 268 frames) are transmitted with an overhead of 4.48% (3 frames in every 67) for synchronisation, and determining thresholds and alignment. This overhead can be reduced, depending on the number of data frames per transmitted block. A pseudorandom sequence of  $2^{14}$  useful bits were transmitted in order to measure a bit-error-ratio (BER). The emitted light was lens-focused

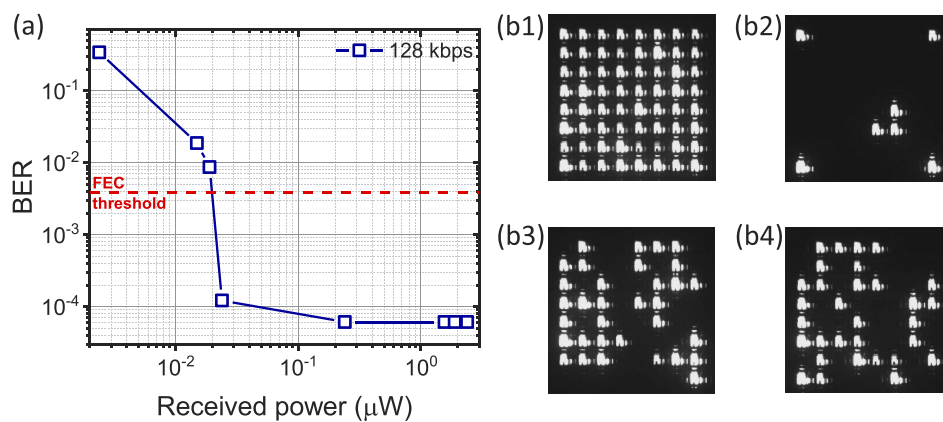


**Fig. 4.** (a) Bit-error-ratio (BER) measured as a function of received power by the ultrafast camera; (b1)–(b4) show the captured frames from the 8000 fps video for all active micro-LEDs, alignment conditions, and two different pseudo-random patterns, respectively.

(Nikon Plan Fluor 4x/0.13) onto an ultrafast camera (Photron Fastcam UX100). The camera acquisition parameters were set at 8000 frames per second (fps), resolution of 1280x616, and a total acquisition time of 302 ms. Figure 4(a) shows the BER as a function of the received power by the camera. The received power was changed by placing different neutral density filters at the receiver. The BER floor of  $6.10 \times 10^{-5}$  ( $1/2^{14}$ ) occurs as  $2^{14}$  total bits were transmitted, so a lower BER cannot be measured. For optical power values lower than  $0.02 \mu\text{W}$  the BER is larger than the  $3.8 \times 10^{-3}$  limit for forward error correction (FEC) coding [21]. Example image frames for the full array, alignment frame and two example data frames are shown in Figs. 4(b1)–4(b4), respectively.

#### 4. On-chip single micro-LED/SPAD operation

The multifunctional capability of the  $\mu\text{TP}$ -enabled CMOS-driven integrated emitter and receiver, has been demonstrated by its application as an optical communication transceiver and ToF ranging device. A single  $\mu\text{TP}$  DC biased micro-LED pixel was used for both experiments. It was experimentally verified that the on-chip crosstalk between the micro-LED and SPAD is insignificant, and therefore it is impossible to establish a direct detection link without additional optics. Thus, the  $\mu\text{TP}$  micro-LED (identified in red - Fig. 5(a)) light was lens-collected, back reflected, and focused onto the SPAD (identified in yellow - Fig. 5(a)). This setup provides an estimation of the device performance as an integrated transceiver. Figure 5(b) shows a schematic drawing of the input electrical signal for the VLC and ToF ranging experiments.

##### 4.1. VLC transceiver

In the first demonstration a free-space VLC link is implemented. For this, the micro-LED was modulated with an on-off signal provided by an FPGA module (Opal Kelly XEM6310-LX45) and applied to the CMOS control electronics. An aspheric lens (Thorlabs ACL25416U-A) was used to approximately collimate the emission. The light was reflected by a mirror at a distance of approximately 2 cm, and transmitted back through the lens. The angle of the mirror was adjusted to focus the light back on to the SPAD, which is laterally  $\sim 2$  mm away from the emitting micro-LED. The output signal from a SPAD is a series of digital pulses indicating the detection of a photon, including noise and dark counts. Therefore, to produce a meaningful data signal, counts must be summed over a time interval. Photon counts per data period can then be compared to a threshold value to decode a data signal. The output of the SPAD was captured by an oscilloscope and processed offline in MATLAB. A pseudorandom bit sequence of length  $2^{12}$  bits was transmitted, and repeated to transmit a total of over  $4 \times 10^4$  bits, sufficient to justify a BER of less than  $1 \times 10^{-4}$ . Figure 6(a) shows the BER as a function of incident power on the SPAD. VLC links of 500 kbps and 1 Mbps, below the FEC threshold, are demonstrated. For the 500 kbps link, communication, below FEC, is possible down to 58 pW of incident power. By increasing the data rate to 1 Mbps the minimum incident power for communication below the

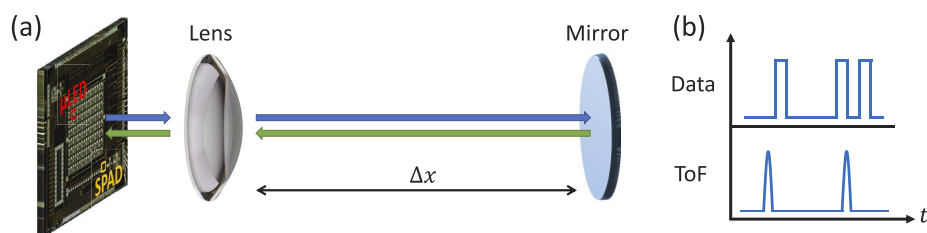


**Fig. 5.** (a) Schematic drawing of the experimental setup used in VLC ( $\Delta x \sim 2$  cm) and ToF ranging ( $\Delta x = 0 : 0.2 : 1.2$  m) demonstrations; (b) Schematic drawing of the input electrical signal for the VLC and ToF experiments.

FEC limit is 135 pW.

#### 4.2. Time-of-flight ranging

To demonstrate ranging capability, the micro-LED was operated in a pulsed manner. The FPGA module was used to generate 20 ns wide electrical pulses at a repetition rate of 3.13 MHz. This rate was chosen as a compromise between rapid acquisition of ranging data and the ability to fully resolve individual pulses. As the CMOS and the micro-LED bandwidth limit the rise and fall times, applying this signal to the CMOS driver generates optical pulses from the micro-LED with a full width at half maximum of 19 ns. An aspheric lens (Thorlabs ACL50832U-A) was used to collimate the micro-LED output. A large mirror (COMAR 250 MC 160) was used to reflect the light back to the chip and refocus on to the SPAD. The distance from the CMOS chip to the mirror was changed from 0 to 1.2 m in 0.2 m intervals. The SPAD output was used as the start signal to trigger a time-to-digital converter (Texas Instruments TDC7200), with a stop signal provided by the FPGA module. Thus, time of flight for single photons is recorded using reverse time-correlated single photon counting (TCSPC) methods [22]. By repeating the single photon arrival time measurements and building up a histogram, the optical pulse shape is recovered, and time of flight can be measured by finding the centroid of the received peak [23]. For these experiments,  $10^4$  arrival times were measured in dark laboratory conditions. Using a repetition rate of 3.13 MHz ( $Rep$ ) and  $10^4$  samples ( $N$ ) gives an acquisition time ( $T$ ) of  $\sim 3$  ms ( $T = N/Rep$ ), which provides an adequate capture for simple time of flight ranging. In addition, at this repetition rate, an effective accessible range (i.e. spatial pulse separation divided by two) of 48 m is achieved. The resulting distance measurements are shown in Fig. 6(b), along with the histogram acquired at 1.2 m. While the precision is limited by the width of the optical pulses, this proof-of-concept demonstration shows cm-scale distance measurements over a 1.2 m distance with a root-minimum-square (RMS) deviation of 8.14 cm.

### 5. Conclusion

In conclusion, we have demonstrated the direct integration of an 8x8 array of GaN-based micro-LEDs onto CMOS circuitry by micro-transfer printing, without any adhesion-enhancement layer. A representative CMOS-driven micro-LED exhibits a forward diode voltage of 3.65 V and an optical power density of 11 W/cm<sup>2</sup> at 161 A/cm<sup>2</sup>. The CMOS-driven micro-LED modulation bandwidth of 48 MHz at 165 A/cm<sup>2</sup> is limited by the CMOS driver and its high modulation depth output. The reported  $\mu$ TP-enabled integration process exhibits a 100% yield with mean

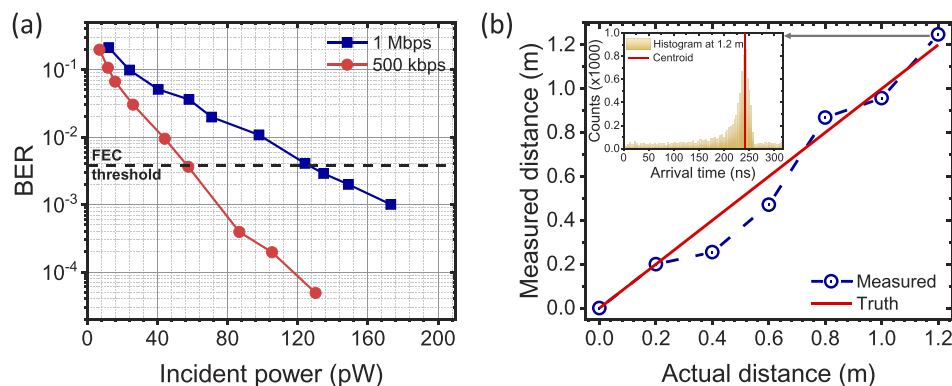


**Fig. 6.** (a) Bit-error-ratio (BER) measured as a function of the incident power on the SPAD; (b) measured distance plotted as a function of the actual distance in a ranging setup (inset shows the histogram acquired at 1.2 m).

and standard deviation values for the forward voltage and power density, across the full array, of  $3.9 \pm 0.3$  V and  $6 \pm 1$  W/cm<sup>2</sup>, respectively. The high yield and uniformity led to a demonstration of a 128 kbps OCC link below BER for optical power larger than  $0.02 \mu\text{W}$ . On-chip excitation and detection enabled the demonstration of an 1 Mbps VLC link and ToF ranging up to 1.2 m with a RMS deviation of 8.14 cm.

Due to its low temperature and minimal mechanical pressure the  $\mu\text{TP}$ -enabled integration process can be extended to a wide range of materials/devices. In particular, the integration of full color micro-emitters onto CMOS is highly sought for virtual/augmented reality applications, and can be achieved using the techniques demonstrated here. Furthermore, we envisage the hybrid integration of micro-LEDs and SPAD, shown in this work, to find further applications in single chip architecture, low size, weight, power and cost (SWaP-C) VLC transceivers and ToF ranging devices.

Supporting data can be found at <https://doi.org/10.15129/718b2ab0-16fe-43eb-9a4c-490c01ad0b29>.

## Funding

Engineering and Physical Sciences Research Council (EP/T00097X/1, EP/R03480X/1, EP/S001751/1).

## Acknowledgments

Plessey Semiconductors Ltd. is acknowledged for providing the GaN-on-Si wafer.

## Disclosures

The authors declare no conflicts of interest.







## References

1. J. J. D. McKendry, B. R. Rae, Z. Gong, K. R. Muir, B. Guilhabert, D. Massoubre, E. Gu, D. Renshaw, M. D. Dawson, and R. K. Henderson, "Individually Addressable AlInGaN Micro-LED Arrays With CMOS Control and Subnanosecond Output Pulses," *IEEE Photonics Technol. Lett.* **21**(12), 811–813 (2009).
2. J. Day, J. Li, D. Y. C. Lie, C. Bradford, J. Y. Lin, and H. X. Jiang, "III-Nitride full-scale high-resolution microdisplays," *Appl. Phys. Lett.* **99**(3), 031116 (2011).
3. S. Zhang, S. Watson, J. J. D. McKendry, D. Massoubre, A. Cogman, E. Gu, R. K. Henderson, A. E. Kelly, and M. D. Dawson, "1.5 Gbit/s Multi-Channel Visible Light Communications Using CMOS-Controlled GaN-Based LEDs," *J. Lightwave Technol.* **31**(8), 1211–1216 (2013).
4. J. Herrnsdorf, M. J. Strain, E. Gu, R. K. Henderson, and M. D. Dawson, "Positioning and Space-Division Multiple Access Enabled by Structured Illumination With Light-Emitting Diodes," *J. Lightwave Technol.* **35**(12), 2339–2345 (2017).
5. H. W. Choi, C. Liu, E. Gu, G. McConnell, J. M. Girkin, I. M. Watson, and M. D. Dawson, "GaN micro-light-emitting diode arrays with monolithically integrated sapphire microlenses," *Appl. Phys. Lett.* **84**(13), 2253–2255 (2004).
6. J.-Y. Cho, K.-J. Byeon, H. Park, J. Kim, H.-S. Kim, and H. Lee, "Improvement of photon extraction efficiency of GaN-based LED using micro and nano complex polymer structures," *Nanoscale Res. Lett.* **6**(1), 578 (2011).
7. A. Carlson, A. M. Bowen, Y. Huang, R. G. Nuzzo, and J. A. Rogers, "Transfer Printing Techniques for Materials Assembly and Micro/Nanodevice Fabrication," *Adv. Mater.* **24**(39), 5284–5318 (2012).
8. C. A. Bower, M. A. Meitl, B. Raymond, E. Radauscher, R. Cok, S. Bonafede, D. Gomez, T. Moore, C. Prevatte, B. Fisher, R. Rotzoll, G. A. Melnik, A. Fecioru, and A. J. Trindade, "Emissive displays with transfer-printed assemblies of  $8 \mu\text{m} \times 15 \mu\text{m}$  inorganic light-emitting diodes," *Photonics Res.* **5**(2), A23–A29 (2017).
9. S.-I. Park, Y. Xiong, R.-H. Kim, P. Elvikis, M. Meitl, D.-H. Kim, J. Wu, J. Yoon, C.-J. Yu, Z. Liu, Y. Huang, K.-c. Hwang, P. Ferreira, X. Li, K. Choquette, and J. A. Rogers, "Printed Assemblies of Inorganic Light-Emitting Diodes for Deformable and Semitransparent Displays," *Science* **325**(5943), 977–981 (2009).
10. J. Zhang, G. Muliuk, J. Juvert, S. Kumari, J. Goyvaerts, B. Haq, C. Op de Beeck, B. Kuyken, G. Morthier, D. Van Thourhout, R. Baets, G. Lepage, P. Verheyen, J. Van Campenhout, A. Gocalinska, J. O'Callaghan, E. Pelucchi, K. Thomas, B. Corbett, A. J. Trindade, and G. Roelkens, "III-V-on-Si photonic integrated circuits realized using micro-transfer-printing," *APL Photonics* **4**(11), 110803 (2019).

11. M. Choi, B. Jang, W. Lee, S. Lee, T. W. Kim, H.-J. Lee, J.-H. Kim, and J.-H. Ahn, "Stretchable Active Matrix Inorganic Light-Emitting Diode Display Enabled by Overlay-Aligned Roll-Transfer Printing," *Adv. Funct. Mater.* **27**(11), 1606005 (2017).
12. P. Tian, J. J. D. McKendry, Z. Gong, S. Zhang, S. Watson, D. Zhu, I. M. Watson, E. Gu, A. E. Kelly, C. J. Humphreys, and M. D. Dawson, "Characteristics and applications of micro-pixelated GaN-based light emitting diodes on Si substrates," *J. Appl. Phys.* **115**(3), 033112 (2014).
13. A. J. Trindade, B. Guilhabert, D. Massoubre, D. Zhu, N. Laurand, E. Gu, I. M. Watson, C. J. Humphreys, and M. D. Dawson, "Nanoscale-accuracy transfer printing of ultra-thin AlInGaN light-emitting diodes onto mechanically flexible substrates," *Appl. Phys. Lett.* **103**(25), 253302 (2013).
14. B. R. Rae, J. Yang, J. McKendry, Z. Gong, D. Renshaw, J. M. Girkin, E. Gu, M. D. Dawson, and R. K. Henderson, "A Vertically Integrated CMOS Microsystem for Time-Resolved Fluorescence Analysis," *IEEE Transactions on Biomed. Circuits Syst.* **4**(6), 437–444 (2010).
15. A. D. Griffiths, J. Herrnsdorf, M. J. Strain, and M. D. Dawson, "Scalable visible light communications with a micro-LED array projector and high-speed smartphone camera," *Opt. Express* **27**(11), 15585–15594 (2019).
16. C. Niclass, M. Sergio, and E. Charbon, "A Single Photon Avalanche Diode Array Fabricated in Deep-Submicron CMOS Technology," *Proc. Des. Autom. Test Eur. Conf.* **1**, 1–6 (2006).
17. E. F. Schubert, *Light-Emitting Diodes* (Cambridge University Press, 2006).
18. J. F. C. Carreira, E. Xie, R. Bian, C. Chen, J. J. D. McKendry, B. Guilhabert, H. Haas, E. Gu, and M. D. Dawson, "On-chip GaN-based dual-color micro-LED arrays and their application in visible light communication," *Opt. Express* **27**(20), A1517–A1528 (2019).
19. K. Rae, P. P. Manousiadis, M. S. Islim, L. Yin, J. Carreira, J. J. D. McKendry, B. Guilhabert, I. D. W. Samuel, G. A. Turnbull, N. Laurand, H. Haas, and M. D. Dawson, "Transfer-printed micro-led and polymer-based transceiver for visible light communications," *Opt. Express* **26**(24), 31474–31483 (2018).
20. X. Cao, J. Teetsov, F. Shahedipour-Sandvik, and S. Arthur, "Microstructural origin of leakage current in GaN/InGaN light-emitting diodes," *J. Cryst. Growth* **264**(1-3), 172–177 (2004).
21. I. T. Union, "Forward error correction for high bit-rate DWDM submarine systems," ITU, Geneva, Switzerland, Tech. Rep. ITU-T G.975.1 (2013).
22. W. Becker, *Advanced Time-Correlated Single Photon Counting Techniques* (Springer Series in Chemical Physics, 2005).
23. A. D. Griffiths, H. Chen, D. D.-U. Li, R. K. Henderson, J. Herrnsdorf, M. D. Dawson, and M. J. Strain, "Multispectral time-of-flight imaging using light-emitting diodes," *Opt. Express* **27**(24), 35485–35498 (2019).



# Gigabit per second visible light communication based on AlGaInP red micro-LED micro-transfer printed onto diamond and glass

J. F. C. CARREIRA,<sup>1,3</sup>  E. XIE,<sup>1,4</sup>  R. BIAN,<sup>2</sup> J. HERRNSDORF,<sup>1</sup>  H. HAAS,<sup>2</sup>  E. GU,<sup>1,5</sup> M. J. STRAIN,<sup>1</sup>  AND M. D. DAWSON<sup>1</sup> 

<sup>1</sup>Institute of Photonics, Department of Physics, University of Strathclyde, Glasgow G1 1RD, UK

<sup>2</sup>Institute for Digital Communications, Li-Fi R&D Centre, University of Edinburgh, Edinburgh EH9 3JL, UK

<sup>3</sup>jose.correia-carreira@strath.ac.uk

<sup>4</sup>enyuan.xie@strath.ac.uk

<sup>5</sup>erdan.gu@strath.ac.uk

**Abstract:** Full-color smart displays, which act both as a display and as a high-speed visible light communication (VLC) transmitter, can be realized by the integration of red-green-blue micron-sized light emitting diodes (micro-LEDs) onto a common platform. In this work, we report on the integration of aluminum gallium indium phosphide red micro-LEDs onto diamond and glass substrates by micro-transfer printing and their application in VLC. The device on-diamond exhibits high current density and bandwidth operation, enabled by diamond's superior thermal properties. Employing an orthogonal frequency division multiplexing modulation scheme, error-free data rates of 2.6 Gbps and 5 Gbps are demonstrated for a single micro-LED printed on-glass and on-diamond, respectively. In a parallel configuration, a 2x1 micro-LED array achieves error-free data rates of 3 Gbps and 6.6 Gbps, on-glass and on-diamond, respectively.

Published by The Optical Society under the terms of the [Creative Commons Attribution 4.0 License](https://creativecommons.org/licenses/by/4.0/). Further distribution of this work must maintain attribution to the author(s) and the published article's title, journal citation, and DOI.

## 1. Introduction

Micron-sized light emitting diodes (micro-LEDs or  $\mu$ LEDs) are expected to become the next-generation of self-emissive displays and microdisplays [1]. Full-color micro-LED displays have been realized by mass transfer techniques, such as micro-transfer printing (micro-TP or  $\mu$ TP), of red-green-blue (RGB) singulated chiplets onto a common platform [2,3]. Blue and green pixels are fabricated from indium gallium nitride (InGaN) alloys grown on sapphire or silicon substrates [4]. Typically, the red emission is based on aluminum gallium indium phosphide (AlGaInP) LED structures grown on gallium arsenide (GaAs) [5,6]. These inorganic micron-sized pixels exhibit exceptional brightness, contrast and low power consumption. In addition, due to their smaller device capacitance and current density dependent differential carrier lifetime, micro-LEDs show extremely high modulation bandwidth, supporting visible light communication (VLC) up to several gigabits per second (Gbps) [7]. This opens the possibility for smart micro-LED displays acting both as a display and as a high-speed VLC transmitter [8].

In the past years, several demonstrations of Gbps VLC, employing spectrally efficient modulation schemes (such as, orthogonal frequency division multiplexing - OFDM) and GaN-based micro-LEDs (with emission wavelengths covering from the violet to the green) were reported [9–11]. In particular, nonpolar GaN-based micro-LEDs hold great promise for VLC applications, due to their extremely high bandwidth at low current density [12]. However, the internal polarization field effects of nitrides are not prevalent in AlGaInP/GaAs red LEDs, and, to



the best of our knowledge, there are no reports on data transmission capability of AlGaInP LEDs in micro-LED geometries. In this paper, we report on the integration of AlGaInP micro-LEDs onto glass and diamond substrates by micro-TP. The superior thermal properties of diamond over glass are evidenced by ability of the red micro-LED on-diamond to support higher current density, thus achieving 100's MHz of modulation bandwidth. In a free-space VLC link Gbps error-free data rates are demonstrated by both on-diamond and on-glass micro-LED devices. The broader implication of this work include application of these red micro-LED devices with polymer optical fibers and/or high turbidity underwater wireless optical communication systems.

## 2. Device fabrication by micro-TP

In this work, free-standing red (630 nm) micro-LED platelets were printed onto glass and diamond substrates. The epitaxial structure of these red micro-LEDs follows that of conventional AlGaInP epistructures grown on GaAs [13]. Fabrication of the micro-LED platelets started by processing the topside of the AlGaInP/GaAs wafer following typical microfabrication procedures for mesa type LEDs. First, a  $6.96 \times 10^{-6} \text{ cm}^2$  active area pixel was defined by dry etching, exposing the  $n$  layer, followed by deposition of AuGe/Au and Ti/Al/Ti/Au metal stacks on the  $n$  and  $p$  contacts, respectively. Next, the GaAs wafer was flip-chip bonded to a temporary sapphire carrier and the GaAs bulk substrate removed by wet chemical etching [14]. Finally, the platelet was defined through the backside of the AlGaInP film by dry etching. Figure 1(a) shows a 2x2 array of micro-LED platelets on the temporary sapphire carrier.

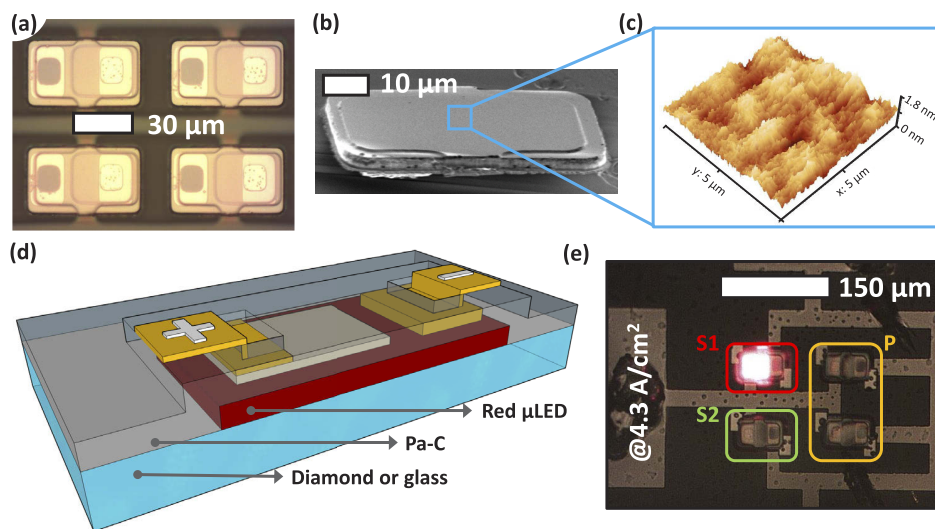


**Fig. 1.** (a) Plan-view photograph of a 2x2 array of micro-LED platelets on the temporary sapphire carrier; (b) scanning electron microscopy micrograph of a micro-LED platelet backside; (c) representative  $5 \times 5 \mu\text{m}^2$  atomic force microscopy micrograph of a micro-LED platelet backside; (d) schematic drawing of the transfer printed micro-LED after Parylene-C (Pa-C) encapsulation and metallization; (e) plan-view photograph of a finalised 2x2 micro-LED array printed onto glass with a single micro-LED (S1) driven at  $4.3 \text{ A/cm}^2$ .

Figure 1(b) shows a scanning electron microscopy (SEM) micrograph of a micro-LED platelet backside. The micro-LED platelet backside was found to be extremely flat, which can be attributed to the lattice matched and strain-free epitaxial growth of these LED structures on GaAs [5]. In addition, due to the high etching selectivity between the GaAs and the etch stop layer, the backside of the micro-LED platelet is extremely smooth, as shown by a representative  $5 \times 5 \mu\text{m}^2$

atomic force microscopy micrograph (Fig. 1(c)). The micro-LED platelet backside exhibits a root-mean-square (RMS) roughness of 0.2 nm, approaching the instrument resolution. The flatness and smoothness of the micro-LED platelet backside are important factors for micro-TP applications, as they improve the adhesion between the platelet and the receiving substrate. Furthermore, the good contact between the micro-LED platelet and the receiving substrate ensures efficient heat transfer.

A 2x2 array of micro-LEDs was sequentially printed directly, without any adhesion enhancement layer, onto glass and diamond substrates. The glass and single-crystal (synthetic) diamond substrates had the same dimensions, namely area 4x4 mm<sup>2</sup> and thickness 500 μm. An elastomeric polydimethylsiloxane (PDMS) stamp, with pyramidal protrusions, was used to pick-up the micro-LED platelets from the temporary sapphire carrier and print them onto both substrates [15]. The micro-LED platelets are bonded to the temporary sapphire carrier by a weak adhesive interlayer, which was optimized to allow retrieval of the platelets with the PDMS stamp. Due to PDMS viscoelastic properties, quick retraction of the stamp results in an adhesion strength between the micro-LED platelet and the stamp larger than the adhesion strength between the platelet and the weak adhesion interlayer; thus the micro-LED platelet is retrieved. On the other hand, when in contact with the receiving substrate, slow retraction of the stamp results in an adhesion strength between the platelet and the stamp smaller than the one between the platelet and the receiving substrate; thus the platelet is released [16]. After micro-TP, a Parylene-C (Pa-c) layer (thickness 4 μm) was deposited as an insulation and encapsulation layer. Next, Ti/Au (thicknesses 100/200 nm) metal tracks were lithographically defined, contacting the micro-LEDs through, previously defined by reactive ion etching, localized apertures in the Pa-C layer. Using lithographically processed electrical contacts allows efficient planar registration of the transfer printed micro-LEDs, without pre-processing the receiving substrate. In addition, this method can be easily extended to a variety of substrates, such as flexible polymers [17]. Figure 1(d) shows a schematic drawing of the transfer printed micro-LED after Pa-C encapsulation and metallization. The 2x2 array was arranged in order to have two individually addressable single micro-LEDs (identified in Fig. 1(e) as S1 and S2) and a 2x1 in-parallel micro-LED array (identified in Fig. 1(e) as P). Figure 1(e) shows the single micro-LED S1 driven at 4.3 A/cm<sup>2</sup>. It was found experimentally that the micro-LEDs S1 and S2 exhibit the same electrical and optical properties, on both substrates. Thus, for clarity sake, the device performance and application results are only shown for the micro-LED S1.

### 3. Device performance and application

#### 3.1. Micro-LED electrical, optical, and bandwidth characteristics

Figure 2(a) shows the current density vs voltage (JV) and current density vs optical power density (JL) of the single micro-LED S1 on-diamond and on-glass. The JV characteristic was measured by a voltage source, through scanning each data point under direct current (DC) conditions (Yokogawa GS610). The JL characteristic was measured using a calibrated Si photodiode detector (Thorlabs PM100D) placed in close proximity to the micro-LED backside. The forward diode voltage (at 32 A/cm<sup>2</sup>) of the single micro-LED on-diamond and on-glass was found to be 2.2 V and 2.1 V, respectively. The red micro-LED on-glass optical power density reaches a plateau of 16.6 W/cm<sup>2</sup> at 359 A/cm<sup>2</sup>. Due to diamond's superior thermal conductivity properties ( $k = 2200$  W/m.K) over glass ( $k = 1.42$  W/m.K) [18] the micro-LED on-diamond sustains current densities up to 790 W/cm<sup>2</sup> without any thermal roll-over. At the current density of 790 A/cm<sup>2</sup> the micro-LED on-diamond exhibits a near chip face optical power density of 39 W/cm<sup>2</sup> (more than twofold increase compared to the micro-LED on-glass).

The -6 dB electrical modulation bandwidth of the single micro-LED S1 on different substrates was measured by applying a DC bias combined with a small-signal modulation from an HP8753ES network analyzer. The optical response was lens-focused onto a silicon avalanche photodetector



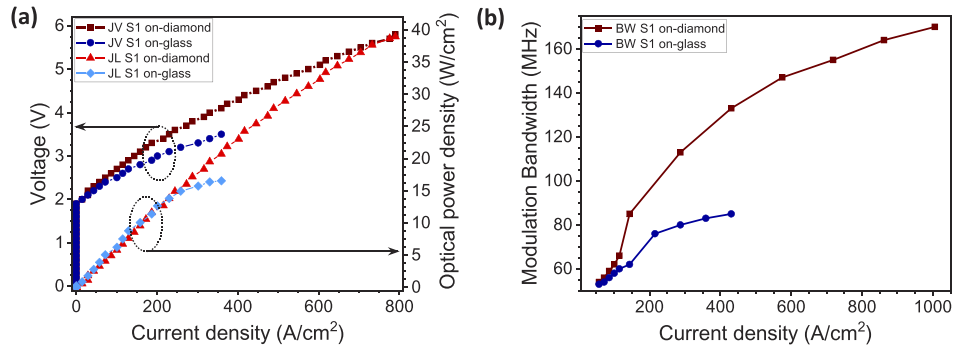


**Fig. 2.** (a) Current density vs voltage (JV) and current density vs optical power density (JL) curves of the single micro-LED S1 on-diamond and on-glass; (b) -6 dB electrical modulation bandwidth of the single micro-LED S1 on both substrates.

(Thorlabs — APD430A2/M bandwidth 400 MHz). Figure 2(b) shows the -6 dB electrical modulation bandwidth vs current density of the single micro-LED S1 on-diamond and on-glass. Devices on both glass and diamond exhibit similar performance for current densities below 100 A/cm<sup>2</sup>. Above this point, the micro-LED on-glass exhibits a lower modulation bandwidth until it reaches a plateau of 85 MHz at 431 A/cm<sup>2</sup>. On the other hand, the micro-LED on-diamond modulation bandwidth continues to increase up to 170 MHz at 1000 A/cm<sup>2</sup>.

Figure 3(a) shows the electroluminescence (EL) spectra of the single micro-LED S1 driven at 359 A/cm<sup>2</sup> on both substrates. The inset in Fig. 3(a) shows the CIE1931 color coordinates of the single micro-LED S1 on both substrates on the color space chromaticity diagram. The EL spectra were acquired using an optical fiber-coupled spectrometer (Avantes AvaSpec-2048L spectrometer). Both spectra show fringes due to refractive index contrast between the LED epitaxial material ( $n=3.5$  [19]) and both substrates (glass  $n=1.46$  [20], diamond  $n=2.41$  [21]). The micro-LED on-diamond exhibits an EL peak centered at 631.8 nm and a full width at full maximum (FWHM) of 19 nm. While, the micro-LED on glass EL peak is red-shifted (peak emission centered at 634.5 nm) and broadened (FWHM = 22 nm) due to bandgap shrinkage

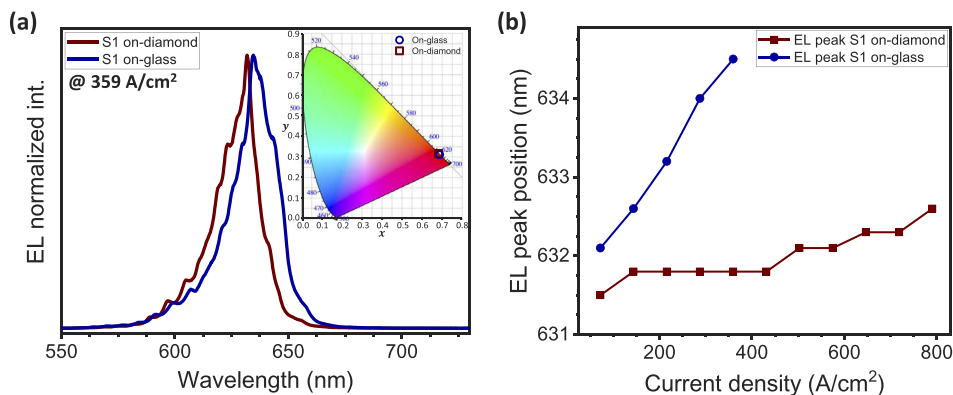


**Fig. 3.** (a) Electroluminescence (EL) spectra of the single micro-LED S1 (at 359 A/cm<sup>2</sup>) on both substrates (inset: CIE1931 color coordinates of the single micro-LED S1 on both substrates (at 359 A/cm<sup>2</sup>)); (b) EL spectra peak position vs current density of the single micro-LED S1 on both substrates.

and band filling effects, respectively. Nevertheless, these variations have a marginal effect on the perceived color, with the micro-LED on-diamond ( $x = 0.68, y = 0.32$ ) and on-glass ( $x = 0.69, y = 0.31$ ) showing similar  $(x, y)$  CIE1931 color coordinates. Figure 3(b) shows the EL peak position vs current density for the single micro-LED S1 printed on-diamond and on-glass. For the device on-glass, increasing the current density from  $72 \text{ A/cm}^2$  to  $359 \text{ A/cm}^2$  results in a steep red-shift of the peak position from  $632.1 \text{ nm}$  to  $634.5 \text{ nm}$  ( $\Delta\lambda = 2.4 \text{ nm}$ ). On the other hand, for the device on-diamond, under the same current density interval, the peak only red-shifts by  $0.3 \text{ nm}$ . In fact, due to diamond's excellent thermal conductivity varying the current density from  $72 \text{ A/cm}^2$  to  $790 \text{ A/cm}^2$  results in a red-shift from  $631.5 \text{ nm}$  to  $632.6 \text{ nm}$  ( $\Delta\lambda = 1.1 \text{ nm}$ ).

### 3.2. VLC application

Optical orthogonal frequency division multiplexing (O-OFDM) has proven to be spectrally efficient in VLC [22,23]. In this work, an implementation of direct current biased optical OFDM (DCO-OFDM) is used for the wireless data transmission due to its simplicity and high spectral efficiency [24]. As intensity modulation and direct detection (IM/DD) is used in VLC, the transmitted signal should be both real and non-negative. Thus Hermitian symmetry is applied and a DC bias is added.

A schematic drawing of the VLC experimental set-up is shown in Fig. 4. A random bit stream is encoded into an OFDM signal by MATLAB and then generated by an arbitrary waveform generator (AWG, Keysight M8195A). The analogue signal is amplified by a power amplifier (SHF S126A) and then combined with a DC bias (Yokogawa GS610) through a bias-tee (Tektronix PSPL5575A). The output of the bias-tee is connected to the micro-LED device. The link distance is set to  $40 \text{ cm}$ , as in this case we wish to assess the upper modulation limits of the devices, and aspheric condenser lenses (ACL4532A) have been used at both transmitter and receiver side. The optical signal is detected by a photoreceiver (Femto HSPR-X-I-1G4-SI). The output electrical signal is captured by an oscilloscope (Keysight DSA90804B) and then sent to the PC for processing using MATLAB.

Within each measurement, a channel estimation is first done to estimate the signal-to-noise ratio (SNR) at each subcarrier. Then the signal is generated using an adaptive bit and power loading algorithm based on the estimated SNR and a target bit-error-ratio (BER). Such signal is transmitted and the achieved data rate and BER are measured.

The VLC results of the red micro-LED devices on both substrates are summarized in Fig. 5. The DC bias and the modulation signal peak-to-peak voltage, after the amplifier, were set to  $359 \text{ A/cm}^2$  ( $862 \text{ A/cm}^2$ ) and  $2.68 \text{ V}$  ( $7.19 \text{ V}$ ), respectively, for the single micro-LED S1 on-glass (on-diamond). The sampling frequency was set at  $16 \text{ GSa/s}$  and the number of samples per symbol was optimized for each substrate. The estimated SNR and number of allocated bits, at the highest data rate below the FEC threshold of  $3.8 \times 10^{-3}$  BER, for the single micro-LED S1

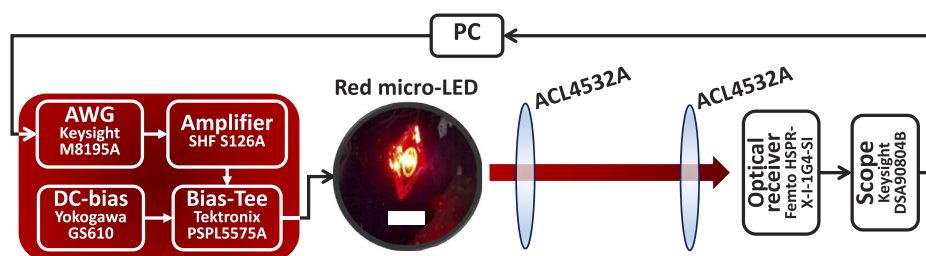


**Fig. 4.** Schematic diagram of the visible light communication experimental set-up. The photograph inset is the micro-LED on-diamond device (white scale bar corresponds to  $1 \text{ cm}$ ).

on-glass (blue curve and blue bar plot) and on-diamond (red curve and red bar plot) are shown in Fig. 5(a).

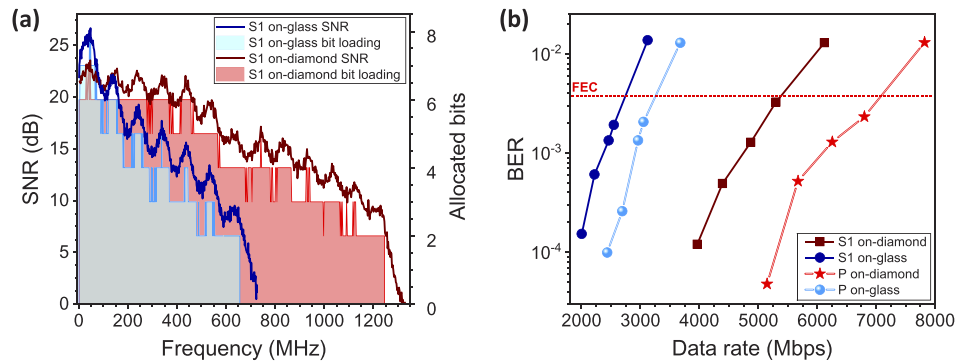


**Fig. 5.** (a) Signal-to-noise ratio and number of allocated bits (at maximum data rate below forward error correction) for the single micro-LED S1 on both substrates (glass and diamond); (b) bit-error-ratio (BER) vs data rate for the single micro-LED S1 and in-parallel micro-LED array P on both substrates.

As the micro-LED on-glass exhibits lower optical power and bandwidth its SNR suffers a sharp drop with frequency, supporting bit loading only up to 656 MHz. On the other hand, the micro-LED on-diamond higher optical power and bandwidth (due to its higher current density operation) results in a smooth decrease of the SNR with frequency and bit loading up to 1245 MHz. These differences in SNR and bit loading lead to the difference in BER vs data rate curves shown in Fig. 5(b). At the BER of  $3.8 \times 10^{-3}$  a single micro-LED on-glass achieves a data rate of 2749 Mbps, with the device on-diamond achieving 5391 Mbps (roughly a twofold increase). These results show the importance of efficient thermal management in LED-based VLC transmitters. Applying the 7% FEC overhead reduction, error-free data rates of 2557 Mbps and 5014 Mbps are achieved for the single micro-LED S1 on-glass and on-diamond, respectively. Also shown in Fig. 5(b) is the BER vs data rate performance of the 2x1 in-parallel micro-LED array P on both substrates. For this purpose, the DC bias and the modulation signal peak-to-peak voltage, after the amplifier, were set to 323 A/cm<sup>2</sup> (718 A/cm<sup>2</sup>) and 3.26 V (6.62 V), respectively, for the in-parallel micro-LED array on-glass (on-diamond). Although the current density is lower than a single micro-LED, the total optical power of the array is roughly two times higher than of a single micro-LED. This translates into an increase in SNR and capacity to allocate more bits to the in-parallel micro-LED arrays. Thus, the in-parallel micro-LED array on-glass achieves 3262 Mbps below FEC threshold (a 1.2x increase compared to its single counterpart). For the device transfer printed on-diamond a data rate of 7093 Mbps, below FEC, is achieved (a 1.3x increase compared to a single device on-diamond). Again, applying the 7% FEC overhead reduction, error-free data rates of 3034 Mbps and 6596 Mbps are obtained for the in-parallel micro-LED array on-glass and on-diamond, respectively.

Table 1 compares the data rate, BER, and link distance achieved by the single micro-LED S1 and by the in-parallel micro-LED array P on-diamond, with other red LED-based VLC reports from our previous work. The data rates achieved in this work are higher than the ones obtained using commercially available LEDs [25,27] or resonant cavity LEDs [26] employing similar modulation schemes. Due to the micro-LEDs lower optical power the link distance is shorter than for commercial LEDs. However, it has been shown that the optical power can be increased, without any penalty in modulation bandwidth, by simply arranging several micro-LEDs in-parallel or in-series configurations [28].

**Table 1. State-of-the-art of red LED-based VLC.**

Transmitter	Data rate (Mbps)	BER	Link distance (m)	Ref.
Micro-LED	5391 (S1)	$3.8 \times 10^{-3}$	0.4	This work
	7093 (P)			
Commercial LED	4904	$2.5 \times 10^{-3}$	1.6	[25]
Resonant cavity LED	4000	$3.4 \times 10^{-3}$	1.5	[26]

#### 4. Conclusion

In conclusion, we have demonstrated the integration of AlGaInP micro-LED platelets onto diamond and glass by micro-transfer printing, without any adhesion-enhancement layer. A single micro-LED printed onto diamond can be driven up to  $790 \text{ A/cm}^2$  displaying an optical power of  $39 \text{ W/cm}^2$  (more than two times the optical power density of the counterpart device on-glass). The ability of the device on-diamond to sustain higher current density allows to achieve modulation bandwidths up to 170 MHz (with the device on-glass plateauing at 85 MHz). The heat-spreading properties of the diamond substrate are supported by the marginal red-shift of 1.1 nm of the micro-LED emission with increasing current density. Error-free data rates of 5014 Mbps and 6596 Mbps are obtained for a single micro-LED and a 2x1 in-parallel micro-LED array transfer printed onto diamond, respectively. These data rates are the highest reported values in literature for red LED-based VLC.

This work benchmarks the application of AlGaInP micro-LEDs in VLC and paves the way towards full-color pixelated clusters in micro-LED displays operating as wavelength division multiplexing VLC transmitters. In addition, the devices reported in this work are of importance for data transmission in plastic optical fibers and/or in high-turbidity water media.

Supporting data is available at DOI: [10.15129/593ca4b1-1184-4b0f-8dd3-aa9c63382d6f](https://doi.org/10.15129/593ca4b1-1184-4b0f-8dd3-aa9c63382d6f).

#### Funding

Engineering and Physical Sciences Research Council (EP/R03480X/1, EP/S001751/1, EP/T00097X/1).

#### Disclosures

The authors declare no conflicts of interest.

#### References

1. T. Wu, C.-W. Sher, Y. Lin, C.-F. Lee, S. Liang, Y. Lu, S.-W. Huang Chen, W. Guo, H.-C. Kuo, and Z. Chen, "Mini-LED and Micro-LED: Promising Candidates for the Next Generation Display Technology," *Appl. Sci.* **8**(9), 1557 (2018).
2. C. A. Bower, M. A. Meitl, B. Raymond, E. Radauscher, R. Cok, S. Bonafede, D. Gomez, T. Moore, C. Prevatte, B. Fisher, R. Rotzoll, G. A. Melnik, A. Fecioru, and A. J. Trindade, "Emissive displays with transfer-printed assemblies of  $8 \mu\text{m} \times 15 \mu\text{m}$  inorganic light-emitting diodes," *Photonics Res.* **5**(2), A23–A29 (2017).
3. Y. Li, J. Tao, Y. Zhao, J. Wang, J. Lv, Y. Qin, J. Liang, and W. Wang, "48x48 pixelated addressable full-color micro display based on flip-chip micro leds," *Appl. Opt.* **58**(31), 8383–8389 (2019).
4. G. Li, W. Wang, W. Yang, Y. Lin, H. Wang, Z. Lin, and S. Zhou, "GaN-based light-emitting diodes on various substrates: a critical review," *Rep. Prog. Phys.* **79**(5), 056501 (2016).
5. T. Gessmann and E. F. Schubert, "High-efficiency AlGaInP light-emitting diodes for solid-state lighting applications," *J. Appl. Phys.* **95**(5), 2203–2216 (2004).
6. J.-T. Oh, S.-Y. Lee, Y.-T. Moon, J. H. Moon, S. Park, K. Y. Hong, K. Y. Song, C. Oh, J.-I. Shim, H.-H. Jeong, J.-O. Song, H. Amano, and T.-Y. Seong, "Light output performance of red AlGaInP-based light emitting diodes with different chip geometries and structures," *Opt. Express* **26**(9), 11194–11200 (2018).
7. S. Rajbhandari, J. J. D. McKendry, J. Herrnsdorf, H. Chun, G. Faulkner, H. Haas, I. M. Watson, D. O'Brien, and M. D. Dawson, "A review of gallium nitride LEDs for multi-gigabit-per-second visible light data communications," *Semicond. Sci. Technol.* **32**(2), 023001 (2017).

8. X. Li, L. Wu, Z. Liu, B. Hussain, W. C. Chong, K. M. Lau, and C. P. Yue, "Design and Characterization of Active Matrix LED Microdisplays With Embedded Visible Light Communication Transmitter," *J. Lightwave Technol.* **34**(14), 3449–3457 (2016).
9. M. S. Islim, R. X. Ferreira, X. He, E. Xie, S. Videv, S. Viola, S. Watson, N. Bamiedakis, R. V. Penty, I. H. White, A. E. Kelly, E. Gu, H. Haas, and M. D. Dawson, "Towards 10 Gb/s orthogonal frequency division multiplexing-based visible light communication using a GaN violet micro-LED," *Photonics Res.* **5**(2), A35–A43 (2017).
10. D. Tsonev, H. Chun, S. Rajbhandari, J. J. D. McKendry, S. Videv, E. Gu, M. Haji, S. Watson, A. E. Kelly, G. Faulkner, M. D. Dawson, H. Haas, and D. O'Brien, "A 3-Gb/s Single-LED OFDM-Based Wireless VLC Link Using a Gallium Nitride  $\mu$ LED," *IEEE Photonics Technol. Lett.* **26**(7), 637–640 (2014).
11. J. F. C. Carreira, E. Xie, R. Bian, C. Chen, J. J. D. McKendry, B. Guilhabert, H. Haas, E. Gu, and M. D. Dawson, "On-chip GaN-based dual-color micro-LED arrays and their application in visible light communication," *Opt. Express* **27**(20), A1517–A1528 (2019).
12. A. Rashidi, M. Monavarian, A. Aragon, A. Rishinaramangalam, and D. Feezell, "Nonpolar  $m$ -Plane InGaN/GaN Micro-Scale Light-Emitting Diode With 1.5 GHz Modulation Bandwidth," *IEEE Electron Device Lett.* **39**(4), 520–523 (2018).
13. R. Horng, H. Chien, K. Chen, W. Tseng, Y. Tsai, and F. Tarntair, "Development and Fabrication of AlGaInP-Based Flip-Chip Micro-LEDs," *IEEE J. Electron Devices Soc.* **6**, 475–479 (2018).
14. M.-C. Tseng, C.-L. Chen, N.-K. Lai, S.-I. Chen, T.-C. Hsu, Y.-R. Peng, and R.-H. Horng, "P-side-up thin-film AlGaInP-based light emitting diodes with direct ohmic contact of an ITO layer with a GaP window layer," *Opt. Express* **22**(S7), A1862–A1867 (2014).
15. J. F. C. Carreira, A. D. Griffiths, E. Xie, B. J. E. Guilhabert, J. Herrnsdorf, R. K. Henderson, E. Gu, M. J. Strain, and M. D. Dawson, "Direct integration of micro-LEDs and a SPAD detector on a silicon CMOS chip for data communications and time-of-flight ranging," *Opt. Express* **28**(5), 6909–6917 (2020).
16. M. Meitl, Z. Zhu, V. Kumar, K. Lee, X. Feng, Y. Huang, I. Adesida, R. Nuzzo, and J. Rogers, "Transfer printing by kinetic control of adhesion to an elastomeric stamp," *Nat. Mater.* **5**(1), 33–38 (2006).
17. H. Zhang and J. A. Rogers, "Recent Advances in Flexible Inorganic Light Emitting Diodes: From Materials Design to Integrated Optoelectronic Platforms," *Adv. Opt. Mater.* **7**(2), 1800936 (2019).
18. A. J. Trindade, B. Guilhabert, E. Y. Xie, R. Ferreira, J. J. D. McKendry, D. Zhu, N. Laurand, E. Gu, D. J. Wallis, I. M. Watson, C. J. Humphreys, and M. D. Dawson, "Heterogeneous integration of gallium nitride light-emitting diodes on diamond and silica by transfer printing," *Opt. Express* **23**(7), 9329–9338 (2015).
19. X. Lin, D. Liu, G. Lin, Q. Zhang, N. Gao, D. Zhao, R. Jia, Z. Zuo, and X. Xu, "Periodic indentation patterns fabricated on AlGaInP light emitting diodes and their effects on light extraction," *RSC Adv.* **4**(108), 63143–63146 (2014).
20. S. Franssila, *Introduction to Microfabrication* (John Wiley & Sons, Ltd, 2010).
21. R. P. Mildren, *Intrinsic Optical Properties of Diamond* (John Wiley & Sons, Ltd, 2013), , chap. 1, pp. 1–34.
22. M. Z. Afgani, H. Haas, H. Elgala, and D. Knipp, "Visible light communication using OFDM," in *2nd International Conference on Testbeds and Research Infrastructures for the Development of Networks and Communities, 2006. TRIDENTCOM 2006.*, (2006), pp. 6–134.
23. J. Armstrong and A. J. Lowery, "Power efficient optical OFDM," *Electron. Lett.* **42**(6), 370–372 (2006).
24. H. Haas, L. Yin, Y. Wang, and C. Chen, "What is LiFi?" *J. Lightwave Technol.* **34**(6), 1533–1544 (2016).
25. R. Bian, I. Tavakkolnia, and H. Haas, "15.73 Gb/s Visible Light Communication With Off-the-Shelf LEDs," *J. Lightwave Technol.* **37**(10), 2418–2424 (2019).
26. H. Chun, S. Rajbhandari, G. Faulkner, D. Tsonev, E. Xie, J. J. D. McKendry, E. Gu, M. D. Dawson, D. C. O'Brien, and H. Haas, "LED Based Wavelength Division Multiplexed 10 Gb/s Visible Light Communications," *J. Lightwave Technol.* **34**(13), 3047–3052 (2016).
27. Y. Wang, X. Huang, L. Tao, J. Shi, and N. Chi, "4.5-Gb/s RGB-LED based WDM visible light communication system employing CAP modulation and RLS based adaptive equalization," *Opt. Express* **23**(10), 13626–13633 (2015).
28. E. Xie, X. He, M. S. Islim, A. A. Purwita, J. J. D. McKendry, E. Gu, H. Haas, and M. D. Dawson, "High-Speed Visible Light Communication Based on a III-Nitride Series-Biased Micro-LED Array," *J. Lightwave Technol.* **37**(4), 1180–1186 (2019).